HYDROGEN GENERATION FROM HYDROUS HYDRAZINE DECOMPOSITION OVER SOLUTION COMBUSTION SYNTHESIZED NICKEL-BASED CATALYSTS

by

**Wooram Kang**

A Dissertation

Submitted to the Faculty of Purdue University

In Partial Fulfillment of the Requirements for the degree of

Doctor of Philosophy
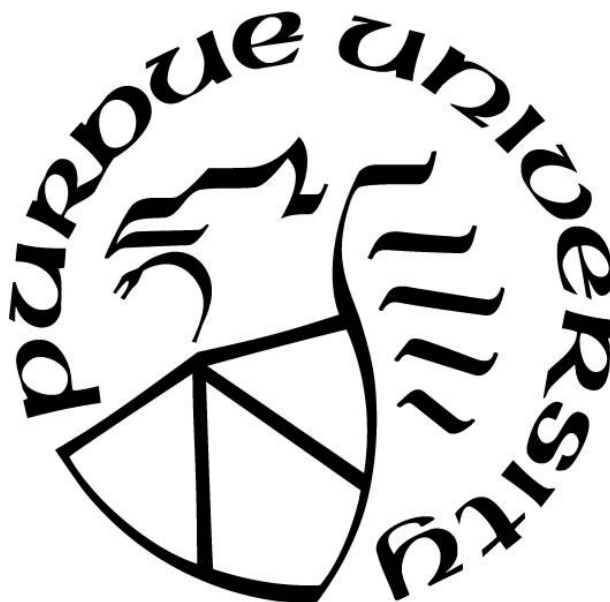
Davidson School of Chemical Engineering

West Lafayette, Indiana

August 2019

THE PURDUE UNIVERSITY GRADUATE SCHOOL
STATEMENT OF COMMITTEE APPROVAL

Dr. Arvind Varma, Chair

    Davidson School of Chemical Engineering

Dr. Rajamani Gounder

    Davidson School of Chemical Engineering

Dr. Vilas Pol

    Davidson School of Chemical Engineering

Dr. Jay Gore

    School of Mechanical Engineering

Approved by:

    Dr. John Morgan

        Head of the Graduate Program

For my family, with love

ACKNOWLEDGMENTS

I would first like to express my deep and sincere gratitude to my advisor, Prof. Arvind Varma for his guidance and support throughout the period of my research. Despite his cancer diagnosis and ongoing treatment, his untiring passion for the research inspired me to pursue my own passions. It was a great privilege and honor to work and study under his guidance.

I would also like to thank Prof. Gounder, Prof. Pol and Prof. Gore for serving on my committee. Their valuable comments helped strengthen this dissertation.

I would like to acknowledge my research group members, Dr. Hyun-Tea Hwang, Dr. Shinbeom Lee, Dr. Gregory Honda, Dr. Yang Xiao, Ryan Adams and Rexonni Lagare for their encouragement and support on my research work.

I am grateful to the visiting scholars, Dr. Derya Ozgur, Dr. Xiahong Wang, Chunxiao Xu, Heng Guo, Eric Walter and Yuan Wang. It was a great honor to work with them and to know each other.

I am thankful to my many colleagues and friends in our department, the alumni association of Korea University at Purdue University and the Energy Materials and Processes Laboratory at Korea University.

I appreciate my parent, Jae Gu Kang and Jong Bun Jang, and my sister, Hyerin Kang, for their endless love and support while I've been away.

Last but not least, I am very much thankful to my wife, Kuijung Lee, for her enduring love and support, and my lovely children, Naeun Sophia Kang and Eunchan Andrew Kang. This journey towards a Ph.D. degree would not have been possible without the dedicated support of my family.

TABLE OF CONTENTS

LIST OF TABLES

LIST OF FIGURES

NOMENCLATURE

a	Catalyst activity
A_i	Integrated area of XPS subpeak i
$C_{N_2H_{4,0}}$	Initial concentration of hydrous hydrazine (mol L^{-1})
$C_{N_2H_4}$	Concentration of hydrous hydrazine at any time $t>0$ (mol L^{-1})
C_{N_2}	Concentration of nitrogen at any time (mol L^{-1})
d	Deactivation order
d_p	Mean size of crystallites or particles (nm or µm)
d_{metal}	Metal dispersion
E_a	Apparent activation energy (kJ mol^{-1})
g	Gas phase
ΔH_{ads}	Enthalpy change of the adsorption process (kJ mol^{-1})
k_0, k_1, k_n	Reaction rate constant of power-law model (0, 1, nth orders) (mol^{1-n} L^n g^{-1} min^{-1})
k_{LH}	Reaction rate constant of Langmuir-Hinshelwood model (mol g^{-1} min^{-1})
k_d	Deactivation rate constant (L^m mol^{-m} min^{-1})
K	Adsorption equilibrium constant (L mol^{-1})
K'	Adsorption pre-exponential factor (L mol^{-1})
K'_0	Adsorption equilibrium constant at reference temperature T_0 (L mol^{-1})
l	Liquid phase
m	Reaction order with respect to concentration of nitrogen for catalyst deactivation

m_{cat}	Weight of catalyst (g)
n	Reaction order with respect to concentration of hydrous hydrazine
$n(i)$	Moles of component i (mol)
N	Total number of experimental data points
P	Pressure of reactor (psi)
t	Time (min or hour)
T	Reaction temperature (°C or K)
T_0	Reference temperature (K)
T_{ad}	Adiabatic combustion temperature (°C)
T_{ig}	Ignition temperature (°C)
T_{max}	Maximum combustion temperature (°C)
r	Reaction rate (h^{-1})
$r_{N_2H_4}$	Maximal reaction rate of N_2H_4 consumption without deactivation (mol L^{-1} min^{-1})
$r'_{N_2H_4}$	Reaction rate of N_2H_4 consumption involving deactivation kinetics (mol L^{-1} min^{-1})
R	Ideal gas constant (8.314 J mol^{-1} K^{-1})
ΔS^o	Entropy change of the adsorption process (kJ mol^{-1} K^{-1})
V	Volume of reactor (L)
V_{sol}	Volume of reactive solution (L)
$X_{i,obs}$, $X_{i,calc}$	i^{th} observed and calculated conversion of hydrous hydrazine (%)
α	Selectivity towards hydrogen generation from hydrous hydrazine (%)
β	Full width at half maximum

θ	Surface coverage of adsorbed hydrous hydrazine on catalyst surface
θ_B	Bragg's diffraction angle
λ	X-ray wavelength of CuKα radiation (= 1.54 Å)
ϕ	Fuel-to-oxidizer ratio

ABSTRACT

Author: Kang, Wooram. PhD
Institution: Purdue University
Degree Received: August 2019
Title: Hydrogen Generation from Hydrous Hydrazine Decomposition over Solution
   Combustion Synthesized Nickel-based Catalysts
Committee Chair: Arvind Varma

Hydrous hydrazine ($N_2H_4 \cdot H_2O$) is a promising hydrogen carrier for convenient storage and transportation owing to its high hydrogen content (8.0 wt%), low material cost and stable liquid state at ambient temperature. Particularly, generation of only nitrogen as byproduct, in addition to hydrogen, thus obviating the need for on-board collection system for recycling, ability to generate hydrogen at moderate temperatures (20-80 °C) which correspond to the operating temperature of a proton exchange membrane fuel cell (PEMFC), and easy recharging using current infrastructure of liquid fuels make hydrous hydrazine a promising hydrogen source for fuel cell electric vehicles (FCEVs). Since hydrogen can be generated from catalytic hydrazine decomposition, the development of active, selective and cost-effective catalysts, which enhance the complete decomposition ($N_2H_4 \rightarrow N_2+2H_2$) and simultaneously suppress the incomplete decomposition ($3N_2H_4 \rightarrow 4NH_3+N_2$), remains a significant challenge.

In this dissertation, CeO_2 powders and various Ni-based catalysts for hydrous hydrazine decomposition were prepared using solution combustion synthesis (SCS) technique and investigated. SCS is a widely employed technique to synthesize nanoscale materials such as oxides, metals, alloys and sulfides, owing to its simplicity, low cost of precursors, energy- and time-efficiency. In addition, product properties can be effectively tailored by adjusting various synthesis parameters which affect the combustion process.

The first and second parts of this work (Chapters 2 and 3) are devoted to investigating the correlation between the synthesis parameters, combustion characteristics and properties of the resulting powder. A series of CeO_2, which is a widely used material for various catalytic applications and a promising catalyst support for hydrous hydrazine decomposition, and Ni/CeO_2 nanopowders as model catalysts for the target reaction were synthesized using conventional SCS technique. This demonstrated that crystallite size,

surface property and concentration of defects in CeO_2 structure which strongly influence the catalytic performance, can be effectively controlled by varying the synthesis parameters such as metal precursor (oxidizer) type, reducing agent (fuel), fuel-to-oxidizer ratio and amount of gas generating agent. The tailored CeO_2 powder exhibited small CeO_2 crystallite size (7.9 nm) and high surface area (88 m^2/g), which is the highest value among all prior reported SCS-derived CeO_2 powders. The Ni/CeO_2 catalysts synthesized with 6 wt% Ni loading, hydrous hydrazine fuel and fuel-to-oxidizer ratio of 2 showed 100% selectivity for hydrogen generation and the highest activity (34.0 h^{-1} at 50 °C) among all prior reported catalysts containing Ni alone for hydrous hydrazine decomposition. This superior performance of the Ni/CeO_2 catalyst is attributed to small Ni particle size, large pore size and moderate defect concentration.

As the next step, SCS technique was used to develop more efficient and cost-effective catalysts for hydrous hydrazine decomposition. In the third part (Chapter 4), noble-metal-free NiCu/CeO_2 catalysts were synthesized and investigated. The characterization results indicated that the addition of Cu to Ni/CeO_2 exhibits a synergistic effect to generate significant amounts of defects in the CeO_2 structure which promotes catalytic activity. The 13 wt% $Ni_{0.5}Cu_{0.5}$/CeO_2 catalysts showed 100% H_2 selectivity and 5.4-fold higher activity (112 h^{-1} at 50 °C) as compared to the 13 wt% Ni/CeO_2 (20.7 h^{-1}). This performance is also superior to that of most reported non-noble metal catalysts and is even comparable to several noble metal-based catalysts. In the fourth part (Chapter 5), low Pt loading NiPt/CeO_2 catalysts were studied. The modified SCS technique was developed and applied to prepare NiPt/CeO_2 catalysts, that overcomes the typical problem of conventional SCS which leads to deficiency of Pt at catalyst surface due to the diffusion of Pt into bulk CeO_2. The $Ni_{0.6}Pt_{0.4}$/CeO_2 catalysts with 1 wt% Pt loading exhibited high activity (1017 h^{-1} at 50 °C) along with 100% H_2 selectivity owing to the optimum composition of NiPt alloy, high metal dispersion and a large amount of CeO_2 defects. Its activity is higher than most of the reported NiPt-based catalysts which typically contain high Pt loading (3.6-42 wt%).

Next, the intrinsic kinetics of hydrous hydrazine decomposition over the NiPt/CeO_2 catalysts, which are necessary for efficient design and optimization of the hydrous hydrazine-based hydrogen generator system, were investigated (Chapter 6). From the

experimental data obtained at different reaction temperatures, the intrinsic kinetic model based on the Langmuir-Hinshelwood mechanism was established. The developed model provides good predictions with the experimental data, especially over a wide range of initial reactant concentration, describing well the variation of reaction order from low to high reactant concentration.

Finally, the conclusions of the dissertation and recommendations for future work are summarized in Chapter 7.

CHAPTER 1.   INTRODUCTION

1.1   Hydrogen as alternative energy carrier in transportation applications

Concerns about energy supply security and climate change prompt one to reduce the reliance on fossil fuels as primary energy carrier while stimulating the development of clean and sustainable energy carriers. Hydrogen (H_2) has been considered as a promising alternative energy carrier. Hydrogen is the most abundant element on Earth and is a sustainable source since hydrogen can be obtained from water and biomass. When it is used in a fuel cell to generate power, no air pollutants and greenhouse gases are produced, and its energy efficiency is 2-3 times higher than that of traditional combustion technologies.

Accordingly, efforts are globally underway to transform the energy economy from one dependent on fossil fuels to that based on hydrogen. This movement is particularly notable in the transportation sector. The first mass-produced hydrogen fuel cell electric vehicles (FCEVs), which utilize polymer electrolyte membrane fuel cells (PEMFCs), were introduced in 2013-2014 by Hyundai, Toyota and Daimler [1]. As shown in Figure 1.1, the number of FCEVs on the road is increasing gradually [2]. In addition, according to the national hydrogen scenarios report, sales of FCEVs will reach 8.9 million per year by 2050, which is roughly half of all light duty vehicle sales in the U.S [3]. However, the adoption of FCEVs has so far been heavily dictated by government policy instruments, such as financial incentives, sales mandates and free vehicle charging [1]. It implies that there are still many technological barriers in FCEVs, preventing its widespread use.
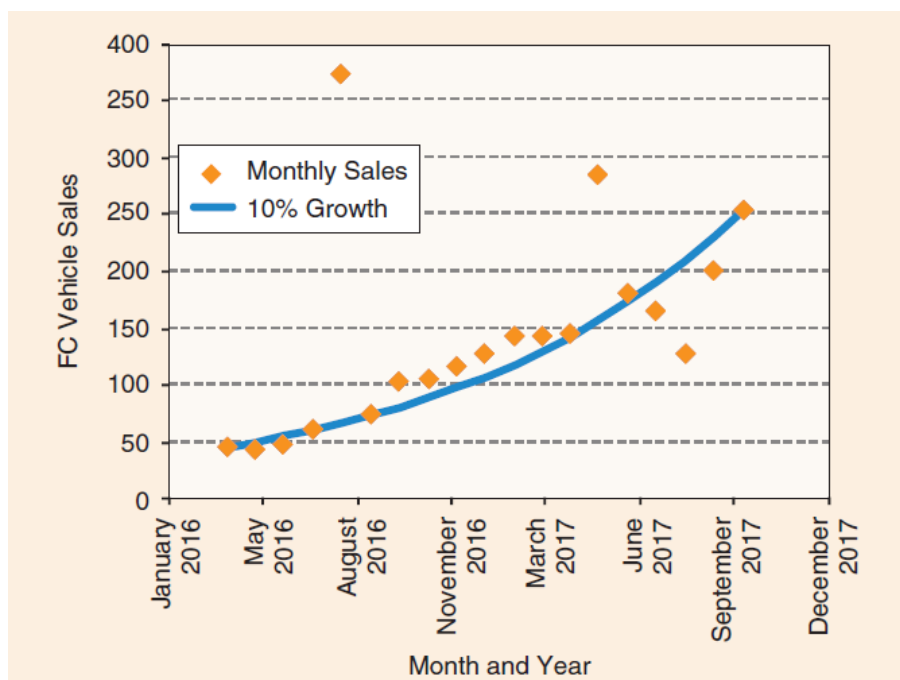
Figure 1.1 The monthly U.S. FCEV sales from April 2016 to October 2017 [2]

Hydrogen is the lightest gas and hence has low volumetric energy density although its mass energy density is much higher as compared to conventional fuels such as gasoline and diesel (Figure 1.2) [4-6]. This issue presents significant difficulty in storing large quantity of hydrogen for FCEVs. All FCEVs which are currently available on the market adopt the high-pressure hydrogen storage tank system (700 bar). As shown in Figure 1.2, its volumetric energy density (~1.3 kWh/L) remains poor and is lower than the ultimate technical system target (1.7 kWh/L) of onboard hydrogen storage for light-duty FCEVs proposed by the U.S. Department of Energy [7]. Despite the high energy efficiency of a fuel cell system, due to the low volumetric energy density of hydrogen gas, the average driving range of FCEVs on the market is about 350 miles, which is somewhat shorter than that of gasoline cars (400 miles).
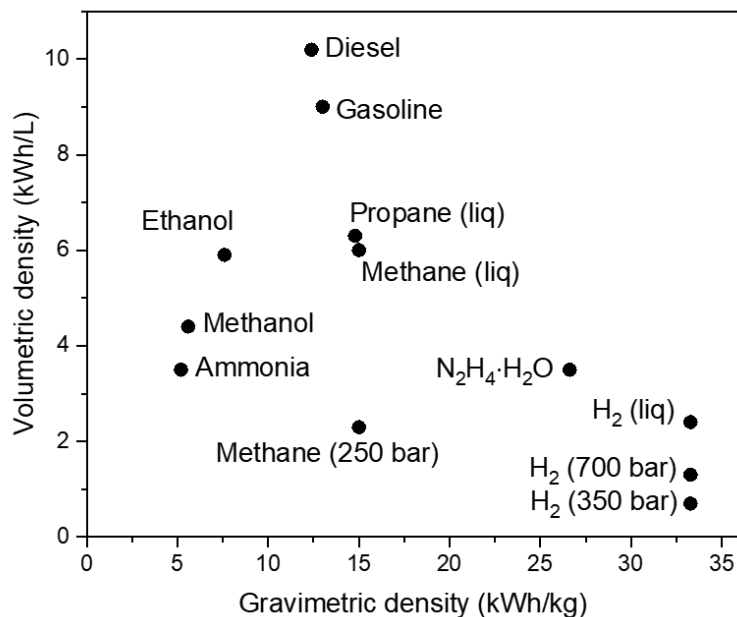
Figure 1.2 Gravimetric and volumetric energy density of various H_2 carriers (Data sourced from refs. [4-6])

In addition, using the high-pressure hydrogen storage tank system is responsible for the high cost of hydrogen fuel to customers. The average price at retail hydrogen fueling stations currently operating in California is \$13-16 per gallon gasoline equivalent (gge) which is about 4~5 times as much as gasoline fuel (~\$3 per gallon) [8]. Most of this high cost (86-88%) is related to delivery, storage and refueling of hydrogen gas (Figure 1.3) [8]. Hence, efficient hydrogen carrier which can overcome the drawbacks of compressed hydrogen storage is a key for the widespread commercialization of FCEVs [9,10].
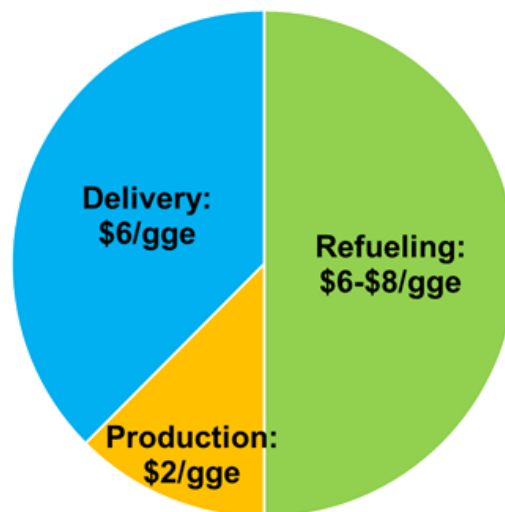
Figure 1.3 Major components of the average retail price of hydrogen fuel in U.S., 2018 [8]

1.2   Hydrous hydrazine as H_2 carrier for FCEVs

Towards this aim, various liquid-phase hydrogen carriers have received much attention as a feasible alternative owing to their convenient transportation, handling, refueling, and potential use of existing infrastructure for conventional fuels such as gasoline and diesel, which can significantly reduce the price of hydrogen fuel at retail hydrogen stations [11,12]. Several liquid-phase hydrogen carriers are presented in Table 1.1.

Table 1.1 Various liquid-phase hydrogen carriers [13-19]

H_2 carriers	H_2 capacity (wt%)	Operating temperature (°C)	Yield (%)	H_2 generation rate (mol/mol$_{cat}$/min)	Catalyst
Indoline (C_8H_9N)	1.7	>100	81	1.35 (at 100 °C)	Pd/silica
H_8-N-ethlyindole ($C_{10}H_{19}N$)	5.23	160–190	100	0.13 (at 190 °C)	Pd/Al$_2$O$_3$
H_{18}-dibenzyltoluene ($C_{21}H_{38}$)	6.2	>250	97	166.52 (at 310 °C)	Pt/C
H_{12}-N-ethyl carbazole ($C_{14}H_{25}N$)	5.8	200–270	95	176.79 (at 230 °C)	Pt/Al$_2$O$_3$
Tetrahydroquinoline ($C_9H_{11}N$)	2.9	138	100	0.08 (at 138 °C)	Ir-complex
2-aminoethanol (C_2H_7ON)	6.6	105-135	77	0.05 (at 105 °C)	Ru-complex
Formic acid (CH_2O_2)	4.4	25-90	100	63.50 (at 50 °C)	Pd/PDA-rGO
Hydrous hydrazine ($N_2H_4 \cdot H_2O$)	8.0	25-80	100	34.27 (at 50 °C)	NiPt/PDA-rGO

Among them, hydrous hydrazine such as hydrazine monohydrate ($N_2H_4 \cdot H_2O$) is promising for FCEV application owing to its high hydrogen content (8.0 wt%), low material cost as compared to other chemical hydrides and ability to generate hydrogen at moderate temperatures which correspond to the operating temperature of a PEMFC used for FCEVs [5,20]. In addition, generation of only nitrogen as byproduct obviates the need for on-board collection system for spent fuel regeneration.

Basically, hydrogen can be generated from hydrazine decomposition which occurs via two competing pathways: complete decomposition [$N_2H_4 \, (l) \rightarrow N_2 \, (g) + 2H_2 \, (g)$] and incomplete decomposition [$3N_2H_4 \, (l) \rightarrow 4NH_3 \, (g) + N_2 \, (g)$]. Only the complete decomposition leads to hydrogen generation while the incomplete decomposition liberates

ammonia which is poison for PEMFCs [21,22]. Therefore, to maximize the efficiency of hydrous hydrazine as an on-board hydrogen carrier, one must develop highly active and selective catalysts which facilitate hydrogen generation and suppress the incomplete decomposition.

1.3   Solution combustion synthesis

Solution combustion synthesis (SCS) is a self-sustained thermal process where the main source of heat comes from combustion reaction between reducing agent (fuel) and metal oxidizer. In general, since the combustion reaction is completed within a short time with high temperature, various solid products (e.g., metals, metal oxides, alloys and sulfides) can be obtained simply and rapidly [23,24]. More importantly, the mixing of precursors in aqueous solution at the molecular level and the generation of a large amount of gaseous byproducts during combustion allow the formation of highly porous nanosized products with uniform composition and high metal dispersion. Further, the properties of products are influenced strongly by combustion characteristics which can be also influenced by adjusting the SCS parameters such as ratio of precursor oxidizers, fuel-to-oxidizer ratio and fuel type [24,25]. Thus, the SCS technique can enable one to effectively control the combustion process, by optimizing the SCS parameters and hence to tailor catalysts for a specific application. A schematic representation of the SCS technique is shown in Figure 1.4.
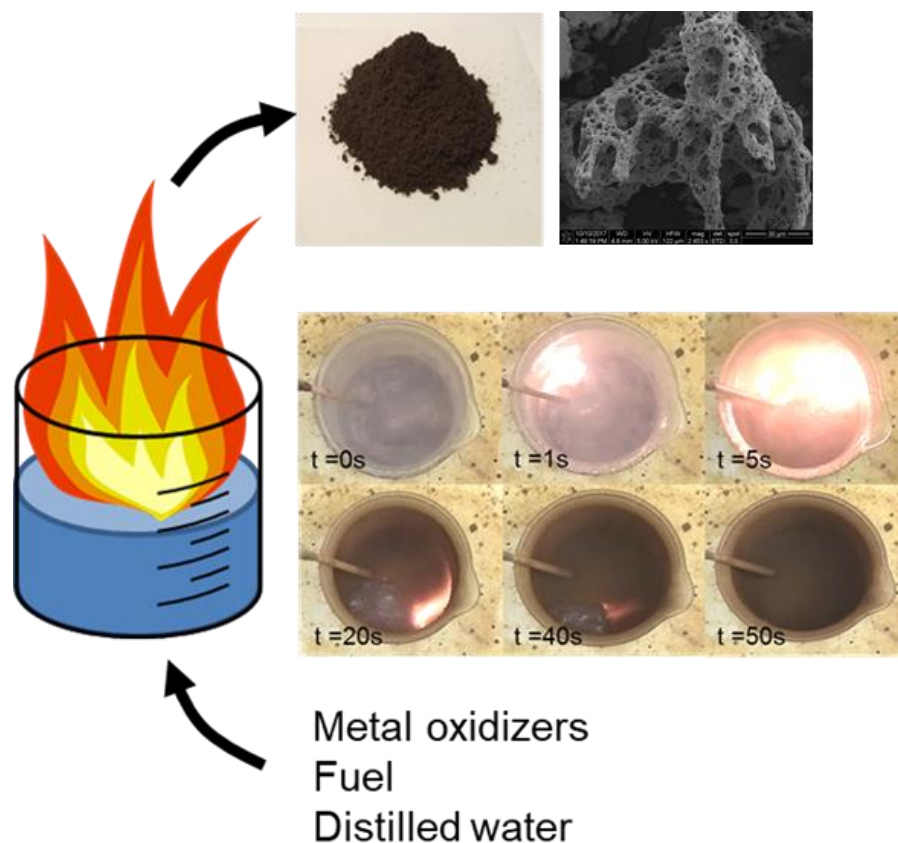
Figure 1.4 Schematic representation of solution combustion synthesis (SCS)

The typical temperature-time profile of an aqueous precursor solution during SCS is shown in Figure 1.5. It shows that after evaporation of the solvent from the aqueous precursor solution, ignition occurs, leading to combustion along with gas evolution. During combustion, the temperature rapidly increases to a maximum value, followed by rapid cooling due to gas evolution and heat loss to the surroundings. Therefore, combustion characteristics of SCS can be expressed in terms of the ignition temperature, flame temperature and the amount of gases released during combustion. The ignition temperature is related to the temperature of a specific phase transformation, that is, decomposition of the oxidizer or fuel in mixture [25-27]. The maximum combustion temperature refers to

the heating effect of combustion. Adequate amount of heat, namely adequate maximum combustion temperature, is necessary for sustaining combustion and formation of products with desired crystallinity but too high temperature may cause agglomeration and sintering of nanoparticles. On the other hand, the gas evolution during combustion dissipates the heat, restrains agglomeration and promotes the porosity of products. Generally, combustion temperatures such as ignition temperature and maximum combustion temperature can be determined by measuring the temperature change using sensitive thermocouple while the amount of gases released during combustion can be estimated from the stoichiometric equilibrium combustion reaction equation.
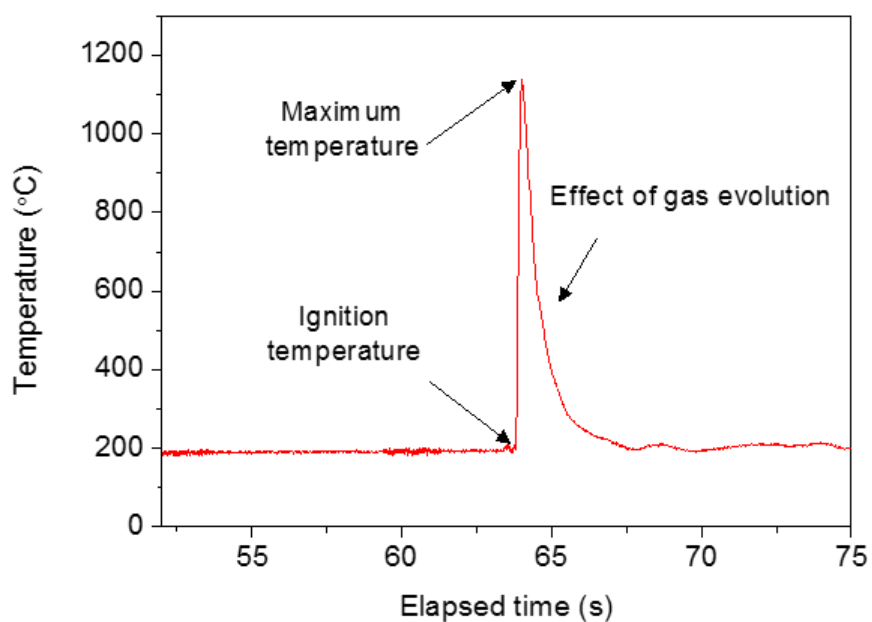
Figure 1.5 Typical temperature-time profile of a precursor solution during combustion

1.4   Research objectives

This study is directed towards developing active, selective and cost-effective catalysts using SCS technique for the decomposition of hydrous hydrazine. For SCS, understanding the effects of various SCS parameters on combustion characteristics and reaction mechanism, and their correlation with product properties, is important to effectively control the synthesis process and to find optimum conditions where the product has favorable properties for the target reaction. Towards this aim, cerium oxide (CeO_2) and nickel catalyst supported on CeO_2 (Ni/CeO_2) were selected as a model material and a model catalyst, respectively, for SCS study and prepared with systematic variation of SCS parameters. CeO_2 has been widely used as a component or support of catalysts for various catalytic applications including the decomposition of hydrous hydrazine owing to its unique properties (e.g. ability to disperse metals on its surface and strong interaction with metals) to enhance catalytic performance [28]. Ni has been also widely studied as a catalyst component for hydrous hydrazine decomposition owing to its decent activity and low cost as compared to other active metals such as Rh and Ir [29]. Although there are some prior studies using SCS to produce CeO_2 and Ni/CeO_2, they have not systematically addressed the quantitative effects of synthesis parameters on product properties, and the combustion mechanism for the formation of CeO_2 and Ni/CeO_2, has also not been investigated. Moreover, there have been no studies preparing catalysts using SCS technique for hydrous hydrazine decomposition.

Various catalysts containing noble (Ir, Rh, Pd and Pt) and transition metals (Ni, Fe, Co and Cu) have been investigated for efficient catalytic decomposition of hydrous hydrazine [30-38]. Since it was reported that the addition of Pt significantly promotes

catalytic property of Ni for hydrous hydrazine decomposition, NiPt bimetallic catalysts on various supports are currently the most promising ones, exhibiting 100% selectivity towards hydrogen generation and high activity. All the reported catalysts, however, contain large amount of Pt up to 42 wt% [39-50]. Therefore, to make the on-board system based on hydrous hydrazine more affordable, it is essential to substantially decrease or eliminate the amount of Pt in catalysts, without losing the catalytic performance. The obtained knowledge from the SCS studies of CeO_2 and Ni/CeO_2 can be utilized to develop efficient and cost-effective Ni-based catalysts supported on CeO_2 (e.g. noble-metal-free bimetallic or low Pt loading catalysts).

Recently, beyond the development of efficient catalysts for the decomposition of hydrous hydrazine, the reaction studies under practical conditions (e.g. continuous hydrogen generation, non-diluted $N_2H_4 \cdot H_2O$ and large scale) have been reported [48,51]. In contrast, there are very few kinetic studies for the reaction which is essential for the design of reactor and to examine the feasibility of hydrous hydrazine-based hydrogen generator system for FCEVs. Only one kinetic model based on power-law expression has been reported [49]. This study found that the reaction order varies with the concentration of hydrous hydrazine and proposed multiple parameter sets to capture the reaction behavior according to the range of hydrous hydrazine concentration. Therefore, a more robust and reliable kinetic model to describe the reaction behavior over various operating conditions is required. In summary, the research objectives of this dissertation are as follows:

- Synthesize CeO_2 and Ni/CeO_2 catalysts using SCS and investigate the effects of SCS parameters on combustion characteristics, reaction mechanism and their correlation with product properties, and determine the SCS condition where the products have favorable properties for hydrous hydrazine decomposition.

- Evaluate catalytic performance of SCS-derived Ni/CeO_2 catalysts for hydrous hydrazine decomposition and compare with that of reported catalysts prepared by different methods.

- Develop active, selective and cost-effective Ni-based catalysts (e.g. noble-metal-free bimetallic or low Pt loading catalysts) for hydrous hydrazine decomposition using SCS technique.

- Determine intrinsic reaction kinetics for hydrous hydrazine decomposition and develop a robust and reliable kinetic model.

CHAPTER 2. SOLUTION COMBUSTION SYNTHESIS OF HIGH SURFACE AREA CERIUM OXIDE POWDERS FOR CATALYTIC APPLICATIONS

2.1 Introduction

Cerium (IV) oxide (CeO_2), one of the most important rare-earth materials, is technologically important owing to its widespread applications such as i) catalysts for fluid cracking in oil refineries [52], hydrocarbon oxidation [53], methanol dissociation [54], water–gas shift reaction [55] and automotive exhaust treatment [56,57], (ii) electrolytes for solid oxide fuel cells [58], (iii) oxygen sensors [59], (iv) polishing agents [60] and (v) anodes for solar cells [61]. Recently, nanocrystalline CeO_2 has received much attention in catalytic applications owing to its unique redox properties, high oxygen storage capacity and ability to disperse metal on its surface [28,62,63]. One of the most beneficial properties for catalytic applications is high surface area which can provide more active sites and thus promote catalytic activity. Specific surface area of commercial CeO_2 materials, however, is low (<10 m^2/g) since these are prepared by calcination of cerium oxalate or hydroxide [28,64,65]. Accordingly, synthesis of high surface area CeO_2 is among the challenges in catalytic applications.

Towards this aim, various methods have been used to develop high surface area CeO_2 nanomaterials [66-72]. Up to now the specific surface areas of CeO_2 reported in the literature are as high as 349 m^2/g for solvothermal synthesis of unheated ceria aerogels from cerium alkoxides in alcoholic solvent and supercritical drying [73], 277 m^2/g for combined sol-gel and solvothermal synthesis of cerium alkoxides [65], and 250 m^2/g for micro-emulsion synthesis of cerium nitrate with surfactants [74]. These methods, however,

have some limitations for practical applications because they require expensive precursors, surfactants and/or complicated preparation processes such as multi-step synthesis, harsh synthesis conditions and long reaction time. In this respect, solution combustion synthesis (SCS), a non-conventional one-step method, is a promising approach for the production of nanosized materials with high surface area [24]. Although there are some prior studies using SCS to produce CeO_2, they have not systematically addressed the quantitative effects of synthesis parameters on product properties and the combustion mechanism for the formation of CeO_2 has also not been investigated. Most of the studies have focused on the effect of a new combustion system (e.g. different fuel type or addition of template) on properties of CeO_2 and not on a systematic investigation as in the present work [75-79].

In this chapter, nanocrystalline CeO_2 powders were prepared by varying the SCS parameters including fuel type (glycine and hydrous hydrazine), cerium oxidizer (cerium nitrate hexahydrate and ceric ammonium nitrate), fuel-to-oxidizer ratio and addition of gas generating agent (ammonium nitrate). Detailed characterization was conducted to determine the combustion characteristics and the physical properties of CeO_2 powder. Finally, the combustion mechanism for the formation of CeO_2 and the correlation between the SCS parameters and the product properties was established. In addition, the SCS condition, where the CeO_2 powder has the highest specific surface area, was determined.

2.2   SCS systems under investigation

Cerium nitrate hexahydrate and cerium ammonium nitrate were used as oxidizer precursors because both not only have good solubility in water and relatively low decomposition temperature that results in the formation of active component for

combustion reaction, but also are relatively inexpensive and readily available commercially. For similar reasons, glycine and hydrous hydrazine were selected as typical carbonaceous and non-carbonaceous fuels, respectively. In addition, it has been reported that both reductive compounds easily form complexes with various metal ions, thus facilitating homogeneous mixing of cations in solutions [25,77,80,81]. Based on cerium precursor and fuel types, the investigated combustion systems can be classified into four cases, for which the stoichiometric equations under equilibrium conditions are presented below.

(i) Cerium nitrate hexahydrate [Ce(NO$_3$)$_3$·6H$_2$O] and glycine(C$_2$H$_5$NO$_2$)

$$Ce(NO_3)_3 \cdot 6H_2O + (\phi + \frac{5}{9})C_2H_5NO_2 + \frac{9}{2}(\phi - 1)O_2$$

$$\rightarrow CeO_2 + \left[2\left(\phi + \frac{5}{9}\right)\right]CO_2 + \frac{\left[3 + \left(\phi + \frac{5}{9}\right)\right]}{2}N_2 + \frac{\left[12 + 5\left(\phi + \frac{5}{9}\right)\right]}{2}H_2O \quad (2.1)$$
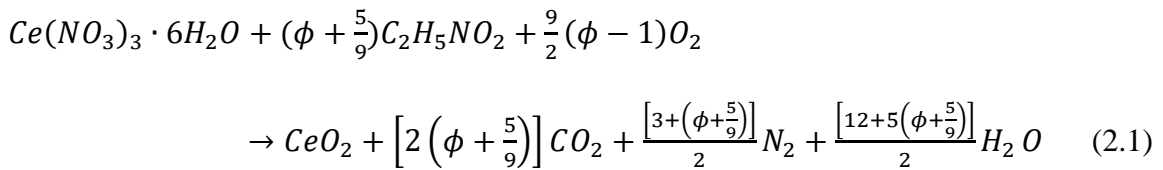
(ii) Cerium ammonium nitrate [(NH$_4$)$_2$Ce(NO$_3$)$_6$] and glycine(C$_2$H$_5$NO$_2$)

$$(NH_4)_2Ce(NO_3)_6 + (\phi + \frac{5}{3})C_2H_5NO_2 + \frac{9}{4}(\phi - 1)O_2$$

$$\rightarrow CeO_2 + \left[2\left(\phi + \frac{5}{3}\right)\right]CO_2 + \frac{\left[8 + \left(\phi + \frac{5}{3}\right)\right]}{2}N_2 + \frac{\left[8 + 5\left(\phi + \frac{5}{3}\right)\right]}{2}H_2O \quad (2.2)$$
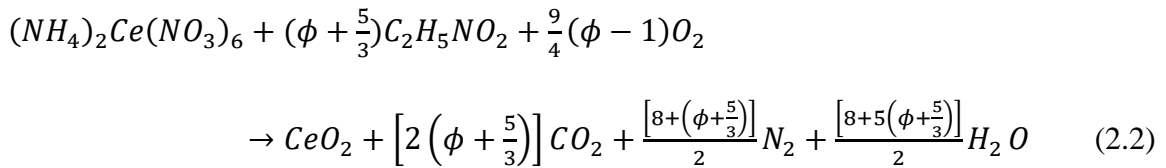
(iii) Cerium nitrate hexahydrate [Ce(NO$_3$)$_3$·6H$_2$O] and hydrous hydrazine (N$_2$H$_4$·H$_2$O)

$$Ce(NO_3)_3 \cdot 6H_2O + (\phi + 5/2)N_2H_4 \cdot H_2O + (\phi - 1)O_2$$

$$\rightarrow CeO_2 + \frac{[3 + 2(\phi + 5/2)]}{2}N_2 + [6 + 3(\phi + 2.5)]H_2O \quad (2.3)$$
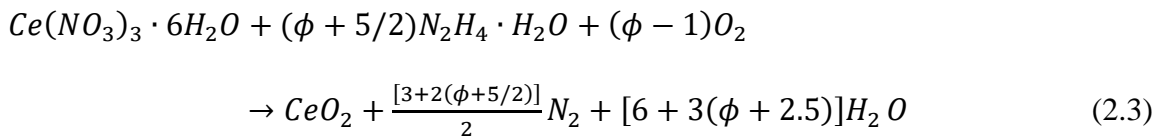
(iv) Cerium ammonium nitrate [$(NH_4)_2Ce(NO_3)_6$] and hydrous hydrazine ($N_2H_4 \cdot H_2O$)

$$(NH_4)_2Ce(NO_3)_6 + (\phi + 5)N_2H_4 \cdot H_2O + (\phi - 1)O_2$$

$$\rightarrow CeO_2 + \frac{[8+2(\phi+5)]}{2}N_2 + \frac{[8+6(\phi+5)]}{2}H_2O \qquad (2.4)$$
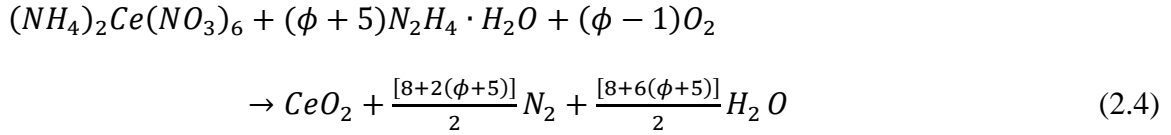
In the above equations, ϕ is defined as the fuel-to-oxidizer ratio. ϕ=1 means that the initial mixture does not require atmospheric oxygen for complete oxidation of fuel, whereas ϕ>1 and ϕ<1 imply fuel-rich and fuel-lean conditions, respectively [25]. In addition, in some experiments, ammonium nitrate was used as a gas generating agent to increase surface area of products [25]. For ease of comparison in cases where ammonium nitrate was used, the molar ratio of ammonium nitrate to metal nitrate (AN/MN ratio) was defined.

2.3   Experimental

2.3.1   Solution combustion synthesis procedure

The CeO_2 powders were prepared by solution combustion synthesis (SCS). In a typical experiment, a cerium precursor [$(NH_4)_2Ce(NO_3)_6$ (CAN, Alfa Aesar, ≥98%) or $Ce(NO_3)_3.6H_2O$ (CN, Alfa Aesar, ≥99.5%)], a fuel [NH_2CH_2COOH (GL, J.T.Baker, ≥99.5%) or $N_2H_4 \cdot H_2O$ (HH, Alfa Aesar, ≥99%)] and a gas generating agent [NH_4NO_3 (AN, Alfa Aesar, ≥95%)] were dissolved in minimum amount of distilled water with different fuel-to-oxidizer ratios (ϕ=0.5-3) and molar ratios of ammonium nitrate to metal nitrate (AN/MN ratio=0-9). The mixture was then heated over a hot plate to induce self-sustained combustion. At the point of complete dehydration (within 5–10 min), the solution started to boil with frothing and foaming, and ignition took place, followed by rapid increase of temperature and evolution of a large quantity of gases. Meanwhile, the temperature change

during combustion was monitored using a K-type thermocouple (0.125 mm diameter) in order to determine the ignition temperature (T_{ig}) and the maximum combustion temperature (T_{max}). The experimental error for the measurement of ignition temperature and maximum combustion temperature was determined to be less than ±5 °C and ±10%, respectively. The standard deviation is indicated by error bars. The combustion behavior was also monitored by video recording (Phantom V5.1, Vision Research Inc.).

2.3.2 Thermodynamic calculations of adiabatic combustion temperature

To calculate the adiabatic temperature (T_{ad}) and equilibrium products for a given SCS condition [Eqs. (2.1-4)], thermodynamic calculations were conducted using the "Thermo" software package [82]. This software is based on optimizing the Gibbs free energy of multicomponent and multiphase combustion systems.

2.3.3 Material characterization

To determine the phase composition and crystallinity of the products, X-ray diffraction (XRD) experiments were carried out using Rigaku SmartLab X-Ray Diffractometer with CuKα radiation ($\lambda = 0.1541$ nm) and power 40 kV × 40 mA. The intensity data were collected by step-scanning over 10-90º with a step of 0.02º. The crystallite size of CeO_2 was calculated using the Scherrer equation [83]:

$$d_p = \frac{0.94\lambda}{\beta \cos \theta_B} \tag{2.5}$$

where d_p is average crystallite or particle size, λ (1.54 Å) is wavelength of CuKα radiation, β is the full width at half maximum and θ_B is Bragg's diffraction angle. To measure the

specific surface area and pore volume, nitrogen adsorption–desorption analysis was conducted using a Quantachrome Autosorb instrument. Raman spectra were acquired using a Thermo Scientific DXR2 spectrometer with a 50X objective, 633 nm filter and a power of 5 mW. The spectral resolution was about 3 cm^{-1}. The thermal decomposition behavior of the precursors was examined from TGA experiments (Instrument Specialists), where the samples were heated in air to 800 $^{\circ}$C at 10 $^{\circ}$C/min heating rate. The measurements were duplicated 2-5 times to ensure repeatability and each reported data (i.e. crystallite size, specific surface area and pore volume) is an average value. The standard deviation was less than 10%.

X-ray photoelectron spectroscopy (XPS) studies were carried out using a Kratos Axis Ultra DLD system with monochromatic AlKa (1486.6 eV) X-ray source to examine surface and defect properties of the CeO_2 samples. The binding energy of C1s was used as an internal standard. The spectra were fitted with linear background and 50% Gaussian/50% Lorentzian (product form) function using the CASA-XPS software. To investigate the morphology of the as-synthesized CeO_2 samples, scanning electron microscopy (SEM) images were obtained using a FEI Nova NanoSEM at 5 kV acceleration voltage. The microstructural properties were studied using transmission electron microscopy (TEM) and high resolution TEM (HRTEM). Both TEM and HRTEM images were obtain using a FEI Tecnai G2 20 at 200 kV. To prepare the TEM samples, the as-synthesized powders were grounded and dispersed in water by ultrasound, and then a few drops of the resultant suspension were deposited on a carbon-coated copper grid and dried at ambient temperature.

2.4   Results and discussion

2.4.1   The glycine fuel systems

2.4.1.1   Cerium nitrate-glycine system (CN+GL)

The TGA is an effective method to understand thermal decomposition behavior of materials, which enables one to clarify the SCS mechanism. The TGA curves for decomposition of precursors in $Ce(NO_3)_3 \cdot 6H_2O$-glycine (CN+GL) system are shown in Figure 2.1. Figure 2.1a shows that the decomposition of $Ce(NO_3)_3 \cdot 6H_2O$ proceeds in two stages which, based on TG-DTG analysis, involve one step for dehydration and three steps for decomposition of nitrate species, as follows [84]:

Dehydration

$$Ce(NO_3)_3 \cdot 6H_2O \rightarrow Ce(NO_3)_3 + 6H_2O \tag{2.6}$$

Decomposition to CeO_2

$$Ce(NO_3)_3 \rightarrow Ce(NO_3)_2 + NO_2 \uparrow + {}^1\!/_2\, O_2 \uparrow \tag{2.7}$$

$$Ce(NO_3)_2 \rightarrow CeNO_3 + NO_2 \uparrow + {}^1\!/_2\, O_2 \uparrow \tag{2.8}$$

$$CeNO_3 \rightarrow CeO_2 + NO \uparrow \tag{2.9}$$
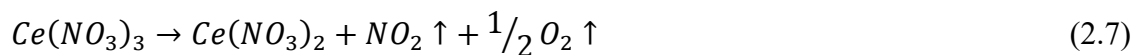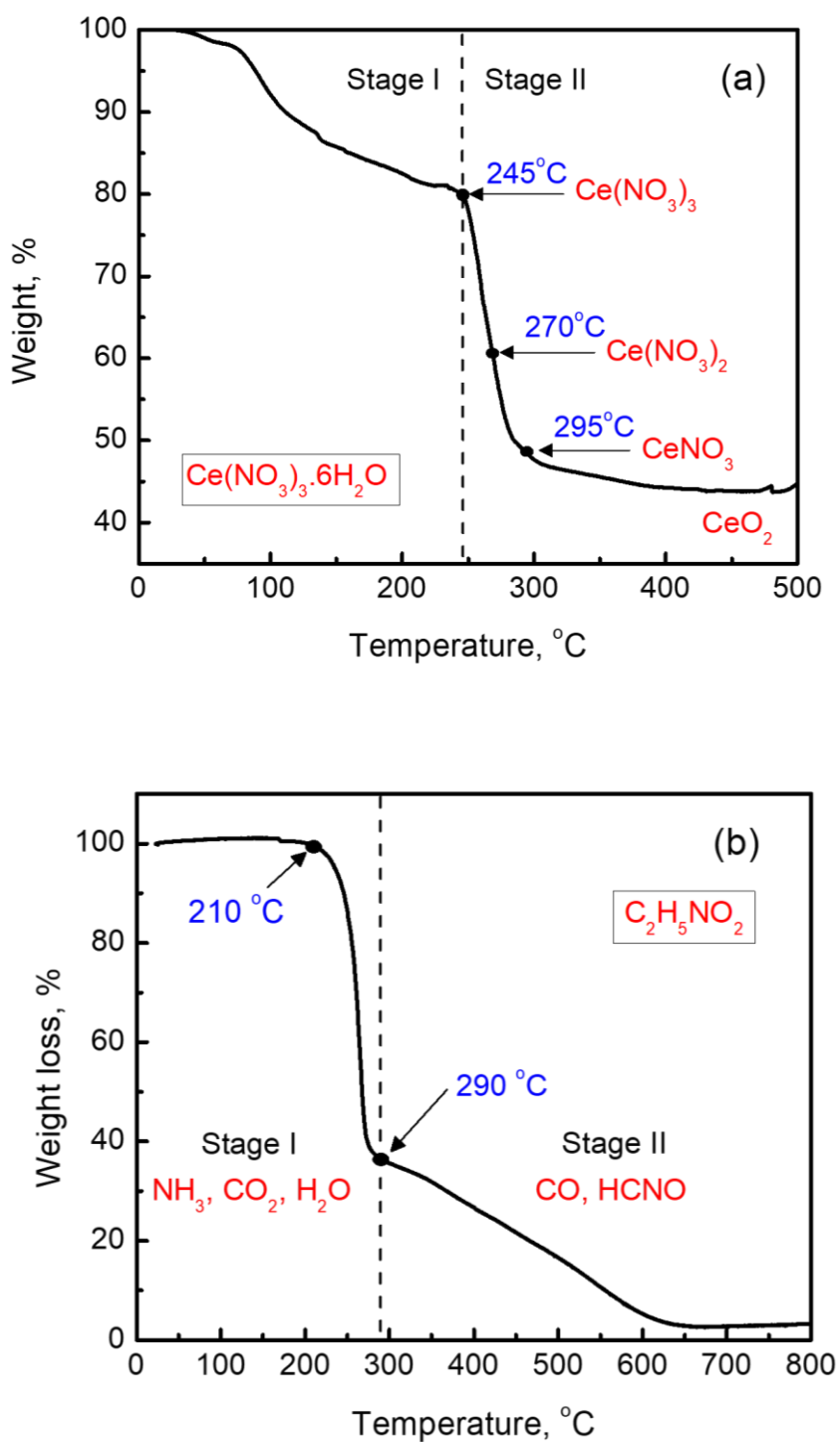
Figure 2.1 TGA curves of (a) $Ce(NO_3)_3 \cdot 6H_2O$ and (b) glycine

Based on this knowledge, the theoretical weight loss for each step was calculated and is presented in Figure 2.1a. It shows that the first stage (<245 °C) of weight loss is associated with dehydration. The following second (245-400 °C) stage is related to decomposition of the nitrate groups. The thermal decomposition of glycine has been studied previously [85,86] and can be summarized as follows: (i) first weight loss takes place in the temperature range 230–310 °C, and the main gaseous products of the decomposition are NH_3, H_2O, and CO_2. (ii) The second stage occurs in the temperature range 310–700 °C, where CO, HCN and HNCO are released. The TGA curve for thermal decomposition of glycine (Figure 2.1b) shows this two-stage feature. First, a sharp weight loss starts at 210 °C, and is followed by a gradual weight change from 290 °C until all glycine is decomposed. The temperature range of each stage agrees well with the prior literature.

The temperature-time profile for SCS in CN+GL system with ϕ=2 is shown in Figure 2.2. After dehydration of the aqueous precursor solution, ignition occurred at 265 °C, leading to sharp temperature increase to a maximum value (T_{max}= 695 °C). It is important to note that according to TGA results (Figure 2.1), $Ce(NO_3)_3 \cdot 6H_2O$ releases NO_2 and O_2 while glycine produces NH_3, CO_2 and H_2O at ~265 °C. This suggests that ignition is triggered by reaction between these gaseous products. It is known that NO_2 reacts with NH_3, leading to a highly exothermic reaction [87]. Therefore, the generation of NO_2 and NH_3 from decomposition of $Ce(NO_3)_3 \cdot 6H_2O$ and glycine, respectively, followed by their reaction, is the trigger for ignition in the present system.
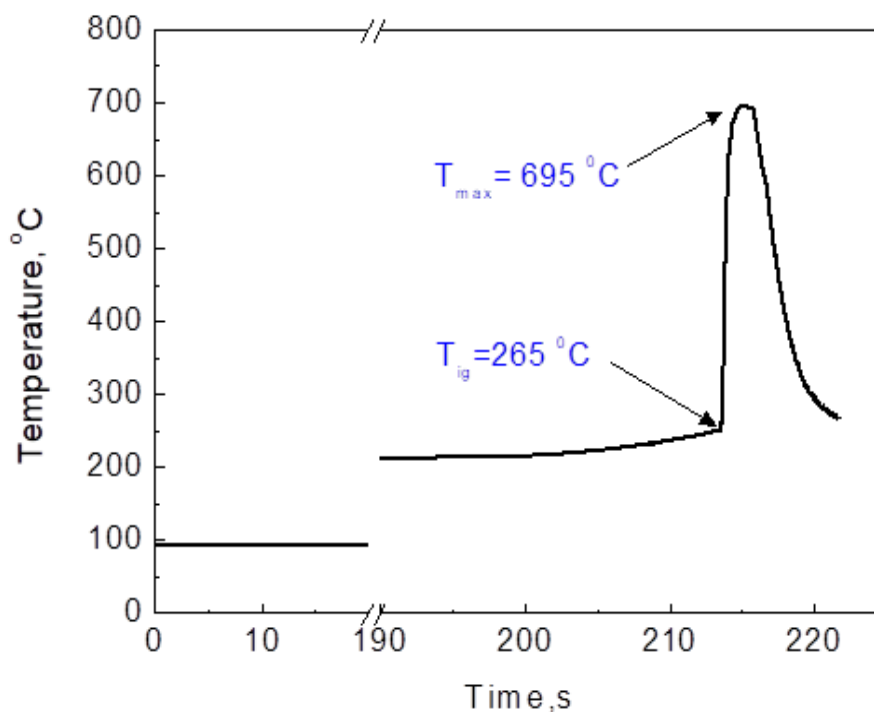
Figure 2.2 Temperature-time profile for SCS in CN+GL system ($\phi=2$)

The combustion process for CN+GL system, recorded by the digital camera, is shown in Figure 2.3. Visually, combustion was initiated from a local spot in the condensed phase and then flame propagated to the gas phase along with the gases released from the spot. The flame spread rapidly and widely in the gas phase, leading to vigorous combustion in the entire volume of the reaction mixture for a short duration (~4 sec). This feature corresponds to the volume combustion synthesis mode [24]. In addition, Figure 2.3 shows that combustion propagation is governed mainly by the gas phase, while condensed phase reactions, which lead to the formation of SCS products, do not directly contribute to the combustion process. For this mechanism, physical properties and microstructure of SCS products should primarily depend on the temperature-time history and gas evolution amount [24].
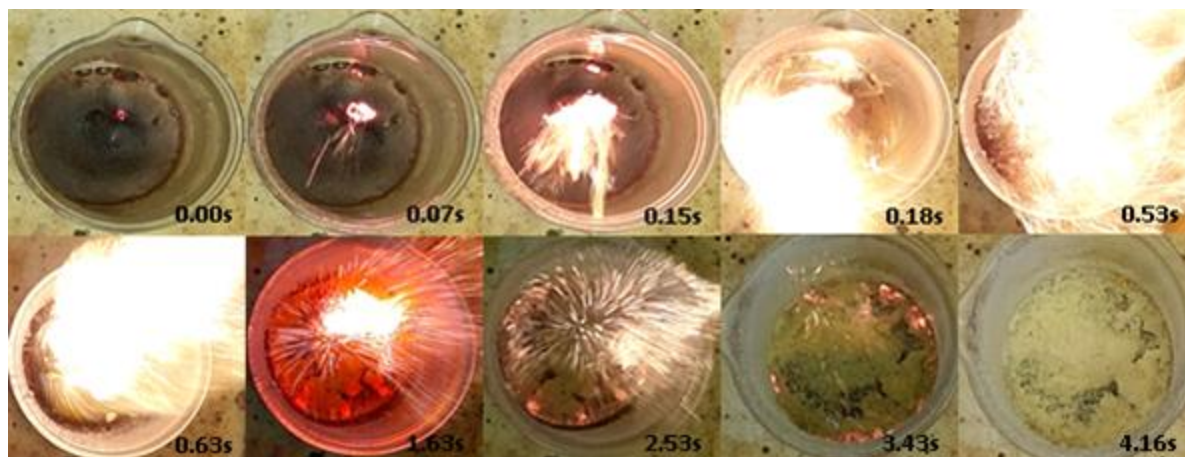
Figure 2.3 Combustion process for CN+GL system (ϕ=2)

2.4.1.2 Cerium ammonium nitrate-glycine system (CAN+GL)

To examine the effect of metal precursor type on the combustion mechanism, $(NH_4)_2Ce(NO_3)_6$ instead of $Ce(NO_3)_3\cdot6H_2O$ was used as the cerium precursor and the $(NH_4)_2Ce(NO_3)_6$-glycine (CAN+GL) system was investigated using the same experimental procedure. The TGA curve of $(NH_4)_2Ce(NO_3)_6$ is shown in Figure 2.4a, where a sharp weight loss may be seen in the temperature range 185-250 °C and agrees well with prior work [88,89]. The overall decomposition of $(NH_4)_2Ce(NO_3)_6$ may be represented as follows [88]:

$$(NH_4)_2Ce(NO_3)_6 \rightarrow CeO_2 + 2N_2O + 4NO_2 + O_2 + H_2O \qquad (2.10)$$
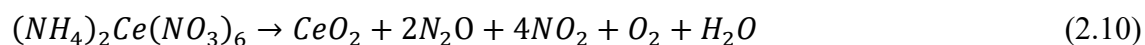
where the final product CeO_2 corresponds to 31.4% of the initial weight. Figure 2.4b shows the temperature-time profile during SCS for the CAN+GL system, where it may be seen that ignition occurs at ~210 °C which corresponds to the formation of NH_3 from the decomposition of glycine (Figure 2.1b). This suggests that the formed NH_3 reacts with the

NO_2 and N_2O gases produced from the decomposition of $(NH_4)_2Ce(NO_3)_6$. These reactions

$(2NH_3 + 2NO_2 \rightarrow N_2 + N_2O + 3H_2O$, -147.0 kJ/mol; $2NH_3 + 3N_2O \rightarrow 4N_2 + 3H_2O$, -277.9

kJ/mol) are exothermic, leading to combustion [90,91]. Consequently, this combustion

process is characterized by two temperature peaks at about 1010 and 1095 $^\circ$C,

corresponding to the two exothermic reactions between NO_2-NH_3 and N_2O-NH_3,

respectively. The video frames of the CAN+GL system are not shown here because its

combustion behavior is essentially the same as that of the CN+GL system. Based on the

TGA curves and SCS temperature profiles, it may be concluded that the combustion

reaction for both CN+GL and CAN+GL systems is triggered by the exothermic reaction

between NH_3 and nitrogen oxides (NO_2 and N_2O).
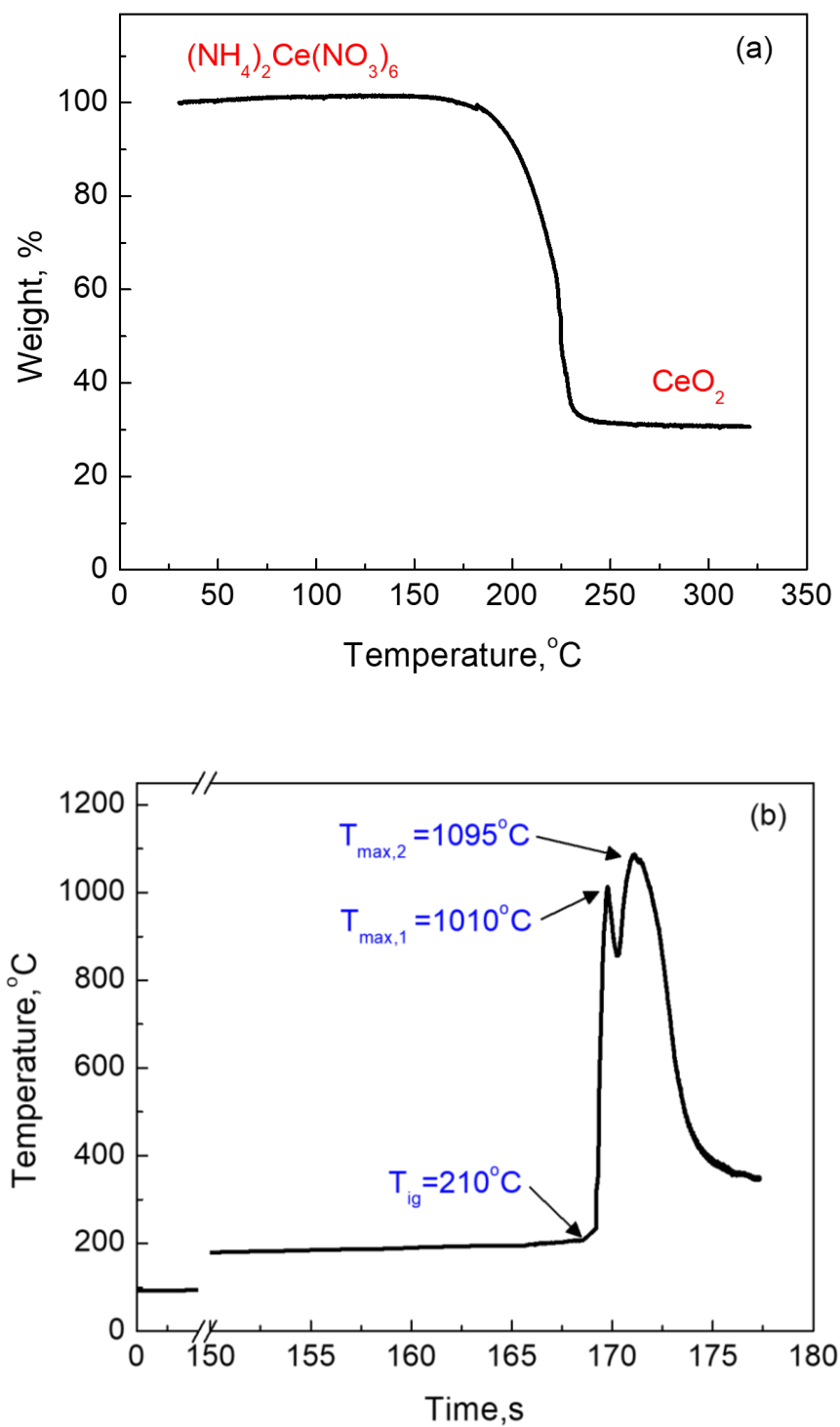
Figure 2.4 (a) TGA curves for $(NH_4)_2Ce(NO_3)_6$ and (b) temperature-time profile for SCS in CAN+GL system ($\phi=2$)

2.4.1.3   Effect of fuel-to-oxidizer ratio (ϕ)

The SCS experiments for the above systems were conducted for different ϕ values to understand its effect on combustion behavior. Figure 2.5a shows the measured T_{max} values for both systems, where it may be seen that both exhibit a maximum at $\phi=1$ and that T_{max} for the $(NH_4)_2Ce(NO_3)_6$ system is always higher than that for $Ce(NO_3)_3 \cdot 6H_2O$. These features were also confirmed by thermodynamic calculations (Figure 2.5b). As expected, the trends of the calculated T_{ad} agree well with the measured T_{max} although there is a significant difference between the T_{ad} and T_{max} values. The T_{ad} is always higher than T_{max} due to nonadiabatic experimental conditions. Since combustion experiments were carried out using a glass beaker and hot plate, heat generated during combustion could easily transfer to the surroundings. Also, heat could be rapidly carried away from the system by gases evolved during combustion (advection effect). Other possible reason is delay of the thermocouple signal during the sudden change of the temperature.

For both systems, it was visually observed that the color of CeO_2 powders become darker from light yellow at $\phi > 2$. This could be attributed to formation of black carbon by incomplete combustion which is commonly observed at fuel-rich conditions [92]. As shown in Figure 2.5, away from stoichiometry ($\phi=1$), reaction temperature decreases due to dilution of either reducing or oxidizing species in precursor solution, resulting in incomplete combustion which leave residual nitrate and carbon species from metal nitrate and glycine, respectively.
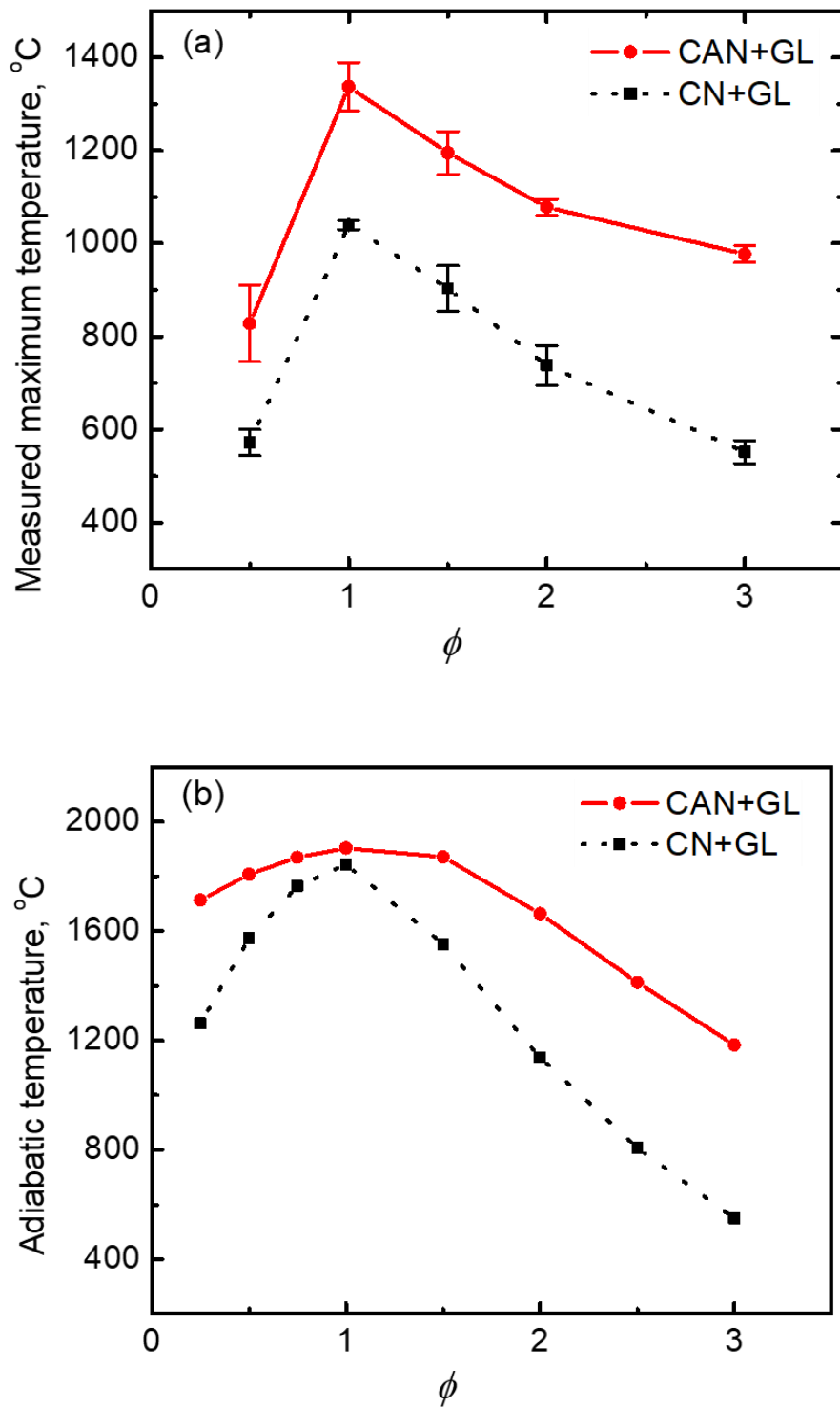
Figure 2.5 Comparison of the (a) experimentally measured maximum combustion temperature (T_{max}) and (b) adiabatic combustion temperature (T_{ad}) for CAN+GL and CN+GL systems

2.4.2   The hydrous hydrazine fuel systems (CN+HH and CAN+HH)

To investigate the effect of fuel type on SCS, hydrous hydrazine ($N_2H_4 \cdot H_2O$) was used as fuel along with the same two Ce precursors as with glycine, $Ce(NO_3)_3 \cdot 6H_2O$ and $(NH_4)_2Ce(NO_3)_6$. In contrast to the glycine system, in both cases it was observed that a brownish precipitate formed once hydrous hydrazine was added to the solution. It has been reported that some specific metal ions react with hydrazine to form metal-hydrazine complexes, which have been investigated as combustion initiators [93,94]. To our knowledge, however, there are no studies reporting such complexes with cerium.

The Raman spectra for the precipitates of both $Ce(NO_3)_3 \cdot 6H_2O$-$N_2H_4 \cdot H_2O$ (CN+HH) and $(NH_4)_2Ce(NO_3)_6$-$N_2H_4 \cdot H_2O$ (CAN+HH) systems are shown in Figure 2.6. The presence of hydrazine (965, 1080, 1630 and 3300 cm^{-1}), ionic NO_3^- (720, 740 and 1045 cm^{-1}) and metal (465 cm^{-1}) were confirmed in both precipitates, suggesting the formation of cerium hydrazine complex [95-98]. Interestingly, the precipitates for both systems show almost identical Raman spectra, which implies that the structure of precipitate does not depend on the cerium precursor type. In fact, when $N_2H_4 \cdot H_2O$ was added to $(NH_4)_2Ce(NO_3)_6$ solution, it led to formation of brownish precipitate as well as the evolution of ammonia gas, while for cerium nitrate it yielded only the precipitate. Thus, it appears that for CAN+HH system, the ammonium ion in the solution escapes in the form of gas during the precipitation, leaving only cerium nitrate to react with hydrazine. It was also confirmed that there were no Raman peaks corresponding to NH_4 (2870 and 3040 cm^{-1}) for the precipitate of CAN+HH system [99].
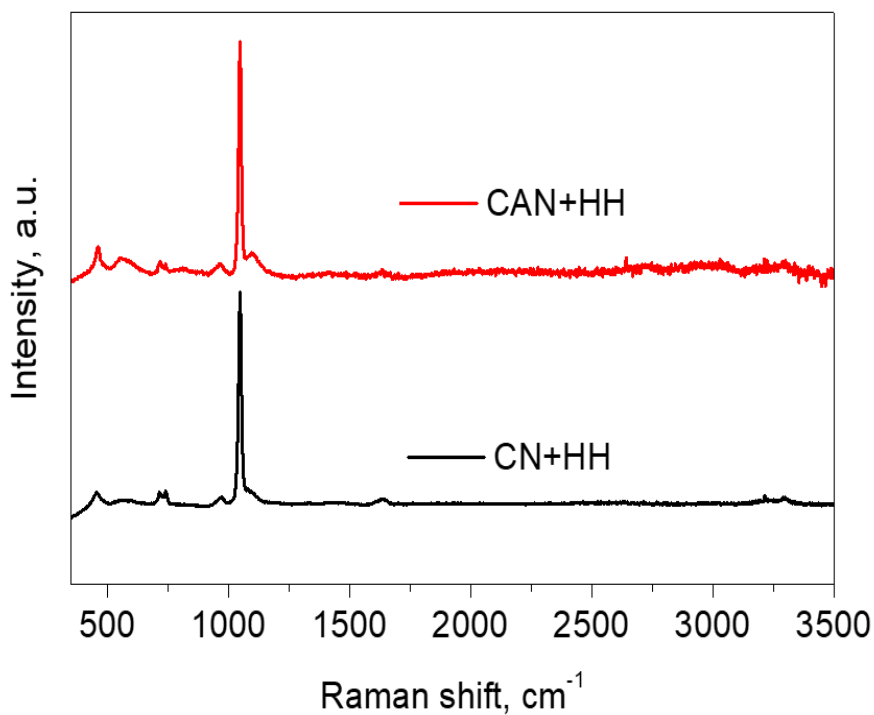
Figure 2.6 Raman spectra of precipitate in CAN+HH and CN+HH systems

Generally, the structure of metal-hydrazine complexes can be expressed as $Ce(NO_3)_x(N_2H_4)_y$. It is reported that the combustion behavior of metal hydrazine complexes, which can be classified into three types based on the propellant chemistry: decomposition, detonation and deflagration, depends on the nature of metal ions and its anion (NO_3^-, SO_4^{2-}, $C_2O_4^{2-}$ or etc.) [93,94]. Since there are no prior studies investigating the cerium hydrazine nitrate complex and its structure is unknown, determining the structure of the complex and defining the stoichiometric coefficients (x and y) are important to understand the correlation between its structure and combustion behavior. In order to define the stoichiometric coefficients, the prepared cerium hydrazine complex was fully dried at 110 °C to remove water and unreacted hydrous hydrazine, and then the weight loss by thermal decomposition was investigated using TGA (Figure 2.7a). Also, the weight

losses for thermal decomposition of various possible cerium hydrazine complexes were calculated and are listed in Table 2.1. As shown in Figure 2.7a, the observed weight loss for $Ce(NO_3)_x(N_2H_4)_y$ was 59.25%, which agrees with the calculated weight loss 59.24% for $Ce(NO_3)_3(N_2H_4)_3$, suggesting that the structure of the cerium hydrazine complex is $Ce(NO_3)_3(N_2H_4)_3$.
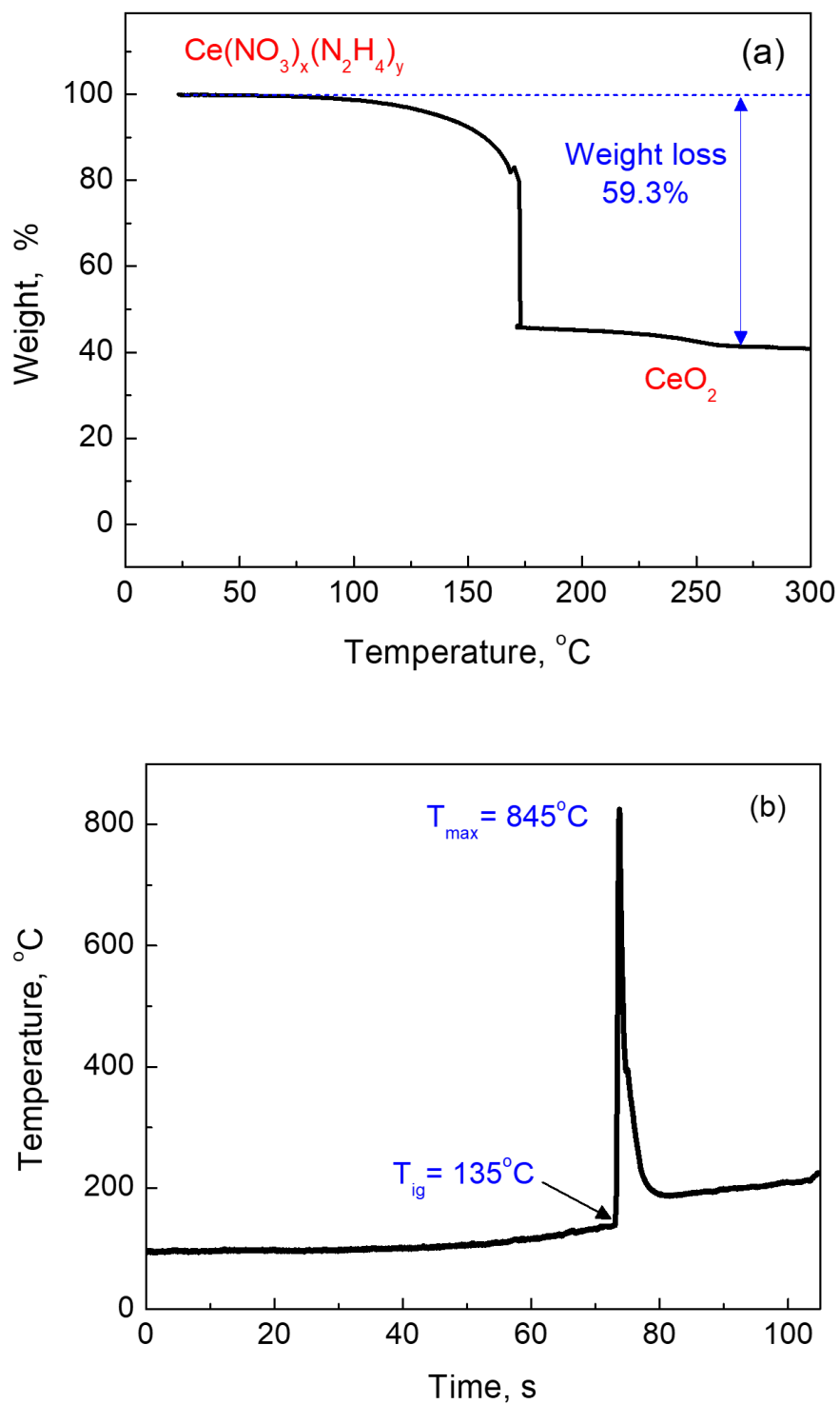
Figure 2.7 (a) TGA curve of cerium hydrazine complex (b) temperature-time profiles for SCS in CAN+HH system (ϕ=2)

Table 2.1 Theoretical weight loss of different cerium hydrazine complexes

	Weight loss, %
$Ce(NO_3)_2(N_2H_4)_3$	52.2
$Ce(NO_3)_3(N_2H_4)_2$	55.9
$Ce(NO_3)_3(N_2H_4)_3$	59.2
$Ce(NO_3)_3(N_2H_4)_4$	62.1

Figure 2.7b shows the temperature-time profile for SCS in the CAN+HH system. The case of CN+HH is not shown because both systems formed the same cerium hydrazine complex and hence produced the same combustion features. The ignition temperature was observed to be ~135 °C, which is related to the boiling point of hydrazine (~114 °C). For SCS of hydrazine fuel systems, it has been shown that ignition is triggered by the reaction of hydrazine vapor with ambient oxygen [25,100].

The video frames during the SCS process are shown in Figure 2.8. As expected, the flame was initiated in the gas phase, resulting from the reaction between hydrazine vapor and ambient oxygen. Then the flame triggered combustion in the condensed phase, followed by steady wave propagation with moderate velocity along the cerium hydrazine complex. These features correspond to the self-propagating high-temperature synthesis mode, and also deflagration, based on the principles of propellant chemistry [24,101]. As noted above, combustion type is determined by the nature of metal ion and its anion. Therefore, it can be concluded that the cerium hydrazine complex consisting of Ce^{3+} and NO_3^- ions leads to deflagration-type combustion. Typically, the deflagration of metal hydrazine complexes is caused by the decomposition of N-N bond in hydrazine to N_2,

which releases ~622 kJ/mol energy [94]. Thus, combustion in the condensed phase is governed by the highly exothermic reaction between N_2H_4 and NO_3^- in the complex.
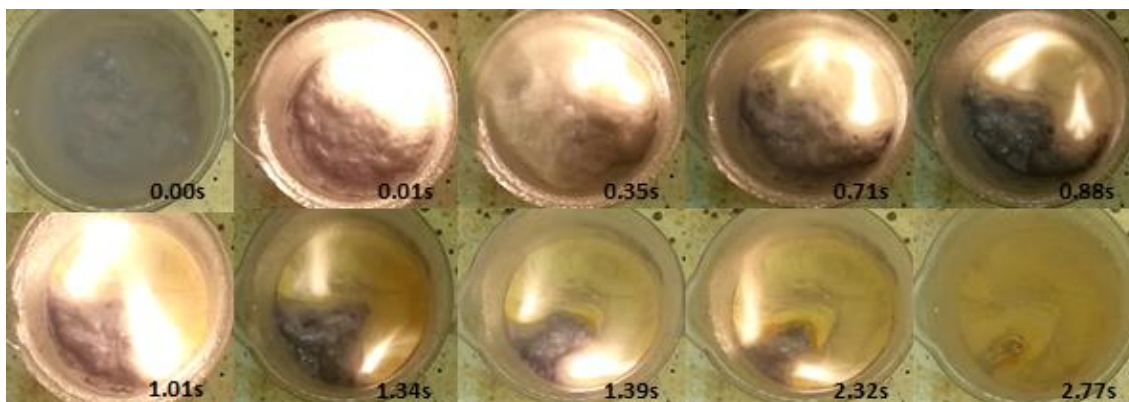
Figure 2.8 Combustion process for CAN+HH system

Based on the above considerations, the combustion mechanism of hydrazine-cerium nitrate system can be described as follows. First, water is evaporated from the precursor solution which initially contains cerium hydrazine complex, unreacted hydrazine and water. As the temperature approaches the boiling point of hydrazine, unreacted hydrazine is released to the gas phase and reacts with ambient oxygen to initiate the reaction. Then, the flame produced by the reaction triggers combustion of the cerium hydrazine complex in the condensed phase. Finally, the combustion wave, which is driven by the exothermic reaction between N_2H_4 and NO_3^- species, propagates along the cerium hydrazine complex, producing fine and fluffy CeO_2 powders.

2.4.2.1 Effect of fuel-to-oxidizer ratio (ϕ)

Experiments were also carried out to determine the effect of fuel-to-oxidizer ratio (ϕ). The T_{max} values are shown in Figure 2.9, along with the computed T_{ad} values, both curves exhibiting a maximum at ϕ ~1.5. As expected, the adiabatic temperatures, T_{ad} are

always larger than the measured T_{max} values. The feature of both T_{ad} and T_{max} reaching maximum value under fuel-rich conditions (ϕ ~1.5) is different from the glycine fuel cases (Figure 2.5) and relates to the reaction mechanism. As noted in section 2.4.1, the ignition trigger for glycine cases is exothermic reaction between NH_3 and nitrogen oxides (NO_2 and N_2O), both released from solution phase precursors. Away from stoichiometry ($\phi = 1$), the proportions of reducing and oxidizing species result in dilution, decreasing reaction temperature. In the hydrous hydrazine fuel cases, the ignition trigger is reaction of hydrazine vapor with ambient oxygen. Owing to formation of the metal-hydrazine complex, there is less free hydrazine in solution, requiring $\phi > 1$ for combustible mixture to form in the vapor phase. For hydrous hydrazine fuel case, no color change of the CeO_2 powders with variation of ϕ was observed because incomplete combustion of this system may leave only residual nitrate species which is not visually distinguishable.
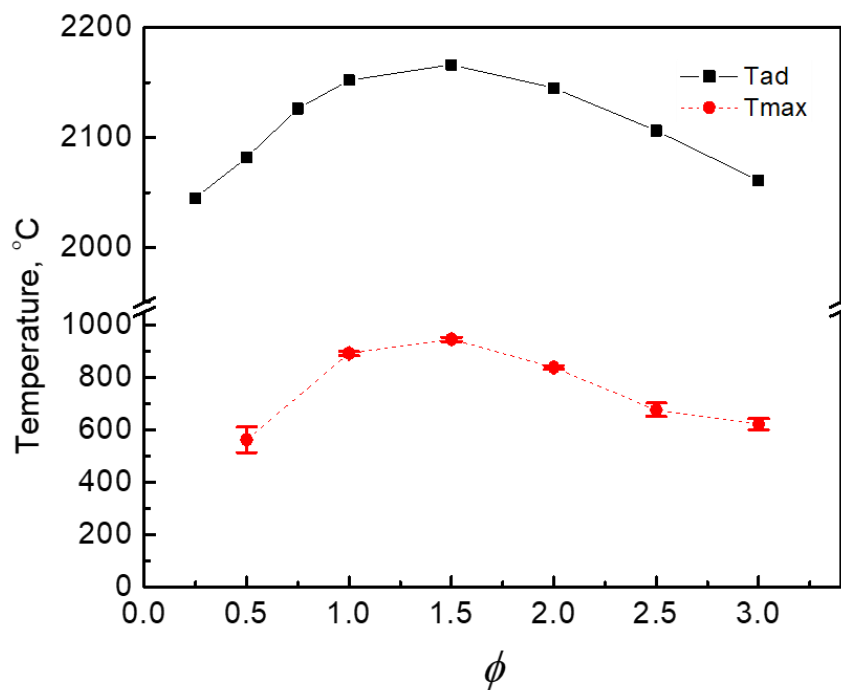
Figure 2.9 Comparison of the measured maximum combustion temperature (T_{max}) and adiabatic combustion temperature (T_{ad}) for the CAN+HH system

2.4.3 Cerium ammonium nitrate/ammonium nitrate-hydrous hydrazine system [(CAN/AN)+HH]

To investigate the influence of a gas generating agent on the SCS process and product properties, ammonium nitrate (AN) was added to the precursor solution for CAN+HH system (ϕ=2). It is known that the thermal decomposition of ammonium nitrate occurs in the temperature range 230-260 °C, generating N_2O and H_2O gases [102]. Therefore, the addition of ammonium nitrate not only promotes gas evolution but also affects the combustion temperature since N_2O can cause combustion reaction when combined with fuel.

Figure 2.10 shows that the measured T_{max} increases from 845 to 1081°C with an increase of AN/MN ratio from 0 to 1.5. When this ratio increases further up to 9, T_{max} decreases to about 700°C. Since AN serves as an oxidizer in the combustion reaction, addition of AN to CAN+HH system lowers the fuel-to-oxidizer ratio (ϕ). As shown in Figure 2.10, as AN/MN ratio increases from 0 to 9, ϕ value of (CAN/AN)+HH system decreases from 2 to 0.65 and notably the change in combustion condition occurs at AN/MN ratio of 2 (ϕ=1) from fuel-rich to fuel-lean mode. For the fuel-rich combustion cases (AN/MN ratio=0-1.5), addition of AN leads to increase of T_{max}, while combustion under fuel-lean conditions (AN/MN ratio=4-9) results in a lower T_{max} value. The T_{max} value reaching maximum under fuel-rich conditions follows from the discussion above in the context of Figure 2.9.
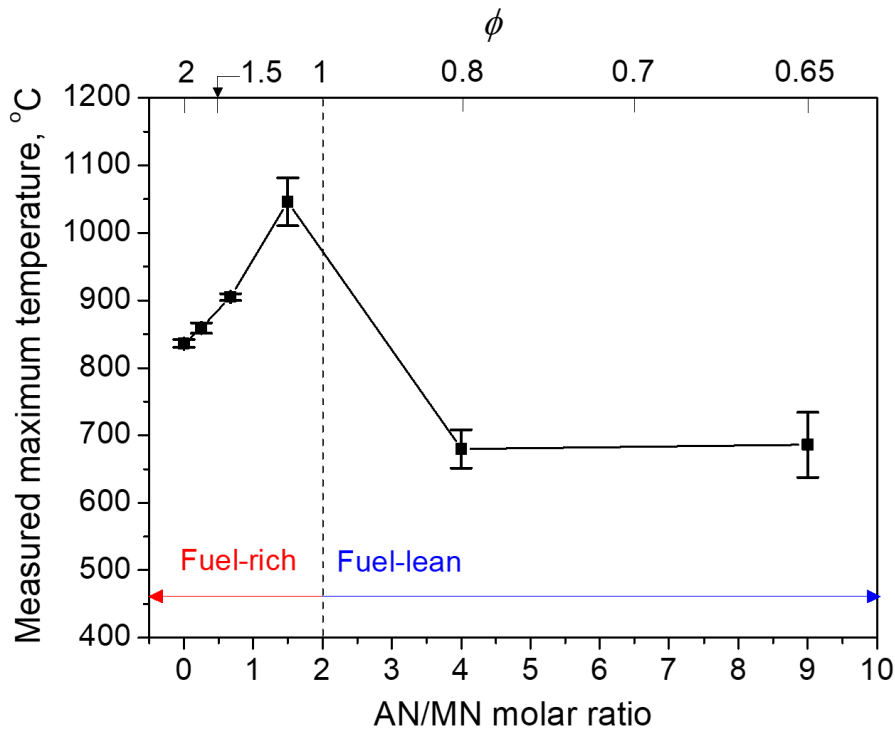
Figure 2.10 The measured maximum combustion temperature (T_{max}) for (CAN/AN)+HH system

2.4.4   Physicochemical properties of CeO$_2$ powders

2.4.4.1   Crystallite size

The SCS parameters such as fuel type, metal precursor type, fuel-to-oxidizer ratio (ϕ) and gas generating agent affect the reaction mechanism as well as combustion characteristics including the maximum temperature and the amount of evolved gas [24,25]. In general, the combustion temperature is related to formation of products with desired crystallinity and purity, although too high temperature may lead to particle agglomeration, causing pore shrinkage. The gases produced during SCS dissipate the heat, suppress particle agglomeration and promote pore formation. Therefore, the properties of the resulting powders depend strongly on the utilized SCS parameters.

Figure 2.11a shows the XRD patterns of the representative CeO_2 samples for each system [CN+GL, CAN+GL, CAN+HH and (CAN/AN)+HH]. All XRD peaks clearly exhibit a typical cubic fluorite structure of CeO_2 (JCPDS No. 34-0394), corresponding to the (111), (200), (220), (311), (222) and (400) planes. It may be noted that the crystallinity of CeO_2 samples depends on the SCS systems. This may be attributed to the differences in combustion temperature which is mainly determined by SCS parameters (cerium precursor, fuel and gas generating agent). Thus, with GL fuel, CAN exhibits higher crystallinity than CN owing to higher T_{max} values (CAN+GL, 1080 °C; CN+GL, 740 °C). With CAN precursor, GL fuel yields higher crystallinity as compared to HH due to higher T_{max} values (CAN+GL, 1080 °C; CAN+HH, 840 °C). Similarly, the addition of AN produces lower crystallinity as compared to CAN+HH [(CAN/AN)+HH, 680 °C; CAN+HH, 840 °C]. The XRD patterns of all samples with different ϕ and AN/MN ratio are not shown but the trends between crystallinity and T_{max} were similar. Meanwhile, although the formation of residual carbon by incomplete combustion was visually confirmed for glycine fuel system with fuel-rich conditions ($\phi \geq 2$), any impurity phases such as carbon and nitrate were not observed from XRD patterns likely due to low content or low crystallinity.
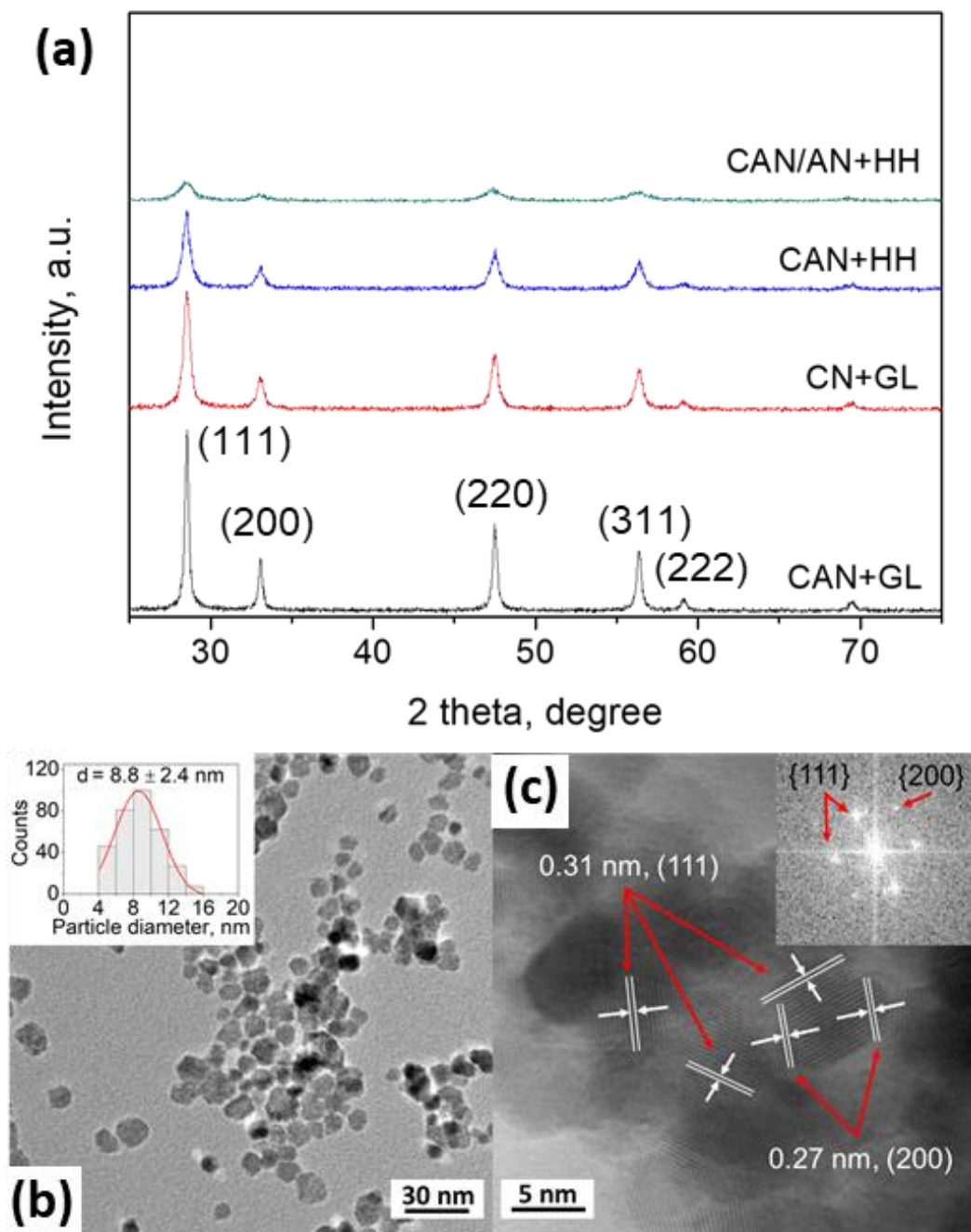
Figure 2.11 (a) XRD patterns of CeO$_2$ powders prepared from CAN+GL, CN+GL, CAN+HH and (CAN/AN)+HH systems (ϕ=2, AN/MN ratio=4), (b) TEM image (Inset: particle size distribution) and (c) HRTEM image (Inset: FFT) of CeO$_2$ powder prepared from (CAN/AN)+HH system (AN/MN ratio=4)

The average crystallite size of CeO_2 samples was estimated from most prominent XRD peak corresponding to (111) plane using the Scherrer equation and is shown in Table 2.2. As expected, owing to higher T_{max} values which increase particle agglomeration, CeO_2 of CAN+GL system with $\phi=2$ exhibited larger crystallite size (21.7 nm) than those of both CN+GL (18.3 nm) and CAN+HH systems (10.2 nm). Table 2.2 also shows the crystallite sizes of CeO_2 prepared at different ϕ value for both fuel systems. The relatively high T_{max} of glycine fuel cases yields CeO_2 with larger crystallite size (21.7-38.7 nm) as compared to hydrazine cases (10.2-14.8 nm). It may also be seen that the trends of crystallite size by ϕ value for both glycine and hydrazine fuel cases corresponds well to T_{max} (Figures 2.5 and 2.9). For CAN+GL system, the crystallite size increases with increase of ϕ value from 0.5 to 1. When ϕ increases further up to 2, the crystallite size decreases. Similarly, for the hydrazine system, the crystallite size increases with increasing ϕ value from 0.5 to 1.5 and then decreases for $\phi=2$. It was observed for both fuel cases that the crystallite size increases again from $\phi>2$ despite continuous decrease of T_{max}. This may result from the incomplete combustion which leads to formation of residual impurities as well as a decrease of the total amount of produced gases. The effect of gas evolution which prevents particle agglomeration diminishes, resulting in the formation of crystallites with larger size.

For the (CAN/AN)+HH system, the crystallite size increases with increasing AN/MN ratio from 0 to 1.5. The addition of AN increases combustion temperature as well as amount of gas evolved which have the opposite effect on crystallite size. It appears that for AN/MN ratio = 0-1.5, the former effect predominates. When the AN/MN ratio increases further up to 9, the crystallite size decreases significantly due to the enhanced gas evolution and lower T_{max} by the decrease of ϕ, resulting in the formation of crystallites with smaller

size (~8 nm). Figure 2.11b shows the TEM bright field image of CeO_2 powders prepared from (CAN/AN)+HH with AN/MN ratio of 4. The particles exhibit irregular shapes but with uniform size distribution. The estimated particle size distribution obtained after counting 300 particles is shown in Figure 2.11b (inset). The mean particle size (d) is 8.8 ± 2.4 nm, which is in agreement with the XRD analyzed value. The HRTEM image (Figure 2.11c) with FFT analysis (inset) shows that the particles exposed mainly {111} planes together with {100} planes, which correspond to lattice spacing of 0.31 and 0.27 nm, respectively. It has been reported that different crystal planes of CeO_2 exhibit different properties (e.g. surface stability, oxygen vacancies formation energy, and interaction with surface molecules) and {100}, which has high surface energy and thus is a highly reactive plane, could provide active sites for catalytic reactions using CeO_2 [103,104].

Table 2.2 Textural and structural properties of CeO_2 as a function of fuel type, cerium precursor, fuel-to-oxidizer ratio (ϕ), and amount of gas generating agent

System	ϕ	AN/MN ratio	CeO_2 crystallite size (nm)	Pore volume (cm^3/g)	BET surface area (m^2/g)
CAN+GL	0.5	-	27.0	0.026	29
	1	-	38.7	0.040	13
	1.5	-	24.5	0.055	21
	2	-	21.7	0.100	30
	2.5	-	22.7	0.066	25
	3	-	26.5	0.045	19
CN+GL	2	-	18.3	0.135	34
CAN+HH	0.5	-	10.4	0.051	47.9
	1	-	11.7	0.063	43.7
	1.5	-	13.1	0.060	37.7
	2	-	10.2	0.064	44.3
	2.5	-	12.6	0.060	44.1
	3	-	14.8	0.056	38.0
CAN/AN+ HH	2	0.25	12.8	0.064	45.7
	2	0.67	13.5	0.065	47.1
	2	1.50	17.4	0.075	53.2
	2	4.00	7.9	0.084	87.7
	2	9.00	8.4	0.081	85.9

2.4.4.2 Defect structure in cerium oxide

Raman spectroscopy was applied to clarify the structural and chemical details of the CeO_2 samples. Figure 2.12 shows the Raman spectra of the representative CeO_2 samples for each system. For the samples prepared from CN+GL and CAN+GL systems (ϕ=2), a characteristic strong F_{2g} band at 465 cm^{-1} of cubic fluorite structured CeO_2 was observed [105,106]. This F_{2g} band is attributed to a symmetrical stretching mode of oxygen atoms around each Ce^{4+} cation. The weak peak at 636 cm^{-1} was also observed, indicating the presence of impurities which could not be detected from the XRD measurement. To further confirm the impurity phases, Raman spectra in the range 850-1900 cm^{-1} of the CeO_2 powders prepared from CAN+GL system with different ϕ were investigated (Figure 2.13). The sample prepared by combustion at stoichiometric condition (ϕ=1) shows only a Raman band at 1177 cm^{-1} due to second-order longitudinal optical (2LO) mode [105,106]. Whereas the sample prepared at fuel-rich condition (ϕ=2) shows the 2LO band as well as the Raman bands around 1045, 1360 and 1570 cm^{-1}. The 1045 cm^{-1} band corresponds to symmetric stretching mode of NO^{3-} ion while 1360 and 1570 cm^{-1} bands belong to defect-derived and graphite structure-derived modes of carbon materials, respectively [98,106,107]. This result suggests that, for glycine fuel cases with fuel-rich condition ($\phi{\geq}2$), incomplete combustion between metal nitrate and glycine containing carbon species occurs, leading to the formation of nitrate and carbon residues.
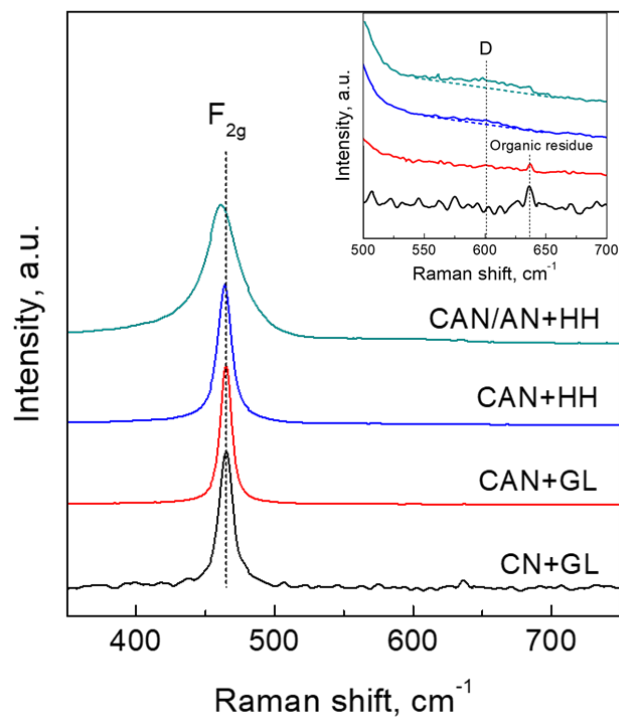
Figure 2.12 Raman spectra CeO₂ powders prepared from CAN+GL, CN+GL, CAN+HH and (CAN/AN)+HH systems ($\phi=2$, AN/MN ratio=4)
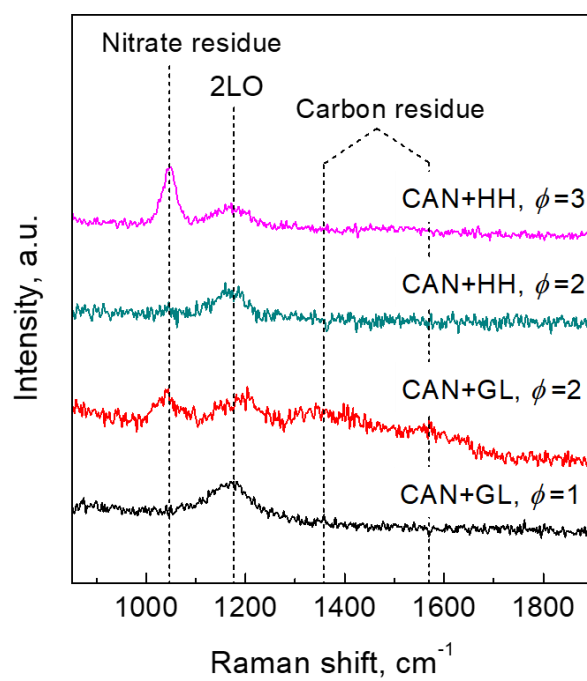
Figure 2.13 Raman spectra CeO₂ powders prepared from CAN+GL ($\phi=1$, 2) and CAN+HH ($\phi=2$, 3) systems

Meanwhile, the F_{2g} band of the CeO_2 powders prepared from CAN+HH and (CAN/AN)+HH systems was broadened and shifted towards lower wavenumber compared to that of CN+GL and CAN+GL systems. It has been reported that the width and position of the F_{2g} band depend strongly on phonon confinement, strain, crystallite size and defects. The broadening of the F_{2g} band can be explained by phonon confinement associated with the presence of smaller CeO_2 crystallites [106,108,109]. This is consistent with the XRD results where the CeO_2 sample for (CAN/AN)+HH system at $\phi=2$ and AN/MN ratio=4 has the smallest crystallite size. On the other hand, the peak shift relates to CeO_2 crystallite size as well as presence of oxygen vacancies as a defect in the CeO_2 lattice. It has been reported that, when CeO_2 crystallite size decreases, the defect concentration increases and the increased defects cause shift of the F_{2g} band [110-112]. Indeed, the certain extent of defects was identified from the broad mode at 550-650 cm^{-1} (D band), attributed to punctual defects in the ceria lattice induced the formation of oxygen vacancies (Figure 2.12). The CeO_2 sample prepared from (CAN/AN)+HH system showed the highest degree of defects, which was estimated from the peak area of D band, likely owing to its smaller crystallite size. It is known that the defects in CeO_2 have an important role to improve redox properties of Ce^{4+}/Ce^{3+} and thus promote catalytic activity of CeO_2 for many applications [113-115]. For the samples prepared with hydrous hydrazine fuel and $\phi=2$, impurity phases could not be observed (Figure 2.13), because the combustion reaction was conducted near the stoichiometric condition ($\phi=1.5$). However, when ϕ increases to 3, the incomplete combustion occurred, resulting in nitrate residues.

Surface and defect properties of the CeO_2 samples were investigated using XPS analysis. The Ce 3d spectra of representative CeO_2 powders for each system [CN+GL,

CAN+GL, CAN+HH and (CAN/AN)+HH] are shown in Figure 2.14. The spectra of Ce 3d can be deconvoluted into a superposition of eight subpeaks: v (882.2 eV), v' (884.5 eV), v'' (889.1 eV), v''' (898.3 eV), u (900.7 eV), u' (902.4 eV), u'' (907.3 eV) and u''' (916.6 eV), where v and u indicate the spin-orbit coupling $3d_{3/2}$ and $3d_{5/2}$, respectively [116]. The subpeaks labeled as v′ and u′ are attributed to Ce^{3+} and the other six peaks are assigned to Ce^{4+}. From the ratio of integrated peak areas of Ce^{3+} to that of total Ce^{3+} and Ce^{4+}, the concentration of Ce^{3+} of the samples can be calculated as shown [117]:

$$[Ce^{3+}] = \frac{A_{v'}+A_{u'}}{A_v+A_{v'}+A_{v''}+A_{v'''}+A_u+A_{u'}+A_{u''}+A_{u'''}} \qquad (2.11)$$

where A_i is the integrated area corresponding to subpeak i. It was found that the Ce^{3+} concentration on the samples prepared from CN+GL, CAN+GL, CAN+HH and (CAN/AN)+HH systems is 19.4, 18.6, 22.7 and 24.3%, respectively. Thus, the proportion of Ce^{3+} on hydrous hydrazine fuel cases was higher than that of glycine fuel cases and the highest value was found for the sample of (CAN/AN)+HH system. It has been known that oxygen vacancies (defect) can be produced through the transformation between Ce^{3+} and Ce^{4+}, and thus the higher the concentration of Ce^{3+}, the more oxygen vacancies [118]. Therefore, this result agrees well with the Raman analysis. Moreover, the defect concentration (up to 24.3%) of our samples was compared with that of pure CeO_2 reported in the literature (7-35%), indicating that our samples have a moderate defect concentration [77,112,115,119,120].
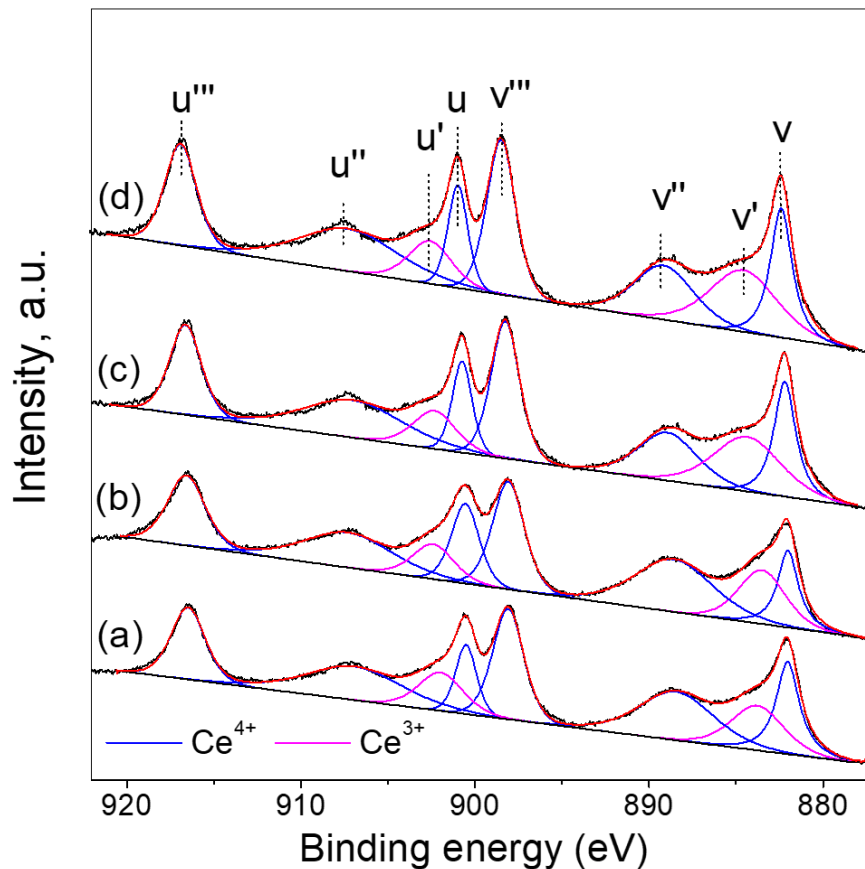
Figure 2.14 X-ray photoelectron spectra of CeO$_2$ powders prepared from (a) CN+GL, (b) CAN+GL, (c) CAN+HH and (d) (CAN/AN)+HH systems (ϕ=2, AN/MN ratio=4)

2.4.4.3 Surface area

The N$_2$ adsorption-desorption isotherms for the representative samples are shown in Figure 2.15. The samples exhibited the isotherm shape of a composite type II and IV according to the IUPAC classification [121]. This is characteristic isotherm of materials with a broad pore size distribution in the meso and macro ranges. Also, the hysteresis loop belongs to type H3 which is a feature of disordered porous materials with non-uniform pore network [121]. This pore structure may be related to the nature of SCS where pore structure is formed by gases evolved during the combustion process.
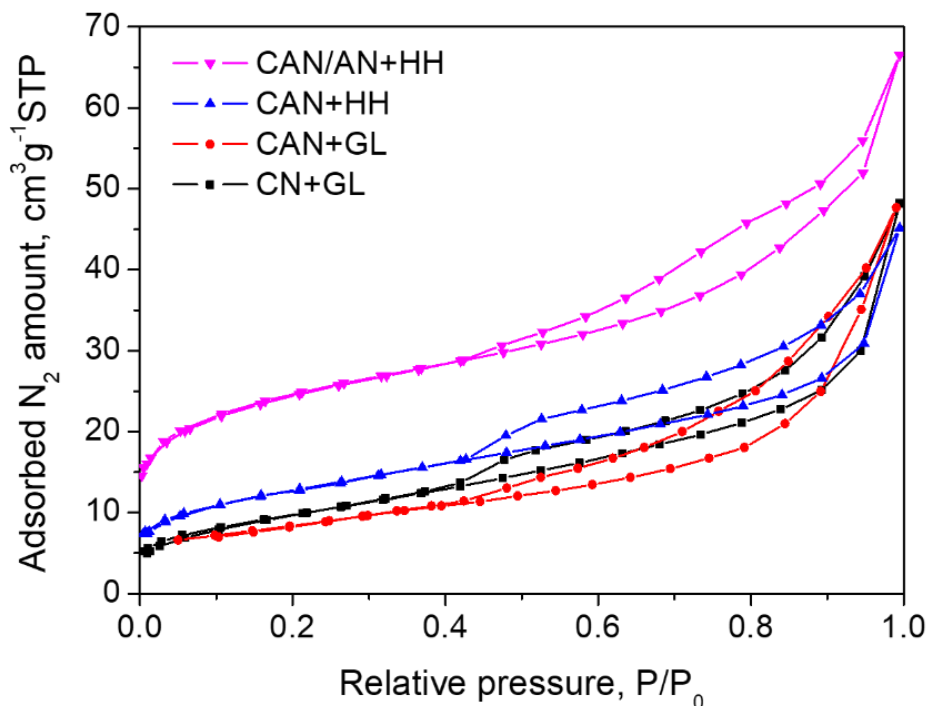
Figure 2.15 N$_2$ adsorption-desorption isotherms of CeO$_2$ powders prepared from (a) CN+GL, (b) CAN+GL, (c) CAN+HH and (d) (CAN/AN)+HH systems (ϕ=2, AN/MN ratio=4)

From the isotherms of all samples, the pore volume and the BET surface area were derived and are presented in Table 2.2. For CAN+GL system, as ϕ increases from 1 to 2, the pore volume increases owing to an increase in amount of evolved gases during SCS (from 21.3 to 31.3 mol) and a decrease of combustion temperature (Figure 2.5). As more gases are released during combustion, more porosity increases and more heat from combustion is carried away from the system, thereby restraining particle agglomeration. A similar trend for the pore volume was observed for the CAN+HH system. For ϕ from 0.5 to 1, the effect of gas evolution predominates over the effect of combustion temperature, resulting in increase of pore volume, while the opposite holds for ϕ from 1 to 2. For both

CAN+GL and CAN+HH systems, the pore volume decreases for $\phi > 2$ due to mitigation of gas evolution effect by the incomplete combustion. As shown in Table 2.2, the BET surface areas for all investigated systems except (CAN/AN)+HH system mainly depend on the crystallite size of CeO_2 rather than the pore volume. As CeO_2 crystallite size decreases, the BET surface area increases. For glycine fuel systems yielding larger crystallite size (18.3-38.7 nm), CeO_2 powders have lower surface area (13-34 m^2/g), while smaller-sized CeO_2 crystallites (10.2-14.8 nm) produced from hydrazine fuel systems have higher surface area (37.7-47.9 m^2/g). For (CAN/AN)+HH system, the expected effects of AN as a gas generating agent on pore volume and surface area are obviously confirmed. With increasing AN/MN ratio up to 4, both the pore volume and the BET surface area increase considerably due to enhanced gas evolution and the lowered combustion temperature. When AN/MN ratio increases further, the promoting effect of AN becomes insignificant. The effect of AN on morphologies of CeO_2 powders was also confirmed by SEM analysis (Figure 2.16). For AN/MN ratio = 0 case (Figure 2.16a and b), the product has a sponge-like structure with a broad pore size distribution. These roundish pores are formed by the rapid gas evolution during combustion. The AN/MN ratio = 1.5 case exhibits a similar structure but with smaller sized pores owing to the higher T_{max} likely causing pore shrinkage (Figure 2.16c and d). For AN/MN = 4 case, the further enhanced gas evolution leads to a more porous structure with larger macro-pores (Figure 2.16e) and the lower T_{max} prevents agglomeration of ceria particles during combustion, resulting in a nanoscale surface structure (Figure 2.16f). This observed trend is in agreement with the BET results.
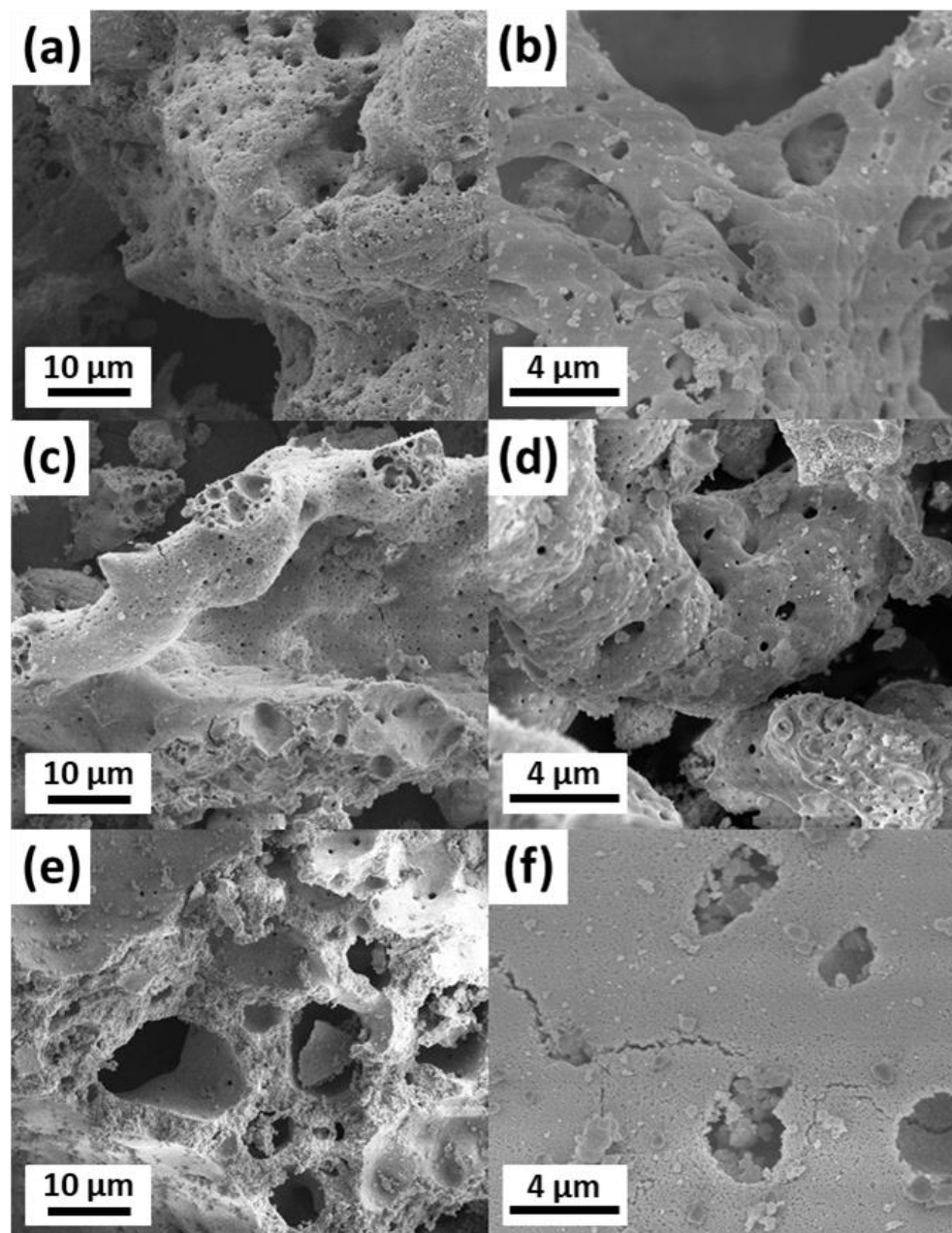
Figure 2.16 SEM images of CeO$_2$ powders prepared from (CAN/AN)+HH system; (a, b) AN/MN ratio= 0, (c, d) 1.5 and (e, f) 4

For many catalytic applications of CeO$_2$ such as emissions control, water gas shift, CO oxidation and methane reforming, high surface area CeO$_2$, which possesses more active sites, is desired to achieve high catalytic activity. In our study, specific surface areas of up

to ~88 m^2/g were obtained using facile SCS route. This value is significantly higher than that of commercial CeO_2 (<10 m^2/g). This result was compared with other CeO_2 powders synthesized by SCS, but under different conditions [75-79]. From the literature, it was found that only two studies reported higher surface area than our sample [furfuryl alcohol (95.3 m^2/g) and EDTA (163.5 m^2/g) fuel systems] [78,79]. However, we could not reproduce these results and indeed the experimental values we obtained were much lower than the reported ones as well as our best result. The BET surface area of CeO_2 for furfuryl alcohol and EDTA fuel systems were 60.7 and 8.6 m^2/g, respectively. Therefore, to our best knowledge, the CeO_2 nanopowder synthesized in this study provides the highest surface area among all CeO_2 prepared by the SCS method. As noted in the section 2.1, although the highest surface areas of CeO_2 reported in the literature are in the range 250-350 m^2/g, higher than SCS-derived products, one-step SCS process is promising in terms of feasibility for practical applications.

2.5   Conclusions

In this chapter, CeO_2 powders were synthesized using SCS, varying the synthesis parameters in terms of fuel [glycine (GL) and hydrous hydrazine (HH)], cerium precursor [$Ce(NO_3)_3 \cdot 6H_2O$ (CN) and $(NH_4)_2Ce(NO_3)_6$ (CAN)], fuel-to-oxidizer ratio (ϕ, 0.5–3) and gas generating agent [NH_4NO_3 (AN)]. The SCS experimental results demonstrated that the combustion mechanism depends strongly on the Ce precursor and fuel type. For CN+GL and CAN+GL systems, ignition is triggered by the gas-phase reaction between NH_3 and nitrogen oxides (NO_2 and N_2O) produced from the decomposition of glycine and cerium precursors, respectively. Owing to the different thermal decomposition properties of Ce

precursors, ignition for the CN+GL case occurs at ~265 °C by NO_2 formation from decomposition of $Ce(NO_3)_3 \cdot 6H_2O$, while for the CAN+GL case, NH_3 formation from decomposition of glycine leads to ignition at ~210 °C. In contrast, for the HH fuel system, the cerium precursor reacts with the fuel and forms a cerium hydrazine nitrate complex. The structure of the complex is the same regardless of the cerium precursor type. The ignition is initiated by evaporation of hydrazine with subsequent reaction of the fuel vapor with ambient oxygen. This induces combustion with the reaction between NO_3^- and N_2H_4 in the complex.

The characterization results revealed that the physicochemical properties such as crystallite size, surface area, pore volume and defect concentration depend on the combustion features, including maximum combustion temperature and amount of gas evolution, which are affected by the synthesis parameters. It was shown that decrease in crystallite size of samples is accompanied by proportional increase in defect concentration and specific surface area. The use of hydrous hydrazine fuel with $\phi = 2$ and AN/MN ratio = 4 allowed one to obtain CeO_2 nanopowder with small crystallite size (~8 nm), moderate defect concentration (24.3%) and high surface area (~88 m^2/g), which is the highest surface area among all CeO_2 samples prepared in this study and all SCS-derived CeO_2 powders reported in the literature. This work demonstrates that SCS is a facile one-step method to prepare high surface area CeO_2 nanopowders for many applications in catalysis. Moreover, controlling physicochemical properties of products by adjustment of synthesis parameters can enable one to achieve its full potential in specific applications.

CHAPTER 3.   SOLUTION COMBUSTION SYNTHESIS OF NICKEL/CERIUM OXIDE CATALYSTS FOR HYDROGEN GENERATION FROM HYDROUS HYDRAZINE DECOMPOSITION

3.1   Introduction

Over the past decades, various metal nanoparticles containing noble (Ir, Rh, Pd and Pt) and transition metals (Ni, Fe, Co and Cu) have been investigated to find a proper catalyst for selective hydrous hydrazine decomposition, which facilitate the complete decomposition $[N_2H_4\ (l)\ \rightarrow\ N_2\ (g)\ +\ 2H_2\ (g)]$ while suppressing the incomplete decomposition $[3N_2H_4\ (l) \rightarrow 4NH_3\ (g) + N_2\ (g)]$ [30,31,33,38,122-126]. Among them, Ni-based catalysts have been actively studied owing to its decent activity and low cost as compared to other active metals such as Rh and Ir. Recent studies also show that the use of metal oxides (Al_2O_3, CeO_2, La_2O_3 and MnO_2) as supports significantly enhances catalyst performance by providing high metal surface area and strong metal-support interaction [44,46,48,50,127-130]. Notably, it was reported that CeO_2 produces strong interaction with Ni metal particles, enhancing significantly the catalytic performance of Ni [46].

This chapter is focused for the first time on a non-conventional one-step method, namely solution combustion synthesis (SCS), as a preparation method of metal catalysts supported on metal oxide for hydrous hydrazine decomposition. Ni/CeO_2 catalysts, as a representative of metal catalysts supported on metal oxide, are prepared by SCS by varying the synthesis parameters to develop efficient catalysts for hydrous hydrazine decomposition and to understand the effects of the synthesis parameters on the SCS process and its correlation with the physical and catalytic properties. Finally, the catalytic

performance of the Ni/CeO$_2$ prepared by SCS is compared with that of catalysts prepared by different prior methods.

3.2   Experimental

3.2.1   Catalyst preparation

The SCS was used for preparation of all the studied catalysts in this work and the experimental procedure is schematically shown in Figure 3.1. In a typical experiment, stoichiometric amount of nickel nitrate hexahydrate [Ni(NO$_3$)$_2$.6H$_2$O, Alfa Aesar, 98%] and cerium ammonium nitrate [(NH$_4$)$_2$Ce(NO$_3$)$_6$, Alfa Aesar, 98+%] as metal oxidizers were dissolved in a minimum amount of distilled water and then added to hydrous hydrazine (N$_2$H$_4$.H$_2$O, Alfa Aesar, 99+%) or glycine (NH$_2$CH$_2$COOH, Alfa Aesar, 99.5%) as fuel. The amounts of metal oxidizers were determined to prepare catalysts with different nickel loading (3 to 68 wt%). The Ni contents of the catalysts were determined by atomic absorption spectroscopy (Table 3.1). The amount of fuel was adjusted by the fuel-to-oxidizer ratio, ϕ and four values (0.5 to 3) were selected to investigate the effect of ϕ on the SCS behavior and properties of the resulting products. After thorough mixing of the obtained solution, the mixture was heated over a hot plate to induce the self-sustained combustion. Typically, after dehydration of the aqueous precursor solution, ignition occurred, leading to combustion along with large gas evolution. During combustion, the temperature abruptly increased to a maximum value, followed by rapid cooling due to gas evolution and heat loss to the surroundings (Figure 3.2). The temperature change during combustion was monitored using an R-type thermocouple (tip diameter 0.125 mm) and the combustion behavior was also monitored by video recording. After cooling to room

temperature, the resulting powders were calcined in air at 400 ℃ for 4 h and then treated at 400 ℃ for 1 h in a flow of 10 vol% hydrogen, balance argon, to reduce NiO to Ni. All the prepared catalysts are designated as x wt% Ni/CeO$_2$-y-z, where 'x' is the wt% of Ni present in the catalyst, 'y' is the type of fuel and 'z' is the ϕ value. For example, 6 wt% Ni/CeO$_2$-HH-2 denotes a Ni/CeO$_2$ catalyst with 5.8 wt% Ni loading, prepared with hydrous hydrazine as fuel and $\phi = 2$.

Metal oxidizers

Ni(NO$_3$)$_2$·6H$_2$O	(NH$_4$)$_2$Ce(NO$_3$)$_6$	Fuel	Distilled water

**Heating Jacket
(350 ºC)**

↓

**Auto Ignition /
Combustion**

↓

**Calcination
(400ºC, 4 hr, air)**

↓

**Reduction
(400ºC, 1 hr, pure H$_2$)**

↓
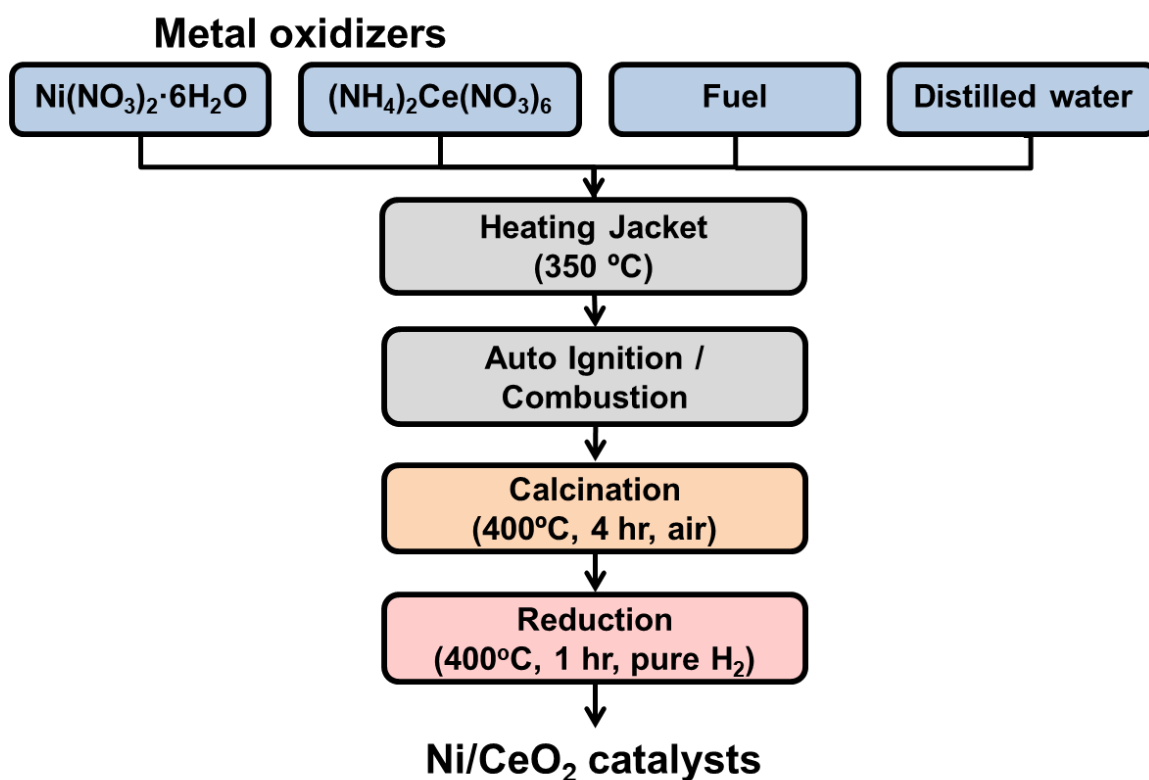
Ni/CeO$_2$ catalysts

Figure 3.1 Schematic diagram for the preparation of Ni/CeO$_2$ catalysts using solution combustion synthesis

Table 3.1 Ni contents of catalysts determined by atomic absorption spectroscopy (AAS)

Sample	Actual Ni content (wt%)
3 wt% Ni/CeO_2	2.8
6 wt% Ni/CeO_2	5.8
13 wt% Ni/CeO_2	12.7
24 wt% Ni/CeO_2	23.6
68 wt% Ni/CeO_2	68.4
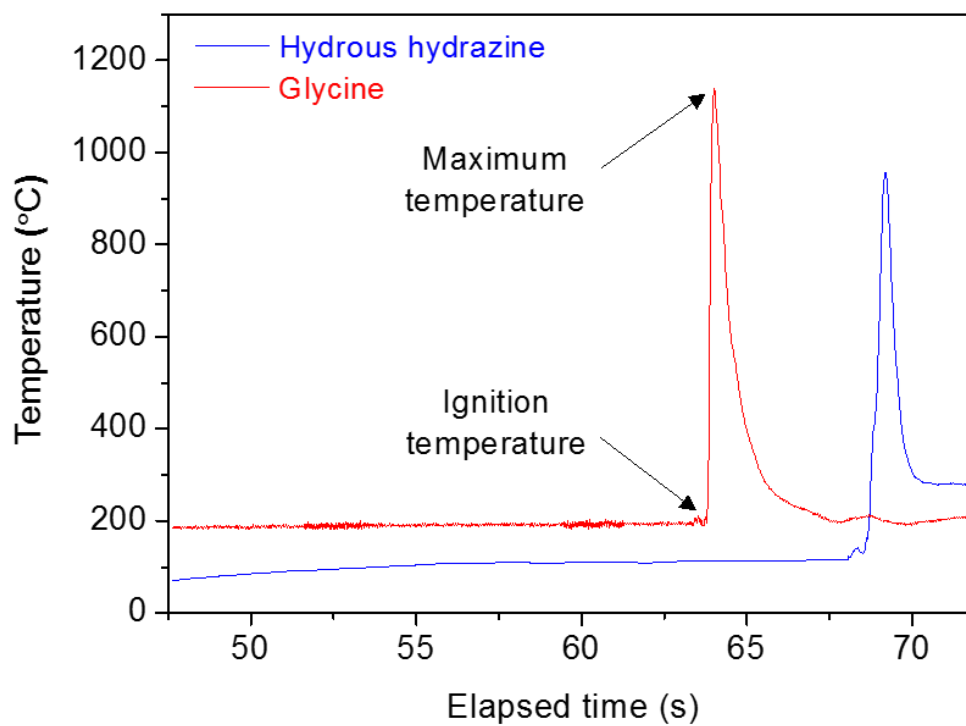
Figure 3.2 Temperature-time profiles for SCS in hydrous hydrazine and glycine fuel systems

To calculate the adiabatic temperature for a given SCS condition and compare to the experimentally measured maximum temperature, thermodynamic calculations were conducted using the "Thermo" software package, which is based on the minimization of thermodynamic potential and includes properties of more than 2500 compounds [82]. The combustion reactions between metal oxidizers and fuel [Eq. (3.1) for hydrous hydrazine and Eq. (3.2) for glycine] considered for the thermodynamic calculations are shown below:

$$\alpha Ni(NO_3)_2 + \beta (NH_4)_2 Ce(NO_3)_6 + \left[\phi + \frac{3}{2}\alpha + 5\beta\right] N_2 H_4 + (\alpha + \beta)(\phi - 1)O_2$$

$$\rightarrow \alpha NiO + \beta CeO_2 + \left[(\alpha + \beta)\phi + \frac{5}{2}\alpha + 9\beta\right] N_2 + [2(\alpha + \beta)\phi + 3\alpha + 9\beta]H_2 O$$

$$(3.1)$$

$$\alpha Ni(NO_3)_2 + \beta (NH_4)_2 Ce(NO_3)_6 + \left[\phi + \frac{1}{9}\alpha + \frac{5}{3}\beta\right] C_2 H_5 NO_2 + \left[\frac{9}{4}(\alpha + \beta)(\phi - 1)\right] O_2$$

$$\rightarrow \alpha NiO + \beta CeO_2 + \left[2\left((\alpha + \beta)\phi + \frac{1}{9}\alpha + \frac{5}{3}\beta\right)\right] CO_2$$

$$+ \left[\frac{1}{2}\left((\alpha + \beta)\phi + \frac{19}{9}\alpha + \frac{29}{3}\beta\right)\right] N_2 + \left[\frac{5}{2}\left((\alpha + \beta)\phi + \frac{1}{9}\alpha + \frac{49}{15}\beta\right)\right] H_2 O$$

$$(3.2)$$
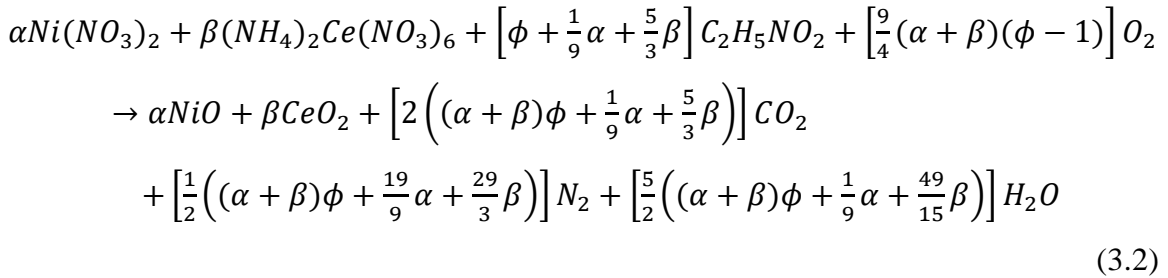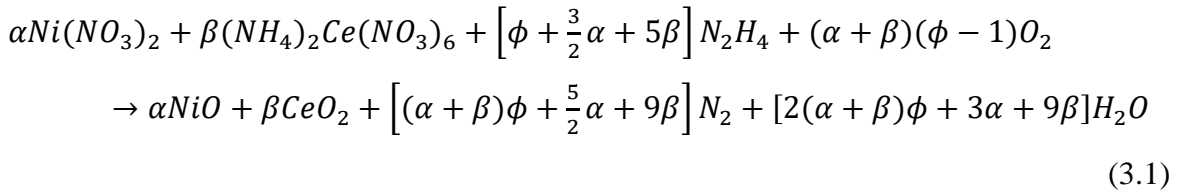
where α and β are the number of moles of Ni and Ce, respectively. The number of moles of evolved gases per mole of product was calculated based on Eqs. (3.1) and (3.2).

3.2.2 Catalyst characterization

The XRD, BET and TEM units which are described in Chapter 2.3.3 were used to examine the structural and morphological properties of the Ni/CeO$_2$ catalysts. The mean particle size of Ni in catalysts was determined from the XRD patterns by the Scherrer equation and confirmed with TEM pictures. The Ni loading in the catalysts was measured

using atomic absorption spectroscopy (AAS) on a PerkinElmer AAnalyst 300. The H_2 temperature programmed reduction (H_2-TPR) experiments were carried out with 200 mg NiO/CeO_2 sample packed in a stainless-steel column, using a Gow-Mac Model 20 thermal conductivity detector. Prior to TPR studies, N_2 gas was passed at 200 ℃ for 1 h to pretreat the sample and then cooled to room temperature. A 10 vol% H_2/N_2 mixture as reducing gas was flowed until the baseline of TCD signal became stable and then the sample temperature was increased at a constant 10 ℃/min rate from room temperature to 700 ℃. The amount of H_2 consumption as a function of temperature was determined from the TCD signal.

3.2.3 Catalytic decomposition of hydrous hydrazine

The catalytic reactions were conducted in a stainless-steel reactor (Parr Instrument Company, Model 4592) with external heating, shown in Figure 3.3. The reactor volume, including added fittings and tubing, was determined to be 63 ml. The catalyst was placed in a small glass vial (3 ml) inside the reactor, under argon (99.999%) atmosphere and then the reactor was preheated and held at the desired temperature (30–90 ℃). Under magnetic stirring of 1100 rpm, the reaction was initiated by injecting 2 ml diluted hydrous hydrazine solution (0.4 M) with NaOH (0.5 M) into the vial containing the catalyst. In all cases, the molar ratio of Ni in the catalyst to hydrous hydrazine was kept fixed at 1:10. The agitation speed where the reaction rate was not controlled by external mass transfer was determined by preliminary experiments to be above 900 rpm, where the highest reaction temperature (90 °C) was tested because the mass transfer limitation would be the most severe (Figure 3.4). The concentration of NaOH (Sigma-Aldrich, 50% in H_2O), which plays an important role in promoting the H_2 selectivity and kinetics of hydrous hydrazine decomposition [19,131-133], was optimized and the highest catalytic activity and H_2 selectivity were

obtained in 0.5 M NaOH solution (Figure 3.5). The reaction progress was monitored by measuring reactor pressure using a transducer (Omega Engineering PX35D1). After reaction completion, the product gas composition was analyzed by mass spectrometer (Hiden Analytical HPR-20) or micro gas chromatography (Agilent Micro GC 3000A), to obtain the molar ratio of N_2 to H_2 and to assess the presence of NH_3. The peak areas of H_2 and N_2 were calibrated using standard gas mixtures with different H_2/N_2 molar ratios.

The selectivity for hydrogen generation (α) was calculated based on the overall decomposition reaction (Eq. 3.3), leading to Eq.3.4.

$$3N_2H_4 \rightarrow 4(1-\alpha)NH_3 + 6\alpha H_2 + (1+2\alpha)N_2 \tag{3.3}$$
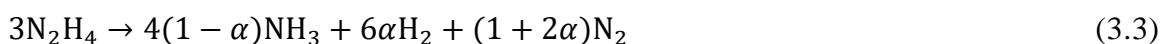
$$\alpha = \frac{1}{6(n(N_2)/n(H_2))-2}, \left(0 \leq \alpha \leq 1\right) \tag{3.4}$$

The reaction rate values for the catalysts were calculated based on all the Ni atoms present, as follows:

$$\text{Reaction rate}(h^{-1}) = \frac{n(H_2)}{n(\text{metal}) \times t} \tag{3.5}$$

where $n(H_2)$ is the moles of produced H_2, n(metal) is the moles of Ni in catalyst, and t is the reaction time for 50% conversion of hydrous hydrazine. The reported reaction rate values are averages from 2–5 experiments. To test recyclability test of the catalyst, the reaction was repeated for three runs under the same conditions as the first cycle. After the

hydrogen generation was completed, the catalyst was separated from the reaction solution by centrifugation, washed with water and tested under the same conditions.
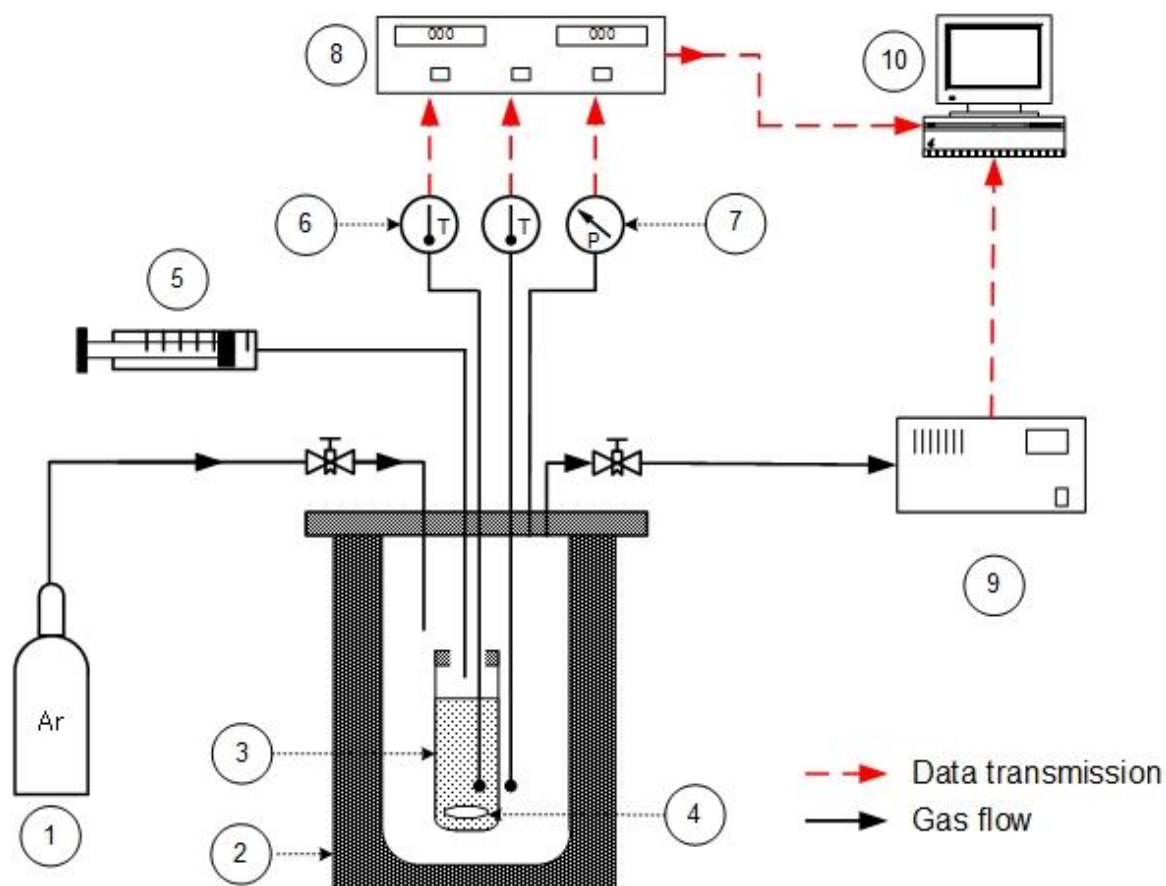
Figure 3.3 Schematic diagram of the experimental setup for hydrous hydrazine decomposition
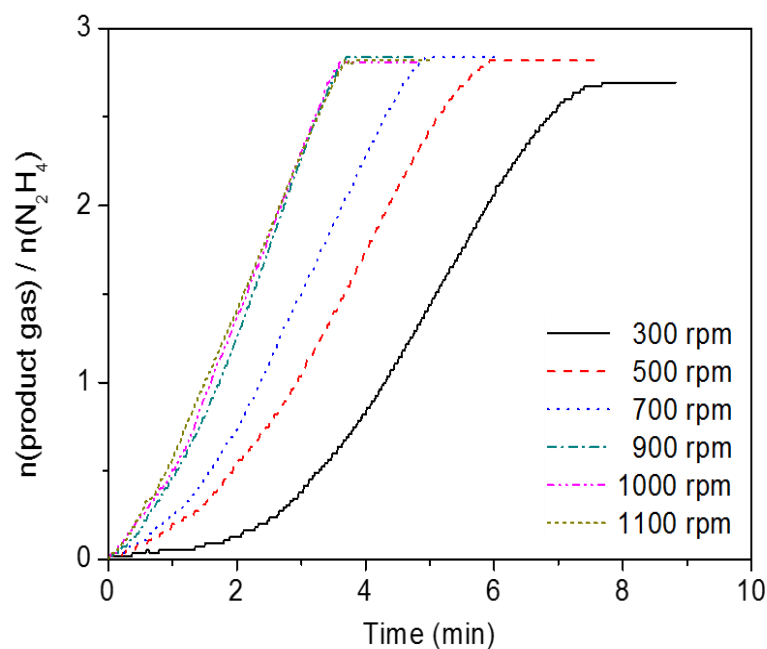
Figure 3.4 Effect of agitation speed on the decomposition of hydrous hydrazine; 6 wt% Ni/CeO$_2$-HH-2 catalyst, n(Ni)/n(N$_2$H$_4$) = 0.1, 90 ℃, 0.5M NaOH
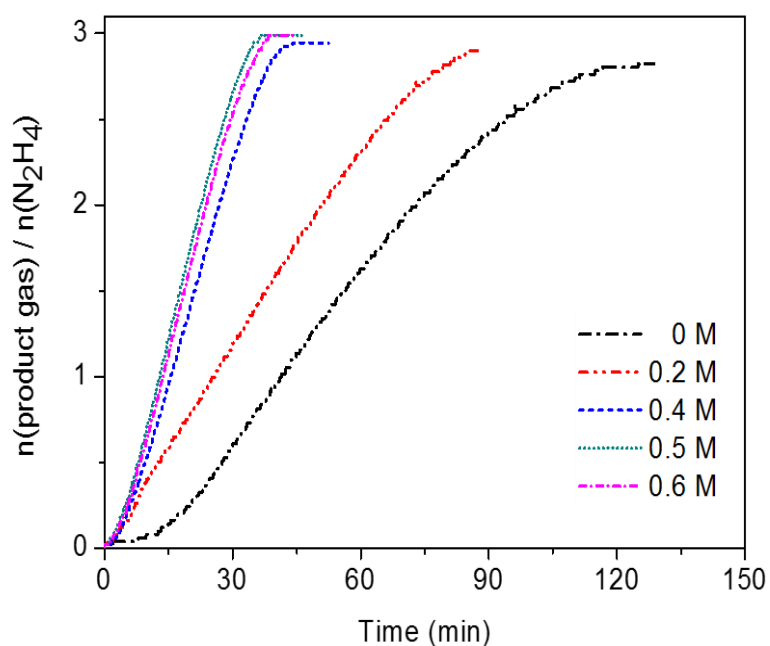
Figure 3.5 Effect of NaOH concentration on the decomposition of hydrous hydrazine over 6 wt% Ni/CeO$_2$-HH-2 catalyst; n(Ni)/n(N$_2$H$_4$) = 0.1, 50 ℃

3.3 Results and discussion

3.3.1 Combustion characteristics

The combustion characteristics including the measured maximum temperature, the calculated adiabatic temperature, and the amount of evolved gas during combustion for all catalysts studied are summarized in Table 3.2. The maximum temperature is an important system characteristic and relates to formation of products with desired crystallinity, although too high temperature may cause agglomeration and sintering of metal particles. The gas evolution during combustion dissipates the heat, inhibits agglomeration and promotes the porosity of products. As expected, the calculated adiabatic temperatures are always higher than the measured maximum temperatures. The discrepancy is due to nonadiabatic experimental conditions and possible delay of the thermocouple signal. Nevertheless, the trends of the adiabatic temperature agree well with the measured maximum temperature.

Table 3.2 Combustion characteristics of catalysts as a function of Ni loading, fuel-to-oxidizer ratio and fuel

Sample	Maximum temperature ($^{\circ}$C)		Amount of produced gases (mol)
	Measured	Adiabatic	
3 wt% Ni/CeO$_2$-HH-2	1100	1650	27.5
6 wt% Ni/CeO$_2$-HH-2	940	1587	26.2
13 wt% Ni/CeO$_2$-HH-2	795	1470	23.7
24 wt% Ni/CeO$_2$-HH-2	800	1310	20.6
68 wt% Ni/CeO$_2$-HH-2	754	933	13.9
6 wt% Ni/CeO$_2$-HH-0.5	396	687	21.7
6 wt% Ni/CeO$_2$-HH-1	454	1046	23.2
6 wt% Ni/CeO$_2$-HH-3	1225	1931	29.2
6 wt% Ni/CeO$_2$-GL-2	1150	1770	24.0

The effect of different fuels on the combustion characteristics is shown in Figure 3.6 and Table 3.2. Visually, combustion with glycine fuel (6 wt% Ni/CeO$_2$-GL-2) took place vigorously within the entire volume of the precursor mixture with high maximum temperature (~1150 ºC) for a short duration (~2 sec). On the other hand, combustion with hydrous hydrazine fuel (6 wt% Ni/CeO$_2$-HH-2) occurred with ignition locally followed by steady wave propagation along the mixture with moderate maximum temperature (~940 ºC), lasting about 50 seconds until combustion was complete. The features of combustion with glycine and hydrous hydrazine fuels correspond to the volume combustion synthesis and the self-propagating high-temperature synthesis modes, respectively [24].
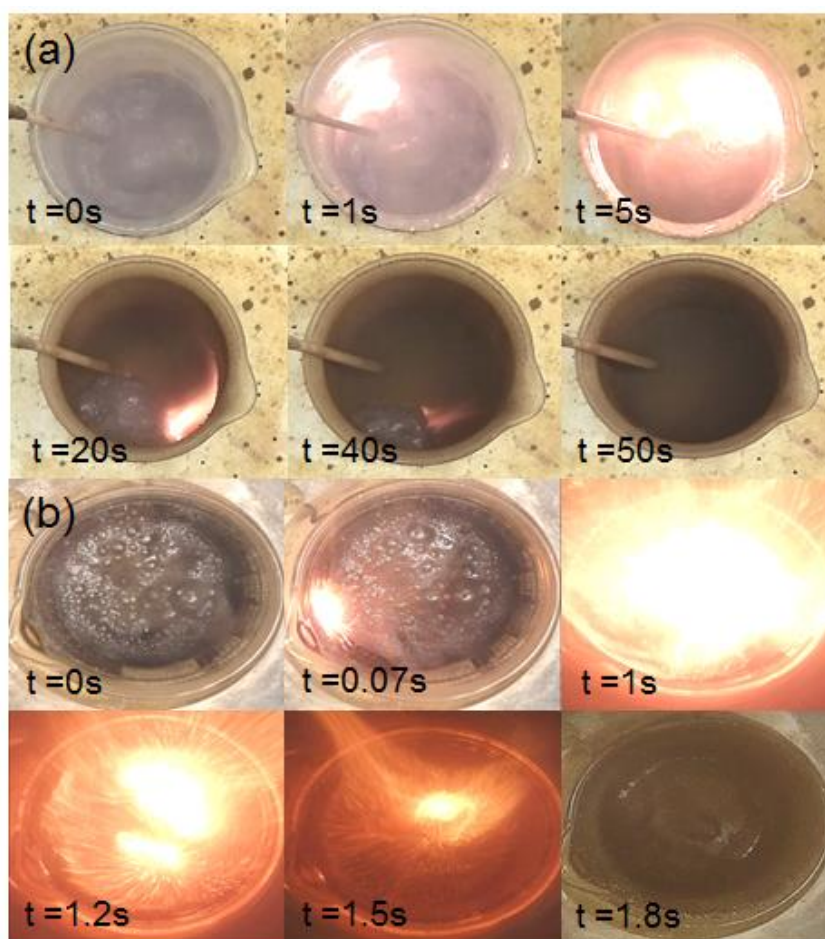
Figure 3.6 Combustion process for different fuel systems (a) hydrous hydrazine, and (b) glycine

The lower measured maximum temperature for the hydrous hydrazine fuel, as compared to glycine, corresponds to the predictions for the adiabatic case (Table 3.2). The different ignition temperatures for the two fuels can be related to their distinct combustion mechanisms. As shown in Figure 3.2, the glycine system ignited at ~200 ℃, which corresponds to the formation of HNO_3 from the decomposition of cerium ammonium nitrate. It is reported that cerium ammonium nitrate decomposes to NO_2 starting at 185 ℃ which, in turn, reacts with H_2O to form HNO_3 and NO [134,135]. The formed HNO_3 then triggers the combustion reaction with the fuel, as noted elsewhere [25,26]. The reaction mixture also contains nickel nitrate but its decomposition to form HNO_3 occurs at higher temperature 252 ℃ [85], hence it is not the trigger for ignition in the present case. In contrast, the ignition temperature of hydrous hydrazine fuel is ~120 ℃ and is related to its boiling point (~114 ℃), with subsequent reaction of the fuel vapor with ambient oxygen [25].

The influence of Ni loading and ϕ value on the combustion characteristics is also presented in Table 3.2, with hydrous hydrazine used as fuel. With increase of Ni loading from 3 to 68 wt%, the maximum measured temperature and amount of gases evolved during combustion decrease. On the other hand, with increasing ϕ, the intensity of combustion becomes significantly stronger and the amount of gases increases. These trends for the effects of Ni loading and ϕ follow the predictions for the adiabatic case.

3.3.2 Physicochemical properties of Ni/CeO$_2$ catalysts

3.3.2.1 Structural properties

The XRD patterns of the 6 wt% Ni/CeO$_2$ catalysts prepared with different fuels at $\phi = 2$ are shown in Figure 3.7. Both catalysts clearly exhibit the CeO$_2$ phase (JCPDS No.

43-1002) while Ni phase was not observed, which suggests that Ni particles are highly dispersed on the support. However, the possibility also exists that the Ni content is too low to be detected by the XRD analysis. It is evident that peaks corresponding to CeO_2 phase for the glycine fuel are sharper than those for the hydrous hydrazine fuel, indicating the higher crystallinity of CeO_2 phase. Considering that the maximum temperature with glycine fuel (1,150 ℃) is higher than with hydrous hydrazine fuel (940 ℃), the difference of crystallinity for the two catalysts is in agreement with the combustion characteristics. In addition, it is noticeable that the peaks of CeO_2 phase in 6 wt% Ni/CeO_2-HH-2 significantly shift to higher degrees relative to those for the reference, whereas the peak shifting is less obvious in 6 wt% Ni/CeO_2-GL-2 catalyst. This peak shifting which indicates the lattice contraction can be due to the partial incorporation of smaller Ni^{2+} ions (0.81 Å) into the lattice of Ce^{4+} (0.97 Å) to form a Ni-O-Ce solid solution [136]. Liu et al. reported that the formation of such solid solution is favorable at lower calcination temperature and it may decompose with high-temperature calcination [137]. Thus, the higher maximum temperature with glycine fuel may hinder the formation of Ni-O-Ce solid solution. It is known that formation of the solid solution yields the oxygen vacancies due to the charge unbalance and lattice distortion caused by the differences between the radii and oxidation states of Ni^{2+} and Ce^{4+} ions [138-140]. This oxygen vacancy in the Ni-O-Ce solid solution of Ni/CeO_2 catalysts modifies the electronic ability of Ni as an electron donor and alters the interaction between the Ni and N_2H_4 molecules, which facilitates N-H bond dissociation instead of N-N bond on Ni and makes the H_2 generation easier [46].
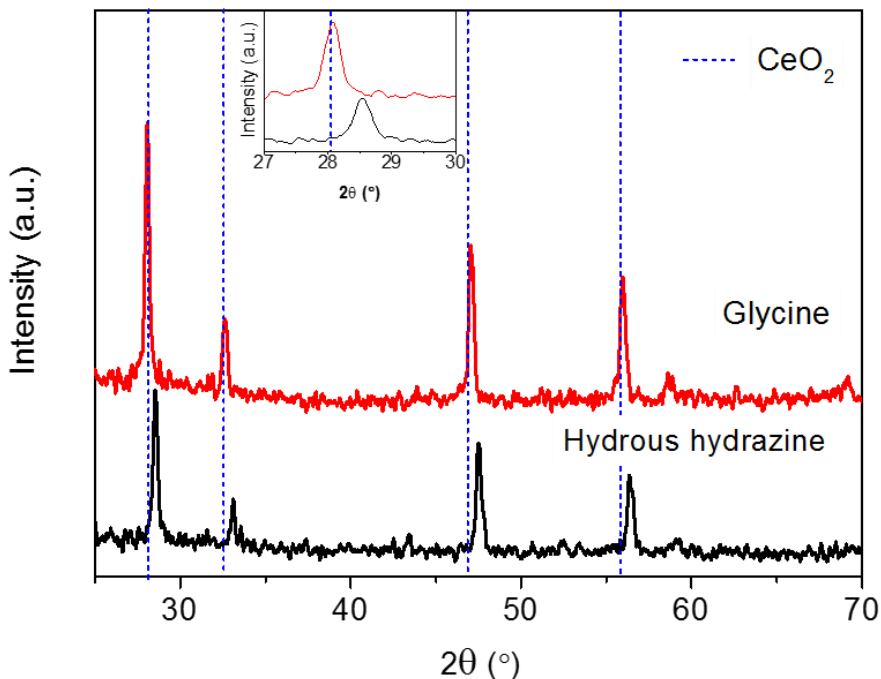
Figure 3.7 XRD patterns of 6 wt% Ni/CeO$_2$-HH-2 and 6 wt% Ni/CeO$_2$-GL-2 catalysts, compared with the reference of CeO$_2$ (JCPDS No. 43-1002)

For the XRD patterns of the 6 wt% Ni/CeO$_2$-HH-z catalysts prepared at different ϕ values (Figure 3.8), the peaks of CeO$_2$ phase become sharper and stronger as ϕ increases, indicating that the crystallinity of CeO$_2$ phase increases. In addition, the peak shifting is more pronounced for the catalysts prepared at low ϕ value. The change of crystallinity and peak shifting with variation of ϕ is reasonable considering that the maximum temperature increases with an increase of ϕ value. The XRD patterns of the Ni/CeO$_2$-HH-2 catalysts with different Ni loading (Figure 3.9) clearly show the Ni phase (JCPDS No. 04-0850) as well as the CeO$_2$ phase. As expected, the intensity of peaks for Ni phase diminishes with a decrease of Ni loading and the Ni phase was not found for 3 and 6 wt% Ni/CeO$_2$-HH-2 catalysts, possibly due to the high dispersion of Ni particles or the resolution limit of XRD measurement. It may be seen that the peak shifting of CeO$_2$ peaks towards higher degrees

is more pronounced for the catalysts with lower Ni loading. Thus, although higher measured maximum temperature was observed at lower Ni loading, it appears that the formation of Ni-O-Ce solid solution is favored at lower Ni loading. It has been reported that, owing to segregation of Ni particles, formation of the solid solution is less favorable with increase in Ni loading [141,142]. This implies that the formation of Ni-O-Ce solid solution depends on combustion temperature as well as Ni loading, and is more strongly affected by the Ni loading than the combustion temperature.
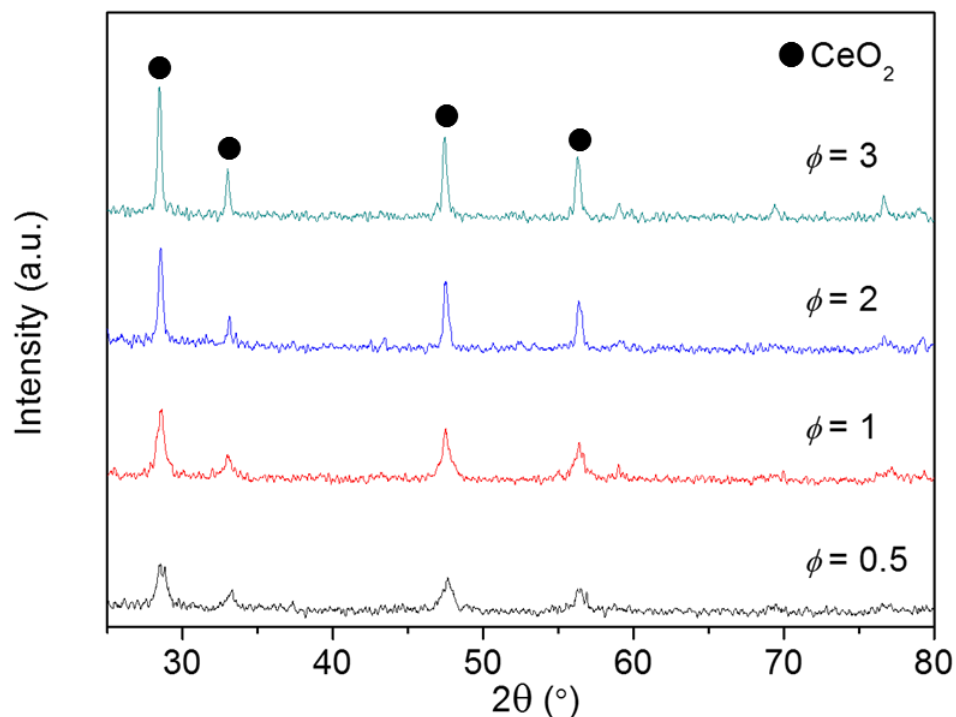
Figure 3.8 XRD patterns of 6 wt% Ni/CeO_2-HH-z catalysts as a function of ϕ ($0.5 \leq z \leq 3$)
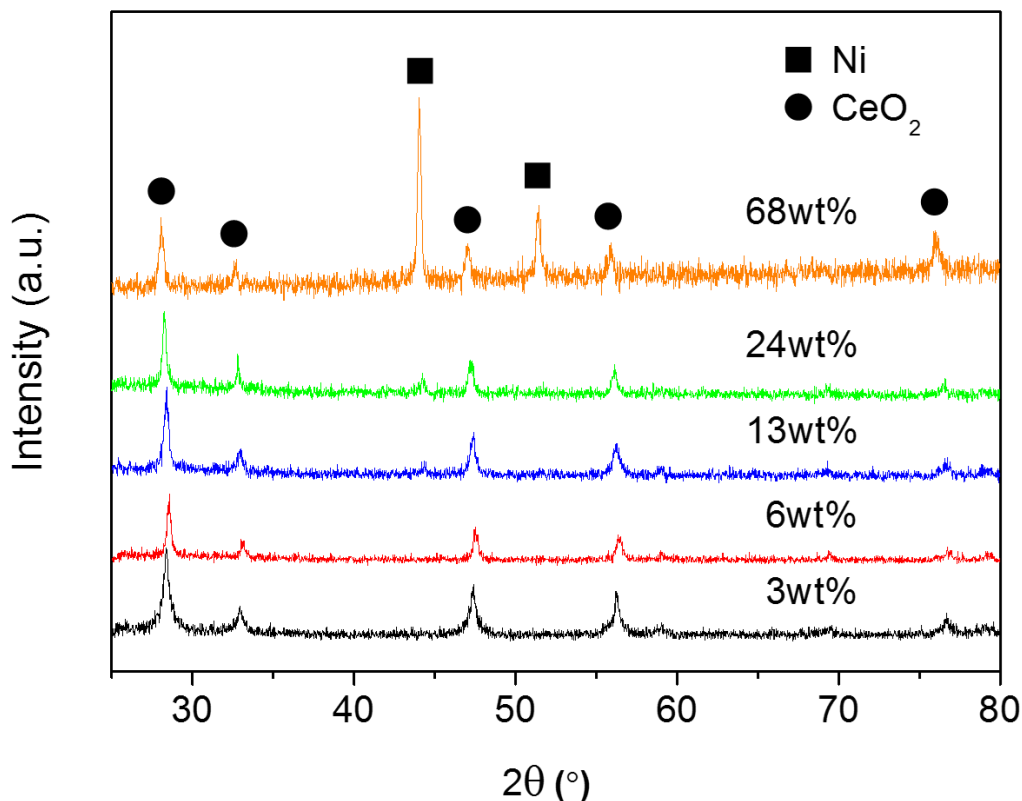
Figure 3.9 XRD patterns of Ni/CeO$_2$-HH-2 catalysts as a function of Ni loading

3.3.2.2 Morphological properties

The morphologies of the catalysts were observed by TEM analysis (Figure 3.10). The average Ni particle size and size distribution histograms of the catalysts, obtained from TEM images, is presented in Table 3.3 and Figure 3.11. The images show Ni particle size ranging from 10.3 to 38.9 nm, close to those calculated from the XRD patterns using the Scherrer equation [83]. It may be seen that the catalyst using hydrous hydrazine fuel has smaller Ni particle size than that prepared using glycine fuel, due to the lower maximum temperature which decreases agglomeration and sintering of particles [24]. Similarly, the Ni particle size of the catalysts increases with increase of ϕ value. With an increase of Ni loading from 3 to 6 wt%, the Ni particle size decreases due to the smaller maximum

temperature. When the Ni loading increases further, however, the Ni particle size increases significantly despite a decrease of the maximum temperature. It appears that for higher Ni loadings (13-68 wt%), the effect of nickel segregation dominates the heating effect by combustion.
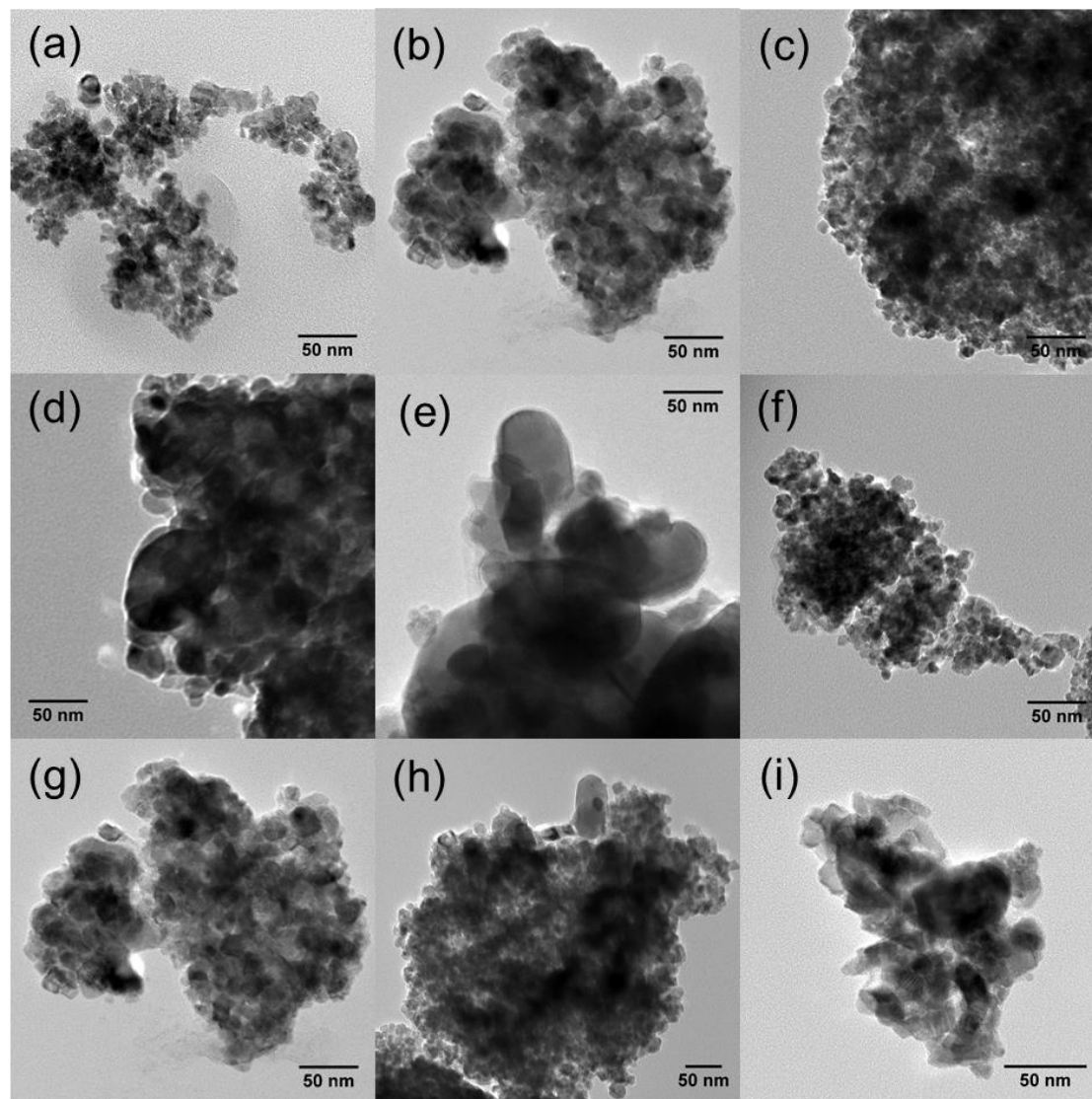
Figure 3.10 TEM images of different catalysts. (a) 3 wt% Ni-CeO$_2$-HH-2, (b) 6 wt% Ni-CeO$_2$-HH-2 (c) 13 wt% Ni-CeO$_2$-HH-2, (d) 24 wt% Ni-CeO$_2$-HH-2, (e) 68 wt% Ni-CeO$_2$-HH-2, (f) 6 wt% Ni-CeO$_2$-HH-0.5, (g) 6 wt% Ni-CeO$_2$-HH-1, (h) 6 wt% Ni-CeO$_2$-HH-3 and (i) 6 wt% Ni-CeO$_2$-GL-2

Table 3.3 Physical properties of Ni/CeO$_2$ catalysts

Sample	Ni particle size (nm)		BET surface area (m^2/g)	Pore size (nm)
	XRD	TEM		
3 wt% Ni/CeO$_2$-HH-2	NA	16.5	10.2	16.6
6 wt% Ni/CeO$_2$-HH-2	NA	14.7	12.5	18.8
13 wt% Ni/CeO$_2$-HH-2	20.9	19.2	14.7	15.5
24 wt% Ni/CeO$_2$-HH-2	23.1	23.9	13.8	15.2
68 wt% Ni/CeO$_2$-HH-2	37.4	38.9	6.8	12.7
6 wt% Ni/CeO$_2$-HH-0.5	NA	10.3	12.0	14.8
6 wt% Ni/CeO$_2$-HH-1	NA	11.9	12.1	15.7
6 wt% Ni/CeO$_2$-HH-3	NA	17.5	5.2	17.0
6 wt% Ni/CeO$_2$-GL-2	NA	16.2	11.9	13.2
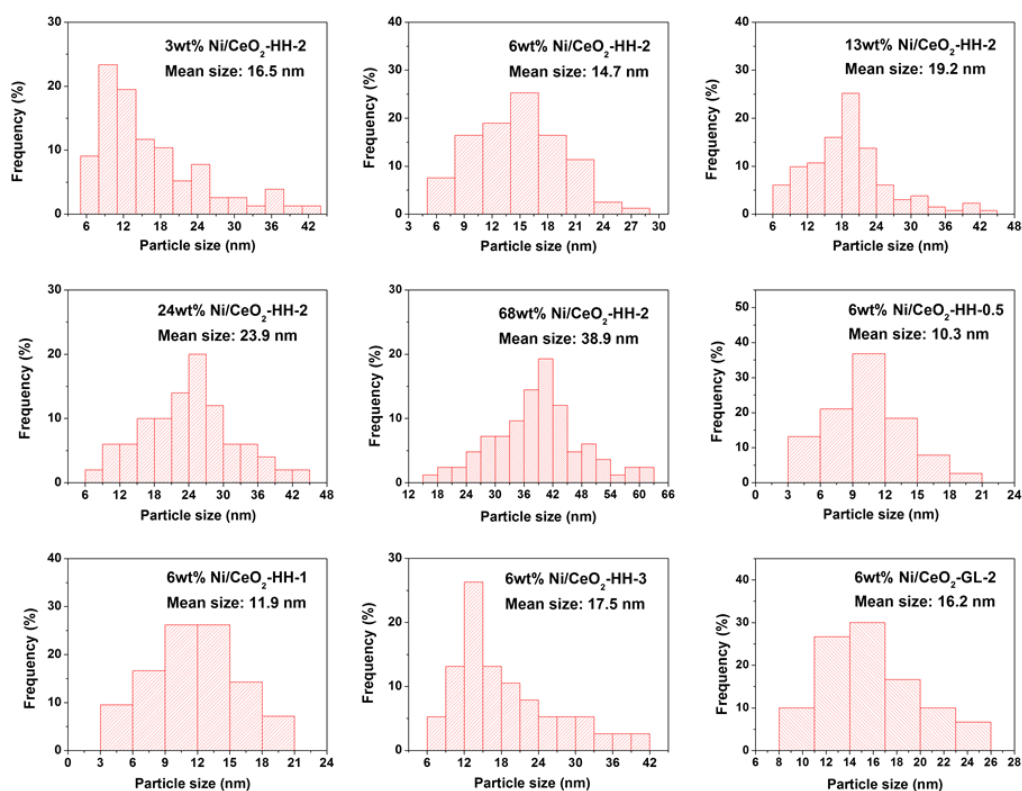
Figure 3.11 Ni particle size distribution histograms of Ni/CeO$_2$ catalysts

The BET surface areas and pore sizes for all catalysts are also presented in Table 3.3. The BET surface areas are in the range 5.2 to 14.7 m^2/g, although there was no clear trend with the combustion characteristics. The pore size, on the other hand, increases with increased amount of gases released during combustion. For samples with high maximum temperature above 1100 ℃, however, shrinkage of pore structure occurred regardless of the level of gas evolution owing to sintering. In such cases, the heating effect by combustion dominates the heat dissipation by gas evolution. Consequently, among the investigated catalysts in this study, 6 wt% Ni/CeO_2-HH-2 catalyst has the largest pore size (18.8 nm).

3.3.2.3   Catalyst reducibility

The reducibility of the samples was investigated using H_2-TPR experiments to confirm the interaction between Ni and CeO_2, namely existence of the Ni-O-Ce solid solution. The H_2-TPR profiles of 6 wt% Ni/CeO_2-HH-2 and 6 wt% Ni/CeO_2-GL-2 samples are shown in Figure 3.12. For the sample prepared with hydrous hydrazine fuel, two hydrogen consumption peaks (α and β) were observed while, in contrast, only the β peak was observed for the sample prepared with glycine fuel. The α peak is due to the reduction of adsorbed oxygen which is linked to the oxygen vacancy on the Ni-O-Ce solid solution, while the β peak corresponds to the reduction of NiO particles [140]. This feature indicates that hydrous hydrazine fuel produces larger amount of Ni-O-Ce solid solution while it is low or negligible for glycine fuel. This result agrees with the XRD analysis. Moreover, the β peak of 6 wt% Ni/CeO_2-GL-2 is positioned at slightly higher temperature as compared to that of 6 wt% Ni/CeO_2-HH-2. This indicates presence of larger NiO particles which are more difficult to reduce and agrees with the average Ni particle sizes obtained from TEM

analysis. As noted above, smaller Ni particle size and larger amount of solid solution for 6 wt% Ni/CeO_2-HH-2 are both attributed to the relatively milder combustion characteristics.
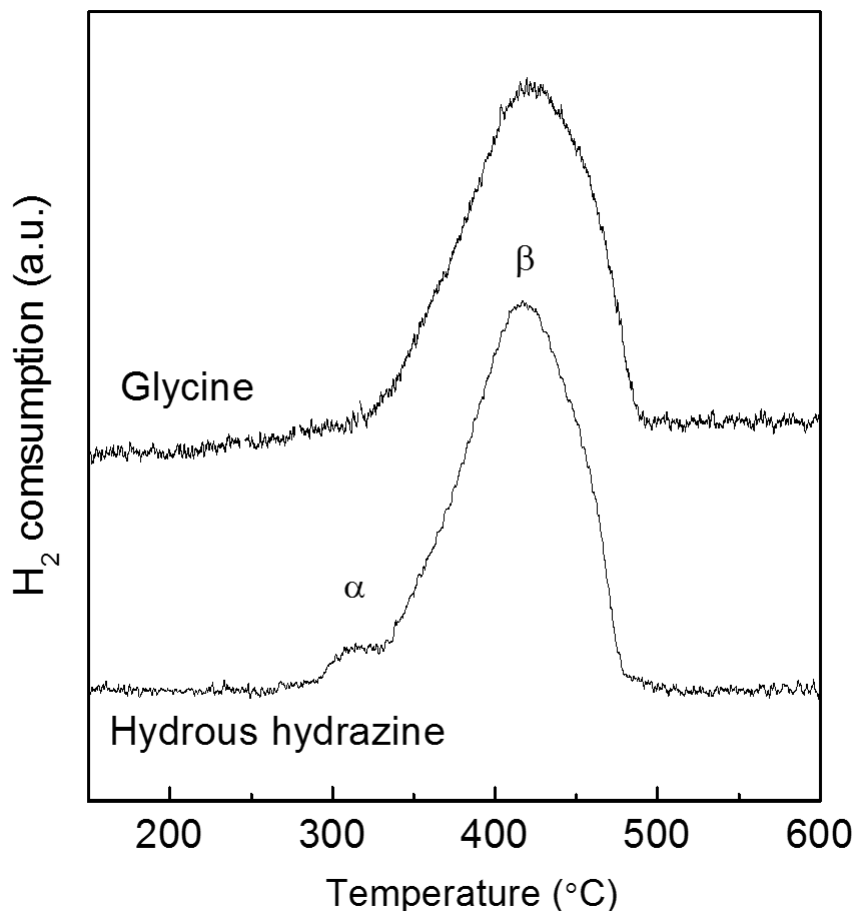
Figure 3.12 H_2-TPR profiles of 6 wt% Ni/CeO_2-HH-2 and 6 wt% Ni/CeO_2-GL-2 samples

The H_2-TPR profiles of 6 wt% Ni/CeO_2 samples prepared at different ϕ (Figure 3.13) shows that the intensity of α peak decreases while the β peak shifts to higher temperatures with increasing ϕ values. These features further confirm that the formation of Ni-O-Ce solid solution becomes more unfavorable, while the Ni particle size increases, with increase of maximum temperature during SCS. The H_2-TPR profiles of samples with different Ni loadings (Figure 3.14) illustrate that the concentration of Ni-O-Ce solid

solution depends on the Ni loading. For the samples with 68 and 24 wt% Ni loading, no α

peak was observed. As the Ni content decreases to 13 wt%, the α peak appears and its area

increases slightly with a decrease from 13 to 6 wt%. This indicates that the formation of

Ni-O-Ce solid solution is favorable at lower Ni loading, which agrees with the XRD results.

For the sample with 3 wt% Ni loading, the area of the α peak is slightly smaller than for 6

wt% Ni loading and the γ peak is found, which is responsible for the reduction of oxygen

vacancies of free CeO_2 [138]. This implies that 3 wt% Ni loading leads to lower Ni-O-Ce

solid solution and is not sufficiently high for Ni particles to cover the CeO_2 phase. The

temperature for the β peak generally increases with Ni loading, except for 6 wt% sample,

suggesting that it has the smallest Ni particle size which is confirmed from the TEM and

XRD analysis shown in Table 3.3. Prior studies also reported a minimum Ni loading for

the highest metal dispersion in Ni/CeO_2 catalysts [138,143].
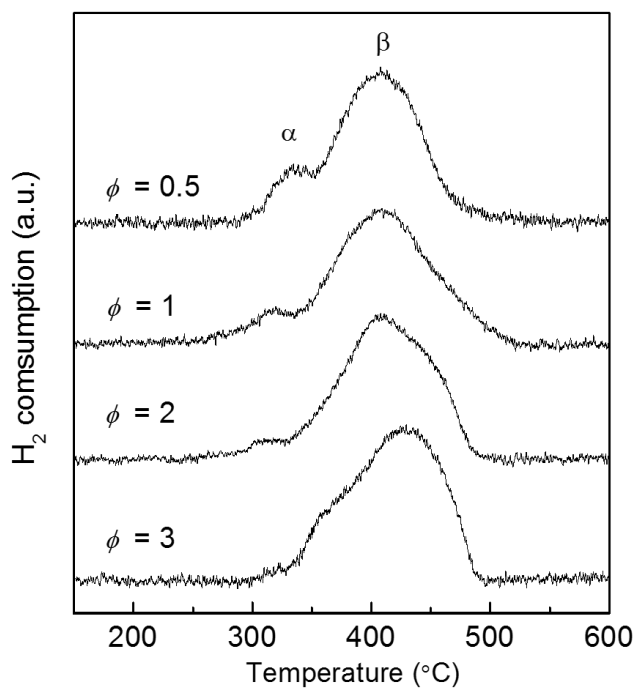
Figure 3.13 H_2-TPR profiles of 6 wt% Ni/CeO_2-HH-z samples as a function of ϕ ($0.5 \leq z \leq 3$)
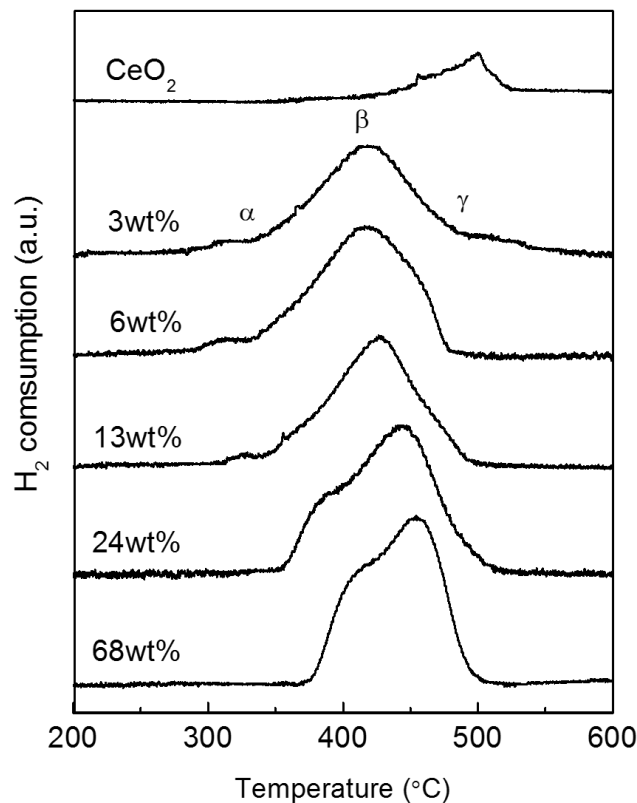
Figure 3.14 H$_2$-TPR profiles of CeO$_2$ and Ni/CeO$_2$-HH-2 samples as a function of Ni loading

3.3.3 Catalytic performance of Ni/CeO$_2$ catalysts

3.3.3.1 Effect of SCS parameters

The catalytic performance of different Ni/CeO$_2$ catalysts for hydrous hydrazine decomposition was evaluated at 50 ℃ [n(Ni)/n(N$_2$H$_4$) = 0.1] and is summarized in Table 3.4. It was found that the catalytic activity and selectivity for hydrogen generation depend strongly on the SCS synthesis parameters (ratio of precursor oxidizers, ϕ value and fuel type). This finding aligns with the trend of physicochemical properties such as Ni particle size, pore size and amount of Ni-O-Ce solid solution by changing the SCS synthesis parameters. In summary, catalysts with smaller Ni particle size, larger pore size and higher concentration of Ni-O-Ce solid solution show good catalytic performance. Too much

concentration of the solid solution, however, was unfavorable for the catalytic performance because the solid solution acts as a promoter but not an active site by itself [46]. It is well known that small metal particle size increases the number of active sites [144], larger pore size improves mass transport within pores [145], and Ni-O-Ce solid solution can enhance catalytic activity and H_2 selectivity of Ni/CeO_2 catalysts by modifying the electronic properties of nearby metallic Ni [45,46,146]. The best catalytic activity was observed for the 6 wt% Ni/CeO_2-HH-2 catalyst, for which the reaction took 17.7 min for 50% conversion of hydrous hydrazine, corresponding to a reaction rate of 34.0 h^{-1}. Also, its H_2 selectivity was 100%, with the product gas containing only H_2 and N_2 in the molar ratio $H_2/N_2 = 2$. This catalytic performance may be related to its physicochemical properties such as relatively small Ni particle size (14.7 nm), large pore size (18.8 nm) and moderate concentration of Ni-O-Ce solid solution.

Table 3.4 Catalytic performance of Ni/CeO_2 catalysts for hydrous hydrazine decomposition [$n(Ni)/n(N_2H_4) = 0.1$, 50 ℃].

Sample	H_2 selectivity (%)	Reaction rate $(h^{-1})^a$
3 wt% Ni/CeO_2-HH-2	100	20.9 ± 0.7
6 wt% Ni/CeO_2-HH-2	100	34.0 ± 1.9
13 wt% Ni/CeO_2-HH-2	99	21.8 ± 1.2
24 wt% Ni/CeO_2-HH-2	95	22.3 ± 1.9
68 wt% Ni/CeO_2-HH-2	94	5.1 ± 0.1
6 wt% Ni/CeO_2-HH-0.5	100	21.1 ± 0.9
6 wt% Ni/CeO_2-HH-1	100	29.0 ± 0.6
6 wt% Ni/CeO_2-HH-3	98	26.6 ± 1.3
6 wt% Ni/CeO_2-GL-2	98	19.6 ± 1.4

[a] reaction rate was calculated at 50% conversion of hydrous hydrazine.

3.3.3.2 Effect of reaction temperature

The hydrous hydrazine decomposition plots over the 6 wt% Ni/CeO$_2$-HH-2 catalyst at different temperatures are shown in Figure 3.15. As expected, the reaction rate significantly increased about 30-fold with increase of reaction temperature from 30 to 90 ℃ (Figure 3.15a). The reaction times for 50% conversion were 67.0 ± 3.9, 5.9 ± 0.2, and 1.9 ± 0.1 min at 30, 70 and 90 ℃, respectively. The standard deviation of the reaction time for 50% conversion is indicated by the error bars in Figure 3.15a. As shown in Figure 3.15b, the selectivity to hydrogen generation is 99% at 30 ℃ and remains 100% in the temperature range 40–70 ℃. When the temperature increases further to 90 ℃, the H$_2$ selectivity decreases sharply to 93% owing to thermodynamic reasons, as reported elsewhere [37,147]. The reaction rate for 50% conversion are shown in Figure 3.15b and reported in Table 3.5. Based on these data, the apparent activation energy (E_a) for catalytic decomposition of hydrous hydrazine over the 6 wt% Ni/CeO$_2$-HH-2 catalyst was determined to be 56.2 ± 1.7 kJ/mol (Figure 3.16), which compares well with values for Ni catalysts reported in the literature [43,50,146]. In recycling tests to assess catalyst reusability, the 6 wt% Ni/CeO$_2$-HH-2 catalyst retained 100% H$_2$ selectivity over 3 cycles and exhibited relatively small decrease in catalytic activity, which has also been observed by others (Figure 3.17) [37,123,133].
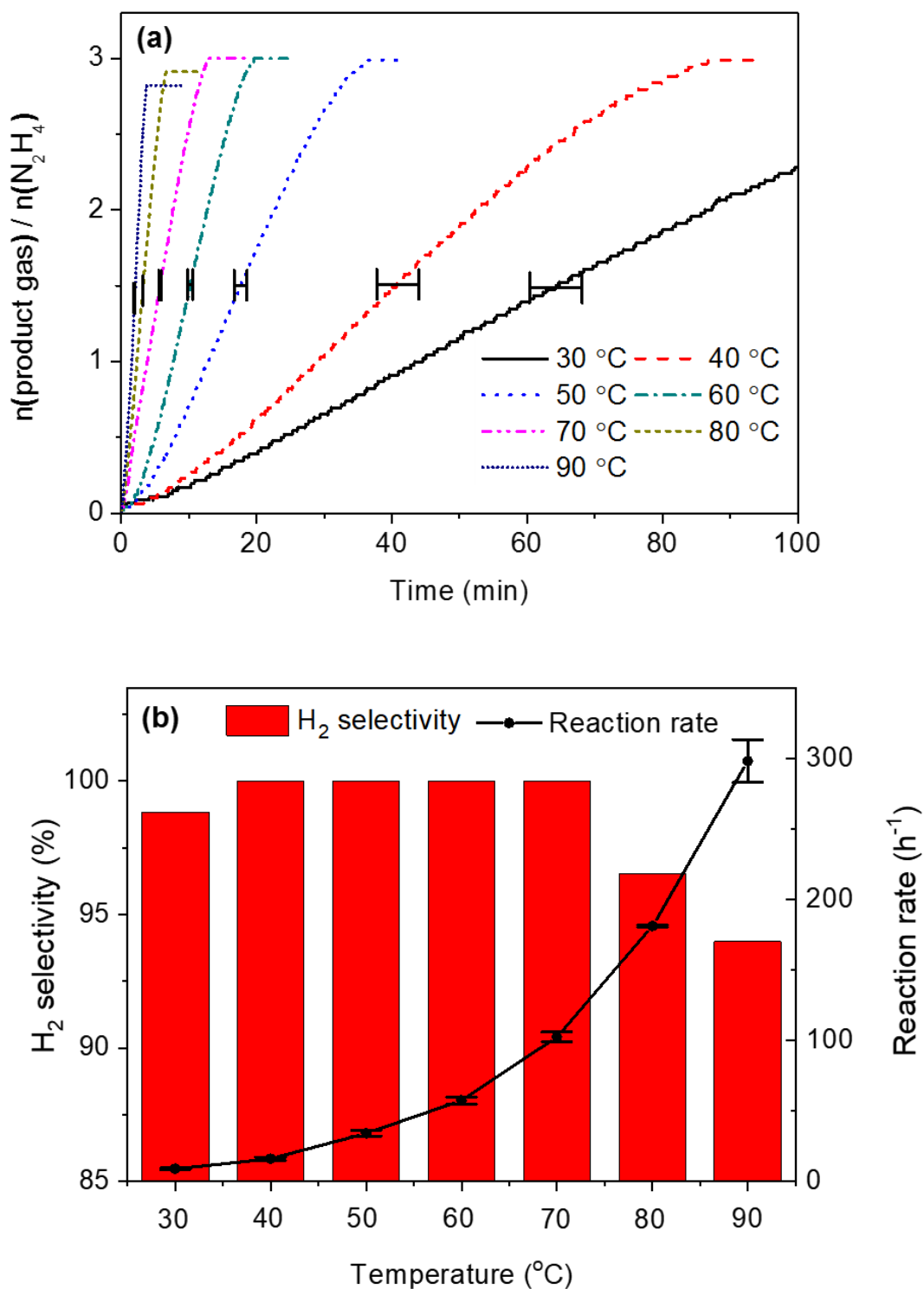
Figure 3.15 (a) Time-course profiles and (b) H$_2$ selectivity and reaction rate values for the decomposition of hydrous hydrazine over 6 wt% Ni/CeO$_2$-HH-2 catalyst as a function of temperature [n(Ni)/n(N$_2$H$_4$) = 0.1]

Table 3.5 Reaction rate for the decomposition of hydrous hydrazine over 6 wt% Ni/CeO$_2$-HH-2 catalyst at different temperatures

Temperature (°C)	Reaction rate (h^{-1})
30	8.9 ± 0.5
40	16.0 ± 1.3
50	34.0 ± 1.9
60	57.3 ± 2.4
70	102.5 ± 3.5
80	181.1 ± 0.9
90	297.9 ± 15.2

Ea = 56.2 ± 1.7 kJ/mol
R^2 = 0.995
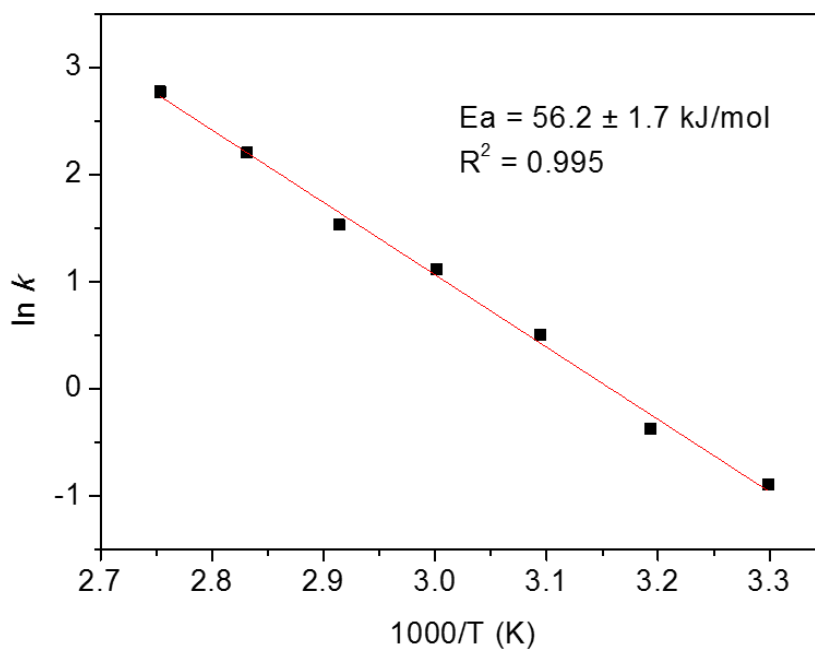
Figure 3.16 Arrhenius plot showing the apparent activation energy for hydrous hydrazine decomposition over 6 wt% Ni/CeO$_2$-HH-2 catalyst

3.3.3.3 Catalytic recyclability

In recycling tests to assess catalyst reusability, the 6 wt% Ni/CeO$_2$-HH-2 catalyst retained 100% H$_2$ selectivity over 3 cycles and exhibited relatively small decrease in catalytic activity, which has also been observed by others (Figure 3.17) [37,123,133].
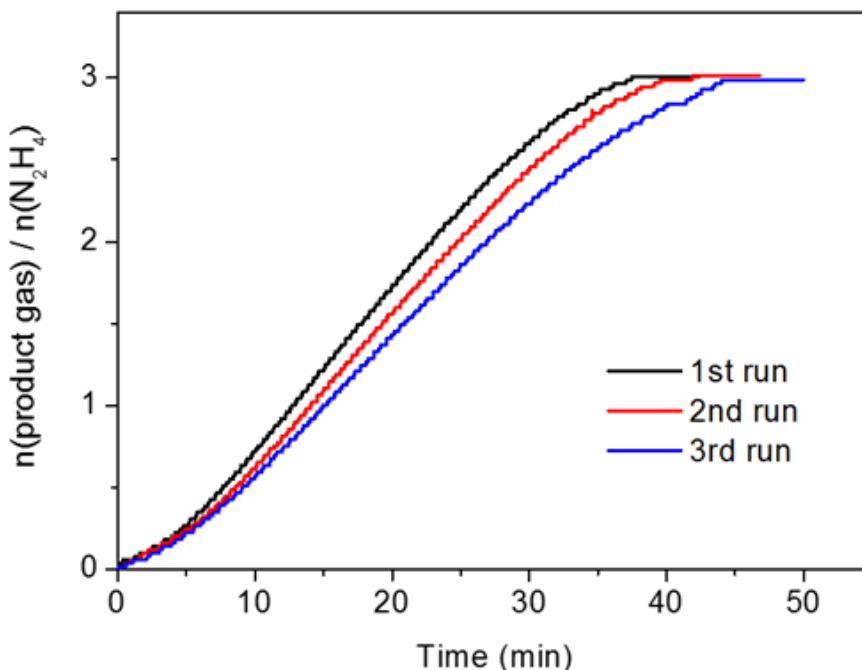
Figure 3.17 Recycling test for hydrous hydrazine decomposition over 6 wt% Ni/CeO$_2$-HH-2 catalyst.

3.3.3.4 Comparison of catalytic performance with literature

The performance of the 6 wt% Ni/CeO$_2$-HH-2 catalyst was compared to other Ni catalysts synthesized by different methods (Table 3.6). Although a rigorous comparison is difficult due to the variety of experimental conditions utilized, it indicates that the catalyst prepared by SCS has higher activity, along with high H$_2$ selectivity. The high activity of the catalyst prepared by SCS arises in part from the highly porous structure which is a typical feature of SCS products. As compared to the Ni/CeO$_2$ catalyst prepared by one-pot

EISA method [50], the pore size of the 6 wt% Ni/CeO$_2$-HH-2 catalyst is 6 times larger, which facilitates the accessibility of reactants to the catalyst active sites. It is a possible reason why the 6 wt% Ni/CeO$_2$-HH-2 catalyst of this study exhibits better performance even though the Ni content is much lower than in other works, providing an economic advantage. To our knowledge, the catalyst developed in this study provides the highest performance among all catalysts containing Ni alone. It is known, however, that addition of noble metals significantly enhances the performance of Ni-based catalysts [19,44,48,50]. A current challenge is to develop other non-noble metal containing catalysts that exhibit good performance [33].

Table 3.6 Comparison of catalytic performance of different Ni-based catalysts for hydrous hydrazine decomposition

Catalyst	Preparation method	Reaction conditions		α (%)	Reaction rate (h^{-1})	Ref.
		Metal/N$_2$H$_4$ molar ratio	T (°C)			
6 wt% Ni/CeO$_2$[a]	SCS	0.1	30	99	9.2	This study
		0.1	50	100	34.0	
Ni(53.4 wt%)-0.08CeO$_2$	Co-precipitation	0.45	30	99	4.0	[46]
		0.45	50	99	20.3	
Ni (18.3 wt%)/CeO$_2$	Impregnation	0.45	30	65	1.2	[46]
Ni (67.7 mol%)/CeO$_2$	one-pot EISA	0.1	30	97	5.1	[50]
Ni (78 wt%)-Al$_2$O$_3$-HT	Co-precipitation	0.42	50	93	26.3	[37]

[a] Refers to the 6 wt% Ni/CeO$_2$-HH-2 catalyst.

3.4   Conclusions

In this work, for the first time, SCS was used to prepare Ni/CeO$_2$ catalysts for efficient hydrogen generation from hydrous hydrazine, a promising hydrogen carrier for fuel cell vehicles. By varying the SCS synthesis parameters in terms of ratio of precursor oxidizers (nickel nitrate and ammonium cerium nitrate), fuel-to-oxidizer ratio (ϕ) and fuel type (hydrous hydrazine and glycine), the correlation between combustion characteristics, physicochemical and catalytic properties was investigated in detail. The catalyst characterization demonstrates that Ni particle size, pore structure and amount of Ni-O-Ce solid solution depend strongly on the combustion features, including maximum temperature and amount of gas evolution. The use of hydrous hydrazine fuel with $\phi = 2$ allows to obtain 6 wt% Ni powders with small Ni particle size (14.7 nm), large pore size (18.8 nm) and moderate concentration of Ni-O-Ce solid solution which promote the catalytic performance for hydrogen generation. This material exhibited 100% H$_2$ selectivity and reaction rate of 34.0 h^{-1} at 50 ºC, which is the highest activity among all catalysts tested in this study and all catalysts containing Ni alone reported in the literature. This work demonstrates that SCS is an effective method to prepare catalysts for selective hydrogen generation from hydrous hydrazine decomposition at moderate temperatures for fuel cell vehicle applications. It is also an example which demonstrates that understanding the influence of SCS parameters on combustion characteristics and their correlation with product properties can enable one to effectively control the combustion process and to tailor catalysts for specific applications.

CHAPTER 4.   NOBLE-METAL-FREE NICKEL-COPPER/CERIUM OXIDE CATALYSTS FOR HYDROGEN GENERATION FROM HYDROUS HYDRAZINE DECOMPOSITION

4.1   Introduction

In the previous chapter, it was confirmed that solution combustion synthesis (SCS) is an effective method to prepare catalysts for hydrous hydrazine decomposition and, owing to its high metal dispersion, highly porous structure, and the enhanced strong metal-support interaction (e.g., formation of oxygen vacancy in CeO_2 lattice), Ni/CeO_2 catalysts prepared by SCS with optimized synthesis conditions exhibited 100% H_2 selectivity and the highest catalytic activity among all prior reported catalysts containing Ni alone [148].

For hydrous hydrazine decomposition, bimetallic catalysts containing Ni and noble metals, such as Pt, Rh and Ir, were shown to be effective for the reaction [40,149,150]. Nevertheless, the high cost of noble metals hinders their widespread application, so there has been significant effort devoted to the development of efficient noble metal-free catalysts [33,37,122,126,151-153]. A few studies have developed highly selective non-noble metal catalysts [33,122,151], while their catalytic activity is still much lower than that of noble metal catalysts.

In this chapter, to develop cost-effective and more efficient catalysts, CeO_2 supported Ni-Cu, Ni-Fe and Ni-Co bimetallic catalysts were synthesized using SCS. Although these secondary metals (Cu, Fe and Co) have been widely used together with Ni to obtain synergistic effect for several important reactions such as water-gas shift and reforming,[154-157] the exploration of these CeO_2 supported bimetallic catalysts has not been performed for hydrogen generation from hydrous hydrazine. Remarkably, this study

found for the first time that the concomitant use of Cu with Ni/CeO_2 promotes the catalytic activity significantly. Among the investigated samples, 13wt% $Ni_{0.5}Cu_{0.5}/CeO_2$ catalysts exhibited superior activity with turnover frequency (TOF) of 1450.0 h^{-1} at 50 °C, which is 3.2 times higher than that of Ni/CeO_2, and selectivity for hydrogen generation was 100% in the temperature range 30 to 70 °C. Characterization revealed the reason for the synergistic effect observed for the $NiCu/CeO_2$ catalysts.

4.2   Experimental

4.2.1   Catalyst preparation

Nickel nitrate hexahydrate [$Ni(NO_3)_2 \cdot 6H_2O$, 98%], cerium ammonium nitrate [$(NH_4)_2Ce(NO_3)_6$, 98+%], copper nitrate trihydrate [$Cu(NO_3)_2 \cdot 3H_2O$, 98+%], iron nitrate nonahydrate [$Fe(NO_3)_3 \cdot 9H_2O$, 98+%], cobalt nitrate hexahydrate [$Co(NO_3)_2 \cdot 6H_2O$], and hydrous hydrazine ($N_2H_4 \cdot H_2O$, 99+%) were purchased from Alfa Aesar. Sodium hydroxide (NaOH, 50% in H_2O) was obtained from Sigma-Aldrich. The chemicals were used without further purification. Deionized water was used throughout.

CeO_2 supported bimetallic catalysts [NiM/CeO_2 (M = Cu, Fe, and Co)] were synthesized by solution combustion synthesis (SCS). Typically, to prepare $Ni_{1-x}Cu_x/CeO_2$ catalysts with different Ni:Cu molar ratios ($x = 0$, 0.25, 0.5, 0.75, and 1), a stoichiometric amount of metal oxidizers [$Ni(NO_3)_2.6H_2O$, $Cu(NO_3)_2 \cdot 3H_2O$, and $(NH_4)_2Ce(NO_3)_6$] were dissolved in a minimum amount of deionized water in a glass beaker and then $N_2H_4 \cdot H_2O$ as a fuel, was added into the solution. After thorough stirring, the mixture was placed in a preheated furnace to induce self-sustained combustion. After some time, the solution began to boil and then ignition occurred, followed by rapid increase of temperature and evolution

of a large quantity of gases. The temperature change during the combustion process was monitored using a sensitive K-type thermocouple with a tip diameter of 0.125 mm to determine the maximum combustion temperature. The experimental error for the measurement of maximum combustion temperature was determined to be less than $\pm 10\%$. After combustion, the obtained metal oxide powders were removed from the furnace, calcined at 400 °C for 4 h in air, and then treated at 400 °C for 1 h in a flow of 10 vol% hydrogen (balance nitrogen) to reduce NiO and CuO to Ni and Cu, respectively. For comparison, $Ni_{0.5}Cu_{0.5}/SiO_2$ samples were also prepared using SCS, followed by calcination and reduction process similar to that for $Ni_{1-x}Cu_x/CeO_2$ catalysts. Since the nitrate precursor of silicon as an oxidizer for SCS is not available commercially, $SiO(NO_3)_2$ was first synthesized from the reaction of tetraethyl orthosilicate with nitric acid and then was used for SCS. The stoichiometric combustion reaction of the system for preparing $Ni_{1-x}Cu_x/CeO_2$ catalysts is shown in the equation below.
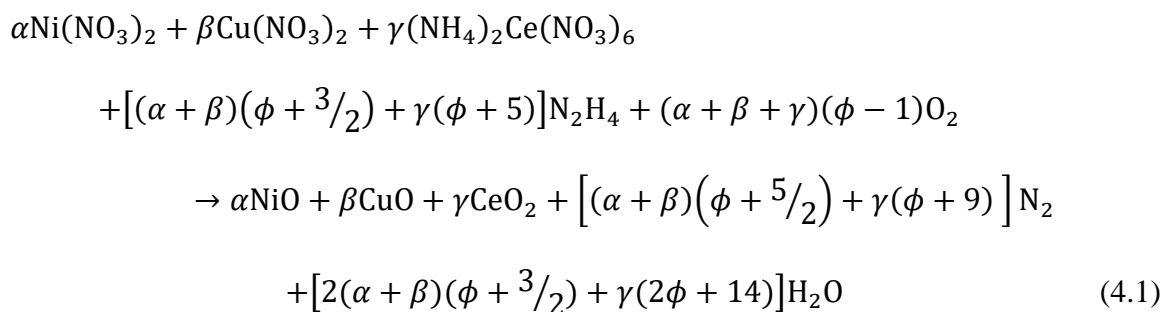
$$\alpha Ni(NO_3)_2 + \beta Cu(NO_3)_2 + \gamma (NH_4)_2 Ce(NO_3)_6$$

$$+\left[(\alpha + \beta)\left(\phi + {}^3\!/_2\right) + \gamma(\phi + 5)\right]N_2H_4 + (\alpha + \beta + \gamma)(\phi - 1)O_2$$

$$\rightarrow \alpha NiO + \beta CuO + \gamma CeO_2 + \left[(\alpha + \beta)\left(\phi + {}^5\!/_2\right) + \gamma(\phi + 9)\right]N_2$$

$$+\left[2(\alpha + \beta)(\phi + {}^3\!/_2) + \gamma(2\phi + 14)\right]H_2O \qquad (4.1)$$

In the above equation, ϕ is defined as the fuel-to-oxidizer ratio and α, β, and γ are the number of moles of Ni, Cu, and Ce precursors, respectively. Besides, on the basis of the above equation, the number of moles of evolved gases per mole of product for each case was calculated to estimate the level of gas evolution.

NiFe/CeO$_2$ and NiCo/CeO$_2$ catalysts were synthesized using the same procedure as for NiCu/CeO$_2$ catalysts described above. For all the CeO$_2$ supported catalysts studied in this work, the loading amount of metals (Ni+M) and ϕ were fixed at 13 wt% and 2, respectively.

4.2.2 Catalyst characterization

As described in Chapter 2.3.3 and 3.2.2, XRD, BET, SEM, XPS, Raman, H$_2$-TPR and AAS were used to characterize the physicochemical properties and metal contents of the samples. Semi-quantitative elemental analysis was conducted at 10 kV acceleration voltage using a JCM-6000PLUS NeoScope Benchtop SEM equipped with an energy dispersive spectroscopy (EDS).

4.2.3 Catalyst decomposition of hydrous hydrazine

The catalytic decomposition reaction of N$_2$H$_4$·H$_2$O was performed at the temperature range of 30-80 °C in a stainless-steel reactor (Parr Instrument Company, Model 4592) with external heating jacket, as presented in Chapter 3.2.3 (Figure 3.3). Aqueous reactant solution containing N$_2$H$_4$·H$_2$O (0.4 M) and NaOH (6 M) was prepared by adding 0.2 ml of N$_2$H$_4$·H$_2$O to 10 ml of NaOH solution (6.1 M) under magnetic stirring. The reaction was initiated by injecting 2 ml of the prepared solution into the reactor where the catalyst was placed under stirring of 1100 rpm and argon (99.999%) atmosphere. In all cases, the molar ratio of metal in the catalyst to hydrous hydrazine was kept fixed at 1:5. The reaction progress was monitored by measuring reactor pressure using a transducer (Omega Engineering PX35D1). After reaction completion, the composition of product gas was analyzed by mass spectrometer (Hiden Analytical HPR-20) to obtain the molar ratio

of N_2 to H_2 and to assess the presence of NH_3. The selectivity for H_2 generation (α) was calculated based on the overall reaction as described in Chapter 3.2.3.

$$3N_2H_4 \rightarrow 4(1-\alpha)NH_3 + 6\alpha H_2 + (1+2\alpha)N_2, \quad \alpha = \frac{1}{6\{n(N_2)/n(H_2)\}-2} \qquad (3.3\text{-}4)$$
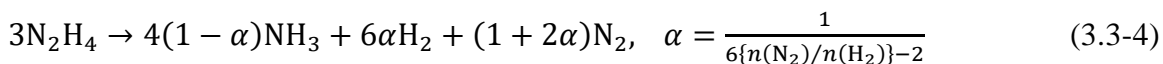
where $n(N_2)$ and $n(H_2)$ are the moles of produced N_2 and H_2, respectively. The TOF was calculated, as follows:

$$TOF\ (h^{-1}) = \frac{n(H_2)}{n(metal) \times d_{metal} \times t} \qquad (4.2)$$

where n(metal) is the moles of metal in the catalyst, t is the reaction time for 50% conversion of hydrous hydrazine and d_{metal} is the metal dispersion of Ni or NiCu alloy. The value of d_{metal} was calculated from mean metal particle size, Ni or NiCu, determined by XRD [144]. The reported TOF values are averages from 2 to 5 experiments. For testing the durability of catalysts, the catalytic reaction was repeated 6 times by adding another equivalent of $N_2H_4 \cdot H_2O$ into the reactor after completion of the previous run.

4.3   Results and discussion

4.3.1   Catalyst performance of CeO$_2$ supported Ni-based bimetallic catalysts

4.3.1.1   Effect of secondary metal (Cu, Fe and Co) additions

To examine the effect of concomitant use of Ni/CeO$_2$ with another metal (M= Cu, Fe and Co) on catalytic performance for the decomposition of hydrous hydrazine, Ni$_{0.5}$M$_{0.5}$/CeO$_2$ catalysts were prepared by SCS. The loading amount of metals (Ni+M) was

fixed at 13 wt% for all samples, while the actual metal contents were determined by atomic absorption spectroscopy (Table 4.1). The catalytic decomposition of hydrous hydrazine was performed in the presence of NaOH (6 M) at 50 °C under magnetic stirring of 1100 rpm [n(metal)/n(N_2H_4) = 0.2].

The time course plots of the decomposition of hydrous hydrazine at 50 °C over Ni/CeO_2 and $Ni_{0.5}M_{0.5}/CeO_2$ (M= Cu, Fe and Co) catalysts are shown in Figure 4.1a. It indicates that gas evolution from the decomposition of hydrous hydrazine over the Ni/CeO_2 catalyst is complete within 24 min and the molar ratio of product gas to N_2H_4 [n(product gas)/n(N_2H_4)] reaches 3 which implies only at 100% conversion and 100% H_2 selectivity. The H_2 selectivity was further confirmed by mass spectroscopy, revealing that the product gas contains only H_2 and N_2 in the molar ratio H_2/N_2 = 2.0.

Table 4.1 Metal contents of catalysts determined by atomic absorption spectroscopy

Sample	Metal content (wt%)				Ni:M molar ratio (M= Cu, Fe and Co)
	Ni	Cu	Fe	Co	
Ni/CeO_2	12.7	-	-	-	1.00:0.00
$Ni_{0.75}Cu_{0.25}/CeO_2$	8.4	3.4	-	-	0.73:0.25
$Ni_{0.5}Cu_{0.5}/CeO_2$	6.5	6.5	-	-	0.52:0.48
$Ni_{0.25}Cu_{0.75}/CeO_2$	3.1	10.0	-	-	0.25:0.75
Cu/CeO_2	-	12.5	-	-	0.00:1.00
$Ni_{0.5}Fe_{0.5}/CeO_2$	6.5	-	7.9	-	0.50:0.50
$Ni_{0.5}Co_{0.5}/CeO_2$	6.4	-	-	6.6	0.49:0.51
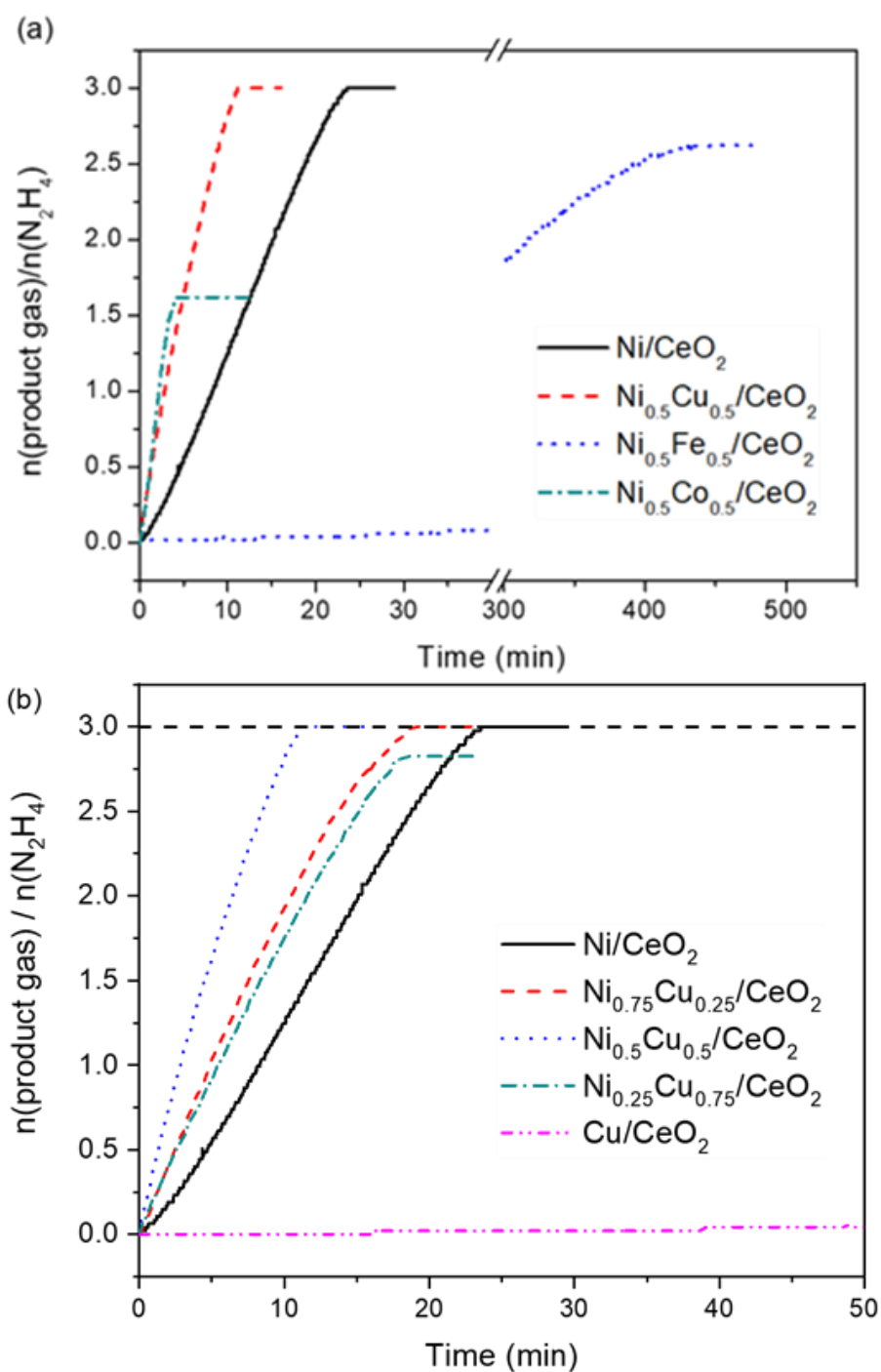
Figure 4.1 Time course plots of the decomposition of hydrous hydrazine at 50 °C over (a) Ni/CeO_2 and $Ni_{0.5}M_{0.5}/CeO_2$ (M = Cu, Fe, and Co) catalysts and (b) $Ni_{1-x}Cu_x/CeO_2$ ($x = 0$, 0.25, 0.5, 0.75, and 1) catalysts

For the $Ni_{0.5}M_{0.5}/CeO_2$ (M= Cu, Fe and Co) catalysts, the synergistic effect of Ni/CeO_2 and secondary metal (M) on hydrous hydrazine decomposition was observed for only the $Ni_{0.5}Cu_{0.5}/CeO_2$ catalyst, for which the catalytic activity is significantly enhanced while H_2 selectivity remains at 100%. On the other hand, the addition of Fe or Co as a secondary metal leads to decrease in H_2 selectivity (86 % for $Ni_{0.5}Fe_{0.5}/CeO_2$ and 48 % for $Ni_{0.5}Co_{0.5}/CeO_2$). Since the generation of NH_3-free H_2 from hydrous hydrazine is critical for PEM fuel cell applications, only Cu serves as a suitable secondary metal for Ni/CeO_2 catalysts to improve the catalytic performance for the decomposition of hydrous hydrazine.

4.3.1.2 Effect of metal composition

The catalytic performance of the series of $Ni_{1-x}Cu_x/CeO_2$ (x = 0, 0.25, 0.5, 0.75 and 1) samples for the decomposition of hydrous hydrazine is shown in Figure 4.1b. It can be observed that the catalytic performance strongly depends on the metal composition. As the Cu content increases (x = 0 to 0.5), the reaction rate increases gradually while the H_2 selectivity remains at 100%. Increasing the amount of Cu (x = 0.5 to 1) leads to a decrease in both catalytic activity and H_2 selectivity. Notably, the Cu/CeO_2 (x = 1) catalyst is totally inactive, implying that Ni is the key active component for the reaction. This is consistent with previous studies that Ni is the representative active non-noble metal and Cu itself is inert for hydrous hydrazine decomposition [29].

Consequently, the optimal catalytic performance was found for $Ni_{0.5}Cu_{0.5}/CeO_2$ catalysts, exhibiting 100% H_2 selectivity with a TOF of 1450.0 h^{-1} at 50 $^\circ$C which is about 3.2-fold higher than the monometallic Ni/CeO_2 catalyst (447.2 h^{-1}). This catalytic activity is superior to that of most reported non-noble metal catalysts and is even comparable to that of many catalysts containing noble-metals such as Pt, Ir and Pd (Table 4.2)

[33,122,127,153,158,159]. Moreover, the facile one-step SCS method to prepare the catalysts provides some advantages over alternative methods used in the literature which require surfactants and/or time-consuming processes (e.g. aging and drying) [152,160].

Table 4.2 Comparison of catalytic performance of different catalysts for the decomposition of hydrous hydrazine

Sample	Temperature (°C)	H_2 selectivity (%)	Reaction rate* (h^{-1})	Ref.
Ni/CeO_2	50	100	20.8	This study
$Ni_{0.5}Cu_{0.5}/CeO_2$	30	100	13.9	This study
$Ni_{0.5}Cu_{0.5}/CeO_2$	50	100	111.7	This study
$Ni_{0.5}Cu_{0.5}/CeO_2$	70	100	371.1	This study
NiFe	70	100	5.1	[33]
NiFeMo	50	100	58	[151]
NiFe/Cu	70	100	37.5	[122]
$Ni_{1.5}Fe_{1.0}/(MgO)_{3.5}$	26	99	19.0	[152]
$Ni_{0.5}Cu_{0.5}/MCNS$	60	100	21.8	[158]
2D $Ni_{0.6}Fe_{0.4}/CeO_2$	50	100	19.1	[153]
Ni_3Fe/C	20	100	250	[160]
$Ni_{0.93}Pt_{0.07}$	25	100	5.6	[161]
$Ni_{0.9}Ir_{0.1}$	25	100	3.6	[32]
$Ni_{60}Pd_{40}$	50	82	7.5	[34]
$Ni_{30}Fe_{30}Pd_{40}$	50	100	50	[123]
$Pt_{12}Ni_{48}@G4-OH$	70	100	240	[159]
$NiPt_{0.057}/Al_2O_3-HT$	50	99	110.9	[127]
$NiIr_{0.059}/Al_2O_3-HT$	30	99	25	[130]

   * For comparison purposes, reaction rate was calculated with an assumption that all the Ni atoms participated in the reaction (Eq. 3.5).

Note that the reaction was performed under conditions where the reaction is not controlled by mass transfer. The reaction rate at the highest reaction temperature (80 $^\circ$C), where external mass transfer limitation would be the most severe, was independent of the agitation speed range 300-1100 rpm (Figure 4.2) and the average powder size of the $Ni_{0.5}Cu_{0.5}/CeO_2$ catalysts was 13.2 μm (Figure 4.3). Accordingly, the external and internal mass transfer limitations can be assumed to be negligible. Therefore, the synergistic effect observed for the $NiCu/CeO_2$ catalysts originates essentially from the intrinsic performance. More specifically, the enhanced activity of the $NiCu/CeO_2$ samples may be attributed to a combination of the modified electronic structure of catalyst surface, the small particle size of active component, and the increased amount of oxygen vacancy within CeO_2 structure, as discussed later. The $NiFe/CeO_2$ and $NiCo/CeO_2$ catalysts with different Ni:M (M = Fe and Co) molar ratios were also investigated for the reaction. For both Fe and Co cases, H_2 selectivity decreases gradually with increasing the content of the secondary metal (Figure 4.4 and 4.5).
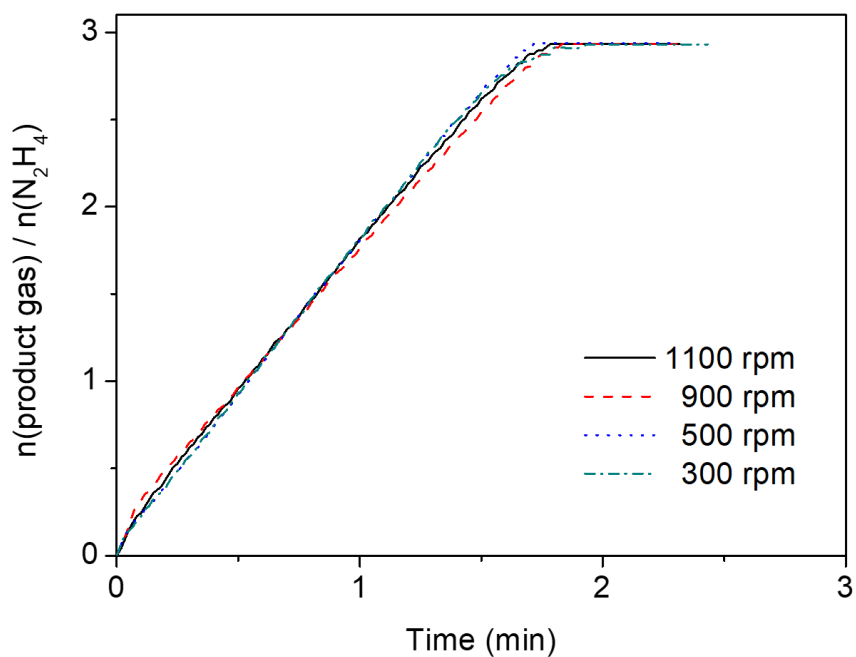
Figure 4.2 Effect of agitation speed on the decomposition of hydrous hydrazine; $Ni_{0.5}Cu_{0.5}/CeO_2$ catalyst [n(metal)/n(N_2H_4) = 0.2, 80 ℃, 6 M NaOH]
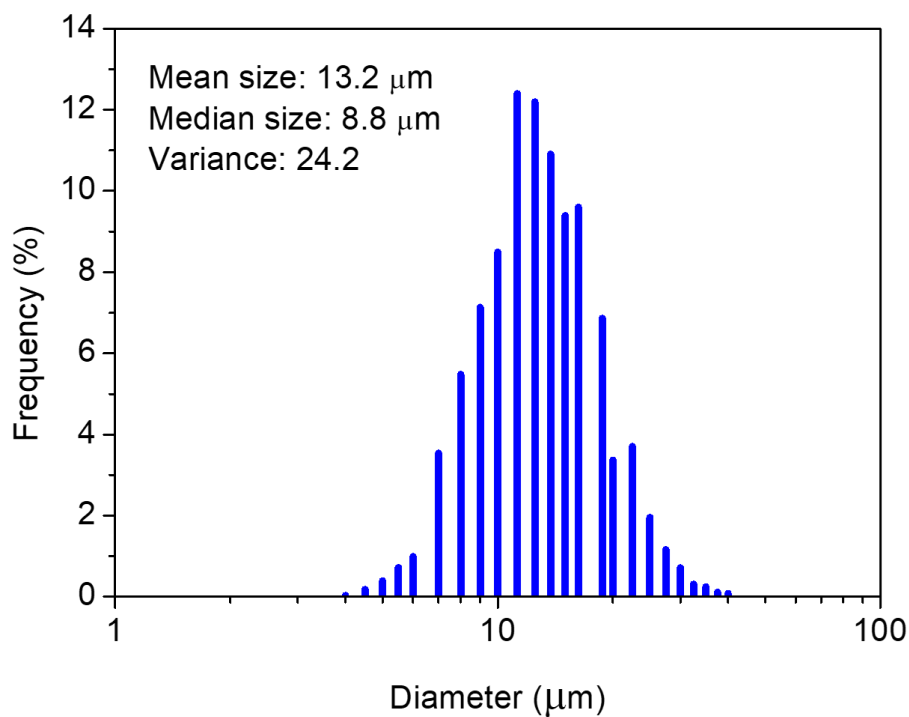
Figure 4.3 Powder size distribution of $Ni_{0.5}Cu_{0.5}/CeO_2$ catalyst
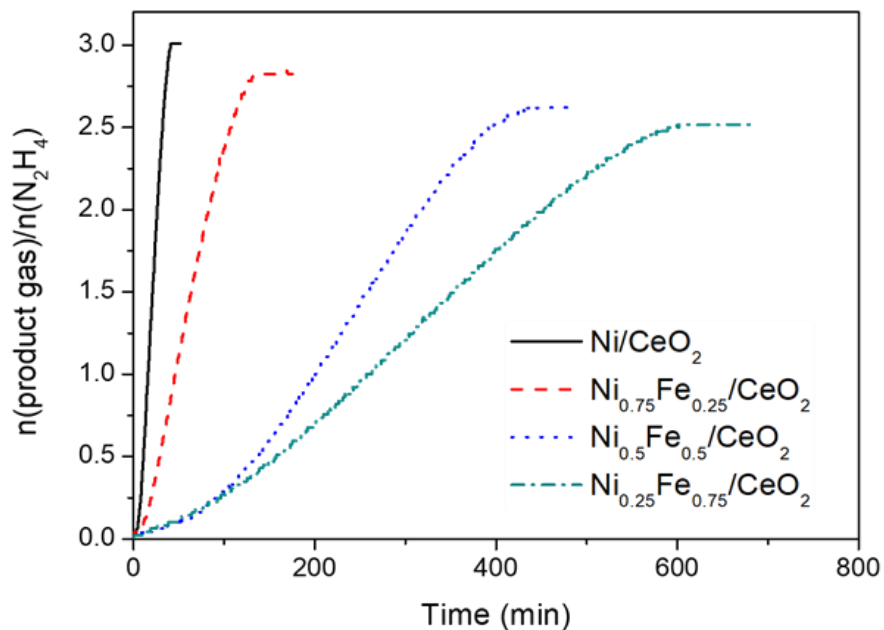
Figure 4.4 Time course plots of the decomposition of hydrous hydrazine at 50 ℃ over NiFe/CeO$_2$ catalyst with different Ni:Fe molar ratios
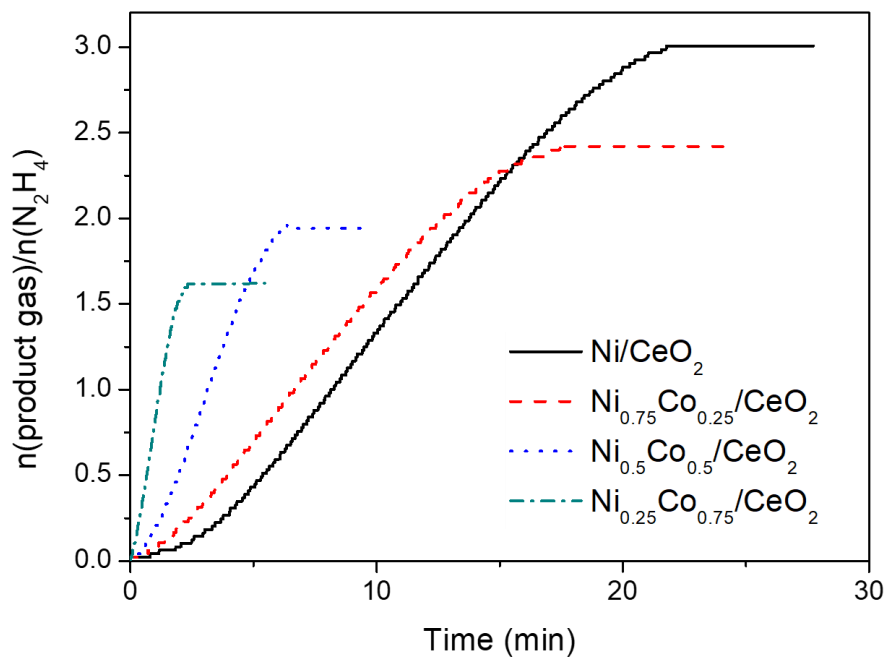
Figure 4.5 Time course plots of the decomposition of hydrous hydrazine at 50 ℃ over NiCo/CeO$_2$ catalyst with different Ni:Co molar ratios

4.3.1.3 Effect of reaction temperature

Figure 4.6 shows that the time course plots for the decomposition of hydrous hydrazine over $Ni_{0.5}Cu_{0.5}/CeO_2$ catalyst at different temperatures. The standard deviation of the reaction time for 50% conversion is indicated by the error bars. The reaction rate significantly increased about 45-fold with increase in the reaction temperature from 30 to 80 °C. The TOFs for 50% conversion were 180.4, 516.6, 1450.0, 2480.5, 4817.0 and 8225.7 h^{-1} at 30, 40, 50, 60, 70 and 80 °C, respectively. The H_2 selectivity remained 100% in the temperature range 30-70 °C. When the temperature increased further to 80 °C, the selectivity decreased to 97% owing to thermodynamic reasons as reported elsewhere [37]. The apparent activation energy (E_a) values for catalytic decomposition of hydrous hydrazine over Ni/CeO_2, $Ni_{0.75}Cu_{0.25}/CeO_2$, $Ni_{0.5}Cu_{0.5}/CeO_2$, and $Ni_{0.25}Cu_{0.75}/CeO_2$ catalyst were determined to be 67.3, 64.2, 63.0, and 64.8 kJ/mol, respectively (Figure 4.7). The Ni/CeO_2 monometallic catalyst exhibits somewhat higher activation energy than the $NiCu/CeO_2$ catalysts, which indicates a synergistic effect in the decomposition of hydrous hydrazine over $NiCu/CeO_2$ bimetallic catalysts.
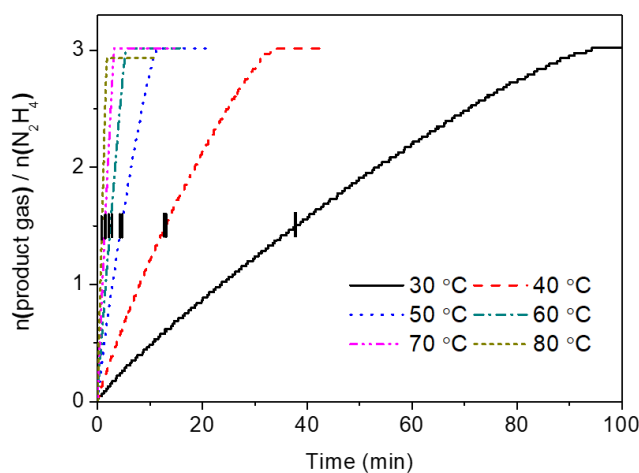
Figure 4.6 Time course plots of the decomposition of hydrous hydrazine over $Ni_{0.5}Cu_{0.5}/CeO_2$ catalyst as a function of temperature
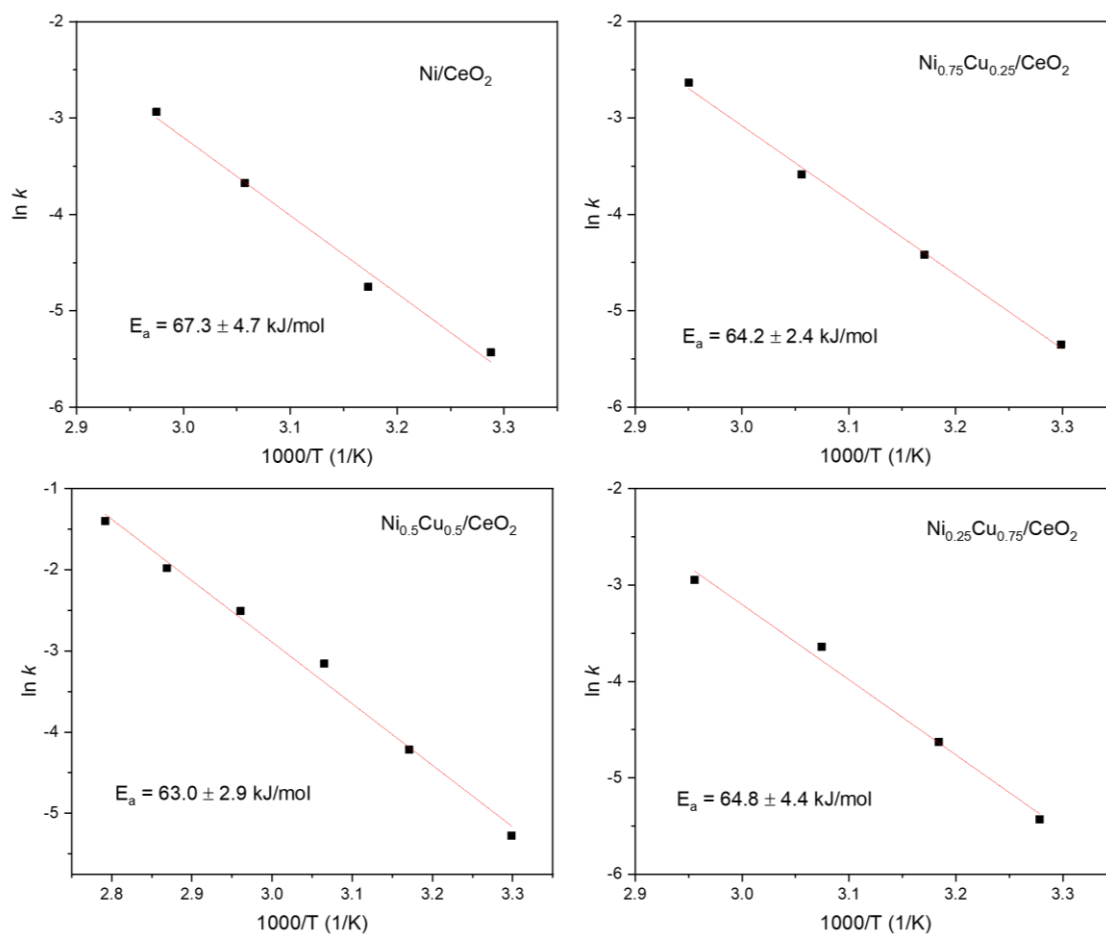
Figure 4.7 Arrhenius plot showing apparent activation energy for the decomposition of hydrous hydrazine over $Ni_{1-x}Cu_x/CeO_2$ catalyst

4.3.1.4 Catalyst durability

Further reaction experiments were conducted for the most active catalyst ($Ni_{0.5}Cu_{0.5}/CeO_2$). In durability test, the $Ni_{0.5}Cu_{0.5}/CeO_2$ catalyst retained 100% H_2 selectivity over 6 runs and exhibited only a small decrease in activity (Figure 4.8). There was not an obvious change of metal phases for the used catalysts according to the X-ray diffraction (XRD) patterns (Figure 4.9). The slight deactivation may be attributed to a

decrease in the active Ni sites by the strong binding of N_2 species on the catalyst surface [162].
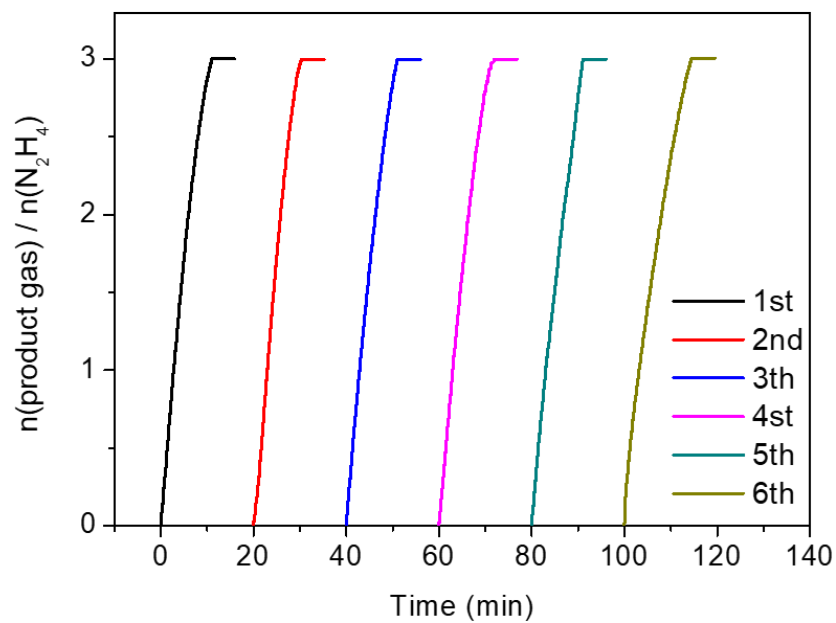
Figure 4.8 Durability test for the decomposition of hydrous hydrazine at 50 ℃ over $Ni_{0.5}Cu_{0.5}/CeO_2$ catalysts
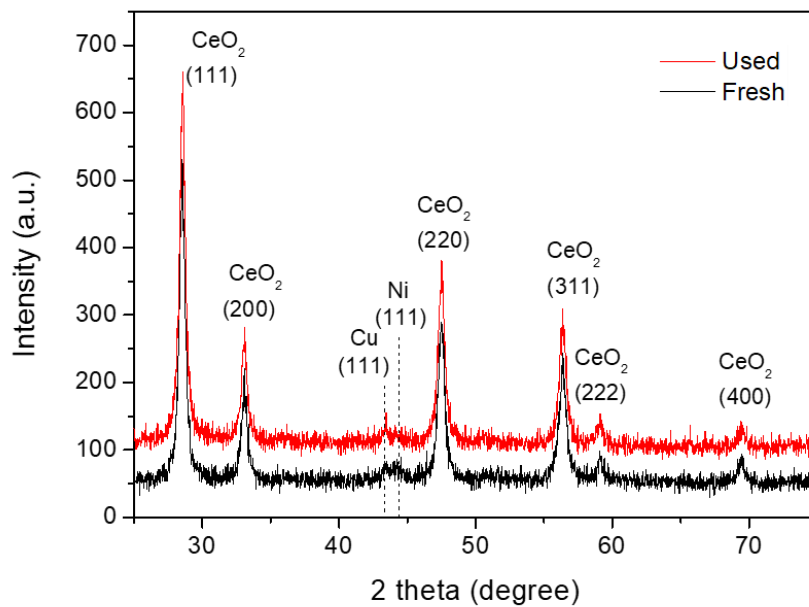
Figure 4.9 XRD patterns of fresh and used $Ni_{0.5}Cu_{0.5}/CeO_2$ catalyst

4.3.2 Physicochemical properties of NiCu/CeO$_2$ catalysts

In this section, the NiCu/CeO$_2$ catalysts were characterized by BET, SEM-EDS, XRD, XPS, Raman, and H$_2$-TPR techniques to identifying the reasons for the promoting effect of Cu on the catalytic performance. These characterizations are described separately below.

4.3.2.1 N$_2$ adsorption-desorption isotherm analysis

The textural properties of Ni$_{1-x}$Cu$_x$/CeO$_2$ (x = 0, 0.25, 0.5, 0.75, and 1) catalysts were confirmed by N$_2$ adsorption-desorption isotherm as shown in Figure 4.10. All the samples showed similar isotherm shapes and exhibited the characteristic feature of a composite type II/IV isotherm with a type H3 hysteresis loop, which indicates disordered porous materials with a non-uniform pore network and a broad pore size distribution in the meso- and macro- ranges [121]. This disordered pore structure may be related to the nature of SCS where pore structure is formed by gases evolved during the combustion process. From the isotherms of the samples, BET specific surface area and total pore volume were obtained (Table 4.3). The samples have similar values of specific surface area (16.7-20.6 m^2/g) and total pore volume (0.077-0.088 cm^3/g). It suggests that the addition of Cu to Ni/CeO$_2$ does not affect strongly the textural properties of the catalysts.

As noted above, the textural properties of SCS-derived products depend strongly on gas evolution during combustion, which promotes porosity of products and inhibits particle agglomeration by dissipating the heat. The degree of gas evolution can be estimated indirectly from the amount of evolved gases. The number of moles of evolved gases per mole of product for each case was calculated based on the combustion reaction equation (Eq. 4.1) and is shown in Table 4.3. As expected, the amounts of gases for each

case are similar (21.6-21.9 mol). The Cu/CeO_2 shows relatively smaller specific surface area because of higher maximum combustion temperature which leads to particle agglomeration and shrinkage of pore structure.
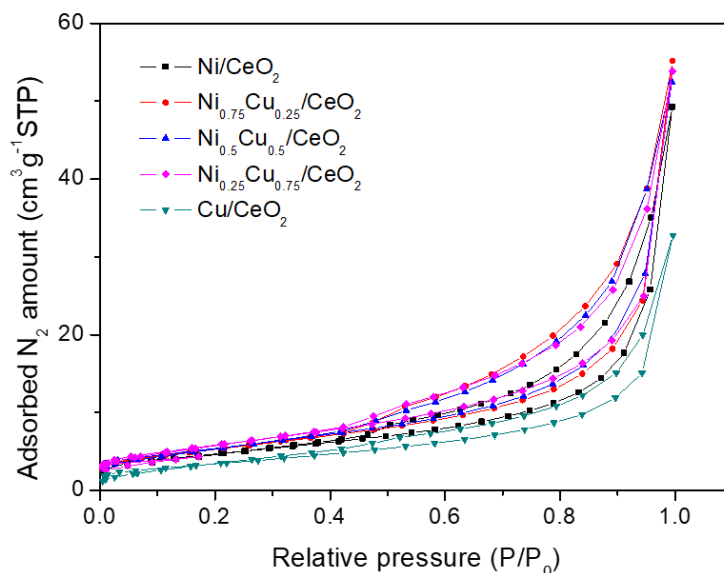
Figure 4.10 N_2 adsorption-desorption isotherms of $Ni_{1-x}Cu_x/CeO_2$ ($x = 0, 0.25, 0.5, 0.75$ and 1) catalysts

Table 4.3 Textural properties and combustion characteristics of $Ni_{1-x}Cu_x/CeO_2$ ($x = 0$, 0.25, 0.5, 0.75 and 1) catalysts

Sample	Particle size (nm)		CeO₂ lattice parameter (Å)	BET surface area (m²/g)	Pore volume (cm³/g)	Max. temp. (°C)	Amount of gases (mol)
	Ni or alloy	CeO₂					
Ni/CeO_2	21.7	27.7	5.4094	16.7	0.077	820	21.6
$Ni_{0.75}Cu_{0.25}/CeO_2$	18.1	22.4	5.4161	18.8	0.088	783	21.7
$Ni_{0.5}Cu_{0.5}/CeO_2$	13.1	18.1	5.4210	19.2	0.083	708	21.6
$Ni_{0.25}Cu_{0.75}/CeO_2$	18.3	20.5	5.4179	20.6	0.083	798	21.9
Cu/CeO_2	-	47.1	5.4099	12.3	0.050	900	21.9

4.3.2.2 Scanning electron micrographs and energy-dispersive X-ray spectroscopy

The morphologies of the $Ni_{0.5}Cu_{0.5}/CeO_2$ catalyst were analyzed by scanning electron microscopy (SEM) analysis and the images are presented in Figure 4.11. Figure 4.11a and b show that the material has a sponge-like porous structure with a broad pore size distribution, revealing the presence of large macro-pores, and small macro-pores and meso-pores, respectively. These roundish pores are formed by the rapid gas evolution during combustion. This porous structure with a broad pore size distribution is consistent with the results of N_2 adsorption-desorption analysis. The elemental mapping analysis by energy dispersive spectroscopy (EDS) demonstrates the uniform dispersion of Cu and Ni elements over CeO_2 support (Figure 4.11c and d). From the SEM-EDS result, the molar ratio of Ni to Cu was determined to be 0.53:0.47 which agrees well with the AAS result (0.52:0.48).
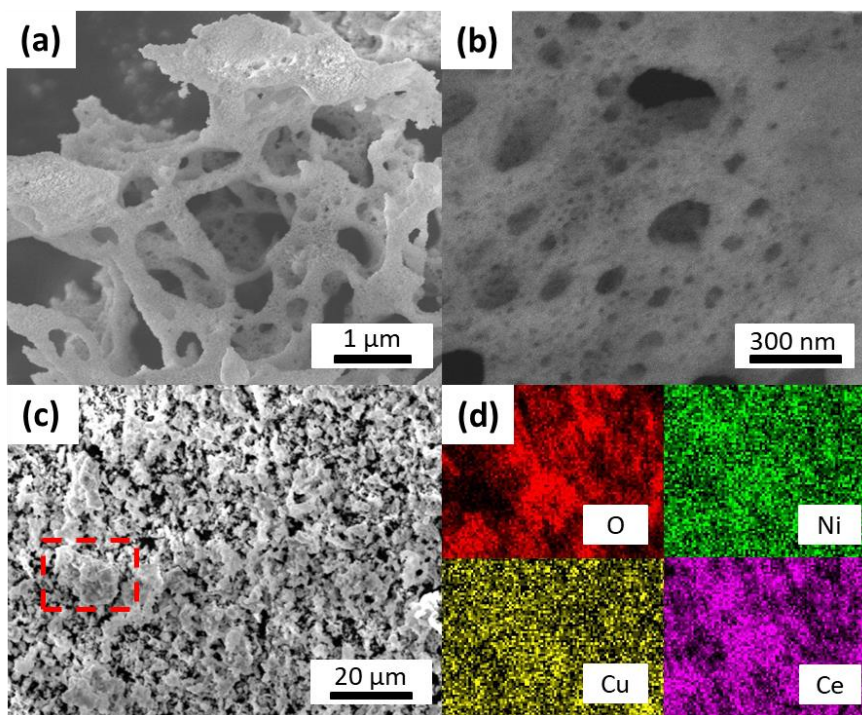
Figure 4.11 (a,b,c) SEM images and (d) EDS elemental mapping of $Ni_{0.5}Cu_{0.5}/CeO_2$ catalyst

4.3.2.3 X-ray diffraction studies

Figure 4.12a shows the XRD patterns of the $Ni_{1-x}Cu_x/CeO_2$ catalysts. All samples clearly exhibit the diffraction pattern of the cubic fluorite-type CeO_2 (PDF No. 01-073-6328). The pattern of Ni/CeO_2 shows a peak at 44.5°, corresponding to Ni(111) phase (PDF No. 01-070-0989) while Cu/CeO_2 exhibits a peak at 43.3°, corresponding to Cu(111) phase (PDF No. 01-089-2838). For the $NiCu/CeO_2$ catalysts, the (111) peak of active component Ni shifts towards the peak of Cu(111) in Cu/CeO_2 as the Cu content increases (Figure 4.12b). It may be attributed to the expansion of the Ni lattice due to the partial incorporation of larger Cu (lattice parameter = 0.362 nm) into the lattice of Ni (0.352 nm), indicating the formation of NiCu alloy phase. Meanwhile, Figure 4.12b reveals that the peak position of Cu phase is not changed by the metal composition. This clearly indicates that the $NiCu/CeO_2$ catalysts have a composite structure consisting of NiCu alloy and Cu phases.
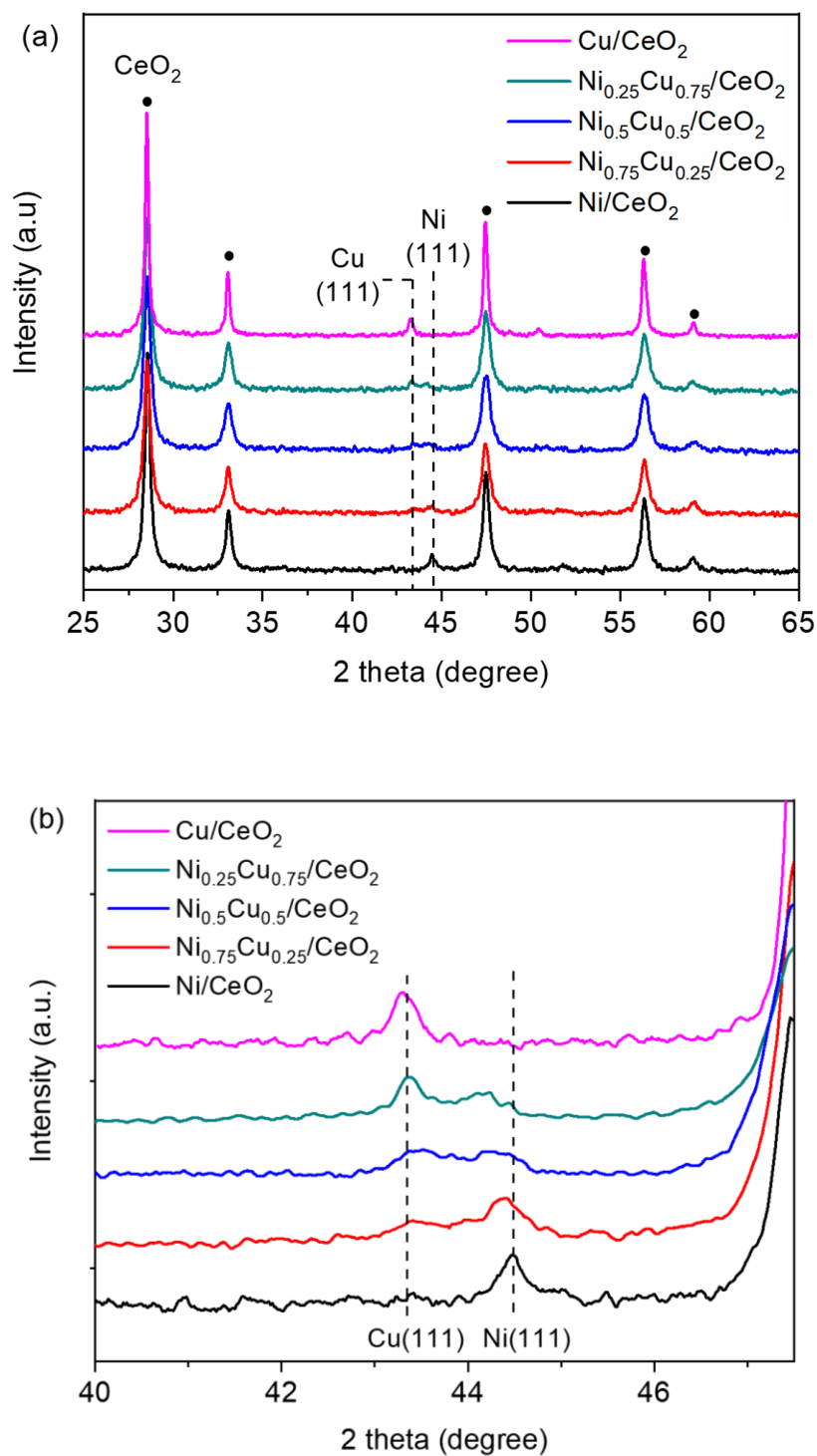
Figure 4.12 (a) XRD patterns of $Ni_{1-x}Cu_x/CeO_2$ (x = 0, 0.25, 0.5, 0.75 and 1) catalysts and (b) detail of the range $2\theta = 40$-$47.5°$

The NiCu alloying may be one of the possible reasons for the variation of catalytic performance and activation energy with metal composition. For NiCu bimetallic systems, it was shown theoretically and experimentally that the interaction between reactant and metal surface depends on the electronic structure of the alloy surface which can be altered by metal composition [163-165]. The interaction strength between NiCu alloy surface and reacting species would lie in between Ni and Cu monometallic systems, which possess too strong or too weak interaction. Therefore, according to the Sabatier principle, NiCu alloying explains the improved activity of NiCu/CeO$_2$ catalysts. In addition, Yen et al. reported that NiCu nanoparticles supported on mesoporous carbon nanosphere (MCNS) with different metal composition exhibit improved catalytic performance for hydrous hydrazine decomposition as compared to monometallic catalysts owing to modification of the surface electronic structure by the NiCu alloying and the highest catalytic activity was found for Ni$_{0.5}$Cu$_{0.5}$/MCNS [158].

Figure 4.13 shows the lattice parameter of NiCu alloy for the samples calculated from the XRD results. The lattice parameter gradually increases with bulk Cu content. To evaluate the degree of alloying of Ni with Cu, the theoretical lattice parameter was calculated using Vegard's law, where homogeneous alloying is assumed [166]. With increasing Cu content, the degree of alloying increases from 36% (Ni$_{0.75}$Cu$_{0.25}$/CeO$_2$) to 48% (Ni$_{0.5}$Cu$_{0.5}$/CeO$_2$). When the Cu content increases further, however, the degree of alloying decreases slightly to 45% (Ni$_{0.25}$Cu$_{0.75}$/CeO$_2$). It appears that, at high Cu contents, the individual metal atoms prefer to segregate rather than to form a homogeneous alloy [167].
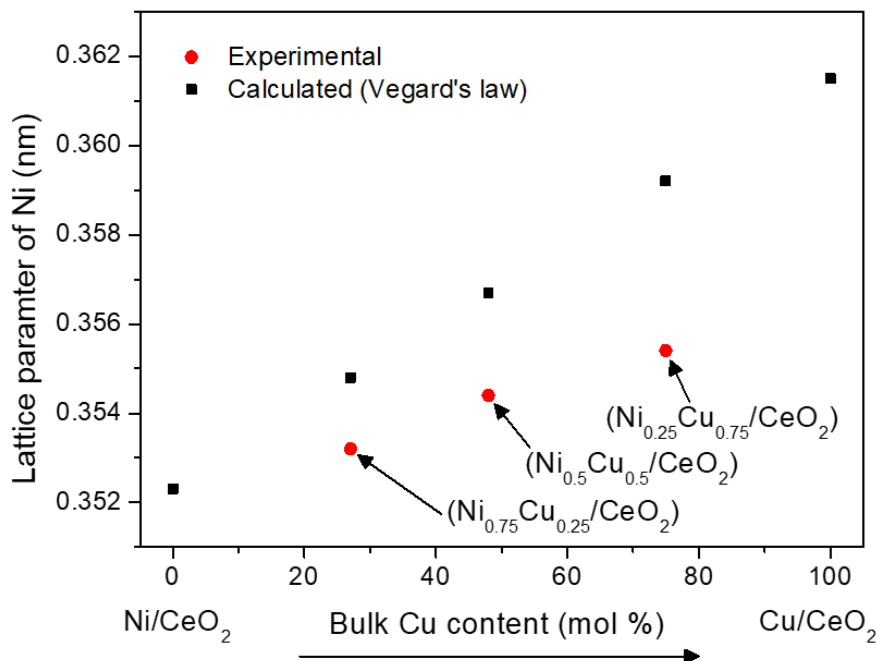
Figure 4.13 Experimentally measured and theoretically calculated lattice parameter of Ni
in $Ni_{1-x}Cu_x/CeO_2$ (x = 0, 0.25, 0.5, 0.75 and 1) catalysts

In addition to NiCu alloying, particle size of the active component is also a critical factor affecting the catalytic performance. For SCS, the particle size of products depends strongly on the combustion temperature which can be controlled by adjusting the type and ratio of precursors. In general, higher combustion temperature leads to larger particle size by particle growth and agglomeration. Table 4.3 shows the measured maximum temperature during combustion process and the average particle size of Ni or NiCu in the catalysts. The particle size was calculated based on the XRD data using the Scherrer equation [83]. As expected, the trend of the particle size agrees well with the maximum combustion temperature. Notably, the combustion temperature of $NiCu/CeO_2$ bimetallic systems is relatively lower than Ni/CeO_2 monometallic case, resulting in smaller metal particles. Owing to the lowest combustion temperature, the smallest NiCu alloy particle

size (13.1 ± 0.4 nm) was obtained for $Ni_{0.5}Cu_{0.5}/CeO_2$. As shown in Figure 4.1b, the activity of the catalysts appears to increase as the active metal particle size decreases since small metal particle size would provide more active sites for catalytic reactions. Therefore, this may be another reason why $NiCu/CeO_2$ bimetallic catalysts show better catalytic performance than Ni/CeO_2 and $Ni_{0.5}Cu_{0.5}/CeO_2$ exhibits the highest catalytic activity.

It is also known that interaction between metals and support has a significant impact on the catalyst performance. To investigate support effect, $Ni_{0.5}Cu_{0.5}/SiO_2$ catalyst with 13wt% total metal loading was synthesized using SCS. The XRD pattern of $Ni_{0.5}Cu_{0.5}/SiO_2$ exhibits the characteristic peaks of amorphous SiO_2, NiCu alloy, and segregated Cu (Figure 4.14a). Average particle size of NiCu alloy and degree of alloying are 15.1 nm and 45%, respectively (Figure 4.14b). These values are close to those found for $Ni_{0.5}Cu_{0.5}/CeO_2$ (13.1 nm and 48%). Further, the $Ni_{0.5}Cu_{0.5}$ catalysts supported on different supports were tested in the decomposition of hydrous hydrazine. To avoid the dissolution of amorphous SiO_2 in NaOH solution during reaction, the experiments were carried out under water medium (0 M NaOH). Due to the absence of NaOH which promotes reaction rate and H_2 selectivity, the catalytic performance of $Ni_{0.5}Cu_{0.5}/CeO_2$ under water medium is worse than that under NaOH solution. Figure 4.15 shows that $Ni_{0.5}Cu_{0.5}/CeO_2$ has much better catalytic activity (892.8 h^{-1}) and H_2 selectivity (75%) than $Ni_{0.5}Cu_{0.5}/SiO_2$ (33.7 h^{-1}, 50%). Interestingly, despite the fact that metal particle size and degree of alloying of both catalysts are similar, the difference in activity and H_2 selectivity is significant, which suggests that the catalyst support plays a critical role in the decomposition of hydrous hydrazine.
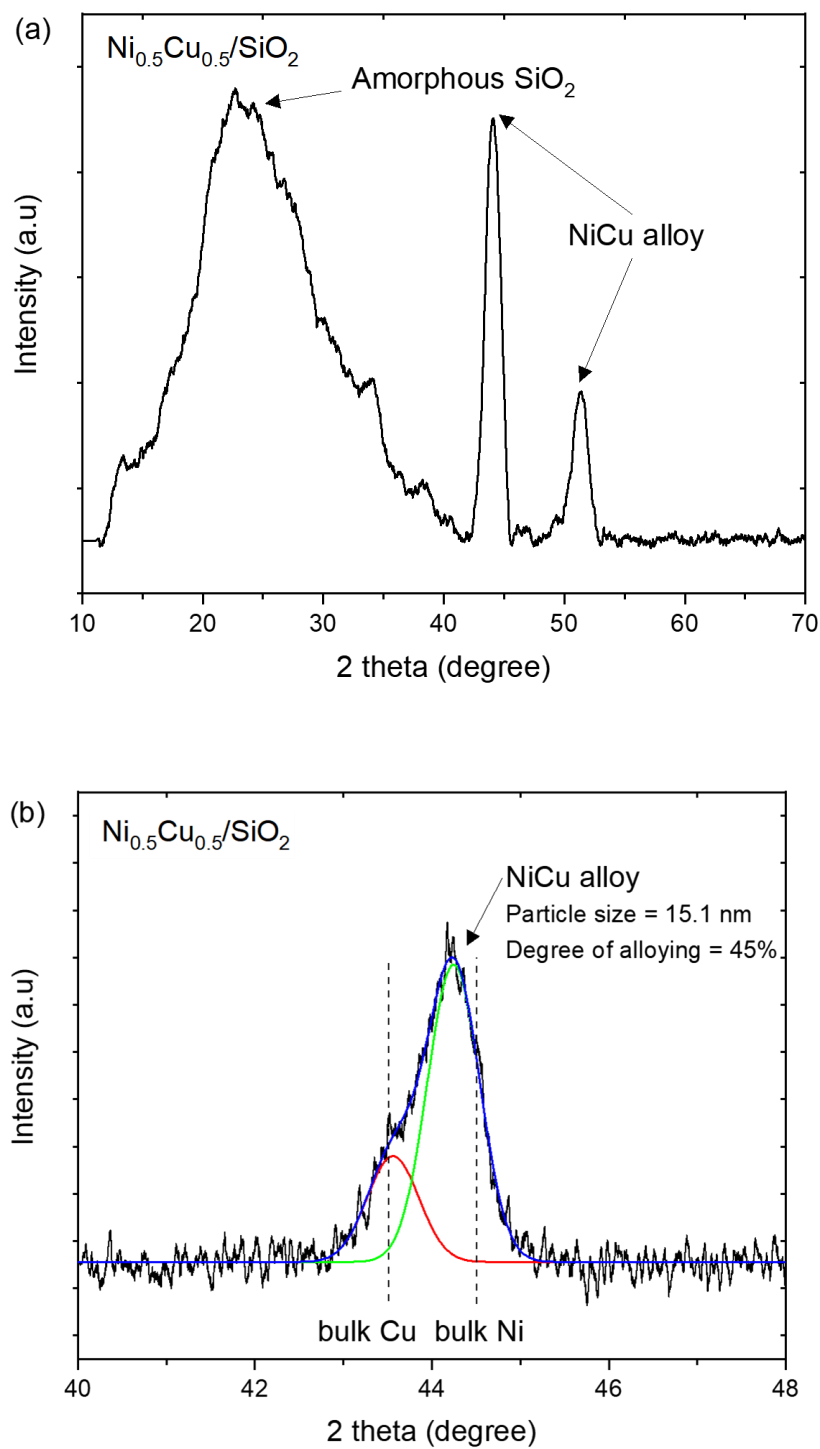
Figure 4.14 (a) XRD patterns of Ni$_{0.5}$Cu$_{0.5}$/SiO$_2$ catalysts and (b) detail of the range $2\theta =$ 40-48°
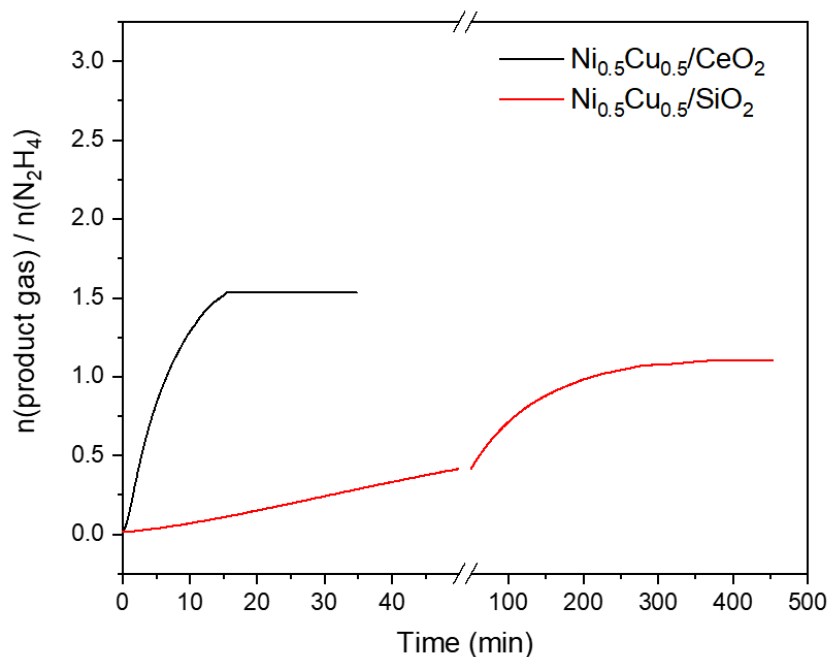
Figure 4.15 Time course plots of the decomposition of hydrous hydrazine at 70 °C over Ni$_{0.5}$Cu$_{0.5}$/CeO$_2$ and Ni$_{0.5}$Cu$_{0.5}$/SiO$_2$ catalysts [n(metal)/n(N$_2$H$_4$) = 0.2, 70 °C, 0M NaOH]

Lattice parameter of CeO$_2$ for the Ni$_{1-x}$Cu$_x$/CeO$_2$ catalysts (x = 0, 0.25, 0.5, 0.75 and 1) is shown in Table 4.3. Notably, it was found that the CeO$_2$ lattice constant of all the Ni$_{1-x}$Cu$_x$/CeO$_2$ catalysts is larger than that of pure CeO$_2$ (5.4082 Å). This lattice expansion may be related to the formation of Ni-O-Ce and/or Cu-O-Ce solid solutions by strong interaction between metals and CeO$_2$. It is known that metal cations such as Ni and Cu ions can incorporate into CeO$_2$ lattice forming Ni-O-Ce and Cu-O-Ce solid solutions. This process is accompanied by reduction of Ce^{4+} to Ce^{3+} as well as generation of oxygen vacancies in CeO$_2$ structure to compensate for the charge difference between metal cations and Ce^{4+} [168,169]. Since the ionic radius of Ce^{3+} (0.107 nm) is about 14% larger than that of Ce^{4+} (0.094 nm), the formation of the solid solutions results in lattice expansion [170]. It was also found that the lattice expansion of CeO$_2$ for the NiCu/CeO$_2$ bimetallic catalysts

is more pronounced than that for monometallic catalysts. This suggests that the presence of Ni and Cu together may promote the formation of oxygen vacancy in CeO_2.

It is known that the oxygen vacancies in CeO_2 have a significant role to improve redox properties of Ce^{4+}/Ce^{3+} and hence promote catalytic activity of CeO_2-based materials for many applications [171-173]. For hydrous hydrazine decomposition reaction over ceria supported catalysts, it was reported that the oxygen vacancy in CeO_2 structure modifies the electronic ability of nearby Ni atoms as an electron donor while Ce^{3+} acts as a Lewis base. Both oxygen vacancy and Ce^{3+} can enhance the adsorption of N_2H_4 molecules on Ni surface and N-H bond dissociation instead of N-N bond on Ni, resulting in high catalytic activity and H_2 selectivity [46,153]. The XRD results indicate that the $Ni_{0.5}Cu_{0.5}/CeO_2$ catalyst has the largest CeO_2 lattice parameter, possibly resulting from the presence of the largest amount of Ce^{3+} ions and oxygen vacancies in the CeO_2 lattice. Therefore, this feature is also related to better performance of the $Ni_{0.5}Cu_{0.5}/CeO_2$ catalyst towards hydrogen generation from hydrous hydrazine.

The enhanced formation of oxygen vacancy for the bimetallic cases may be ascribed to a synergistic interaction among Ni, Cu and CeO_2. It was reported that, for Cu-Ce catalyst system, Cu ions can exist as Cu^+ as well as Cu^{2+} by a strong metal-support interaction ($Ce^{4+} + Cu^+ \leftrightarrow Ce^{3+} + Cu^{2+}$) and the addition of Ni significantly increases the concentration of Cu^+ ion [174-176]. In addition, it is known that Cu^+ can easily incorporate into CeO_2 lattice to form Cu-O-Ce solid solution owing to the similarity of the ion radius of Cu^+ (0.096 nm) and Ce^{4+} (Ce^{4+}, 0.094 nm) [169,170]. Thus, the increased concentration of Cu^+ may increase the number of Ce^{3+} ions and oxygen vacancies in CeO_2 structure. Moreover, the distorted CeO_2 structure by Cu^+ ions may further facilitate the incorporation

of smaller Ni^{2+} (0.072 nm) and Cu^{2+} (0.072 nm) cations into the CeO_2 lattice to form Ni-O-Ce and Cu-O-Ce solid solutions which essentially create oxygen vacancies.

On the other hand, it has also been known that decrease in the particle size of CeO_2 leads to an increase in the lattice strain, causing the formation of oxygen vacancies [110,111]. This effect may also contribute to increase the concentration of oxygen vacancy in the $NiCu/CeO_2$ catalysts which have smaller size of CeO_2 particles than Ni/CeO_2 and Cu/CeO_2 (Table 4.3). This may be attributed to the lower maximum combustion temperature. As observed for the particle size of Ni in the catalysts, the trend of the particle size of CeO_2 corresponds well to the maximum combustion temperature. The effect of the incorporation of metal cations into CeO_2, however, predominates over the effect of CeO_2 particle size. Although the CeO_2 size of the Cu/CeO_2 is larger than that of the Ni/CeO_2, the CeO_2 lattice parameter for the Cu/CeO_2 is larger than that of the Ni/CeO_2.

4.3.2.4 X-ray photoelectron spectroscopy results

In order to investigate the chemical and electronic states of the elements on the catalyst surface, XPS analysis was carried out. Figure 4.16a shows the Ni $2p_{3/2}$ XPS spectra of the samples $NiO_{0.5}CuO_{0.5}/CeO_2$, Ni/CeO_2, $Ni_{0.75}Cu_{0.25}/CeO_2$, $Ni_{0.5}Cu_{0.5}/CeO_2$, and $Ni_{0.25}Cu_{0.75}/CeO_2$. For the $NiO_{0.5}CuO_{0.5}/CeO_2$ oxide sample, a strong peak near 854.5 eV and a satellite feature in the range 858-865 eV are observed and are characteristic of Ni^{2+} [177]. The main peak is composed of two overlapped peaks at a low (853.6 eV) and a high (855.4 eV) binding energy. The peak at lower binding energy corresponds to Ni^{2+} ions in NiO particles while the peak at higher binding energy represents Ni^{2+} ions surrounded by Ce^{4+} ions in the form of Ni-O-Ce solid solution [177]. Thus, this indicates that NiO and Ni-O-Ce solid solution coexist on the surface of the oxide samples. For the Ni/CeO_2 sample,

a peak associated with metallic Ni^0 can be observed at 852.3 eV. In addition, in the oxide sample, the peak intensity of Ni^{2+} in NiO is stronger than that of Ni^{2+} in the solid solution, while the two peaks for Ni^{2+} in Ni/CeO_2 catalysts exhibit similar intensity. This indicates that metallic Ni is mainly formed from the reduction of NiO since the formed Ni-O-Ce solid solution is stable and difficult to reduce [140]. For the $NiCu/CeO_2$ bimetallic samples, it is seen that the binding energy of Ni^0 changes by approximately 0.2 to 0.3 eV. The XPS peak shift of metallic species for alloys of transition metals has been commonly reported since the binding energy can be sensitively changed by formation of alloy structure [178,179]. The formation of NiCu alloy in the $NiCu/CeO_2$ catalysts was also confirmed from the XRD results. Therefore, the shift of Ni^0 peak observed in the $NiCu/CeO_2$ samples may be attributed to NiCu alloying. The XPS spectra of the samples after reduction still exhibit a significant amount of Ni^{2+} ions possibly due to the presence of high concentration of Ni-O-Ce solid solution and the aerobic oxidation of Ni during sample preparation for XPS test.
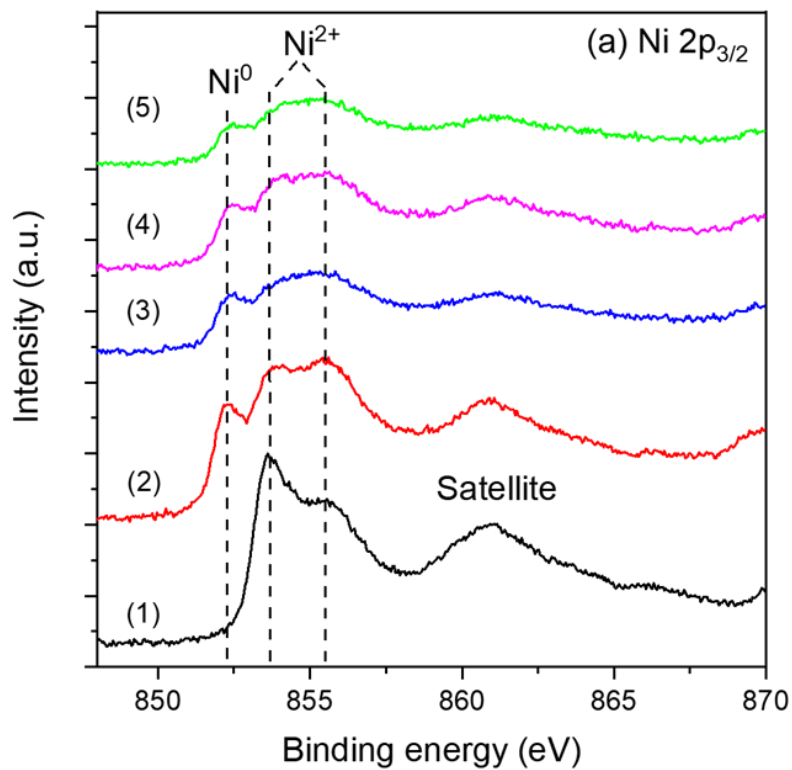
Figure 4.16 (a) Ni 2p$_{3/2}$, (b) Cu 2p$_{3/2}$, and (c) Ce 3d XPS spectra of the samples: (1) NiO$_{0.5}$CuO$_{0.5}$/CeO$_2$; (2) Ni/CeO$_2$; (3) Ni$_{0.75}$Cu$_{0.25}$/CeO$_2$; (4) Ni$_{0.5}$Cu$_{0.5}$/CeO$_2$; (5) Ni$_{0.25}$Cu$_{0.75}$/CeO$_2$; (6) Cu/CeO$_2$

Figure 4.16 continued
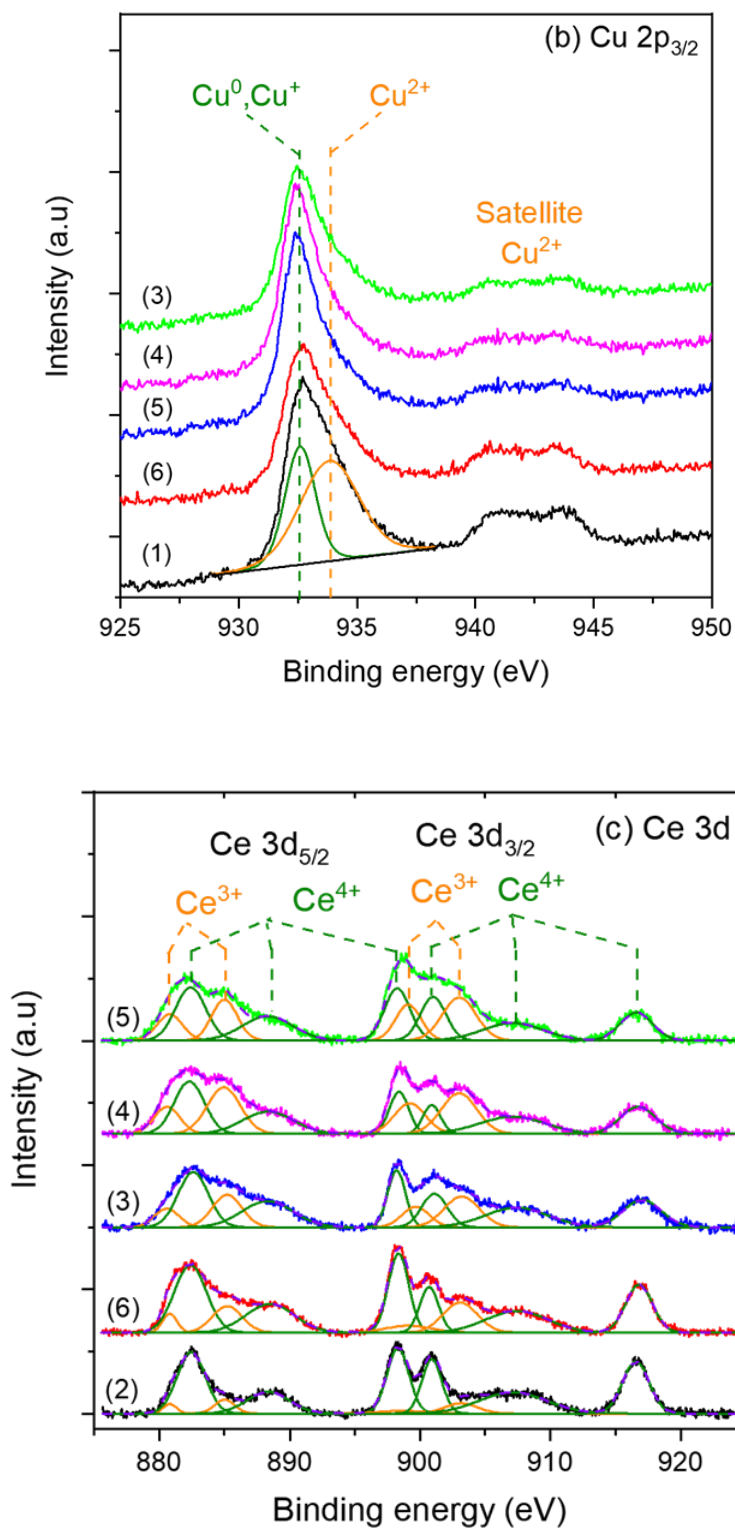
Cu $2p_{3/2}$ XPS spectra of the samples are shown in Figure 4.16b. For NiO$_{0.5}$Cu$_{0.5}$CeO$_2$, two peaks and one satellite peak are observed at 930.0, 931.3, and 940-945 eV, respectively. The peak at 931.3 eV and the satellite peak are attributed to Cu^{2+} while the peak at 930.0 eV is associated with metallic Cu^0 and Cu$^+$ which have essentially identical binding energy [180]. Since the sample, however, is an oxide, the peak at 930.0 eV is solely for Cu$^+$. As noted earlier, Cu$^+$ species which are able to form part of Cu-O-Ce structure can be generated and strongly stabilized by the strong interaction of CuO with CeO$_2$ [174-176]. For all the reduced samples, the intensity of the Cu^{2+} peaks at 931.3 eV and 940-945 eV decreases significantly, resulting from the reduction of Cu^{2+} to Cu^0 on the surface. Thus, Cu species in the reduced catalysts mainly exist in the form of metallic Cu and Cu-O-Ce solid solution. A small quantity of Cu^{2+}, however, still exists due to the surface oxidation during exposure of the samples to air.

Figure 4.16c shows the Ce 3d XPS spectra of the samples. The spectra of Ce 3d can be split into a superposition of ten subpeaks at 880.8, 882.4, 885.0, 888.3, 898.2, 899.0, 901.1, 903.1, 907.1, and 916.6 eV. The four subpeaks at 880.8, 885.0, 899.0, and 903.1 eV are attributed to Ce^{3+} and the other six peaks are assigned to Ce^{4+} [115]. The ratio of integrated peak areas of Ce^{3+} to that of total Ce^{3+} and Ce^{4+} was calculated to estimate Ce^{3+} concentrations in the samples. The Ce^{3+} concentration of Cu/CeO$_2$ (21.8%) is relatively higher than for the Ni/CeO$_2$ (9.6%). As noted previously, owing to the similarity of ionic radius of Cu$^+$ (0.096 nm) and Ce^{4+} (0.094 nm), Cu can easily incorporate into the CeO$_2$ lattice as compared to Ni (0.072 nm), leading to more formation of the solid solution and the oxygen vacancy that essentially accompanies the formation of Ce^{3+} [170,174]. For the NiCu/CeO$_2$ samples, the Ce^{3+} concentration of Ni$_{0.75}$Cu$_{0.5}$/CeO$_2$, Ni$_{0.5}$Cu$_{0.5}$/CeO$_2$, and

$Ni_{0.25}Cu_{0.75}/CeO_2$ is 28.5, 43.2, and 36.0%. The proportion of Ce^{3+} in the bimetallic catalysts is much higher as compared to the monometallic counterparts. It may be ascribed to the increased concentration of Cu^+ by the synergistic interaction between Ni, Cu, and CeO_2. The highest Ce^{3+} concentration (43.2%) was found for $Ni_{0.5}Cu_{0.5}/CeO_2$ catalyst. Notably, the XPS results agree well with the XRD analysis that the CeO_2 lattice parameter of the $NiCu/CeO_2$ catalysts significantly increases due to the enhanced formation of the solid solution.

4.3.2.5 Raman measurements

The Raman spectra of the $Ni_{1-x}Cu_x/CeO_2$ catalysts ($x = 0$, 0.25, 0.5, 0.75 and 1) are shown in Figure 4.17. A characteristic strong F_{2g} band at 463 cm^{-1} of cubic fluorite structured CeO_2 and a broad D band near 550 cm^{-1} were observed. The F_{2g} band is owing to a symmetrical stretching mode of oxygen atoms around each Ce^{4+} cation while the D band indicates the presence of oxygen vacancy (defect) in CeO_2 structure that may result from the formation of solid solution [81]. For the Ni/CeO_2 and Cu/CeO_2, the intensity of the D band for the Cu/CeO_2 catalyst is stronger than that of Ni/CeO_2, corresponding to higher concentration of the oxygen vacancy owing to the ability of Cu^+ to easily enter the CeO_2 lattice. In addition, for the $NiCu/CeO_2$ catalysts, the significant increase in the intensity of the D band is observed as compared to the monometallic counterparts. As noted above, it may be due to the synergistic interaction between Ni, Cu, and CeO_2. The broadening and red-shift of the F_{2g} band for the $NiCu/CeO_2$ also resulted from the increased oxygen vacancies which can lead to the severe distortion of CeO_2 structure [106]. The Raman results indicate that the $Ni_{0.5}Cu_{0.5}/CeO_2$ catalyst has the highest concentration of oxygen vacancy, which is consistent with the XRD and XPS results.
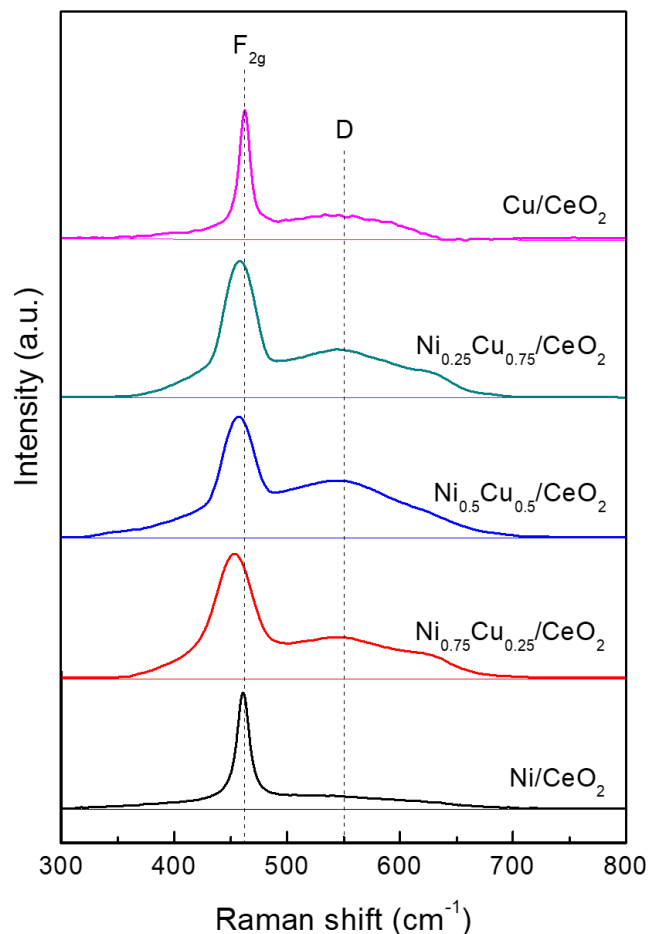
Figure 4.17 Raman spectra of $Ni_{1-x}Cu_x/CeO_2$ (x = 0, 0.25, 0.5, 0.75 and 1) catalysts

4.3.2.6 H₂-temperature programmed reduction analysis

The oxygen vacancy in the CeO_2 for CeO_2 supported metal oxides is known to diffuse to the surface oxygen of metal oxides and promote their reducibility under H_2 atmosphere by facilitating the dissociation of H_2 [181,182]. Accordingly, the synergistic formation of oxygen vacancies in CeO_2 by a strong interaction among Ni, Cu and CeO_2 was confirmed using H_2-temperature-programmed reduction (H_2-TPR) analysis. Figure 4.18 shows the H_2-TPR profiles of $Ni_{1-x}Cu_x/CeO_2$ (x = 0, 0.25, 0.5, 0.75, and 1) catalysts. For the Ni/CeO_2, a broad hydrogen consumption peak (α) at 430 °C was observed, which

is ascribed to reduction of bulk NiO, while the Cu/CeO_2 showed a broad peak (β) at 300 °C owing to reduction of bulk CuO [183]. For both Ni/CeO_2 and Cu/CeO_2, a shoulder peak appears on the low temperature side of the α and β peaks. This shoulder is associated with the reduction of highly dispersed metal oxides (NiO or CuO) on CeO_2. In the cases of $NiCu/CeO_2$, α and β peaks shifted towards lower temperature as compared to that of Ni/CeO_2 and Cu/CeO_2, suggesting that the reducibility of the $NiCu/CeO_2$ samples is substantially enhanced owing to the increased concentration of oxygen vacancies by a synergistic interaction among Ni, Cu and CeO_2. As observed in the XRD measurements, the metal components of the $NiCu/CeO_2$ samples exist in NiCu alloy and Cu phases. Therefore, the NiCu alloying could also contribute to enhancing the reducibility of Ni phase (α peak). Ashok et al. reported that the Cu doped in Ni-Cu alloy catalysts leads to spillover hydrogen, which accelerates the nucleation of metallic Ni and enhances the reducibility of NiO at low temperature [184].
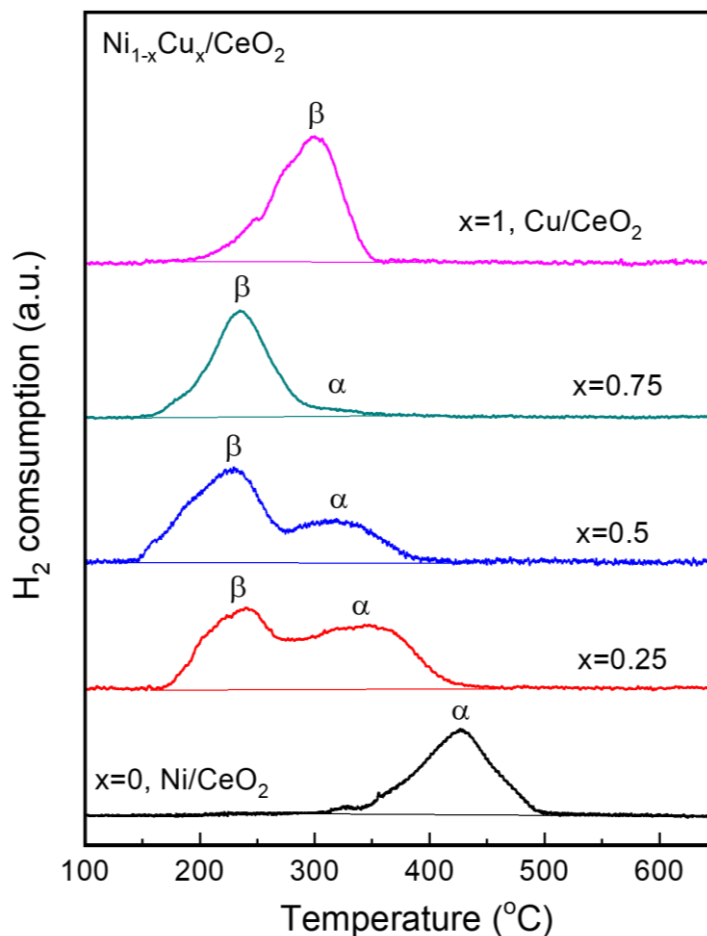
Figure 4.18 H$_2$-TPR profiles of Ni$_{1-x}$Cu$_x$/CeO$_2$ ($x = 0$, 0.25, 0.5, 0.75 and 1) catalysts

When the Cu content increases from 0.25 to 0.5, the α and β peaks shifted slightly further to lower temperature, while, with an increase of the Cu content from 0.5 to 0.75, the peaks shifted towards higher temperature. This feature is in accordance with the trend of concentration variation of oxygen vacancy observed from XRD, XPS, and Raman analysis. It is also seen that the intensity of the α peak becomes negligible for the Ni$_{0.25}$Cu$_{0.75}$/CeO$_2$, suggesting that most of Ni^{2+} ions incorporate into the CeO$_2$ structure and present as a form of Ni-O-Ce solid solutions, which is very stable structure and can be reduced at > 900 °C, rather than bulk NiO particles. It is known that too much concentration

of the solid solution with too little active Ni species in catalysts is unfavorable for hydrogen generation from hydrous hydrazine decomposition because the solid solution acts as a promoter but not an active site by itself [46,81].

The above characterization results indicate that the better catalytic performance of the NiCu/CeO$_2$ catalysts is related to the formation of more oxygen vacancies, which act as a promoter for the reaction, as well as NiCu alloying and particle size of the active component. With increasing the Cu content from $x = 0$ to 0.5, the concentration of oxygen vacancy in CeO$_2$ increases and thereby the catalytic activity increases with 100% H$_2$ selectivity. When the Cu content increases further from $x = 0.5$ to 0.75, the activity and selectivity, however, decrease possibly due to a decreased amount of oxygen vacancy and too little active Ni atoms. It should be noted that the formation of a solid solution between metal ions and CeO$_2$ depends on the synthesis methods and SCS is reported to be an effective way to prepare a solid solution owing to the exothermic nature of combustion process [185,186]. Therefore, the formation of solid solutions in the NiCu/CeO$_2$ catalysts prepared by SCS may be ascribed to the synergistic interaction between Ni, Cu and CeO$_2$ as well as the preparation method. All these possible reasons lead to the best catalytic performance of the Ni$_{0.5}$Cu$_{0.5}$/CeO$_2$ catalyst for hydrogen generation via hydrous hydrazine decomposition.

4.4   Conclusions

In this chapter, noble-metal-free NiM/CeO$_2$ (M= Cu, Fe and Co) bimetallic catalysts with 13 wt% total metal loading were synthesized using a facile one-step SCS method for hydrogen generation from hydrous hydrazine, which is a promising liquid-

phase hydrogen carrier for fuel cell vehicles. The catalytic activity of the $NiCu/CeO_2$ for hydrogen generation was significantly enhanced as compared to their monometallic counterparts while such a synergistic effect was not observed for the $NiFe/CeO_2$ and $NiCo/CeO_2$. The catalyst characterization revealed that NiCu alloying, particle size of the active component, and concentration of the oxygen vacancy in CeO_2 lattice play an important role in the catalytic activity and selectivity. The alloying of Ni and Cu leads to modification of the electronic structure on the metal surface, which consequently improves the reactivity of the metals. The addition of Cu results in formation of more oxygen vacancy, which acts as a promoter for the reaction, by a strong synergistic interaction among Ni, Cu and CeO_2. Besides, the SCS system for the $NiCu/CeO_2$ catalysts exhibits lower combustion temperature as compared to the system for monometallic counterparts, yielding smaller particle size which is beneficial for promoting the catalytic activity. The $Ni_{0.5}Cu_{0.5}/CeO_2$ catalyst possessing the smallest metal particle size and the highest amount of the oxygen vacancy showed 100% H_2 selectivity in the temperature range 30-70 °C and 3.2-fold higher TOF value of 1450.0 h^{-1} at 50 °C than that of the Ni/CeO_2 monometallic catalyst. This reactivity is also superior to that of most reported non-noble metal catalysts and is even comparable to several noble metal-based catalysts (see Table 4.2). Investigating support effects, the $Ni_{0.5}Cu_{0.5}/SiO_2$ shows much lower activity as compared to $Ni_{0.5}Cu_{0.5}/CeO_2$ despite the fact that they have similar metal particle size and degree of alloying. This suggests that the strong interaction between Ni, Cu, and CeO_2, which generates a large amount of oxygen vacancy, may be the main reason for enhanced catalytic performance of $NiCu/CeO_2$.

This work demonstrates that SCS is an effective method to develop catalysts for hydrogen generation from hydrous hydrazine decomposition and the catalytic performance can be improved through a proper selection of secondary metal and catalyst preparation method. The efficient and cost-effective $Ni_{0.5}Cu_{0.5}/CeO_2$ catalyst may further encourage the practical application of hydrous hydrazine as a promising on-board hydrogen carrier for fuel cell vehicles. Finally, the synergistic effect found in this study may have significance in designing CeO_2 supported catalysts for other applications.

CHAPTER 5.   NICKEL-PLATINUM/CERIUM OXIDE CATALYSTS WITH LOW PLATINUM LOADING FOR HYDROGEN GENERATION FROM HYDROUS HYDRAZINE DECOMPOSITION

5.1   Introduction

For the practical application of hydrous hydrazine as a promising hydrogen carrier for on-board hydrogen generation, one must develop highly active, selective and cost-effective catalysts which facilitate the complete decomposition [N_2H_4 (*l*) → N_2 (*g*) + $2H_2$ (*g*)] and suppress the incomplete decomposition [$3N_2H_4$ (*l*) → $4NH_3$ (*g*) + N_2 (*g*)]. Towards this aim, a number of catalysts have been examined for hydrous hydrazine decomposition [12,30,31,33,36,37]. It was found that alloying of Ni with Pt significantly promotes catalytic property of Ni for hydrous hydrazine decomposition and NiPt bimetallic catalysts on various supports exhibit 100% selectivity towards hydrogen generation and superior activity[187]. All the reported catalysts, however, contain large amount of Pt up to 42 wt% (Table 5.1). This high content of Pt in the catalysts may hinder the widespread use of hydrous hydrazine as a hydrogen carrier due to the low abundance and high material cost of Pt. As mentioned in Chapter 4, several prior works have investigated noble-metal-free catalysts, but their activity have remained much lower than that of NiPt catalysts (Table 4.2). Therefore, to make the on-board system based on hydrous hydrazine more affordable, decreasing the amount of Pt in catalysts while increasing catalytic activity may be an effective approach.

The Chapters of 3 and 4 demonstrated that conventional SCS technique is an effective method to prepare catalysts for hydrous hydrazine decomposition owing to enhanced metal dispersion, formation of porous structure, and strong interaction between

metal and support. The conventional SCS, however, is not suitable to prepare Pt containing catalyst because during combustion Pt particles on the support surface diffuse into the bulk support [188]. Therefore, to overcome this problem, advanced synthesis technique or novel methodology is required.

In this chapter, we focused on the investigation of low Pt loading catalysts and report a modified SCS technique for the preparation of highly efficient and cost-effective NiPt catalysts for hydrous hydrazine decomposition. The developed NiPt/CeO$_2$ catalysts contain only 1 wt% Pt loading while exhibiting 100% H$_2$ selectivity and comparable activity as compared to that of the reported NiPt based catalysts.

Table 5.1 Catalytic performance, reaction conditions, and metal contents of different NiPt-based catalysts for hydrous hydrazine decomposition

Catalysts	Metal content [wt%]		NaOH [M]	Temp. [°C]	Selectivity [α, %]	Reaction rate [h^{-1}]	Ref.
	Ni	Pt					
0.4Ni-1Pt(60:40)/CeO$_2$	0.4	1	0.5	50	100	1017	This work
0.4Ni-1Pt(60:40)/CeO$_2$	0.4	1	0.5	30	100	264	
Pt$_{0.5}$Ni$_{0.5}$/NGN	13	38	4[a]	50	100	2116	[39]
(Ni$_5$Pt$_5$)$_1$-(CeO$_x$)$_{0.3}$/NGH	7.1	27.7	0.5	50	100	2043	[40]
Ni$_{0.9}$Pt$_{0.1}$/MIL-101_A	9	3.6	0.5	50	100	621	[41]
Ni$_{37}$Pt$_{63}$/gC$_3$N$_4$	2.5	14.3	0.5	50	100	570	[42]
Ni@NiPt(1/8)/La$_2$O$_3$	12.8	6.1	1	50	100	533	[43]
(Ni$_3$Pt$_7$)$_{0.5}$-(MnO$_x$)$_{0.5}$/NPC	5.4	42	0.5	50	100	470	[44]
Ni$_{87}$Pt$_{13}$/meso-Al$_2$O$_3$	9.9	4.8	0.5	50	100	320	[50]
NiPt$_{0.057}$/Al$_2$O$_3$	39.9	7.6	0	50	99	112	[127]
Ni$_{0.8}$Pt$_{0.2}$@ZIF-8	6.3	5.6	0.5	50	100	90	[47]
Ni$_{60}$Pt$_{40}$/La$_2$O$_3$	8.2	17	3	30	100	514	[48]
Ni$_{60}$Pt$_{40}$/CeO$_2$	12.3	27.3	2	30	100	424	[49]
Ni$_{60}$Pt$_{40}$/meso-CeO$_2$	7.4	16.6	2	30	100	352	[50]

[a] The unit is mmol.

5.2   Experimental

5.2.1   Catalyst preparation

Nickel nitrate hexahydrate [$Ni(NO_3)_2 \cdot 6H_2O$, 98%], cerium ammonium nitrate [$(NH_4)_2Ce(NO_3)_6$, 98+%], and hydrous hydrazine ($N_2H_4 \cdot H_2O$, 99+%) were purchased from Alfa Aesar. Sodium hydroxide (NaOH, 50% in H_2O) and chloroplatinic acid hexahydrate ($H_2PtCl_6 \cdot 6H_2O$, 37.5+% Pt basis) were obtained from Sigma-Aldrich. Oxalyldihydrazide (ODH, $C_2H_6N_4O_2$, 96+%) was provided by TCI America. The chemicals were used without further purification. Deionized water was used throughout.

NiPt/CeO$_2$ catalysts were prepared by both conventional solution combustion synthesis (SCS) and modified SCS. For conventional SCS, a stoichiometric amount of metal oxidizers [$Ni(NO_3)_2 \cdot 6H_2O$, $(NH_4)_2Ce(NO_3)_6$, and $H_2PtCl_6 \cdot 6H_2O$] were dissolved in a minimum amount of deionized water in a glass beaker and then ODH as a fuel was added into the solution. The fuel-to-oxidizer ratio was maintained at 30. Then, the procedures of the conventional SCS described in Chapter 3.2.1 and 4.2.1 were applied to obtain NiPt/CeO$_2$ catalysts which are noted as NiPt/CeO$_2$- SCS.

The modified SCS consisted of two steps. Firstly, NiO/CeO$_2$ powders were prepared using conventional SCS. However, in this case, hydrous hydrazine instead of ODH was used as the fuel and the fuel-to-oxidizer ratio was kept at 2, following prior work [148]. Subsequently, the Pt precursor and ODH were dissolved in a minimum amount of deionized water in a glass beaker. The molar ratio of ODH to Pt precursor was 30. Then, the aqueous solution was added to the prepared NiO/CeO$_2$ powders. The suspension was heated up using a hotplate to trigger combustion. After combustion the obtained metal

oxide powders were removed from the hotplate and reduced at 400 °C for 1 h in a flow of 10 vol% hydrogen (balanced helium). Figure 5.1 schematically illustrates the procedure of the modified SCS for NiPt/CeO₂ catalysts.

Figure 5.1 Schematic diagram for the modified SCS process for NiPt/CeO₂ catalysts

The NiPt/CeO₂ catalysts with different metal compositions (denoted as xNi-yPt(X:Y)/CeO₂; x and y are weight percent of Ni and Pt; X and Y are atomic percent of Ni and Pt) were prepared using the modified SCS. The Ni and Pt contents in the catalysts were measured using atomic absorption spectroscopy (AAS) and are presented in Table 5.2. For comparison, CeO₂, Pt/CeO₂, and Ni/CeO₂ samples were prepared as well. CeO₂ and Ni/CeO₂ were synthesized using conventional SCS but with hydrous hydrazine fuel and the fuel-to-oxidizer ratio of 2, while Pt/CeO₂ was synthesized using the modified SCS.

Table 5.2 Chemical composition of catalysts determined by AAS

Sample	Composition [wt%]			Ni:Pt ratio
	Ni	Pt	CeO_2	
22Ni-1Pt(99:1)/CeO_2	21.80	0.98	77.22	0.99:0.01
16Ni-1Pt(98:2)/CeO_2	15.54	1.23	83.23	0.98:0.02
6Ni-1Pt(95:5)/CeO_2	5.80	1.01	93.19	0.95:0.05
2Ni-1Pt(86:14)/CeO_2	1.82	0.95	97.23	0.86:0.14
0.6Ni-1Pt(66:34)/CeO_2	0.63	1.07	98.30	0.66:0.34
0.4Ni-1Pt(60:40)/CeO_2	0.44	0.99	98.57	0.60:0.40
0.3Ni-1Pt(51:49)/CeO_2	0.31	1.00	98.69	0.51:0.49
0.2Ni-1Pt(45:55)/CeO_2	0.24	0.98	98.78	0.45:0.55
16Ni-36Pt(60:40)/CeO_2	15.70	35.93	48.37	0.59:0.41
5Ni-11Pt(60:40)/CeO_2	5.30	11.20	83.50	0.61:0.39
1.1Ni-2.5Pt(60:40)/CeO_2	1.09	2.49	96.42	0.59:0.41
0.6Ni-1.5Pt(60:40)/CeO_2	0.63	1.45	97.92	0.59:0.41
0.3Ni-0.7Pt(60:40)/CeO_2	0.31	0.66	99.03	0.61:0.39
0.2Ni-0.5Pt(60:40)/CeO_2	0.24	0.53	99.23	0.60:0.40

5.2.2 Catalyst characterization

As described in Chapter 2.3.3 and 3.2.2, AAS, XRD and XPS were utilized to examine the metal contents in the catalysts, structural properties, chemical and electronic states of the elements on the catalyst surface, respectively. The microstructure and element distribution of the samples were analyzed using a FEI Talos 200X transmission electron microscopy (TEM) with ChemiSTEM technology (X-FEG and SuperX energy dispersive X-ray spectrometer with four silicon drift detectors). The hydrogen chemisorption experiments were performed using a Gow-Mac Model 20 thermal conductivity detector. In a typical test, 200 mg of sample was loaded in the middle of a quartz tube reactor, with quartz wool supports on both sides. Before the test, the sample was reduced for 1 h at 400 °C with a heating rate of 10°C/min and flowing 10% vol.% of H_2 balanced with He, degassed at the same temperature for 1 h under 100% He atmosphere, and then cooled down to room temperature under 100% He atmosphere. The adsorption of hydrogen was carried out at room temperature.

5.2.3 Catalytic decomposition of hydrous hydrazine

The catalytic decomposition reaction of $N_2H_4 \cdot H_2O$ over various $NiPt/CeO_2$ catalysts was carried out using the experimental setup described in Chapter 3.2.3 (Figure 3.3). The reaction was initiated by injecting 25 µl of pure $N_2H_4 \cdot H_2O$ solution into the reactor where the catalyst and 10 ml of aqueous NaOH solution (0.5 M) was placed under stirring of 900 rpm and argon (99.999%) atmosphere. The reaction progress was monitored by measuring reactor pressure using a transducer (Omega Engineering PX35D1). After reaction completion, the composition of product gas was analyzed by mass spectrometer (Hiden Analytical HPR-20) to obtain the molar ratio of N_2 to H_2 and to assess the presence

of NH$_3$. As presented in Chapter 3.2.3, the selectivity for H$_2$ generation (α) was calculated based on the overall reaction, as follows:
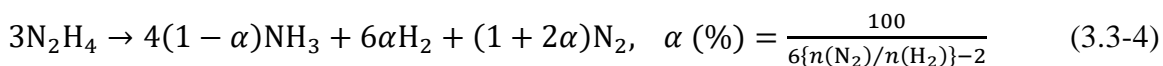
$$3N_2H_4 \rightarrow 4(1-\alpha)NH_3 + 6\alpha H_2 + (1+2\alpha)N_2, \quad \alpha\ (\%) = \frac{100}{6\{n(N_2)/n(H_2)\}-2} \qquad (3.3\text{-}4)$$

where $n(N_2)$ and $n(H_2)$ are the moles of produced N$_2$ and H$_2$, respectively. The reaction rate was calculated, as follows:

$$\text{reaction rate (h}^{-1}) = \frac{n(H_2)}{n(\text{metal})\times t} \qquad (3.5)$$

where n(metal) is the moles of Ni and Pt in the catalyst, and t is the reaction time for 30% conversion of hydrous hydrazine. The reported reaction rate values are averages from 2 to 5 experiments. The recyclability of the catalysts was tested by repeating the reaction for three runs under the same conditions. After the hydrogen generation was completed, the catalyst was separated from the reaction solution by centrifugation, washed with water and tested under the same conditions.

5.3   Results and discussion

5.3.1   Modified SCS method

The surface Pt concentration of 0.2Ni-1Pt(45:55)/CeO$_2$ catalysts prepared by both the typical SCS and modified SCS was obtained using XPS analysis (Figure 5.2). The surface Pt concentration of the sample prepared by the modified SCS is 1.5 at%. This value is higher than the bulk value (0.88 at%) and is about 4 times higher than that of the SCS-

derived sample (0.37 at%). This indicates that, for the modified SCS, most of Pt precursor is deposited on the support surface, which was also confirmed from hydrogen chemisorption test. The ratio of the amount of adsorbed H atom to the total amount of Pt atom was 2.70 and 0.36 for the $0.2Ni-1Pt(45:55)/CeO_2$ catalysts prepared by the modified SCS and the conventional one, respectively. As shown in Figure 5.3, the $0.2Ni-1Pt(45:55)/CeO_2$ catalyst prepared the modified SCS exhibited much better activity than the conventional SCS-derived catalyst. This feature is attributed to the high surface concentration of Pt which enhances the catalytic activity of Ni/CeO_2.
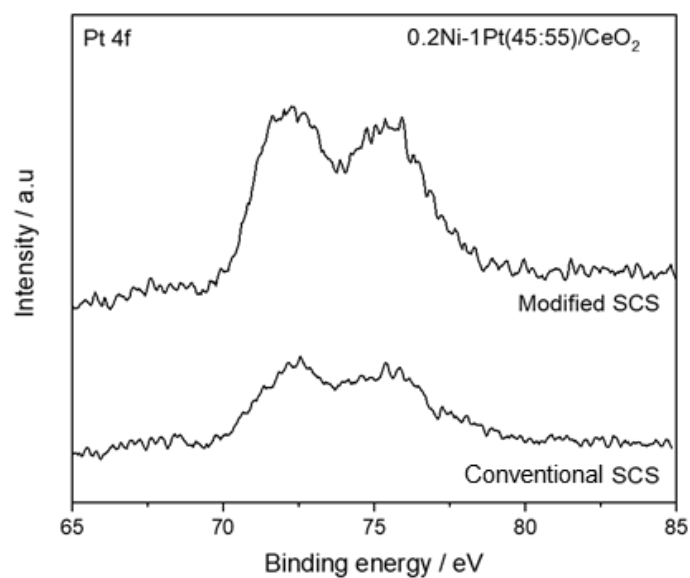
Figure 5.2 Pt 4f XPS spectra for $0.2Ni-1Pt(45:55)/CeO_2$ catalysts prepared by conventional SCS and modified SCS.
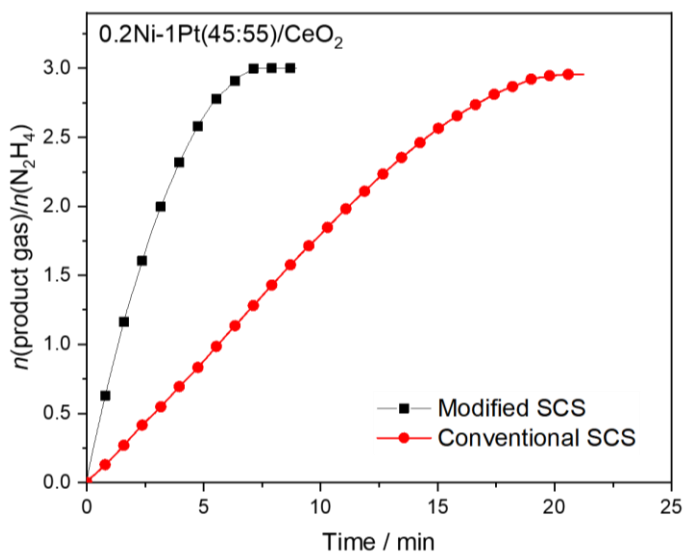
Figure 5.3 Time course plots of hydrous hydrazine decomposition over 0.2Ni-1Pt(45:55)/CeO$_2$ catalysts prepared by conventional SCS and modified SCS. The reaction was conducted at 50 °C, n(metal)/n(N$_2$H$_4$) = 0.17, in the presence of 0.5 M NaOH.

5.3.2 Catalytic performance of NiPt/CeO$_2$ catalysts

5.3.2.1 Effect of Ni loading

Using the modified SCS, NiPt/CeO$_2$ catalysts with different Ni loadings (0.2 – 22 wt%) were prepared. The Pt loading was kept constant at 1wt%. In order to establish an appropriate molar ratio of total metal/N$_2$H$_4$·H$_2$O, preliminary reaction tests were conducted. As shown in Figure 5.4, the catalytic performance in terms of H$_2$ selectivity and reaction rate was independent of molar ratio of total metal/N$_2$H$_4$·H$_2$O over the range 0.085 to 0.255, implying that the reaction is not limited by catalyst loading. Thus, the ratio was kept constant at 0.17 in all reaction experiments.
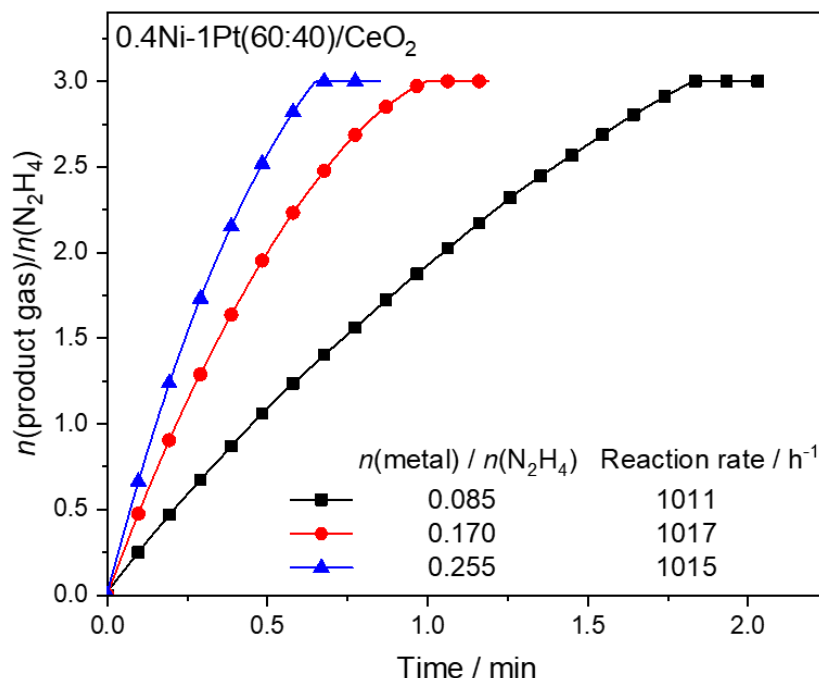
Figure 5.4 Time course plots of hydrous hydrazine decomposition over 0.4Ni-1Pt(60:40)/CeO$_2$ catalysts prepared by modified SCS as a function of molar ratio of metals in the catalyst to hydrous hydrazine [n(metal)/n(N$_2$H$_4$)]. The reaction was conducted at 50 °C in the presence of 0.5 M NaOH

The catalytic performance of the xNi-1Pt(X:Y)/CeO$_2$ catalysts for hydrous hydrazine decomposition was investigated at 50 °C with a constant molar ratio of total metal/N$_2$H$_4$·H$_2$O = 0.17, as shown in Figure 5.5. With decreasing Ni content from 22 wt%, the catalytic activity increases, reaching the highest value with a reaction rate of 1017 h^{-1} at 0.4 wt%, and then decreases with a further decrease of Ni loading. The H$_2$ selectivity also increases with decreasing Ni loading and 100% selectivity was achieved for < 2 wt% Ni loading. It has been well documented that the alloying of Ni with Pt is a prerequisite for the enhanced catalytic activity and selectivity for hydrous hydrazine decomposition and catalytic performance depends on the composition of Ni and Pt in the alloy [39,43]. The atomic percent of Ni to Pt in our best catalyst is 60:40. This composition agrees with prior study of Wang and co-workers, who found that Ni$_{60}$Pt$_{40}$/CeO$_2$ catalyst has the optimum

interaction strength between hydrous hydrazine and Ni active sites on the catalyst, leading

to significant enhancement of catalytic activity [50]. With Ni=7.4 wt% and Pt=16.6 wt%,

however, their metal loadings were much higher than in our work.
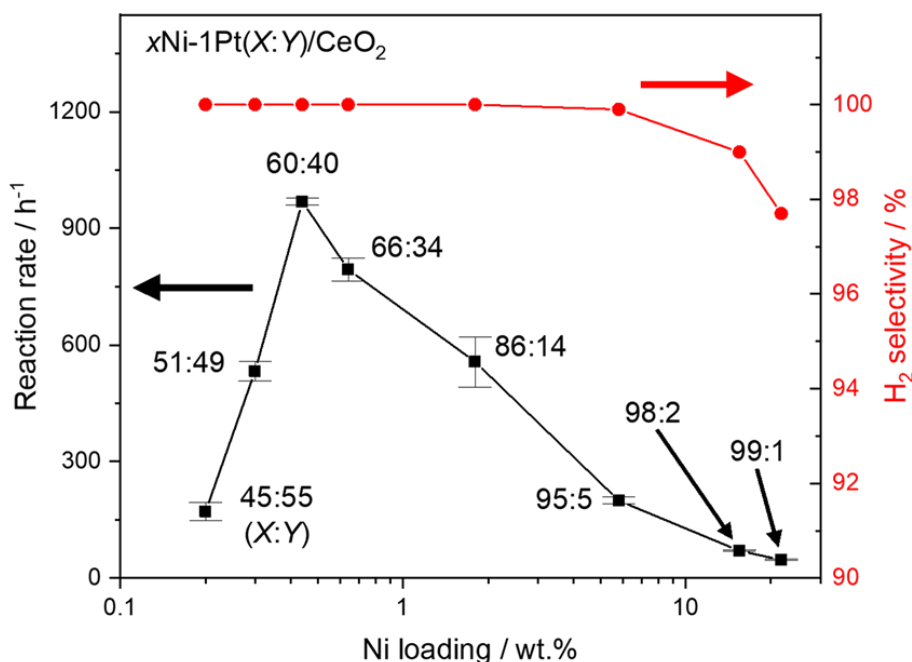
Figure 5.5 Reaction rate and H_2 selectivity of xNi-1Pt(X:Y)/CeO$_2$ catalysts. The reaction was conducted at 50 °C, n(metal)/n(N$_2$H$_4$·H$_2$O) = 0.17, in the presence of 0.5 M NaOH solution.

5.3.2.2 Effect of total metal (Ni+Pt) loading

To optimize the amount of total metal (Ni+Pt) loading on CeO$_2$, additional reaction

tests were conducted with the atomic percent of Ni to Pt kept at 60:40 (Figure 5.6). It shows

that catalytic performance depends strongly on the ratio of metal to support, suggesting

that metal distribution on catalyst surface and interaction between metal particles and

support have a large influence on catalytic performance as well as NiPt alloy formation.

Decreasing the total metal loading from 52 wt%, the reaction rate and H$_2$ selectivity

increase significantly. The 0.4Ni-1Pt(60:40)/CeO₂ catalysts exhibited 100% H₂ selectivity and the highest reaction rate of 1017 h⁻¹ at 50 °C, which is higher than most literature values for the reported NiPt catalysts even though our catalyst contains much lower Pt loading (1 wt%) as compared to 3.6 - 42 wt% for the reported ones (Table 5.1). Although there is a slight change of reaction rate in the metal loading range 0.7 to 3.6 wt%, the H₂ selectivity remains at 100 %. This suggests that these catalysts have similar surface properties since the H₂ selectivity is related to the Pt-induced geometric modification of Ni surface [189].
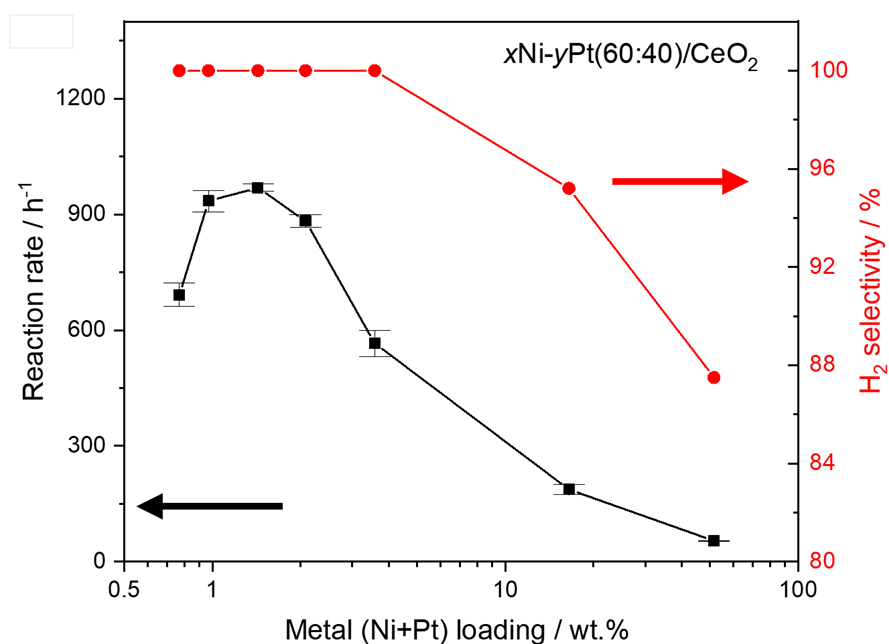
Figure 5.6 Reaction rate and H₂ selectivity of xNi-yPt(60:40)/CeO₂ catalysts. The reaction was conducted at 50 °C, n(metal)/n(N₂H₄·H₂O) = 0.17, in the presence of 0.5 M NaOH solution.

5.3.2.3 Effect of reaction temperature

Figure 5.7a shows the time course plots for the decomposition of hydrous hydrazine over the 0.4Ni-1Pt(60:40)/CeO₂ catalyst at different temperatures (25-70 °C). With an

increase in the reaction temperature, the reaction rate significantly increased while the H_2 selectivity remained 100%. The reaction rate for 50% conversion was 142.4, 269.4, 647.5, 1017, 2636, and 5131 h^{-1} at 25, 30, 40, 50, 60, and 70 °C, respectively. From the Arrhenius plot (Figure 5.7b), the apparent activation energy (E_a) was determined to be 66.4 kJ/mol. The reported apparent activation energy values for this reaction over various catalysts are in the range 30-70 kJ/mol [30,31,33,36,39,43,46,127,146,150,190]. The high activation energy value in the present work implies that the kinetics is controlled by chemical reaction and not by transfer effects. In the recycling test, the 0.4Ni-1Pt(60:40)/CeO_2 catalysts retained 100% H_2 selectivity and rapid reaction rate over 3 cycles (Figure 5.8).
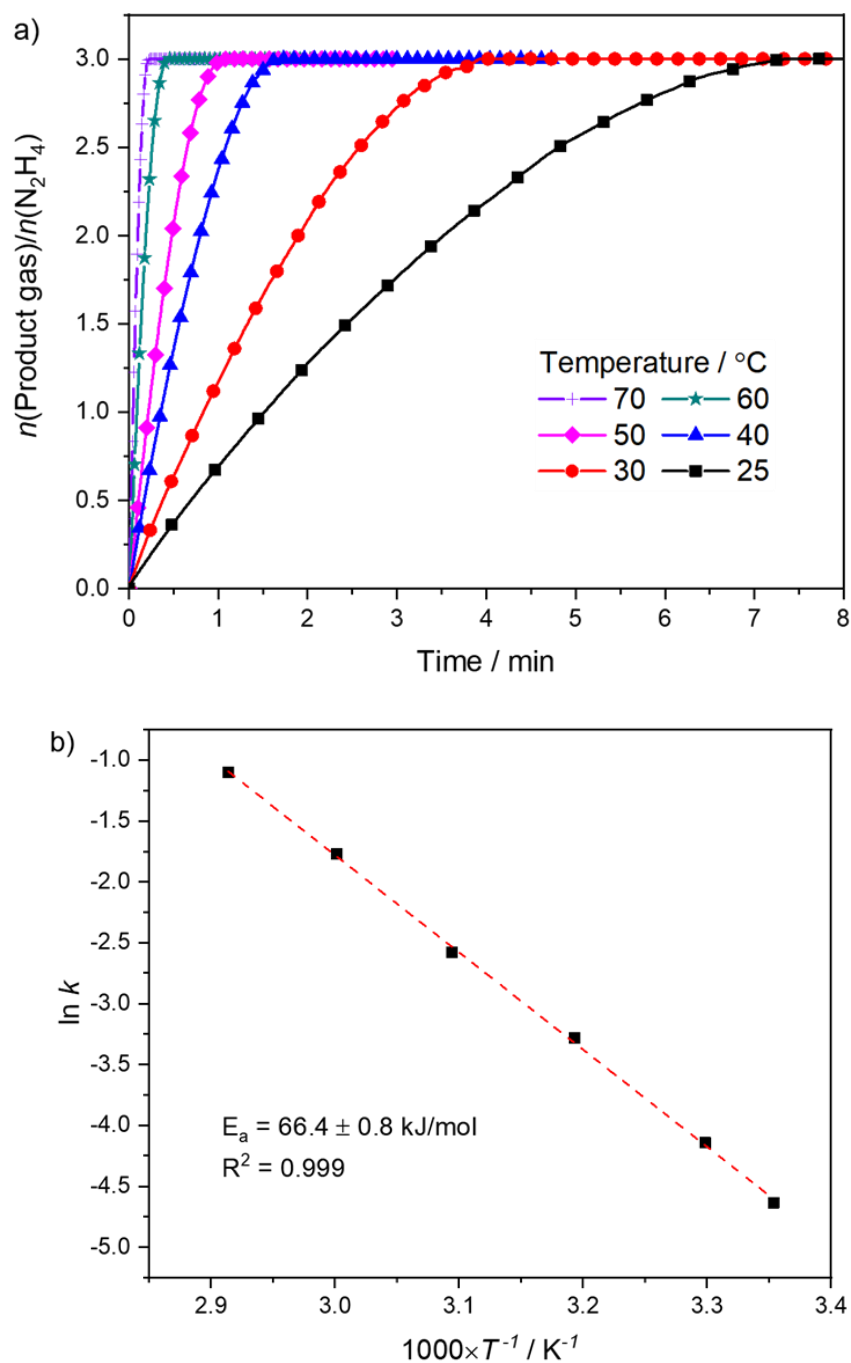
Figure 5.7 a) Time course plots of hydrous hydrazine decomposition over 0.4Ni-1Pt(60:40)/CeO$_2$ catalyst as a function of temperature. b) Arrhenius plot showing apparent activation energy. The reaction was conducted in the presence of 0.5 M NaOH with n(metal)/n(N$_2$H$_4$) = 0.17.

5.3.2.4 Catalyst recyclability

In the recycling test, the 0.4Ni-1Pt(60:40)/CeO$_2$ catalysts retained 100% H$_2$ selectivity and rapid reaction rate over 3 cycles. This indicates that no degradation in the catalytic performance during the recycling process (Figure 5.8).
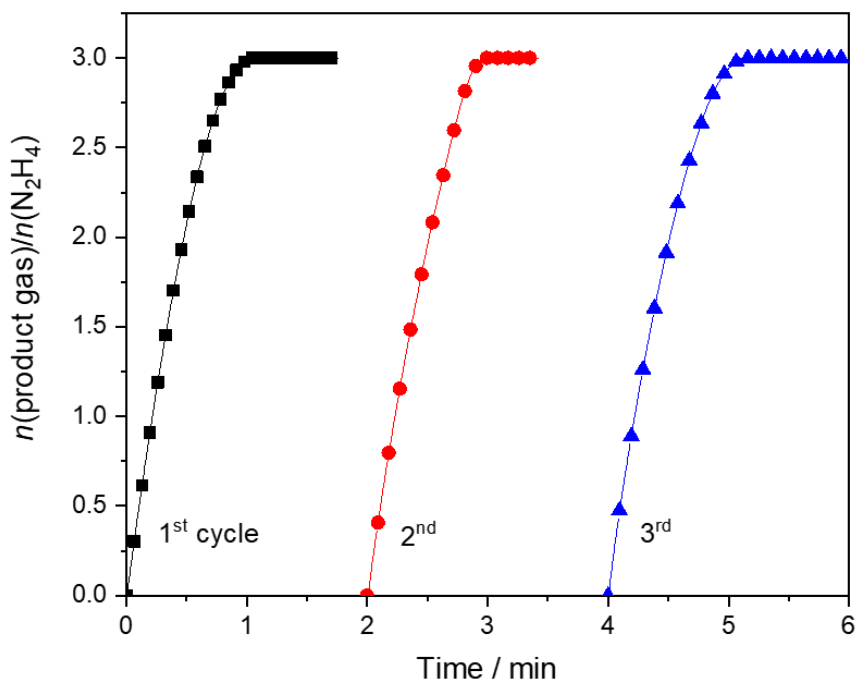
Figure 5.8 Three-run recycling test of 0.4Ni-1Pt(60:40)/CeO$_2$ catalyst for hydrous hydrazine decomposition. The reaction was conducted at 50 °C, n(metal)/n(N$_2$H$_4$) = 0.17, in the presence of 0.5 M NaOH.

5.3.3 Physicochemical properties of NiPt/CeO$_2$ catalysts

5.3.3.1 X-ray diffraction studies

Figure 5.9 shows that XRD patterns of the xNi-1Pt(X:Y)/CeO$_2$, xNi-yPt(60:40)/CeO$_2$, and pure CeO$_2$. All samples clearly show the diffraction peaks of CeO$_2$ with fluorite structure. For the XRD patterns of xNi-1Pt(X:Y)/CeO$_2$ catalysts with different Ni loadings (Figure. 5.9a), the peak for metallic Ni^0 at 44.5° is observed while Pt^0 peak is not detected owing to low loading (1 wt%). With decrease of Ni loading, the intensity of

the Ni^0 peak diminished and eventually disappeared when Ni loading was lower than 6 wt%, due to the high dispersion and/or the resolution limit of XRD measurement. In cases where the Ni peak is visible, there is no structural change of Ni^0 by Pt (e.g. alloy formation) because of much lower Pt loading than Ni. For xNi-yPt(60:40)/CeO$_2$ catalysts with different total metal loadings (Figure 5.9b), there are no peaks of pure Pt^0 and pure Ni^0 while one peak appears between those of pure Pt^0 and pure Ni^0. This indicates the formation of NiPt alloy and is consistent with literature that the peaks of Pt in PtNi alloy catalysts shift to higher angles due to lattice contraction by substitution of the smaller Ni atoms for the larger Pt atoms [191].
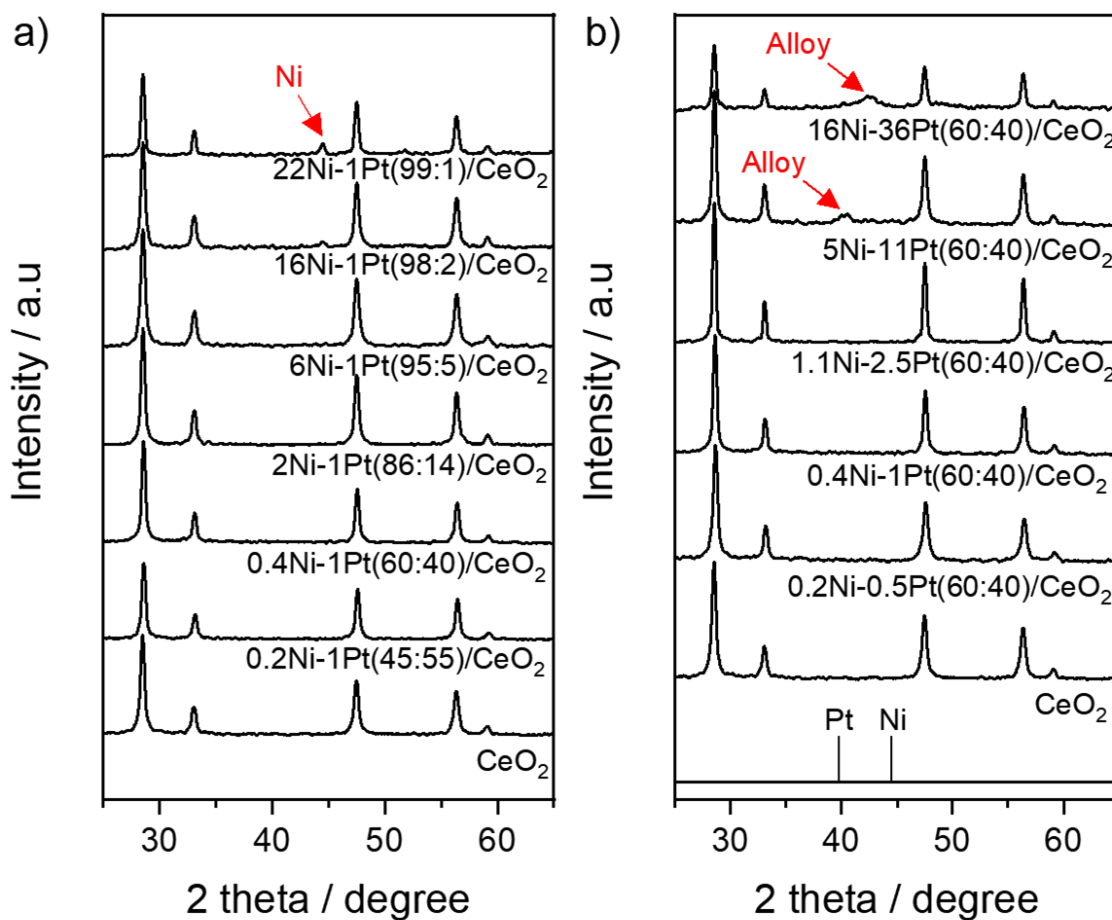
Figure 5.9 XRD patterns of a) xNi-1Pt(X:Y)/CeO$_2$ and b) xNi-yPt(60:40)/CeO$_2$ catalysts

Figure 5.10 shows that the characteristic peak of CeO_2 for the $NiPt/CeO_2$ catalysts relatively shifts to higher degrees as compared to that of pure CeO_2. This peak shifting which indicates the lattice contraction which is attributed to the partial incorporation of smaller Ni^{2+} ions into the lattice of Ce^{4+} to form Ni-O-Ce solid solution [148]. The peak shifting is more pronounced when Ni loading and metal loading decrease for xNi-1Pt(X:Y)/CeO_2 and xNi-yPt(60:40)/CeO_2 catalysts. It is known that for Ni/CeO_2 system, Ni-O-Ce solid solution can be formed by the incorporation of Ni ions into the CeO_2 lattice, leading to reduction of Ce^{4+} to Ce^{3+} and generation of oxygen vacancies in CeO_2 structure to compensate for the charge difference between Ni^{2+} and Ce^{4+}. Moreover, it was reported that both oxygen vacancy and Ce^{3+} enhance catalytic activity and H_2 selectivity for hydrous hydrazine decomposition over ceria supported catalysts [46,148,153].
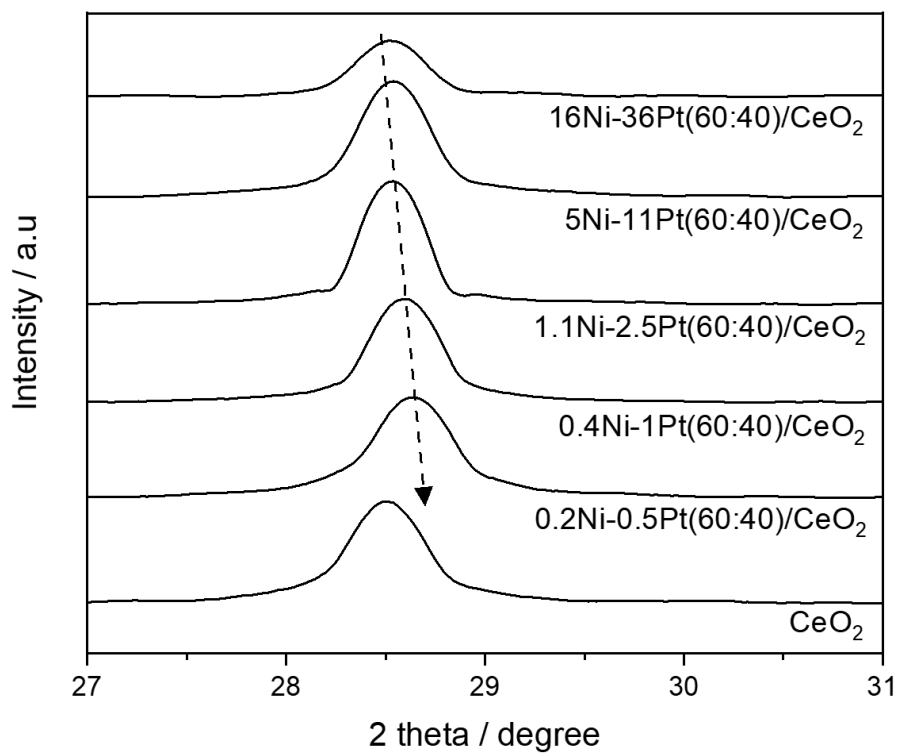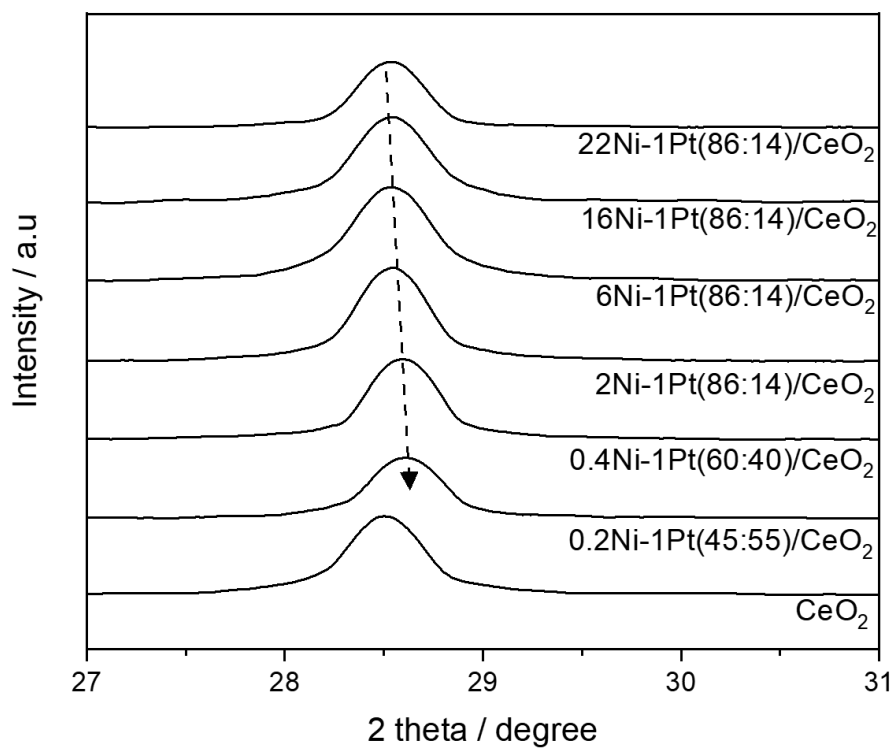
Figure 5.10 Enlarged XRD patterns in the range of 2θ from 27 to 31° for xNi-1Pt(X:Y)/CeO$_2$ catalysts and xNi-yPt(60:40)/CeO$_2$ catalysts.

5.3.3.2 X-ray photoelectron spectroscopy results

The XPS spectra of Pt 4f for 0.4Ni-1Pt(60:40)/CeO$_2$ and Pt/CeO$_2$ samples are shown in Figure 5.11. It indicates that Pt exists in the forms Pt^0 and Pt^{2+}. The presence of Pt^{2+} in the samples is due to strong interaction between Pt and CeO$_2$. It was shown theoretically and experimentally that oxygen spillover from CeO$_2$ to Pt particles occurs favorably[192]. As compared with Pt/CeO$_2$ (71.1 eV), the binding energy corresponding to Pt^0 for 0.4Ni-1Pt(60:40)/CeO$_2$ is positively shifted by 0.3 eV. This shift is attributed to the electron transfer from Ni to Pt upon alloy formation with the lower electronegative Ni [193]. This result confirms that NiPt alloy is formed for the catalysts with low metal loadings where the alloy structure could not be observed from the XRD results.
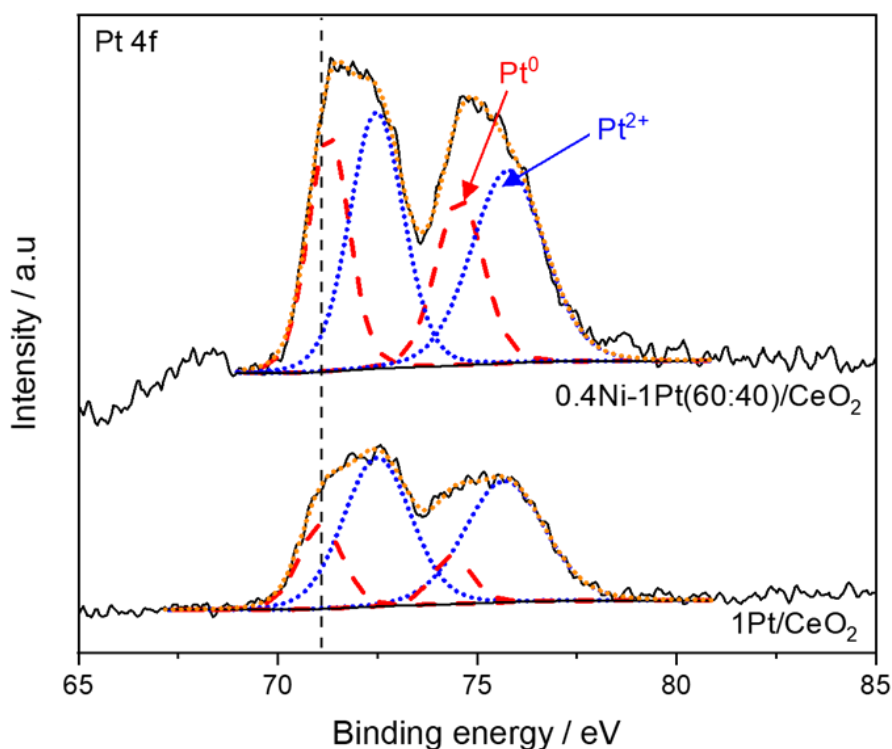
Figure 5.11 Pt 4f XPS spectra of NiPt/CeO$_2$ samples with different metal composition

Figure 5.12 shows the Ni 2p$_{3/2}$ XPS spectra of selected samples. For the 16Ni/CeO$_2$ sample, the Ni 2p$_{3/2}$ spectrum consists of four peaks for metallic Ni^0 at 852.3 eV, Ni^{2+} in NiO and Ni-O-Ce solid solution at 853.9 and 855.6 eV, respectively and shakeup satellite at ~860.9 eV. The presence of NiO is attributed to aerobic oxidation of Ni during sample preparation for the XPS test. A comparison of the relative intensities of the peaks of Ni^{2+} for 16Ni/CeO$_2$ and 16Ni-1Pt(98:2)/CeO$_2$ indicates that Pt inhibits the aerobic oxidation of Ni and promotes the formation of the Ni-O-Ce solid solution. Interestingly, the binding energy of Ni^0 (852.3 eV) for both 16Ni/CeO$_2$ and 16Ni-1Pt(98:2)/CeO$_2$ samples shifts negatively as compared to that of bulk Ni^0 (852.7 eV), suggesting that there is strong interaction between Ni and CeO$_2$ [194]. For 0.4Ni-1Pt(60:40)/CeO$_2$ and 0.4Ni/CeO$_2$, the peak for Ni^0 was not observed due to its low concentration. The positive shift of Ni^{2+} peak for 0.4Ni-1Pt(60:40)/CeO$_2$ as compared to that of 0.4Ni/CeO$_2$ is ascribed to the effect of Pt on Ni^{2+} observed for the 16Ni/CeO$_2$ and 16Ni-1Pt(98:2)/CeO$_2$.
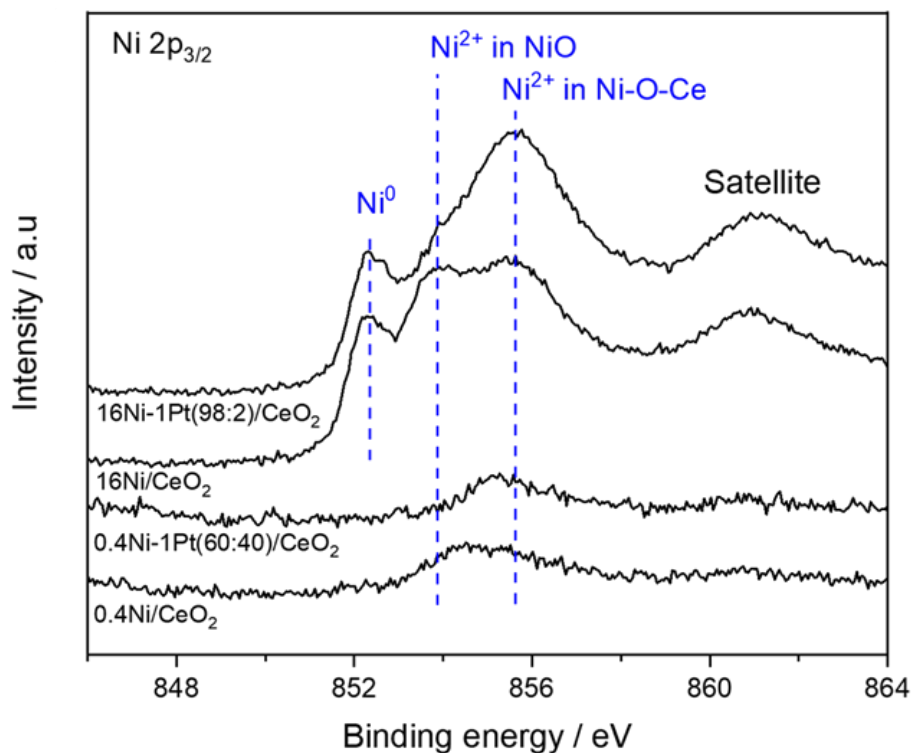
Figure 5.12 Ni 2p$_{3/2}$ XPS spectra of NiPt/CeO$_2$ samples with different metal composition

The existence of Ce^{3+} ions, which are generated from the formation of Ni-O-Ce solid solution, was verified from the Ce 3d XPS spectra (Figure 5.13). The spectra of Ce 3d consists of eight sub peaks. Two peaks are attributed to Ce^{3+} and the other six peaks are assigned to Ce^{4+} [81]. The concentrations of Ce^{3+} were calculated according to literature [194] and are presented in Table 5.3. It shows that pure CeO$_2$ contains considerable amounts of Ce^{3+} (17.4%) which is a typical feature for SCS-derived oxides[195,196]. The Ce^{3+} concentration further increases by the addition of Ni and Pt to CeO$_2$. As expected, with decreasing metal loading, the Ce^{3+} concentration increases gradually, as also reported elsewhere [138,197], and the 0.2Ni-0.5Pt(60:40)/CeO$_2$ catalyst has the highest Ce^{3+} concentration of 33.9%. The 0.4Ni-1Pt(60:40)/CeO$_2$ catalysts also contains a large amount

of Ce^{3+} (28.6%) but is slightly lower than that of $0.2Ni-0.5Pt(60:40)/CeO_2$. In light of the catalytic test results, this suggests that there are other factors affecting the catalytic performance for hydrous hydrazine decomposition.
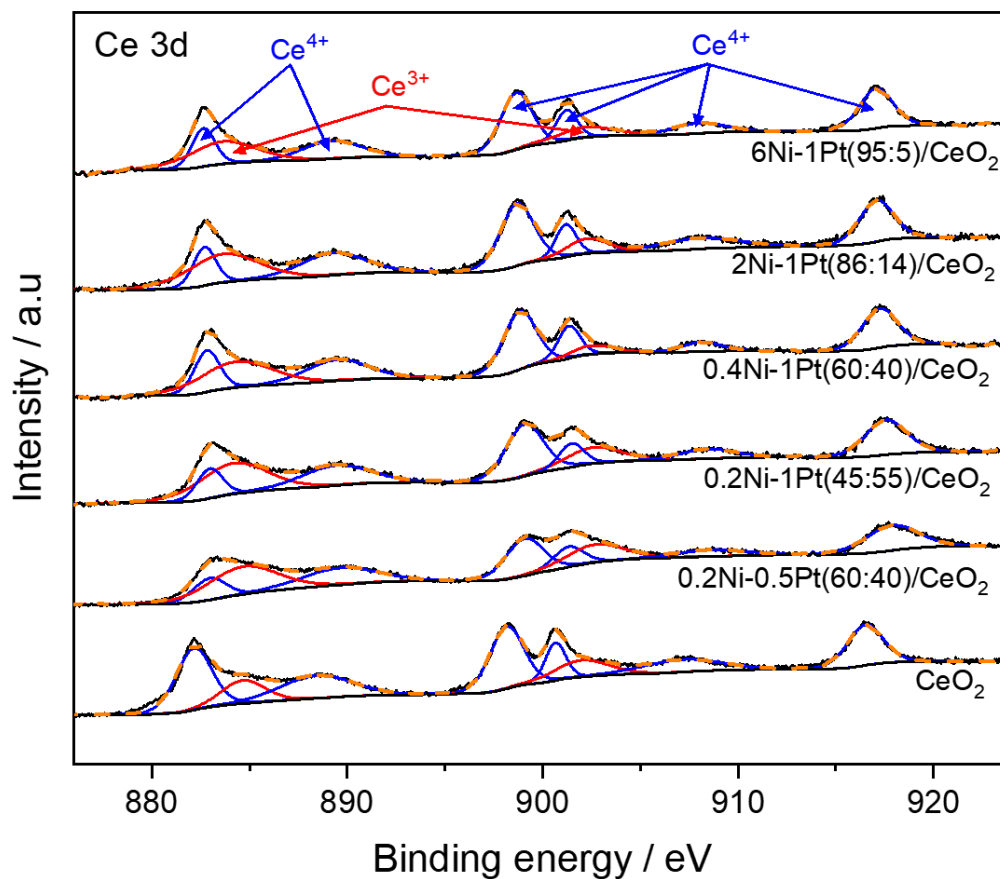
Figure 5.13 Ce 3d XPS spectra of pure CeO_2 and $NiPt/CeO_2$ samples with different metal composition

Table 5.3 Surface Ce^{3+} concentration of the selected samples determined by XPS analysis

Sample	Ce^{3+} / Ce_{total} ratio [at%]
CeO_2	17.3
6Ni-1Pt(95:5)/CeO_2	25.5
2Ni-1Pt(86:14)/CeO_2	26.5
0.4Ni-1Pt(60:40)/CeO_2	28.6
0.2Ni-1Pt(45:55)/CeO_2	31.2
0.2Ni-0.5Pt(60:40)/CeO_2	33.9

5.3.3.3 High-angle annular dark-field scanning transmission electron micrographs and energy-dispersive X-ray spectroscopy

Figure 5.14 shows a typical HAADF-STEM image of 0.4Ni-1Pt(60:40)/CeO_2 catalyst and the corresponding EDS results. The EDS elemental mappings (Figure 5.14b-d) reveal that Ni and Pt are present on the CeO_2 support. Remarkably, Ni is homogeneously distributed throughout the support, indicating the formation of Ni-O-Ce solid solution [148,190]. Figure 5.14a shows that the metal particles (white dots) with size range 1-8 nm are dispersed on the CeO_2 support. The EDS line scanning profiles (Figure 5.14e) corresponding to the red dotted arrow (Figure 5.14a) demonstrate that Ni and Pt occupy the same spatial area, indicating that Ni and Pt metals form an alloy structure. The Ni elements are also present outside the alloy particle due to the Ni-O-Ce solid solution. This matches well with the XRD and XPS results discussed above.
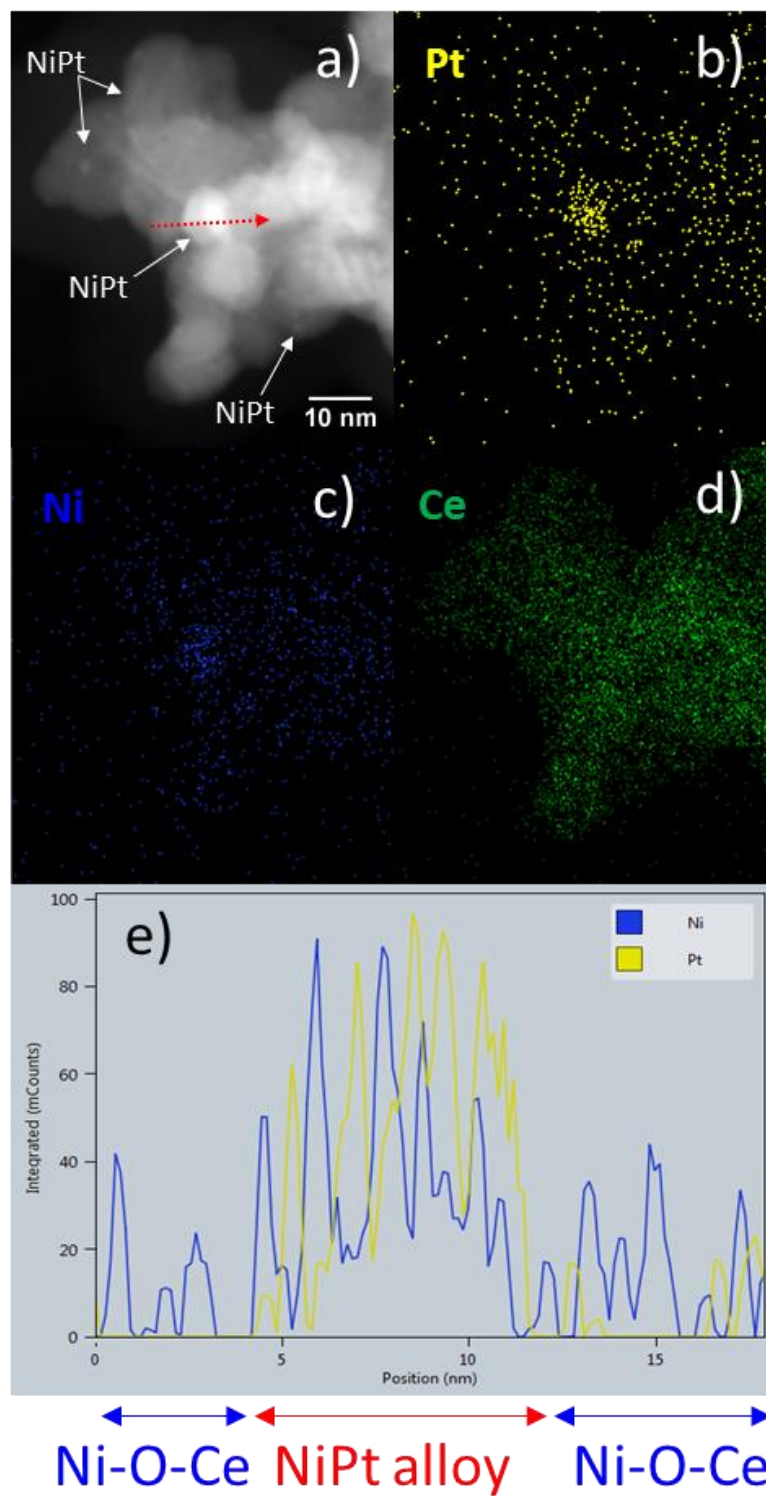
Figure 5.14 a) HAADF-STEM image of 0.4Ni-1Pt(60:40)/CeO$_2$ catalyst, corresponding EDS elemental mappings of b) Pt, c) Ni and d) Ce, and e) EDS line scanning profiles along the red arrow in the HAADF-STEM image

5.3.3.4 Hydrogen chemisorption analysis

Table 5.4 lists the results of hydrogen chemisorption test. For comparison, $0.4Ni/CeO_2$ and $1Pt/CeO_2$ samples were also tested. As expected, the $0.4Ni/CeO_2$ did not uptake hydrogen due to the strong interaction between Ni and CeO_2 while the H/Pt ratio for $1Pt/CeO_2$ (2.79) is much higher than theoretical value of 1 because of the effect of hydrogen spillover originating from the strong interaction between Pt and CeO_2 [198,199]. Even though the obtained H/Pt ratio would be overestimated, it could provide a rough correlation between Pt dispersion and catalyst composition. In addition, given that Ni and Pt form alloy structure for $NiPt/CeO_2$ catalysts, Pt dispersion could represent Ni dispersion. As shown in Table 5.4, the H/Pt ratio increases with decreasing Ni loading for xNi-$1Pt(X:Y)/CeO_2$ catalysts and decreasing metal loading for xNi-yPt$(60:40)/CeO_2$ catalysts. This is an expected result because metal particles tend to aggregate as the metal loading increases. When Ni loading decreases from 0.4 to 0.2 wt% for xNi-$1Pt(X:Y)/CeO_2$ catalysts, the H/Pt ratio remains approximately constant. It suggests that the Pt dispersion remains at maximum value for < 0.4 wt% Ni loading. Although $0.4Ni-1Pt(60:40)/CeO_2$ and $0.2Ni-1Pt(45:55)/CeO_2$ catalysts have similar metal dispersion, the better catalytic activity of the former is attributed to different composition of NiPt alloy. For xNi-yPt$(60:40)/CeO_2$ catalysts, the H/Pt ratio decreases slightly when the total metal loading decreases from 1.4 to 0.7 wt%. This could be ascribed to too low loading amount of metals. Prior studies also reported that the metal dispersion on CeO_2 support increases with decreasing the metal loading and after a certain point the metal dispersion decreases due to strong metal-support interaction [138,143,200]. Consequently, the $0.4Ni-1Pt(60:40)/CeO_2$ catalyst exhibits the highest H/Pt ratio which represents the highest metal dispersion. This demonstrates that

the superior catalytic activity of the 0.4Ni-1Pt(60:40)/CeO$_2$ catalyst may be attributed to the optimum composition of NiPt alloy and the highest metal dispersion.

Table 5.4 Amount of adsorbed H$_2$ during chemisorption and H/Pt ratio of Ni/CeO$_2$, Pt/CeO$_2$, and NiPt/CeO$_2$ catalysts

Sample	H$_2$ uptake [μmol/g$_{cat}$]	H/Pt ratio
22Ni-1Pt(99:1)/CeO$_2$	13.1	0.51
16Ni-1Pt(98:2)/CeO$_2$	34.8	1.36
6Ni-1Pt(95:5)/CeO$_2$	47.3	1.85
0.4Ni-1Pt(60:40)/CeO$_2$	69.8	2.72
0.2Ni-1Pt(45:55)/CeO$_2$	69.0	2.70
0.2Ni-1Pt(45:55)/CeO$_2$-SCS	5.2	0.36
1Pt/CeO$_2$	71.2	2.78
0.4Ni/CeO$_2$	0	-
5Ni-11Pt(60:40)/CeO$_2$	44.4	0.18
1.1Ni-2.5Pt(60:40)/CeO$_2$	40.4	0.90
0.2Ni-0.5Pt(60:40)/CeO$_2$	33.8	2.44

5.4   Conclusions

In summary, to develop a low Pt loading Ni-based catalysts on CeO$_2$ support, the novel SCS technique was developed to overcome the typical problem of conventional SCS which essentially leads to a deficiency of Pt at catalyst surface due to the diffusion of Pt into bulk CeO$_2$. The 0.4Ni-1Pt(60:40)/CeO$_2$ catalyst prepared using the novel method

exhibits 100% H_2 selectivity and high activity (1017 h^{-1}) for hydrous hydrazine decomposition. More importantly, even though this catalyst contains only 1wt.% Pt loading, its activity is higher than most of the reported NiPt-based catalysts which typically contain high Pt loading (3.6-42 wt%) along with the advantage of facile preparation method. This unique catalytic performance is attributed to the optimum composition of NiPt alloy, high metal dispersion, and large amount of Ni-O-Ce solid solution. The efficient and cost-effective 0.4Ni-1Pt(60:40)/CeO_2 catalyst may open up a new avenue for practical application of hydrous hydrazine as an on-board hydrogen carrier. Furthermore, the developed SCS technique may be a good strategy to produce various Pt-based catalysts for other applications.

CHAPTER 6. KINETICS OF HYDROUS HYDRAZINE CONVERSION TO HYDROGEN OVER NICKEL-PLATINUM/CERIUM OXIDE CATALYSTS

6.1 Introduction

Owing to the distinct advantages such as high hydrogen content (8.0 wt%), stable liquid state at ambient temperature, ability to generate hydrogen at moderate temperatures, and benign byproduct (only nitrogen) via complete decomposition reaction, hydrous hydrazine has been actively studied as a hydrogen carrier for FCEVs. Most of the reported studies have concentrated on the development of active and selective catalysts for hydrogen generation from hydrous hydrazine decomposition. Although, beyond the development of efficient catalysts, the reaction studies under practical conditions (e.g. continuous hydrogen generation, non-diluted reactant and large scale) have been reported in recent years [48,51], kinetic studies on this reaction have been performed to date. An understanding of kinetics provides evidence for the reaction mechanism and allows for efficient design and optimization of the hydrous hydrazine-based hydrogen generator system for FCEVs.

Only one kinetic model based on power-law expression for the decomposition of hydrous hydrazine over $Ni_{60}Pt_{40}/CeO_2$ catalysts prepared by one-pot co-precipitation method has been reported [49]. This study demonstrated that the reaction order with respect to hydrous hydrazine concentration varies from 0.52 to 0.043 with increasing of initial amount of the reactant. In addition, the reported catalysts including NiPt catalysts are typically deactivated during the reaction [46,162,201]. There has been no kinetic study addressing this point. Thus, the main objective of this chapter is to establish a more rigorous

and reliable intrinsic kinetic model to capture the reaction behavior involving deactivation over various operating conditions.

In Chapters of 3 through 5, various Ni-based catalysts were developed using SCS for decomposition of hydrous hydrazine which is a promising hydrogen carrier for FCEVs. It demonstrated that SCS is an effective method to prepare catalysts for the decomposition of hydrous hydrazine owing to enhanced metal dispersion, formation of porous structure and strong metal-support interaction (e.g. metal-O-Ce solid solution) [148,190,202]. Notably, $Ni_{60}Pt_{40}/CeO_2$ catalyst prepared by SCS technique exhibited 100% H_2 selectivity and superior catalytic activity as compared to most of the reported catalysts even though this catalyst contains only 1wt% Pt loading which is much lower than those of the reported NiPt-based catalysts (3.6-42 wt%) [202].

Accordingly, in this Chapter, the $Ni_{60}Pt_{40}/CeO_2$ catalysts prepared using SCS were tested to obtain kinetic data for hydrous hydrazine decomposition. Based on the catalytic test results with different temperature, initial concentration of hydrous hydrazine, and the amount of the catalyst, an intrinsic kinetic model based on Langmuir-Hinshelwood mechanism was developed and discussed. In addition, catalyst deactivation during the reaction was studied at a certain temperature. Finally, a kinetic model considering catalyst deactivation was established.

6.2 Experimental

6.2.1 Catalyst preparation

In this chapter, the $Ni_{60}Pt_{40}/CeO_2$ catalysts developed in our prior study [202] were used for the kinetic study. The experimental details of catalyst preparation are described in Chapter 5.2.1.

6.2.2 Kinetic measurement of hydrous hydrazine decomposition

To obtain the kinetic data, the catalytic decomposition of hydrous hydrazine over $Ni_{60}Pt_{40}/CeO_2$ catalysts was conducted in the same experimental setup described in Chapter 5.2.2. The details of experimental procedure are also presented in Chapter 5.2.2. The effects of various operating conditions such as agitation speed (0-1100 rpm), reaction temperature (T, 25-70 $^{\circ}C$), molar ratio of metal (Ni+Pt) to $N_2H_4 \cdot H_2O$ [n(metal)/n(N2H4), 0.085-0.255] and the initial concentration of $N_2H_4 \cdot H_2O$ ($C_{N_2H_{4,0}}$, 0.03-1.0 M) on reaction kinetics were investigated. As a standard operating condition, agitation speed, reaction temperature, molar ratio of metal to $N_2H_4 \cdot H_2O$ and initial concentration of $N_2H_4 \cdot H_2O$ were kept constant at 700 rpm, 50 $^{\circ}C$, 0.17 and 0.05 M, respectively, unless otherwise specified.

For all cases investigated in this study, the value of n(product gas)/n(N_2H_4) at the end of the reaction was 3 and the product gases contained N_2 and H_2 [$n(H_2)/n(N_2) = 2$] without ammonia from mass spectrometer analysis (Figure 6.1). This demonstrates that both the H_2 selectivity and N_2H_4 conversion are 100%. Since the H_2 selectivity remains constant during the reaction [147,203], the N_2H_4 conversion with time was calculated based on the time profile of the amount of product gas, as follows:

$$N_2H_4 \text{conversion (\%)} = \frac{[(\text{measured } P - \text{initial } P)V/(3RT)]}{n(\text{initial } N_2H_4)} \times 100 \qquad (6.1)$$

where R, P, and V are the ideal gas constant (8.314 Jmol^{-1}K^{-1}), pressure and volume of the reactor. The reaction rate was calculated using the same equation as in Chapter 3.2.3.

$$\text{Reaction rate (h}^{-1}) = \frac{n(\text{H}_2)}{n(\text{metal}) \times (t/60)} \qquad (3.5)$$

where t is the reaction time for 30% conversion of N_2H_4 where the effect of catalyst deactivation on reaction kinetic is negligible.

For testing the durability of catalysts, the reaction was repeated by adding another equivalent of $N_2H_4 \cdot H_2O$ into the reactor after completion of the previous run. Following the durability test, the catalyst was separated from the reaction solution by centrifugation, washed with water and reduced at 400 °C for 1 h in a flow of 10 vol% hydrogen (balance helium). Then, the catalyst was tested under the same conditions to evaluate the recyclability. The reported values of reaction rate are averages from 2 to 5 experiments.
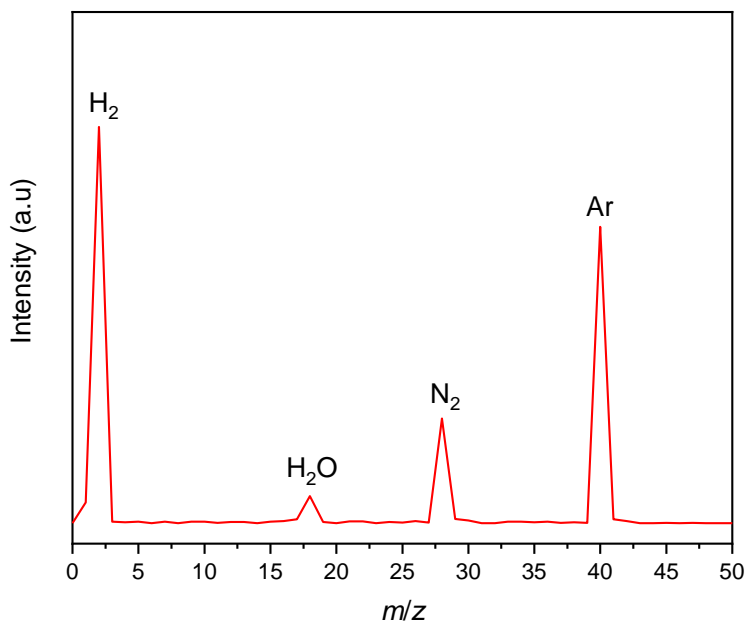
Figure 6.1 Typical mass spectra profile of the product gas from decomposition of hydrous hydrazine over $Ni_{60}Pt_{40}/CeO_2$ catalysts [$T = 50$ °C, n(metal)/n(N_2H_4) = 0.17, $C_{N_2H_{4,0}} = 0.05$ M].

6.3   Results and discussion

6.3.1   Preliminary reaction tests

6.3.1.1   Mass transfer limitations

Before conducting kinetic measurements, a series of preliminary reaction tests using different catalyst particle sizes and agitation speeds were conducted to establish an operating condition where mass transfer limitations are negligible and hence to obtain intrinsic reaction kinetics which is scale independent. In general, reaction rate increases significantly with temperature, while mass transfer rate remains essentially unchanged. For this reason, the preliminary tests were performed at 70 °C which is the highest reaction temperature condition studied, where the mass transfer limitations would be the most severe.
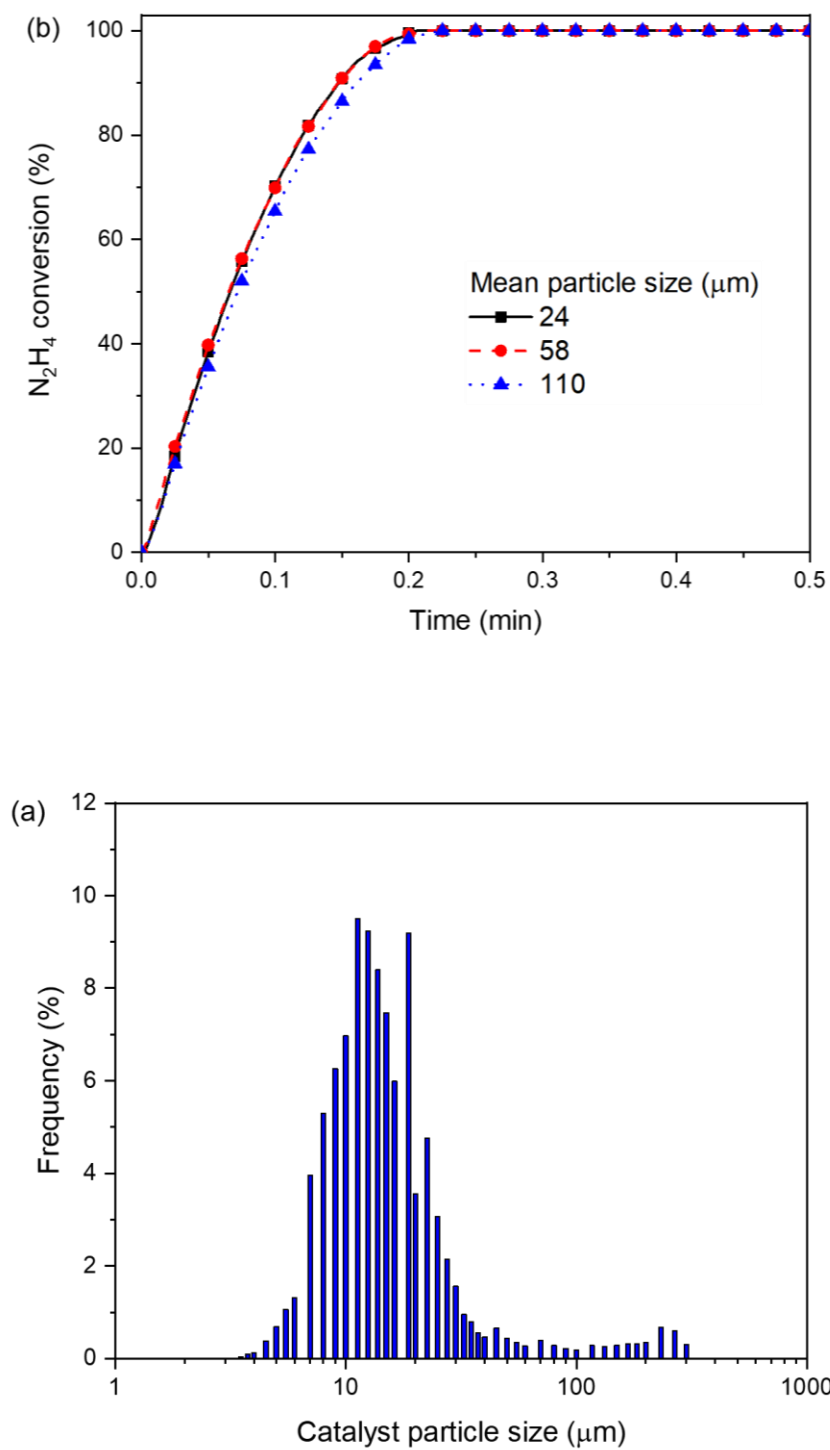
Figure 6.2 (a) Particle size distribution of $Ni_{60}Pt_{40}/CeO_2$ catalysts. The effect of (b) catalyst particle size and (c) agitation speed on decomposition of $N_2H_4 \cdot H_2O$. [$T = 70$ °C, n(metal)/n(N_2H_4) = 0.17, $C_{N_2H_{4,0}} = 0.05$ M]

Figure 6.2 continue
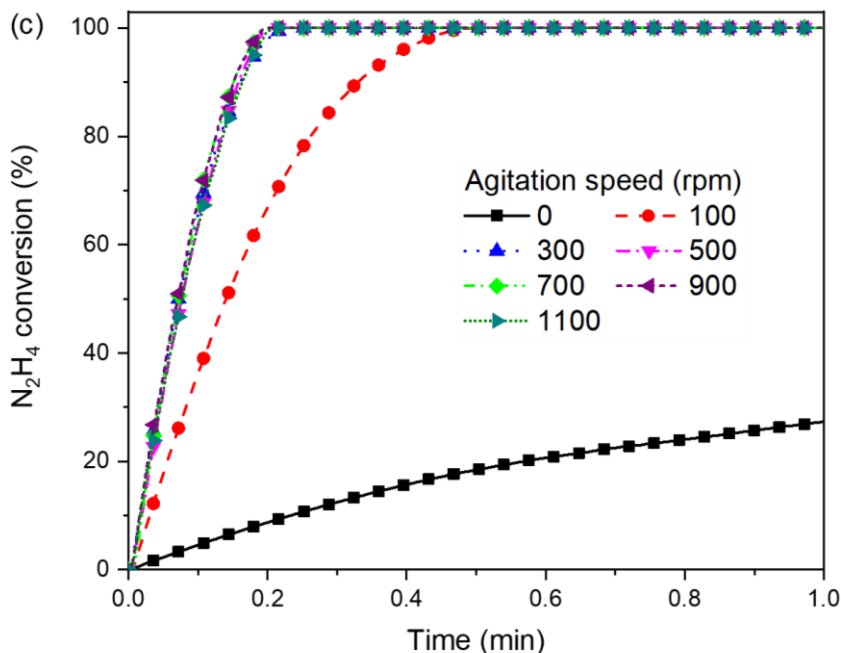
Figure 6.2a shows that the $Ni_{60}Pt_{40}/CeO_2$ catalysts prepared by two-step SCS has a broad particle size distribution (3-200 µm) which was measured using a laser scattering particle size analyzer (Horiba Partica LA-950). It is a typical feature of SCS-derived products because the precursors were exposed to high temperature for a short period of time, which obviously leads to particles with different sizes [24]. To study the effect of different catalyst particle sizes, the catalyst particles were sieved into different size ranges. The mean diameter of the catalyst particles (d_p) trapped in each sieve was assumed to match the average opening sizes of the two adjacent sieves. As shown in Figure 6.2b, hydrogen evolution curves for the catalysts of 58 and 24 µm overlap each other, indicating that the reaction rate is independent of d_p and the internal mass-transfer limitations is negligible. Figure 6.2c shows that no effect of the agitation speed on the reaction rate is observed at >300 rpm, implying that there is no external mass transfer limitation in the range 300-1100

rpm. Consequently, to ensure the absence of internal and external mass transfer limitations, the kinetic experiments were performed using the catalysts with $d_p \leq 58$ μm and at 700 rpm.

6.3.1.2 Effect of reaction temperature

The catalytic decomposition of $N_2H_4 \cdot H_2O$ was conducted at different reaction temperature. As expected, the higher the temperature was, the faster the reaction rate was (Figure 6.3). The N_2H_4 conversion of 30% was reached in ~1.5 min and ~0.05 min at 25 and 70 °C, respectively. Meanwhile, in the temperature range 25-70 °C, the molar ratio of product gas to N_2H_4 reached 3 which can be achieved only at 100% H_2 selectivity as well as 100% N_2H_4 conversion based on the overall reaction equation (Eq. 3.3).
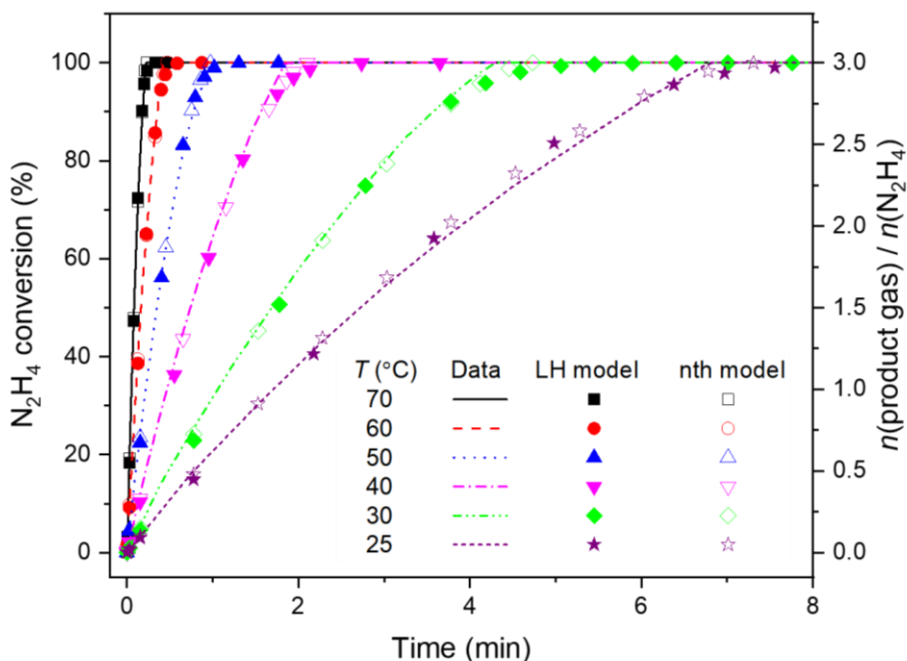
Figure 6.3 The time course plots of the decomposition of $N_2H_4 \cdot H_2O$ over $Ni_{60}Pt_{40}/CeO_2$ catalysts as a function of temperature [$n(\text{metal})/n(N_2H_4) = 0.17$, $C_{N_2H_{4,0}} = 0.05$ M] and predictions based on Langmuir-Hinshelwood model and nth-order model.

6.3.2 Kinetic study

In order to analyze the kinetic data for the decomposition of $N_2H_4 \cdot H_2O$ over $Ni_{60}Pt_{40}/CeO_2$ catalysts, integral method for batch reactor has been implemented [204,205]. Since a kinetic model must be specified first for the integral method, two kinetic models were considered: power-law model and Langmuir-Hinshelwood model.

6.3.2.1 Power-law kinetic model

In general, for a batch reactor with a volume of reactive solution (V_{sol}) and a mass of catalyst (m_{cat}), the reaction rate per unit volume can be expressed as:

$$-r_{N_2H_4} = \frac{m_{cat}k_n}{V_{sol}} C_{N_2H_4}^n \tag{6.2}$$

where k_n is the reaction rate constant for the reaction order n.

In this study, zero-, first- and nth-orders were considered. For each case, by separating and integrating Eq. 6.2, the following integrated reaction rate equations were derived.

$$\frac{m_{cat}k_0}{V_{sol}}t = C_{N_2H_{4,0}} - C_{N_2H_4} \text{ for } t < \frac{V_{sol}C_{N_2H_{4,0}}}{m_{cat}k_0} \text{ and } n = 0 \tag{6.3}$$

$$\frac{m_{cat}k_1}{V_{sol}}t = \ln\left(\frac{C_{N_2H_{4,0}}}{C_{N_2H_4}}\right) \text{ for } n = 1 \tag{6.4}$$

$$\frac{m_{cat}k_n}{V_{sol}}t = \frac{1}{1-n}\left(C_{N_2H_{4,0}}^{1-n} - C_{N_2H_4}^{1-n}\right) \text{ for } n \neq 1 \tag{6.5}$$

Therefore, plots of the right-hand sides of Eqs. (6.3-5) versus time should be linear through the origin, respectively. The reaction rate constant was determined from the slope of the straight line.

The linear regression plots based on zero-, first- and nth-orders for the decomposition of $N_2H_4 \cdot H_2O$ performed at different temperatures (25-70 °C) were shown in Figure 6.4. The data at the end of each experiment (97-100 % conversion) were excluded from the analysis because a diffusion-controlled reaction can occur due to too low concentration of N_2H_4. For the nth-order case, different n values were tried until a linear relationship between ($C_{N_2H_{4,0}}^{1-n} - C_{N_2H_4}^{1-n}$)/(1-n) and t was achieved. The highest linear regression coefficient (R^2=0.9993) was obtained at $n = 0.35$. As shown in Figure 6.4, the nth-order model (n=0.35) was applied well to the whole temperature range and its R^2 value was higher than those of the zero- and first-order models. This fractional order kinetics with respect to N_2H_4 concentration agrees with previous observations [49,50], indicating the decomposition of $N_2H_4 \cdot H_2O$ involves several reactions with a complex mechanism which needs to be further investigated. The reported reaction orders on the decomposition of $N_2H_4 \cdot H_2O$ over $Ni_{60}Pt_{40}/CeO_2$ catalysts prepared by evaporation-induced self-assembly and co-precipitation methods were 0.41 and 0.52, respectively [49,50]. This difference of the reaction order values implies that the kinetics depends on a catalyst preparation method.

a)

b)
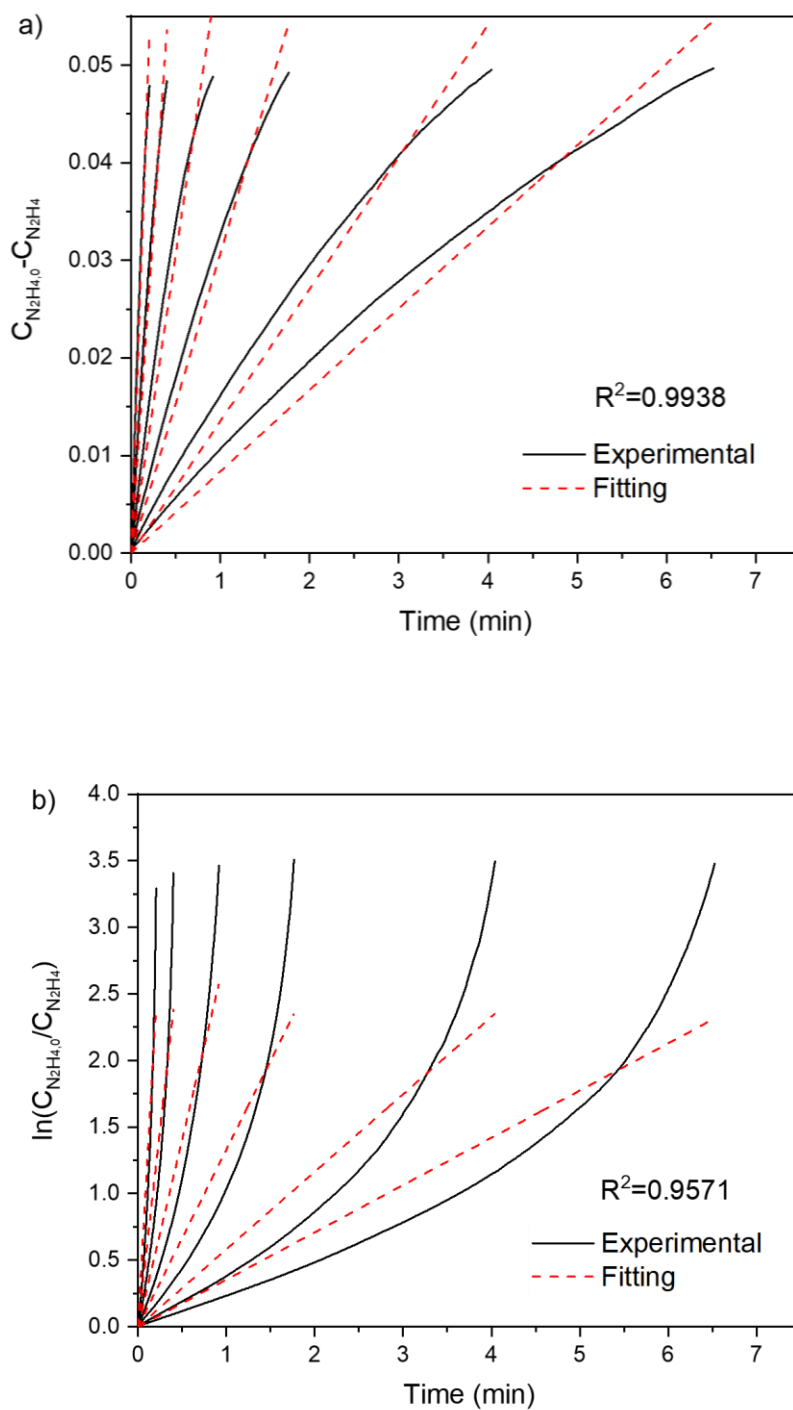
Figure 6.4 Linear regression plots based on a) zero-, b) first- and c) nth-order (n=0.35) models for decomposition of $N_2H_4 \cdot H_2O$ over $Ni_{60}Pt_{40}/CeO_2$ catalysts performed at different temperatures (25-70 °C).

Figur 6.4 continued

c)
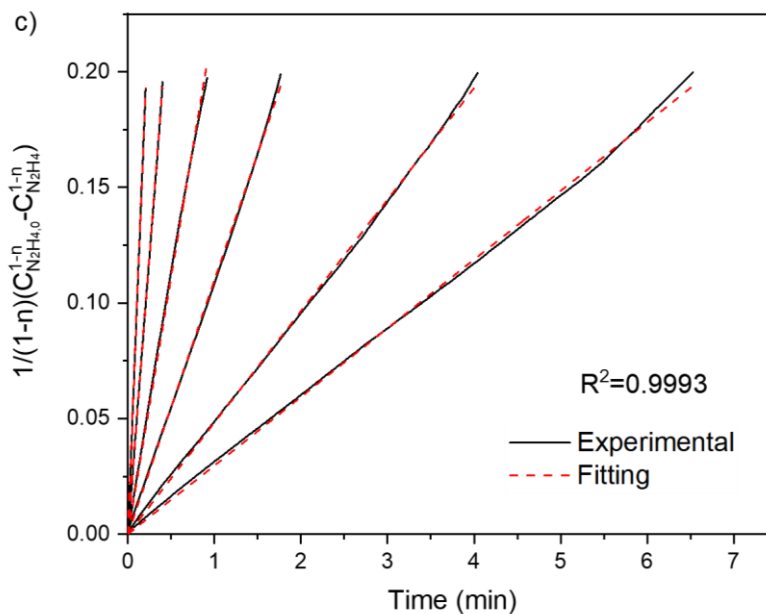
For the nth-order model, the reaction rate constant (k_n) at different temperature were determined from the slope of the linear regression curves (Figure 6.4). Using Arrhenius plot, the activation energy and pre-exponential coefficient were determined to be 65.6 kJ/mol and 1.374×10^8 $L^{0.35}mol^{0.65}g^{-1}min^{-1}$, respectively (Figure 6.5). The reported apparent activation energy values for this reaction over various catalysts are in a range of 30-70 kJ/mol [39-43,45,46,48-51,127,146,150,190,201,203]. The high activation energy value in the present work implies that the kinetics is controlled by the chemical reaction. Finally, the nth-order kinetic model was established as follows:

$$-r_{N_2H_4} = \frac{m_{cat}k_n}{V_{sol}} C_{N_2H_4}^{0.35} \qquad k_n = 1.374 \times 10^8 \exp\left(-\frac{7886.5}{T}\right) \tag{6.6}$$
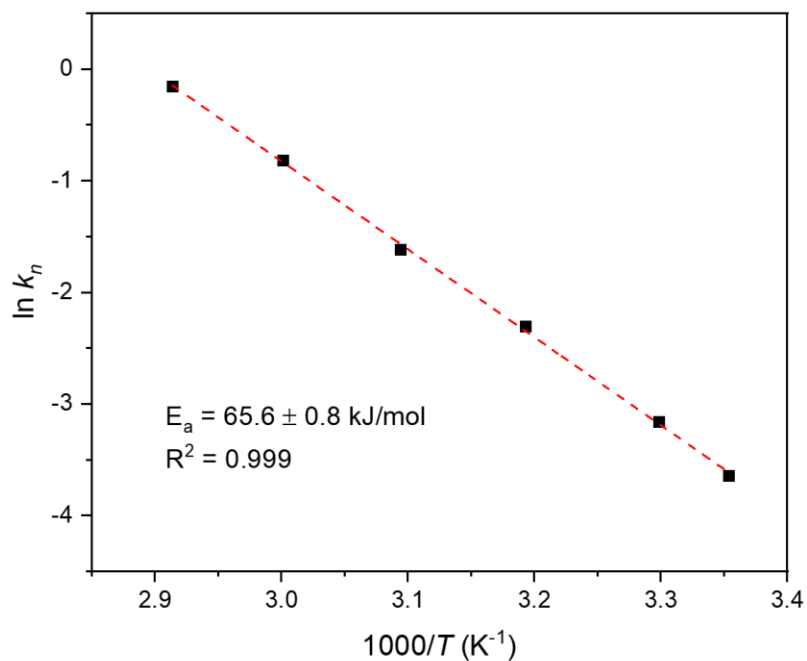
Figure 6.5 Arrhenius plot for decomposition of $N_2H_4 \cdot H_2O$ over $Ni_{60}Pt_{40}/CeO_2$ catalysts. The reaction rate constants were determined based on nth-order model (n=0.35).

The nth-order kinetic model was used to predict the N_2H_4 conversion with time. The prediction results at different reaction temperatures (25-70 °C) are presented in Figure 6.3. As expected, excellent matches were achieved between the predicted curve and the experimental data. To further validate this kinetic model, a series of reaction tests at 50 °C and n(metal)/n(N_2H_4) = 0.17 while varying the initial N_2H_4 concentrations ($C_{N_2H_{4,0}}$= 0.03-1.0 M) were conducted and the experimental data were compared to the predictions. Figure 6.6 shows that the model was found to represent the measured data without high errors when $C_{N_2H_{4,0}} \leq 0.1$M while the deviation between the predictions and the experimental results significantly increases when $C_{N_2H_{4,0}}$ increases from 0.1 M. This result suggests that the reaction order depends on $C_{N_2H_4}$.
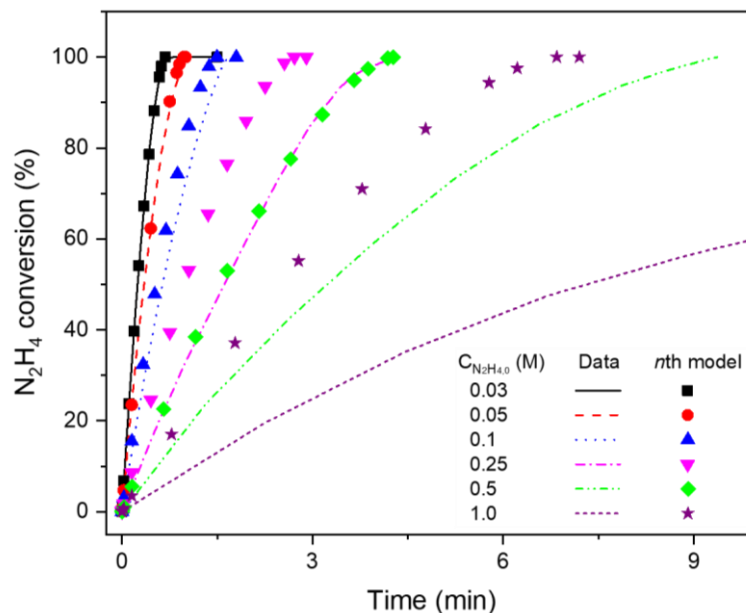
Figure 6.6 The time course plots of the decomposition of $N_2H_4 \cdot H_2O$ over $Ni_{60}Pt_{40}/CeO_2$ catalysts as a function of initial $N_2H_4 \cdot H_2O$ concentration [$T = 50 \,°C$, $n(metal)/n(N_2H_4) = 0.17$] and predictions based on nth-order model.

To gain better understanding, ln(reaction rate) versus $\ln(C_{N_2H_{4,0}})$ was plotted and presented in Figure 6.7. Graphically, the data points in Figure 6.7 can be grouped into two sets. For one set ($C_{N_2H_{4,0}} = 0.03$-0.1 M), the data points were fitted linearly with a slope of 0.354, indicating that the reaction order with respect to $C_{N_2H_4}$ is 0.354. For the other set ($C_{N_2H_{4,0}} = 0.1$-1.0 M), a slope of 0.043 was obtained after linear fitting. Near-zero value of the slope points out the zero-order kinetics with respect to $C_{N_2H_4}$. Dai et al. reported the similar result that the reaction order with respect to $C_{N_2H_4}$ is 0.52 at low $C_{N_2H_4}$ (0.1 to 0.5 M) while the order changes to 0.043 at high $C_{N_2H_4}$ (0.5 to 2.0 M) [49].
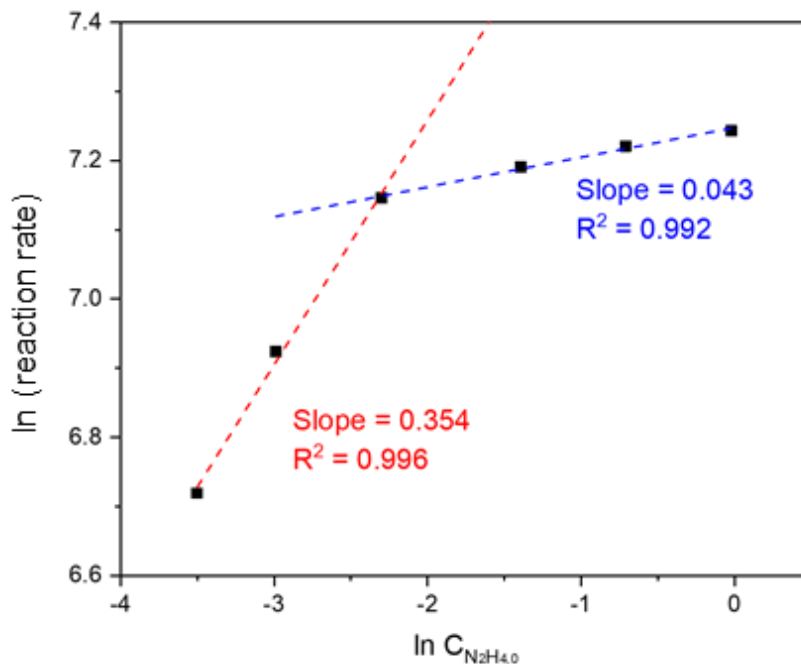
Figure 6.7 Plot of ln (reaction rate) vs. ln (initial $N_2H_4 \cdot H_2O$ concentration) to determine the reaction order with respect to $N_2H_4 \cdot H_2O$ concentration.

The recent DFT study [206] reported that H_2 generation from the decomposition of $N_2H_4 \cdot H_2O$ over Ni surface is strongly dependent upon the surface coverage by N_2H_4 and proceeds primarily through the stepwise intramolecular dehydrogenation route, as follows:

$$N_2H_4 + * \rightarrow N_2H_4 * \xrightarrow{-H} N_2H_3 \xrightarrow{-H} N_2H_2 \xrightarrow{-H} N_2H \xrightarrow{-H} N_2 \tag{6.7}$$
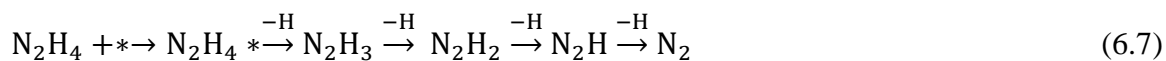
where * is an active site at catalyst surface. Accordingly, it can be inferred that the reaction is initiated by adsorption of N_2H_4 on catalyst surface and this first step plays a critical role in determining the kinetic law. In this scenario, the observed dependence of the reaction order on $C_{N_2H_4}$ can be plausibly explained. At high $C_{N_2H_4,0}$ or initial reaction stage with high $C_{N_2H_4}$, the active sites on the catalyst surface are saturated with N_2H_4 molecules and

therefore the reaction rate is independent of the $C_{N_2H_4}$, exhibiting a near-zero order kinetics. In contrast, at low $C_{N_2H_4}$ or later reaction stage, there are some unsaturated active sites on the surface and hence the fractional order kinetics dominates. Consequently, this result led us to consider the Langmuir-Hinshelwood model.

6.3.2.2 Langmuir-Hinshelwood kinetic model

The Langmuir-Hinshelwood (LH) model is commonly used to describe heterogeneous catalytic reactions (e.g. liquid phase reaction on a solid catalyst surface) [204,205,207]. Basically, the LH model assumes that reactants are adsorbed on a catalyst surface before chemical reaction occurs and hence includes the adsorption effect of reactants (e.g. N_2H_4) over the catalyst surface. This corresponds well to the reaction behavior discussed on the nth-order model study. Therefore, it was assumed that the reaction consists of two important steps: (i) equilibrated adsorption of N_2H_4 on the $Ni_{60}Pt_{40}/CeO_2$ catalyst surface and (ii) stepwise intramolecular dehydrogenation, and the reaction rate is proportional to the quantity of adsorbed N_2H_4 molecules. The surface coverage of adsorbed N_2H_4 (θ) is given by the Langmuir adsorption isotherm:

$$\theta = \frac{KC_{N_2H_4}}{1+KC_{N_2H_4}} \tag{6.8}$$

where K is the adsorption equilibrium constant. Then, for a batch reactor with a volume of reactive solution (V_{sol}) and a mass of catalyst (m_{cat}), the reaction rate per unit volume can be expressed as:

$$-r_{N_2H_4} = \frac{m_{cat}k_{LH}\theta}{V_{sol}} \tag{6.9}$$

where k_{LH} is the reaction rate constant of the LH model. Combining Eqs. (6.8) and (6.9):

$$-r_{N_2H_4} = \frac{m_{cat}k_{LH}}{V_{sol}}\frac{KC_{N_2H_4}}{1+KC_{N_2H_4}} \tag{6.10}$$

The adsorption equilibrium constant (K) can be described as [208,209]:

$$K = K'\exp\left(-\frac{\Delta H_{ads}}{RT}\right) = K_0'\exp\left(\frac{\Delta H_{ads}}{RT_0}-\frac{\Delta H_{ads}}{RT}\right) \tag{6.11}$$

where K' and K_0' are the adsorption pre-exponential factor and adsorption equilibrium constant at reference temperature. ΔH_{ads} and T_0 are enthalpy change of the adsorption process and reference temperature (25 °C), respectively. As shown in Eq. (13), the LH model can describe three situations according to the term $KC_{N_2H_4}$: (i) zero-order ($KC_{N_2H_4}\gg1$), (ii) first-order ($KC_{N_2H_4}\ll1$) and (iii) the combination of both orders. Hence, the LH model is expected to capture the variation in the reaction order by $C_{N_2H_4}$ observed for the nth-order model study.

Integrating Eq. (6.10), it becomes:

$$\frac{k_{LH}m_{cat}}{V_{sol}}t = \frac{1}{K}ln\left(\frac{C_{N_2H_{4,0}}}{C_{N_2H_4}}\right) + \left(C_{N_2H_{4,0}} - C_{N_2H_4}\right) \tag{6.12}$$

A plot of the right-hand side of Eq. (15) as a function of time should be linear through the origin. From the slope of the straight line, the reaction rate constant can be determined.

In the LH model, values of K_0' and ΔH_{ads} in Eq.(14) should be estimated first. K_0' was determined by fitting the kinetic data at 25 °C with Eq. (15). It was found to be 132 Lmol^{-1} (R^2=0.9966). Then, the following objective function was established to determine ΔH_{ads}:

$$\min f(\Delta H_{ads}) = \sum_{T=30\,°C}^{70\,°C}(1 - R_T^2) \tag{6.13}$$

It was found that when ΔH_{ads} = -6.6 kJmol^{-1} the LH model fits well the experimental data obtained at 25, 30, 40, 50, 60 and 70 °C with the highest R^2 value of 0.9979, as shown in Figure 6.8. The small and negative value of ΔH_{ads} confirmed that the adsorption process of N_2H_4 is physisorption and exothermic [210-212].

According to the adsorption thermodynamics, the adsorption pre-exponential factor (K') can be related to the entropy change (ΔS^o) , as follows[208]:

$$K' = \exp\left(-\frac{\Delta S^o}{R}\right) \tag{6.14}$$

Combining Eqs. (6.11) and (6.14), it becomes

$$\Delta S^o = R\ln K_0' + \frac{\Delta H_{ads}}{RT_0} \tag{6.15}$$

Using Eq. (6.15), ΔS^o was found to be 0.018 kJmol^{-1}K^{-1}. This positive value of ΔS^o suggests good binding affinity of N_2H_4 on the catalyst surface and an increase in randomness at the solid-liquid interface during the adsorption process. It might be attributed the OH$^-$ ions in the solution, which are known to promote the catalytic activity and selectivity by enhancing the adsorption of N_2H_4 and affecting the reaction mechanism [12]. Possibly, the OH$^-$ ions around the interface might induce the reorientation of adsorbed

N_2H_4 which is unfavorable in terms of entropy and gain more entropy than that is lost by the adsorption of N_2H_4. The effect of NaOH on the adsorption mechanism needs to be further investigated. Consequently, $\Delta H_{ads}<0$ and $\Delta S^o>0$ implies that Gibb's free energy change is always negative value and the adsorption of N_2H_4 is spontaneous.

The k_{LH} values at different temperatures (25-70 °C) was determined from the slope of the linear regression curves in Figure 6.8. Using the Arrhenius plot, the activation energy and pre-exponential coefficient were determined to be 66.4 kJ/mol and 7.132×10^7 $molg^{-1}min^{-1}$, respectively (Figure 6.9). The LH kinetic model was established as follows:

$$-r_{N_2H_4} = \frac{m_{cat}k_{LH}}{V_{sol}} \frac{KC_{N_2H_4}}{1+KC_{N_2H_4}}$$

$$k_{LH} = 7.132 \times 10^7 \exp\left(-\frac{7875.8}{T}\right), \quad K = 132\exp\left[793.8\left(\frac{1}{T}-\frac{1}{T_0}\right)\right] \tag{6.16}$$
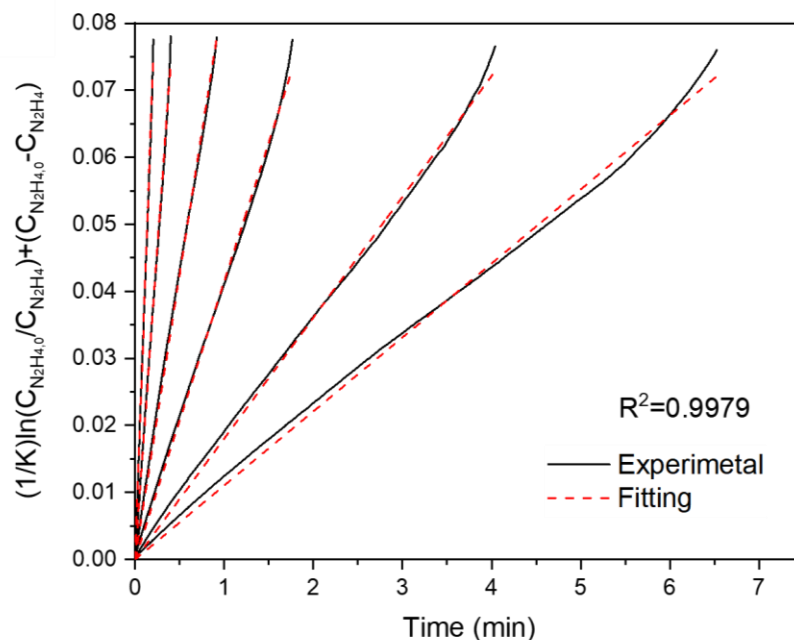
Figure 6.8 Linear regression plots based on Langmuir-Hinshelwood model for decomposition of $N_2H_4 \cdot H_2O$ over $Ni_{60}Pt_{40}/CeO_2$ catalysts performed at different temperatures (25-70 °C).
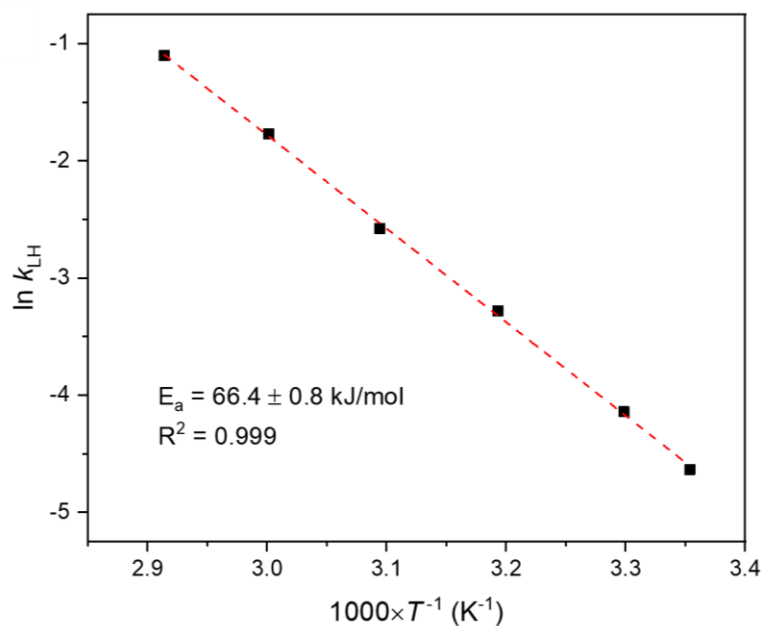
Figure 6.9 Arrhenius plot for decomposition of $N_2H_4 \cdot H_2O$ over $Ni_{60}Pt_{40}/CeO_2$ catalysts. The reaction rate constants were determined based on Langmuir-Hinshelwood model.

As shown in Figure 6.3, the predictions using the LH model are in good agreement with the experimental data obtained at different temperatures (25-70 °C). To further validate the LH kinetic model, a series of reaction tests at 50 °C and $C_{N_2H_{4,0}} = 0.05$ M while varying the catalyst loadings were performed. The catalyst loading was expressed as the molar ratio of metal (Ni+Pt) in the catalyst to initial N_2H_4 and was varied from 0.085 to 0.255. Figure 6.10a shows that the reaction rate for the decomposition of $N_2H_4 \cdot H_2O$ increases with increasing of the catalyst loading due to the increase in the total number of active catalytic sites. It can be also seen that the good agreement between experimental and predicted data. The LH model essentially represents a zero-order reaction at the very beginning stage of the reaction ($KC_{N_2H_4} \gg 1$) and the reaction rate should be proportional to m_{cat}. Figure 6.10b shows the change of $\left(C_{N_2H_{4,0}} - C_{N_2H_4}\right)$ versus reaction time in the initial reaction stage. The slopes of each curve had a ratio of 0.51:1:1.47 which agrees well with the ratio of catalyst loading used in the three experiments (0.085:0.17:0.255=0.5:1:1.5).
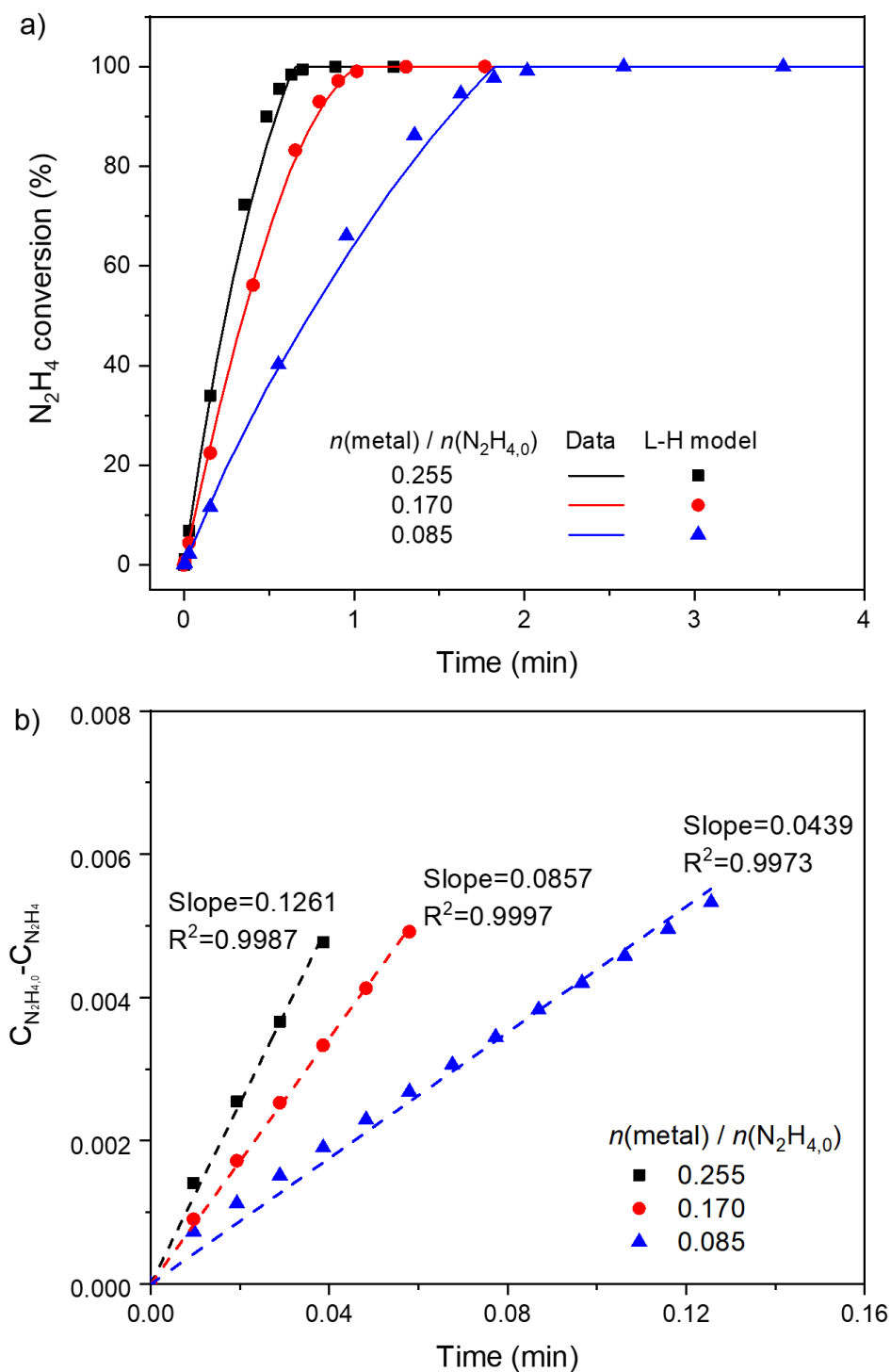
Figure 6.10 a) The time course plots and predictions based on Langmuir-Hinshelwood model for the decomposition of $N_2H_4 \cdot H_2O$ over $Ni_{60}Pt_{40}/CeO_2$ catalysts as a function of catalyst loading ($T = 50\ °C$, $C_{N_2H_{4,0}} = 0.05$ M). b) Linear regression plots based on zero-order for the initial reaction stage of each experiment.

The predictions by the LH model for the reaction behavior at the different $C_{N_2H_{4,0}}$ are depicted in Figure 6.11. As expected, the LH model exhibits better prediction accuracy than the nth-order model for the whole range of $C_{N_2H_{4,0}}$ (0.03-1.0 M). For the LH model, excellent matches between the predictions and the experimental data are shown at low $C_{N_2H_{4,0}}$ (0.03-0.1 M) while the differences exist at high $C_{N_2H_{4,0}}$ (0.25-1.0 M). Notably, for the high $C_{N_2H_{4,0}}$, the LH model well described the reaction behavior in the initial reaction stage while the prediction gradually deviated from the measured result as the reaction progresses. With increasing $C_{N_2H_{4,0}}$, the longer time is necessary for the completion of the reaction and hence the difference becomes more pronounced. As discussed later, this difference is attributed to the catalyst deactivation which is commonly reported for the catalytic decomposition of $N_2H_4 \cdot H_2O$.
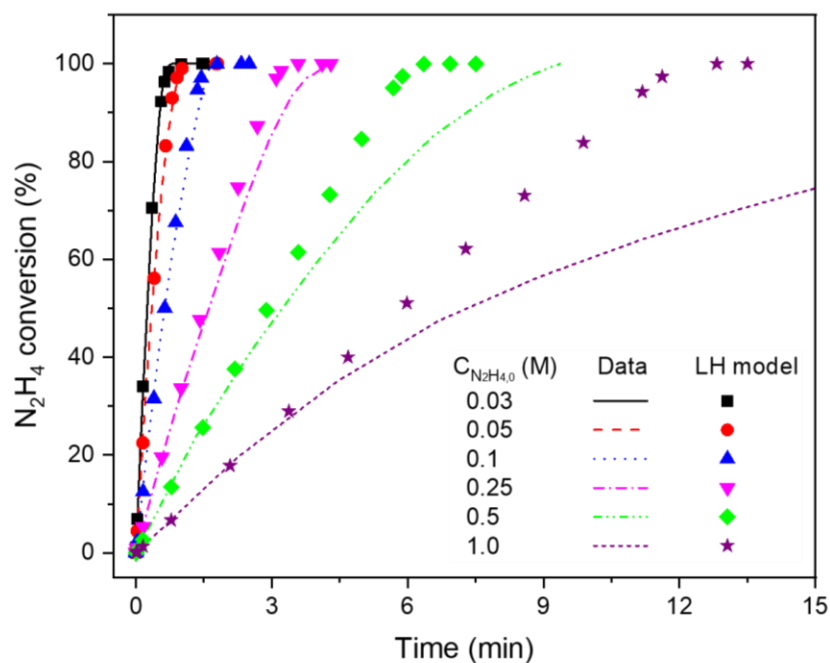
Figure 6.11 The time course plots of the decomposition of $N_2H_4 \cdot H_2O$ over $Ni_{60}Pt_{40}/CeO_2$ catalysts as a function of initial $N_2H_4 \cdot H_2O$ concentration [$T = 50$ °C, n(metal)/n(N_2H_4) = 0.17] and predictions based on LH model.

6.3.3 Catalyst deactivation

To investigate the deactivation characteristics of the $Ni_{60}Pt_{40}/CeO_2$ catalyst for the decomposition of $N_2H_4 \cdot H_2O$, the durability tests of the sample were conducted under the standard operating condition [$T = 50$ °C, $C_{N_2H_{4,0}}$ =0.05 M and n(metal)/$n(N_2H_4) = 0.17$]. Figure 6.12 shows that the catalyst exhibits a reaction rate of 1017 h^{-1} at the first cycle, but the activity continuously diminishes over repeated cycles. The activity becomes stable after 23th cycle and is only 15% of its initial value. Meanwhile, the H_2 selectivity remains unchanged at 100%. The activity degradation over cycles in Figure 6.12 is consistent with that with reaction time observed from Figure 6.11. This catalyst deactivation is ascribed to a decrease in the number of active Ni sites by the strong binding of N_2 molecules which are the by-products for the complete decomposition of $N_2H_4 \cdot H_2O$ [162,213]. It was reported that the degradation degree of the $Ni_{60}Pt_{40}/CeO_2$ catalyst for the decomposition of $N_2H_4 \cdot H_2O$ is linearly correlated to the amount of molecular N_2 bound at Ni sites [162]. Figure 6.12 also shows that the activity is almost recovered after the catalyst regeneration according to the protocol described in Chapter 6.2.2. This confirms that the catalyst deactivation is reversible and is not attributed to the structural change of the catalyst surface. This is consistent with a previous study that most of the bound N_2 molecules at the surface of $Ni_{60}Pt_{40}/CeO_2$ catalyst is eliminated by heat treatment over 200 °C [162].
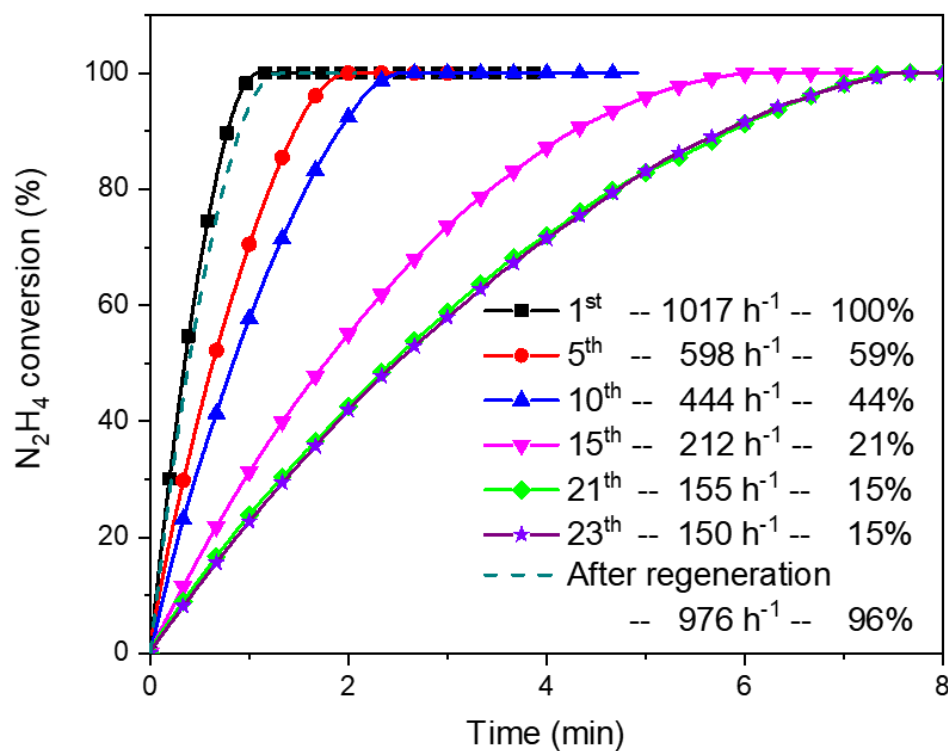
Figure 6.12 The time course plots for the decomposition of $N_2H_4 \cdot H_2O$ over $Ni_{60}Pt_{40}/CeO_2$ catalysts as a function of the number of reaction cycles and after regeneration [$T = 50$ °C, $C_{N_2H_{4,0}} = 0.05$ M, $n(\text{metal})/n(N_2H_4) = 0.17$].

6.3.4 Kinetic model involving catalyst deactivation

The kinetic model considering the catalyst deactivation can be formulated in terms of relative catalyst activity, a, which is defined as the ratio of the reaction rate involving deactivation ($-r'_{N_2H_4}$) to the maximal reaction rate without deactivation ($-r_{N_2H_4}$) [214]:

$$a = \frac{-r'_{N_2H_4}}{-r_{N_2H_4}} \tag{6.17}$$

The type of deactivation observed in our reaction system corresponds to series deactivation in which a product acts as a poison for catalysts. In this case, the deactivation rate equation can be generally expressed as follows [214]:

$$-\frac{da}{dt} = k_d C_{N_2}^m a^d \ (C_{N_2} = 0 \ and \ a = 1 \ at \ t = 0) \tag{6.18}$$

where k_d, m and d are the deactivation rate constant and the reaction order with respect to N_2 concentration for the catalyst deactivation and the order of deactivation, respectively. Combining Eqs. (6.16-18), the kinetic model involving the catalyst deactivation was developed. The following objective function, which is to find the minimum sum of squares of the errors, was used to estimate the deactivation parameters for Eq. (6.18):

$$\min (k_d, m, \ d) = \sum_{i=1}^{N} \left(X_{i,\text{obs}} - X_{i,\text{cal}} \right)^2 \tag{6.19}$$

where $X_{i,\text{obs}}$ is the ith observed value of N_2H_4 conversion, $X_{i,\text{cal}}$ is the corresponding value calculated from the kinetic model, and N is the total number of data points. The experimental data obtained at different $C_{N_2H_{4,0}}$ were used for parameter estimation (Figure 6.11).

The deactivation parameters (k_d, m and d) of the best fitting were 0.085, 0.019 and 1.13, respectively. It was confirmed that the estimated values are not varied with their initial values. The near-zero value of m indicates that deactivation is nearly independent of N_2 concentration. The d value is nearly equal to unity, implying that one active site is

involved in the controlling step of the catalyst deactivation mechanism [215]. Figure 6.13 indicates that there is a good agreement between experimental data and the calculation results obtained from the LH kinetic model involving the catalyst deactivation.
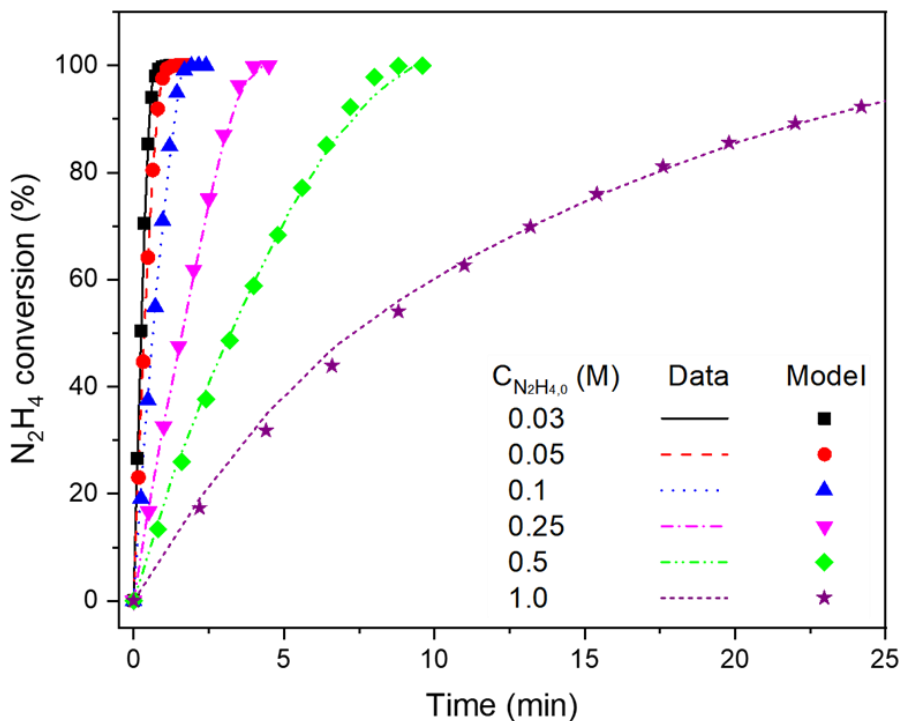
Figure 6.13 Comparison of experimental results at different $C_{N_2H_{4,0}}$ and predictions using the Langmuir-Hinshelwood model involving catalyst deactivation.

6.4   Conclusions

In this chapter, $Ni_{60}Pt_{40}/CeO_2$ catalyst was prepared using two-step solution combustion synthesis, to be used for hydrogen generation from hydrous hydrazine which is a promising hydrogen carrier for fuel cell electric vehicles (FCEVs). The effects of reaction temperature, catalyst loading, and initial reactant concentration were investigated in a stirred batch reactor with the absence of mass transfer limitations to determine a kinetic model. The power-law model and the Langmuir-Hinshelwood (LH) model were used to

correlate the experimental data. The LH model provides a good agreement with the experimental results, especially at a wide range of initial reactant concentration, describing well the variation of reaction order from low to high reactant concentration. Furthermore, the deactivation kinetic model was determined from the durability and recyclability of the $Ni_{60}Pt_{40}/CeO_2$. The LH model coupled with the deactivation kinetics exhibits an excellent correlation with the experimental data by capturing the decay of catalytic activity with time. This kinetic model can contribute to develop a protocol for the design of an on-board hydrogen generator for FCEVs.

CHAPTER 7.   CONCLUSIONS AND RECOMMENDATIONS

7.1   Summary

In this dissertation, in order to develop active, selective and cost-effective catalysts for hydrogen generation from hydrous hydrazine which is a promising hydrogen carrier for fuel cell electric vehicles (FCEVs), CeO_2 and various Ni-based catalysts were prepared using solution combustion synthesis (SCS) technique and investigated. Remarkably, the synthesized materials show promising physical properties and catalytic performance as compared to those reported in the literature along with the advantage of facile preparation method. Specifically, the main conclusions of each chapter are as follows.

In Chapter 2, CeO_2 powders which have been widely used for various catalytic reactions and are as promising catalyst support for hydrous hydrazine decomposition, were synthesized using SCS. Based on SCS experiments and characterization of SCS precursors and products, the combustion reaction mechanism for the formation of CeO_2 was identified for the first time. It turned out that the combustion mechanism depends strongly on fuel type (e.g. hydrous hydrazine and glycine). It was also confirmed that the physical properties such as crystallite size, surface area and defect concentration can be tailored by adjusting the synthesis parameters. Notably, the use of hydrous hydrazine fuel, fuel-to-oxidizer ratio of 2 and ammonium nitrate/metal nitrate ratio of 4 yielded the CeO_2 nanopowder with the highest surface area ($88 \ m^2/g$), which is the highest value among all SCS-derived CeO_2 powders reported in the literature. This work demonstrated that understanding the influence of synthesis parameters on combustion characteristics, and

their correlation with product properties, can enable one to effectively control the combustion process and to tailor nanomaterials for specific applications.

In Chapter 3, for the first time, SCS was used to prepare Ni/CeO_2 nanopowders as model catalysts for hydrogen generation from hydrous hydrazine. Similar to Chapter 2, by varying the synthesis parameters, the correlation between combustion characteristics, physicochemical and catalytic properties was investigated. It revealed that Ni particle size, pore structure, and concentration of defects in CeO_2 structure, which are closely related to the catalytic performance, depend strongly on the combustion features. It was also found that the defect structure was mainly generated by the formation of Ni-O-Ce solid solution. The use of hydrous hydrazine fuel, fuel-to-oxidizer ratio of 2 and 6wt% Ni loading produced the Ni/CeO_2 catalyst with small Ni particle size (14.7 nm), large pore size (18.8 nm) and moderate defect concentration. This sample exhibited 100% selectivity to hydrogen generation in the temperature range 40–70 ºC and the highest activity among all catalysts tested in this study and all catalysts containing Ni alone reported in the literature. This superior catalytic performance may be attributed to the relatively higher defect concentration and larger pore size. These features are essentially related to the exothermic nature of combustion process along with vigorous gas evolution. This work demonstrated that SCS is an effective method to prepare catalysts for hydrogen generation from hydrous hydrazine decomposition.

In Chapter 4, in order to develop cost-effective and more efficient noble-metal-free catalysts, CeO_2 supported Ni-Cu, Ni-Fe and Ni-Co bimetallic catalysts were synthesized using SCS. The testing of the noble-metal-free catalysts showed that addition of Cu to Ni/CeO_2 produces synergistic effect to significantly enhance the activity. The

characterization results revealed that, when adding Cu into Ni/CeO$_2$, the concentration of defects in CeO$_2$ structure, which act as a catalytic promoter for hydrous hydrazine decomposition, increases substantially due to strong interaction between Ni, Cu and CeO$_2$. The tailored Ni$_{0.5}$Cu$_{0.5}$/CeO$_2$ catalyst exhibited 100% H$_2$ selectivity in the temperature range 30-70 °C and 5.4-fold faster reaction rate at 50 °C than that of the monometallic Ni/CeO$_2$ catalyst. This activity is superior to that of most reported non-noble metal catalysts and is even comparable to several noble metal-based catalysts. This work indicated that the catalytic performance can be improved through a proper selection of secondary metal and catalyst preparation method. In addition, the synergistic effect found in this study may have significance in designing CeO$_2$ supported catalysts for other applications.

In Chapter 5, NiPt/CeO$_2$ catalysts with low Pt loading for hydrous hydrazine decomposition were successfully synthesized using a modified SCS technique. This modified SCS method was able to overcome the typical problem of conventional SCS which essentially leads to a deficiency of Pt at catalyst surface due to the diffusion of Pt into bulk CeO$_2$. The low metal loadings (0.4 wt% Ni and 1 wt% Pt) with the optimum composition significantly increased the number of active sites and enhanced the interaction between Ni and CeO$_2$. As a result, the developed 0.4Ni-1Pt(60:40)/CeO$_2$ catalyst exhibited 100% H$_2$ selectivity in the temperature range 30-70 °C and high activity (1017 h^{-1}) for the reaction. More importantly, even though this catalyst contains only 1wt% Pt loading, its activity was higher than most of the reported NiPt-based catalysts which typically contain high Pt loading (3.6-42 wt%) along with the advantage of facile preparation method. This efficient and cost-effective catalyst may open up a new avenue for practical application of

hydrous hydrazine as an on-board hydrogen carrier. Furthermore, the modified SCS technique developed in this study may be a good strategy to produce various Pt-based catalysts for other applications.

In Chapter 6, intrinsic reaction kinetics for hydrous hydrazine decomposition over $Ni_{60}Pt_{40}/CeO_2$ catalyst developed in Chapter 5 were investigated. Based on prior literature reports, a simple Langmuir-Hinshelwood (LH) kinetic model with the assumption that the reaction rate is proportional to the amount of adsorbed N_2H_4 molecules was established for the first time. By fitting the kinetic data, reasonable values of the parameters in the LH model were obtained. The LH model provided good predictions with the experimental results, especially over a wide range of initial reactant concentrations, describing well the variation of reaction order from low to high reactant concentration. Moreover, based on catalyst durability test results, the LH model coupled with deactivation kinetics was developed and exhibited an excellent comparison with the experimental data. This LH kinetic model may contribute to the effective design for an on-board hydrogen generator of hydrous hydrazine-based FCEVs.

7.2   Recommendations for future work

7.2.1   Advanced catalysts for hydrous hydrazine decomposition

The study of $NiPt/CeO_2$ catalysts described in Chapter 5 and 6 exhibited that the catalytic activity is significantly enhanced by the addition of Pt in Ni/CeO_2. This catalyst, however, also showed significant catalyst deactivation with time. Considering that the $NiCu/CeO_2$ catalyst is more durable than $NiPt/CeO_2$, the improved activity may be achieved at the cost of catalyst durability. Likewise, the reported NiPt-based catalysts

always showed poor durability [39-45,48,49,127]. To practically utilize hydrous hydrazine as a hydrogen carrier, it is necessary to improve the durability of catalysts. In this regard, advanced synthesis techniques and novel methodologies which enable to fine-tune the properties of active sites of catalyst surface are needed to pursue an optimal compromise between activity and durability. Meanwhile, the catalyst deactivation for hydrous hydrazine decomposition is reversible and the used catalysts can be regenerated by heat treatment as shown in Chapter 6. Therefore, the catalyst durability problem can be technically solved by alternating the hydrogen generation and catalyst regeneration processes by connecting and disconnecting the feeding hydrous hydrazine in a multiple reactor system. For example, one reactor is used for hydrogen generation from the catalytic decomposition of hydrous hydrazine, while another reactor undergoes catalyst regeneration by heat treatment. In this case, the studies for process design and optimization are required to maximize hydrogen productivity.

Another challenge in hydrous hydrazine decomposition is the use of alkaline solution (e.g., NaOH) as a reaction medium for high catalytic activity and selectivity. This leads to a difficulty in both equipment and operation requirements [216,217]. Therefore, it is recommended for practical application to develop catalysts which possess excellent catalytic performance under non-alkaline conditions. Since a solid base has a similar role to that of alkaline solution [126,152,153], materials which have a large number of basic sites need to be explored and can be utilized as a catalyst support.

7.2.2 Continuous hydrogen generators based on hydrous hydrazine decomposition

The study of the catalytic decomposition of hydrous hydrazine for hydrogen generation is still in the early stage and has been focused on the development of efficient

catalysts. For this reason, most prior works as well as the present work have focused on the simple batch reactor system. Although there are a few studies on the continuous semi-batch system of hydrous hydrazine decomposition [48,218], a semi-batch system has the inevitable problem that the catalytic activity decreases as the reaction cycle is repeated because the solution in a semi-batch reactor is diluted with cycle due to the residual product water from hydrous hydrazine which contains significant amount of water, 36 wt%. Therefore, other reactor types should be investigated for continuous hydrogen generator based on hydrous hydrazine. A continuous flow system based on packed bed reactor may be suitable for practical hydrous hydrazine-based H_2 on-board vehicles, so that hydrogen can be produced on demand, rather than produced and stored as in a batch system.

7.2.3 Selective separation of hydrogen and nitrogen

The decomposition of a hydrazine molecule with 100% selectivity produces one nitrogen and two hydrogen molecules, resulting in the dilution of hydrogen with nitrogen. Zhao B. *et al.* investigated the diluting effect of nitrogen from the decomposition of hydrazine on the performance of PEMFC [219]. They showed that the peak power density by applying the product gas from hydrous hydrazine decomposition with 100% selectivity is ~83% of that by using pure hydrogen gas as the fuel. Typically, in a practical PEMFC system of FCEVs, the excess hydrogen gas discharged from the fuel cell is recirculated and merged with the fresh hydrogen gas to minimize waste and to obtain maximum efficiency. This implies that if the product gas from hydrous hydrazine decomposition is applied directly to PEMFC as a fuel, the concentration of nitrogen in the fuel stream would increase rapidly due to the recirculation and thus the PEMFC performance would decrease quickly. In this regard, the process for selective separation of hydrogen and nitrogen is required.

Typically, for hydrogen separation, pressure swing adsorption, cryogenic separation and membrane separation have been applied to industrial processes. Membrane separation technique is promising due to ease of operation, compactness and low energy consumption [220]. Owing to the quite different molecular size of hydrogen and nitrogen, molecular-sieve membranes may be effective to obtain high purity hydrogen gas [221].

REFERENCES

[1] Cano, Z. P., Banham, D., Ye, S. Y., Hintennach, A., Lu, J., Fowler, M.and Chen, Z. W. (2018). Batteries and Fuel Cells for Emerging Electric Vehicle Markets. *Nature Energy, 3*, 279-289.

[2] Gearhart, C. (2018). Hydrogen: What's Different Now. *IEEE Electrification Magazine, 6*, 4-7.

[3] Melaina, M. W., Bush, B. W., Muratori, M., Zuboy, J.and Ellis, S. (2018). *National Hydrogen Scenarios: How Many Stations, Where, and When?*. Retrieved from https://www.osti.gov/servlets/purl/1461868

[4] Alternative Fuels Data Center, U.S. DOE (2019). Fuel Properties Comparison. Retrieved from https://afdc.energy.gov/fuels/properties

[5] Schmidt, E. W. (2001). *Hydrazine and its Derivatives : Preparation, Properties, Applications* 2nd ed.). New York: Wiley.

[6] Lamb, K. E., Dolan, M. D.and Kennedy, D. F. (2019). Ammonia for Hydrogen Storage; A Review of Catalytic Ammonia Decomposition and Hydrogen Separation and Purification. *International Journal of Hydrogen Energy, 44*, 3580-3593.

[7] Office of Energy Efficiency & Renewable Energy, U.S. DOE (2019). DOE Technical Targets for Onboard Hydrogen Storage for Light-Duty Vehicles. Retrieved from https://www.energy.gov/eere/fuelcells/doe-technical-targets-onboard-hydrogen-storage-light-duty-vehicles

[8] Elgowiny, A., U.S. DOE (2018). Techno-Economic Tools to Simulate the Costs of Hydrogen Infrastructure Technologies. Retrieved from https://www.energy.gov/eere/fuelcells/downloads/techno-economic-tools-simulate-costs-hydrogen-infrastructure-technologies

[9] He, T., Pachfule, P., Wu, H., Xu, Q.and Chen, P. (2016). Hydrogen Carriers. *Nature Reviews Materials, 1*, 1-17.

[10] Hwang, H. T.and Varma, A. (2014). Hydrogen Storage for Fuel Cell Vehicles. *Current Opinion in Chemical Engineering, 5*, 42-48.

[11] Preuster, P., Papp, C.and Wasserscheid, P. (2017). Liquid Organic Hydrogen Carriers (LOHCs): Toward a Hydrogen -free Hydrogen Economy. *Accounts of Chemical Research, 50*, 74-85.

[12] Zhu, Q.-L.and Xu, Q. (2015). Liquid Organic and Inorganic Chemical Hydrides for High-capacity Hydrogen Storage. *Energy & Environmental Science, 8*, 478-512.

[13]   Dean, D., Davis, B.and Jessop, P. G. (2011). The Effect of Temperature, Catalyst and Sterics on the Rate of N-heterocycle Dehydrogenation for Hydrogen Storage. *New Journal of Chemistry, 35*, 417-422.

[14]   Dong, Y., Yang, M., Yang, Z., Ke, H. Z.and Cheng, H. S. (2015). Catalytic Hydrogenation and Dehydrogenation of N-ethylindole as a New Heteroaromatic Liquid Organic Hydrogen Carrier. *International Journal of Hydrogen Energy, 40*, 10918-10922.

[15]   Bruckner, N., Obesser, K., Bosmann, A., Teichmann, D., Arlt, W., Dungs, J.and Wasserscheid, P. (2014). Evaluation of Industrially Applied Heat-Transfer Fluids as Liquid Organic Hydrogen Carrier Systems. *Chemsuschem, 7*, 229-235.

[16]   Yamaguchi, R., Ikeda, C., Takahashi, Y.and Fujita, K. (2009). Homogeneous Catalytic System for Reversible Dehydrogenation-Hydrogenation Reactions of Nitrogen Heterocycles with Reversible Interconversion of Catalytic Species. *Journal of the American Chemical Society, 131*, 8410-8412.

[17]   Hu, P., Fogler, E., Diskin-Posner, Y., Iron, M. A.and Milstein, D. (2015). A Novel Liquid Organic Hydrogen Carrier System based on Catalytic Peptide Formation and Hydrogenation. *Nature Communications, 6*, 6859.

[18]   Song, F. Z., Zhu, Q. L., Tsumori, N.and Xu, Q. (2015). Diamine-akalized Reduced Graphene Oxide: Immobilization of Sub-2 nm Palladium Nanoparticles and Optimization of Catalytic Activity for Dehydrogenation of Formic Acid. *Acs Catalysis, 5*, 5141-5144.

[19]   Song, F. Z., Zhu, Q. L.and Xu, Q. (2015). Monodispersed PtNi Nanoparticles Deposited on Diamine-alkalized Graphene for Highly Efficient Dehydrogenation of Hydrous Hydrazine at Room Temperature. *Journal of Materials Chemistry A, 3*, 23090-23094.

[20]   Steele, B. C. H.and Heinzel, A. (2001). Materials for Fuel-cell Technologies. *Nature, 414*, 345-352.

[21]   Halseid, R., Vie, P. J. S.and Tunold, R. (2006). Effect of Ammonia on the Performance of Polymer Electrolyte Membrane Fuel Cells. *Journal of Power Sources, 154*, 343-350.

[22]   Cheng, X., Shi, Z., Glass, N., Zhang, L., Zhang, J. J., Song, D. T., Liu, Z. S., Wang, H. J.and Shen, J. (2007). A Review of PEM Hydrogen Fuel Cell Contamination: Impacts, Mechanisms, and Mitigation. *Journal of Power Sources, 165*, 739-756.

[23]   Varma, A., Rogachev, A. S., Mukasyan, A. S.and Hwang, S. (1998). Combustion Synthesis of Advanced Materials: Principles and Applications. In J. Wei (Ed.), *Advances in Chemical Engineering* (Vol. 24, pp. 79-226): Academic Press.

[24]   Varma, A., Mukasyan, A. S., Rogachev, A. S.and Manukyan, K. V. (2016). Solution Combustion Synthesis of Nanoscale Materials. *Chemical Reviews, 116*, 14493-14586.

[25]   Deshpande, K., Mukasyan, A.and Varma, A. (2004). Direct Synthesis of Iron Oxide Nanopowders by the Combustion Approach: Reaction Mechanism and Properties. *Chemistry of Materials, 16*, 4896-4904.

[26]   Erri, P., Pranda, P.and Varma, A. (2004). Oxidizer-Fuel Interactions in Aqueous Combustion Synthesis. 1. Iron(III) Nitrate-Model Fuels. *Industrial & Engineering Chemistry Research, 43*, 3092-3096.

[27]   Dinka, P.and Mukasyan, A. S. (2005). In Situ Preparation of Oxide-based Supported Catalysts by Solution Combustion Synthesis. *Journal of Physical Chemistry B, 109*, 21627-21633.

[28]   Montini, T., Melchionna, M., Monai, M.and Fornasiero, P. (2016). Fundamentals and Catalytic Applications of CeO_2-Based Materials. *Chemical Reviews, 116*, 5987-6041.

[29]   Singh, S. K.and Xu, Q. (2013). Nanocatalysts for Hydrogen Generation from Hydrazine. *Catalysis Science & Technology, 3*, 1889-1900.

[30]   Singh, S. K., Zhang, X. B.and Xu, Q. (2009). Room-Temperature Hydrogen Generation from Hydrous Hydrazine for Chemical Hydrogen Storage. *Journal of the American Chemical Society, 131*, 9894-9895.

[31]   Singh, S. K.and Xu, Q. (2009). Complete Conversion of Hydrous Hydrazine to Hydrogen at Room Temperature for Chemical Hydrogen Storage. *Journal of the American Chemical Society, 131*, 18032-18033.

[32]   Singh, S. K.and Xu, Q. A. (2010). Bimetallic Nickel-Iridium Nanocatalysts for Hydrogen Generation by Decomposition of Hydrous Hydrazine. *Chemical Communications, 46*, 6545-6547.

[33]   Singh, S. K., Singh, A. K., Aranishi, K.and Xu, Q. (2011). Noble-Metal-Free Bimetallic Nanoparticle-Catalyzed Selective Hydrogen Generation from Hydrous Hydrazine for Chemical Hydrogen Storage. *Journal of the American Chemical Society, 133*, 19638-19641.

[34]   Singh, S. K., Iizuka, Y.and Xu, Q. (2011). Nickel-Palladium Nanoparticle Catalyzed Hydrogen Generation from Hydrous Hydrazine for Chemical Hydrogen Storage. *International Journal of Hydrogen Energy, 36*, 11794-11801.

[35]   Hannauer, J., Akdim, O., Demirci, U. B., Geantet, C., Herrmann, J. M., Miele, P.and Xu, Q. (2011). High-extent Dehydrogenation of Hydrazine Borane $N_2H_4BH_3$ by Hydrolysis of BH_3 and Decomposition of N_2H_4. *Energy & Environmental Science, 4*, 3355-3358.

[36]   Wang, J., Zhang, X. B., Wang, Z. L., Wang, L. M.and Zhang, Y. (2012). Rhodium-Nickel Nanoparticles Grown on Graphene as Highly Efficient Catalyst for Complete Decomposition of Hydrous Hydrazine at Room Temperature for Chemical Hydrogen Storage. *Energy & Environmental Science, 5*, 6885-6888.

[37]   He, L., Huang, Y. Q., Wang, A. Q., Wang, X. D., Chen, X. W., Delgado, J. J.and Zhang, T. (2012). A Noble-Metal-Free Catalyst Derived from Ni-Al Hydrotalcite for Hydrogen Generation from $N_2H_4 \cdot H_2O$ Decomposition. *Angewandte Chemie-International Edition, 51*, 6191-6194.

[38]   Wang, H.-L., Yan, J.-M., Wang, Z.-L., O, S.-I.and Jiang, Q. (2013). Highly Efficient Hydrogen Generation from Hydrous Hydrazine over Amorphous $Ni_{0.9}Pt_{0.1}/Ce_2O_3$ Nanocatalyst at Room Temperature. *Journal of Materials Chemistry A, 1*, 14957-14962.

[39]   Kumar, A., Yang, X. C.and Xu, Q. (2019). Ultrafine Bimetallic Pt-Ni Nanoparticles Immobilized on 3-Dimensional N-doped Graphene Networks: A Highly Efficient Catalyst for Dehydrogenation of Hydrous Hydrazine. *Journal of Materials Chemistry A, 7*, 112-115.

[40]   Du, X. Q., Liu, C., Du, C., Cai, P., Cheng, G. Z.and Luo, W. (2017). Nitrogen-doped Graphene Hydrogel-supported $NiPt-CeO_x$ Nanocomposites and Their Superior Catalysis for Hydrogen Generation from Hydrazine at Room Temperature. *Nano Research, 10*, 2856-2865.

[41]   Zhang, Z. J., Zhang, S. L., Yao, Q. L., Chen, X. S.and Lu, Z. H. (2017). Controlled Synthesis of MOF-Encapsulated NiPt Nanoparticles toward Efficient and Complete Hydrogen Evolution from Hydrazine Borane and Hydrazine. *Inorganic Chemistry, 56*, 11938-11945.

[42]   Xu, L. X., Liu, N., Hong, B., Cui, P., Cheng, D. G., Chen, F. Q., An, Y.and Wan, C. (2016). Nickel-Platinum Nanoparticles Immobilized on Graphitic Carbon Nitride as Highly Efficient Catalyst for Hydrogen Release from Hydrous Hydrazine. *Rsc Advances, 6*, 31687-31691.

[43]   Zhong, Y.-J., Dai, H.-B., Jiang, Y.-Y., Chen, D.-M., Zhu, M., Sun, L.-X.and Wang, P. (2015). Highly Efficient $Ni@Ni–Pt/La_2O_3$ Catalyst for Hydrogen Generation from Hydrous Hydrazine Decomposition: Effect of Ni–Pt Surface Alloying. *Journal of Power Sources, 300*, 294-300.

[44]   Xia, B. Q., Liu, T., Luo, W.and Cheng, G. Z. (2016). $NiPt-MnO_x$ Supported on N-doped Porous Carbon Derived from Metal-Organic Frameworks for Highly Efficient Hydrogen Generation from Hydrazine. *Journal of Materials Chemistry A, 4*, 5616-5622.

[45]   Jiang, Y., Kang, Q., Zhang, J., Dai, H.-B.and Wang, P. (2015). High-performance Nickel–Platinum Nanocatalyst Supported on Mesoporous Alumina for Hydrogen Generation from Hydrous Hydrazine. *Journal of Power Sources, 273*, 554-560.

[46]   He, L., Liang, B. L., Li, L., Yang, X. F., Huang, Y. Q., Wang, A. Q., Wang, X. D.and Zhang, T. (2015). Cerium-Oxide-Modified Nickel as a Non-Noble Metal Catalyst for Selective Decomposition of Hydrous Hydrazine to Hydrogen. *Acs Catalysis, 5*, 1623-1628.

[47]   Singh, A. K.and Xu, Q. (2013). Metal-Organic Framework Supported Bimetallic Ni-Pt Nanoparticles as High-performance Catalysts for Hydrogen Generation from Hydrazine in Aqueous Solution. *ChemCatChem, 5*, 3000-3004.

[48]   Zhong, Y.-J., Dai, H.-B., Zhu, M.and Wang, P. (2016). Catalytic Decomposition of Hydrous Hydrazine over $NiPt/LaZ_2O_3$ catalyst: A High-Performance Hydrogen Storage System. *International Journal of Hydrogen Energy, 41*, 11042-11049.

[49]   Dai, H., Dai, H. B., Zhong, Y. J., Kang, Q., Sun, L. X.and Wang, P. (2017). Kinetics of Catalytic Decomposition of Hydrous Hydrazine over CeO_2-supported Bimetallic Ni-Pt Nanocatalysts. *International Journal of Hydrogen Energy, 42*, 5684-5693.

[50]   Jiang, Y.-Y., Dai, H.-B., Zhong, Y.-J., Chen, D.-M.and Wang, P. (2015). Complete and Rapid Conversion of Hydrazine Monohydrate to Hydrogen over Supported Ni–Pt Nanoparticles on Mesoporous Ceria for Chemical Hydrogen Storage. *Chemistry – A European Journal, 21*, 15439-15445.

[51]   Dai, H., Qiu, Y.-P., Dai, H.-B.and Wang, P. (2018). Ni–Pt/CeO_2 Loaded on Granular Activated Carbon: An Efficient Monolithic Catalyst for Controlled Hydrogen Generation from Hydrous Hydrazine. *Acs Sustainable Chemistry & Engineering, 6*, 9876-9882.

[52]   Al-Yassir, N.and Le Van Mao, R. (2007). Catalysts for the Thermo-Catalytic Cracking (TCC) Process: Interactions between the Yttria in Yttria-doped Alumina Aerogel and the Mono-oxide MoO_3, CeO_2, and bi-oxide MoO_3-CeO_2 species. *Applied Catalysis a-General, 332*, 273-288.

[53]   Park, S. D., Vohs, J. M.and Gorte, R. J. (2000). Direct Oxidation of Hydrocarbons in a Solid-Oxide Fuel Cell. *Nature, 404*, 265-267.

[54]   Mei, D., Deskins, N. A., Dupuis, M.and Ge, Q. F. (2008). Density Functional Theory Study of Methanol Decomposition on the CeO_2(110) Surface. *Journal of Physical Chemistry C, 112*, 4257-4266.

[55]   Fu, Q., Saltsburg, H.and Flytzani-Stephanopoulos, M. (2003). Active Nonmetallic Au and Pt Species on Ceria-based Water-Gas Shift Catalysts. *Science, 301*, 935-938.

[56]   Kaspar, J., Fornasiero, P.and Graziani, M. (1999). Use of CeO_2-based Oxides in the Three-way Catalysis. *Catalysis Today, 50*, 285-298.

[57]   Lan, L., Li, H. M., Chen, S. H.and Chen, Y. Q. (2017). Preparation of CeO_2-ZrO_2-Al_2O_3 Composite with Layered Structure for Improved Pd-only Three-way Catalyst. *Journal of Materials Science, 52*, 9615-9629.

[58]   Atkinson, A., Barnett, S., Gorte, R. J., Irvine, J. T. S., Mcevoy, A. J., Mogensen, M., Singhal, S. C.and Vohs, J. (2004). Advanced Anodes for High-Temperature Fuel Cells. *Nature Materials, 3*, 17-27.

[59]   Fu, X. Q., Wang, C., Yu, H. C., Wang, Y. G.and Wang, T. H. (2007). Fast Humidity Sensors Based on CeO_2 Nanowires. *Nanotechnology, 18*, 145503.

[60]   Kosynkin, V. D., Arzgatkina, A. A., Ivanov, E. N., Chtoutsa, M. G., Grabko, A. I., Kardapolov, A. V.and Sysina, N. A. (2000). The Study of Process Production of Polishing Powder based on Cerium Dioxide. *Journal of Alloys and Compounds, 303–304*, 421-425.

[61]   Corma, A., Atienzar, P., Garcia, H.and Chane-Ching, J. Y. (2004). Hierarchically Mesostructured doped CeO_2 with Potential for Solar-Cell Use. *Nature Materials, 3*, 394-397.

[62]   Sun, C. W., Li, H.and Chen, L. Q. (2012). Nanostructured Ceria-based Materials: Synthesis, Properties, and Applications. *Energy & Environmental Science, 5*, 8475-8505.

[63]   Trovarelli, A. (2013). *Catalysis by Ceria and Related Materials, 2nd Edition*   Vol. 12). London: Imperial College Press.

[64]   Chowdhury, S., Yasir, M., Bustam, M. A. B.and Lin, K.-S. (2013). Hydrothermal Synthesis and Characterization of One-dimensional Ceria Nanorod for Chromium Ion Removal from Wastewater. *Journal of Energy Technologies and Policy, 3*, 489-494.

[65]   Yang, J. X., Lukashuk, L., Li, H., Fottinger, K., Rupprechter, G.and Schubert, U. (2014). High Surface Area Ceria for CO Oxidation Prepared from Cerium t-Butoxide by Combined Sol-Gel and Solvothermal Processing. *Catalysis Letters, 144*, 403-412.

[66]   Guillou, N., Nistor, L. C., Fuess, H.and Hahn, H. (1997). Microstructural Studies of Nanocrystalline CeO_2 Produced by Gas Condensation. *Nanostructured Materials, 8*, 545-557.

[67]   Laberty-Robert, C., Long, J. W., Lucas, E. M., Pettigrew, K. A., Stroud, R. M., Doescher, M. S.and Rolison, D. R. (2006). Sol-Gel-derived Ceria Nanoarchitectures: Synthesis, Characterization, and Electrical Properties. *Chemistry of Materials, 18*, 50-58.

[68]   Agrafiotis, C., Tsetsekou, A., Stournaras, C. J., Julbe, A., Dalmazio, L., Guizard, C., Boretto, G., Debenedetti, M.and Parussa, F. (2001). Evaluation of Sol-Gel

Methods for the Synthesis of Doped-Ceria Environmental Catalysis Systems - Part II. Catalytic Activity and Resistance to Thermal Aging. *Applied Catalysis B-Environmental, 34*, 149-159.

[69] Ramanathan, S.and Roy, S. K. (2003). Ceria Powders by Homogeneous Precipitation Technique. *Transactions of the Indian Ceramic Society, 62*, 88-91.

[70] Tok, A. I. Y., Du, S. W., Boey, F. Y. C.and Chong, W. K. (2007). Hydrothermal Synthesis and Characterization of Rare Earth Doped Ceria Nanoparticles. *Materials Science and Engineering a-Structural Materials Properties Microstructure and Processing, 466*, 223-229.

[71] Aliotta, C., Liotta, L. F., La Parola, V., Martorana, A., Muccillo, E. N. S., Muccillo, R.and Deganello, F. (2016). Ceria-based Electrolytes Prepared by Solution Combustion Synthesis: The Role of Fuel on the Materials Properties. *Applied Catalysis B-Environmental, 197*, 14-22.

[72] Gonzalez-Delacruz, V. M., Ternero, F., Pereñíguez, R., Caballero, A.and Holgado, J. P. (2010). Study of Nanostructured Ni/CeO_2 Catalysts Prepared by Combustion Synthesis in Dry Reforming of Methane. *Applied Catalysis A: General, 384*, 1-9.

[73] Thundathil, M. A., Lai, W., Noailles, L., Dunn, B. S.and Haile, S. M. (2004). High Surface-area Ceria Aerogel. *Journal of the American Ceramic Society, 87*, 1442-1445.

[74] Bumajdad, A., Zaki, M. I., Eastoe, J.and Pasupulety, L. (2004). Microemulsion-based Synthesis of CeO_2 Powders with High Surface Area and High-Temperature Stabilities. *Langmuir, 20*, 11223-11233.

[75] Mokkelbost, T., Kaus, I., Grande, T.and Einarsrud, M. A. (2004). Combustion Synthesis and Characterization of Nanocrystalline CeO_2-based Powders. *Chemistry of Materials, 16*, 5489-5494.

[76] Chen, W. F., Li, F. S.and Yu, J. Y. (2006). Combustion Synthesis and Characterization of Nanocrystalline CeO_2-based Powders via Ethylene Glycol-Nitrate Process. *Materials Letters, 60*, 57-62.

[77] Voskanyan, A. A., Chan, K. Y.and Li, C. Y. V. (2016). Colloidal Solution Combustion Synthesis: Toward Mass Production of a Crystalline Uniform Mesoporous CeO_2 Catalyst with Tunable Porosity. *Chemistry of Materials, 28*, 2768-2775.

[78] Voskanyan, A. A.and Chan, K. Y. (2015). Solution Combustion Synthesis using Furfuryl Alcohol as Fuel and a Combustible Solvent. *Journal of Experimental Nanoscience, 10*, 466-475.

[79] Ravishankar, T. N., Ramakrishnappa, T., Nagaraju, G.and Rajanaika, H. (2015). Synthesis and Characterization of CeO_2 Nanoparticles via Solution Combustion

Method for Photocatalytic and Antibacterial Activity Studies. *Chemistryopen, 4*, 146-154.

[80] Garcia, R., Hirata, G. A.and McKittrick, J. (2001). New Combustion Synthesis Technique for the Production of $(In_xGa_{1-x})_2O_3$ Powders: Hydrazine/Metal Nitrate Method. *Journal of Materials Research, 16*, 1059-1065.

[81] Kang, W., Ozgur, D. O.and Varma, A. (2018). Solution Combustion Synthesis of High Surface Area CeO_2 Nanopowders for Catalytic Applications: Reaction Mechanism and Properties. *ACS Applied Nano Materials, 1*, 675-685.

[82] Shiryaev, A. A. (1995). Thermodynamics of SHS Processes: Advanced Approach. *Int. J. Self-Propagating High Temp. Synth., 4*, 351-362.

[83] Cullity, B. D.and Stock, S. R. (2001). *Elements of X-ray Diffraction* 3rd ed.). Upper Saddle River, NJ: Prentice Hall.

[84] Ayodele, B. V., Hossain, M. A., Chong, S. L., Soh, J. C., Abdullah, S., Khan, M. R.and Cheng, C. K. (2016). Non-isothermal Kinetics and Mechanistic Study of Thermal Decomposition of Light Rare Earth Metal Nitrate Hydrates using Thermogravimetric Analysis. *Journal of Thermal Analysis and Calorimetry, 125*, 423-435.

[85] Kumar, A., Wolf, E. E.and Mukasyan, A. S. (2011). Solution Combustion Synthesis of Metal Nanopowders: Nickel-Reaction Pathways. *Aiche Journal, 57*, 2207-2214.

[86] Li, J., Wang, Z. Y., Yang, X., Hu, L., Liu, Y. W.and Wang, C. X. (2007). Evaluate the Pyrolysis Pathway of Glycine and Glycylglycine by TG-FTIR. *Journal of Analytical and Applied Pyrolysis, 80*, 247-253.

[87] Bedford, G.and Thomas, J. H. (1972). Reaction between Ammonia and Nitrogen-Dioxide. *Journal of the Chemical Society-Faraday Transactions I, 68*, 2163-2170.

[88] Březina, F.and Rosický, J. (1963). Untersuchung des Thermischen Zerfalles der Cernitratokomplexe. *Monatshefte für Chemie und verwandte Teile anderer Wissenschaften, 94*, 306-311.

[89] Bondioli, F., Corradi, A. B., Leonelli, C.and Manfredini, T. (1999). Nanosized CeO_2 Powders Obtained by Flux Method. *Materials Research Bulletin, 34*, 2159-2166.

[90] Stevenson, S. A.and Vartuli, J. C. (2002). The Selective Catalytic Reduction of NO_2 by NH_3 over HZSM-5. *Journal of Catalysis, 208*, 100-105.

[91] Zhang, X. Y., Shen, Q., He, C., Ma, C. Y., Cheng, J., Li, L. D.and Hao, Z. P. (2012). Investigation of Selective Catalytic Reduction of N_2O by NH_3 over an Fe-Mordenite Catalyst: Reaction Mechanism and O_2 Effect. *Acs Catalysis, 2*, 512-520.

[92]   Sherikar, B. N.and Umarji, A. M. (2011). Effect of Adiabatic Flame Temperature on Nano Alumina Powders During Solution Combustion Process. *Transactions of the Indian Ceramic Society, 70*, 167-172.

[93]   Patil, K. C. (1986). Metal-Hydrazine Complexes as Precursors to Oxide Materials. *Proceedings of the Indian Academy of Sciences-Chemical Sciences, 96*, 459-464.

[94]   Patil, K. C.and Rattan, T. M. (2014). *Inorganic Hydrazine Derivatives: Synthesis, Properties, and Applications*): John Wiley&Sons, Ltd.

[95]   Patil, K. C., Nesamani, C.and Verneker, V. R. P. (1982). Synthesis and Characterization of Metal Hydrazine Nitrate, Azide and Perchlorate Complexes. *Synthesis and Reactivity in Inorganic and Metal-Organic Chemistry, 12*, 383-395.

[96]   Ferraro, J. R. (1971). *Low-frequency Vibrations of Inorganic and Coordination Compounds*). New York,: Plenum Press.

[97]   Kato, R.and Rolfe, J. (1967). Vibration Frequencies of $NO^{2-}$and NO^{3-} Ions in Kbr Crystals. *Journal of Chemical Physics, 47*, 1901-1910.

[98]   Kim, B. S., Hunter, P. L.and Johnston, H. S. (1992). No_3 Radical Studied by Laser-Induced Fluorescence. *Journal of Chemical Physics, 96*, 4057-4067.

[99]   Frezzotti, M. L., Tecce, F.and Casagli, A. (2012). Raman Spectroscopy for Fluid Inclusion Analysis. *Journal of Geochemical Exploration, 112*, 1-20.

[100]   Kang, W., Ozgur, D. O.and Varma, A. (2018). Solution Combustion Synthesis of High Surface Area CeO2 Nanopowders for Catalytic Applications: Reaction Mechanism and Properties. *ACS Applied Nano Materials*.

[101]   Kuo, K. K. (1986). *Principles of Combustion*). New York: Wiley.

[102]   Feick, G.and Hainer, R. M. (1954). On the Thermal Decomposition of Ammonium Nitrate. Steady-state Reaction Temperatures and Reaction Rate. *Journal of the American Chemical Society, 76*, 5860-5863.

[103]   Wang, N., Qian, W. Z., Chu, W.and Wei, F. (2016). Crystal-Plane Effect of Nanoscale CeO_2 on the Catalytic Performance of Ni/CeO_2 Catalysts for Methane Dry Reforming. *Catalysis Science & Technology, 6*, 3594-3605.

[104]   Beste, A.and Overbury, S. H. (2015). Pathways for Ethanol Dehydrogenation and Dehydration Catalyzed by Ceria (111) and (100) Surfaces. *Journal of Physical Chemistry C, 119*, 2447-2455.

[105]   Cui, J. L.and Hope, G. A. (2015). Raman and Fluorescence Spectroscopy of CeO_2, Er_2O_3, Nd_2O_3, Tm_2O_3, Yb_2O_3, La_2O_3, and Tb_4O_7. *Journal of Spectroscopy, 2015*, 940172.

[106] Wu, Z. L., Li, M. J., Howe, J., Meyer, H. M.and Overbury, S. H. (2010). Probing Defect Sites on CeO_2 Nanocrystals with Well-Defined Surface Planes by Raman Spectroscopy and O_2 Adsorption. *Langmuir, 26*, 16595-16606.

[107] Ferrari, A. C. (2007). Raman Spectroscopy of Graphene and Graphite: Disorder, Electron-phononECoupling, Doping and Nonadiabatic Effects. *Solid State Communications, 143*, 47-57.

[108] Babitha, K. K., Sreedevi, A., Priyanka, K. P., Sabu, B.and Varghese, T. (2015). Structural Characterization and Optical Studies of CeO_2 Nanoparticles Synthesized by Chemical Precipitation. *Indian Journal of Pure & Applied Physics, 53*, 596-603.

[109] Ambursa, M. M., Ali, T. H., Voon, L. H., Sudarsanam, P., Bhargava, S. K.and Abd Hamid, S. B. (2016). Hydrodeoxygenation of Dibenzofuran to Bicyclic Hydrocarbons using Bimetallic Cu-Ni Catalysts Supported on Metal Oxides. *Fuel, 180*, 767-776.

[110] Deshpande, S., Patil, S., Kuchibhatla, S. V. N. T.and Seal, S. (2005). Size Dependency Variation in Lattice Parameter and Valency States in Nanocrystalline Cerium Oxide. *Applied Physics Letters, 87*, 133113.

[111] Hailstone, R. K., DiFrancesco, A. G., Leong, J. G., Allston, T. D.and Reed, K. J. (2009). A Study of Lattice Expansion in CeO_2 Nanoparticles by Transmission Electron Microscopy. *Journal of Physical Chemistry C, 113*, 15155-15159.

[112] Mcbride, J. R., Hass, K. C., Poindexter, B. D.and Weber, W. H. (1994). Raman and X-Ray Studies of $Ce_{1-x}Re_xO_{2-y}$, Where Re=La, Pr, Nd, Eu, Gd, and Tb. *Journal of Applied Physics, 76*, 2435-2441.

[113] Jiang, D., Wang, W. Z., Gao, E. P., Sun, S. M.and Zhang, L. (2014). Highly Selective Defect-mediated Photochemical CO_2 Conversion over Fluorite Ceria under Ambient Conditions. *Chemical Communications, 50*, 2005-2007.

[114] Liang, F. L., Yu, Y., Zhou, W., Xu, X. Y.and Zhu, Z. H. (2015). Highly Defective CeO_2 as a Promoter for Efficient and Stable Water Oxidation. *Journal of Materials Chemistry A, 3*, 634-640.

[115] Della Mea, G. B., Matte, L. P., Thill, A. S., Lobato, F. O., Benvenutti, E. V., Arenas, L. T., Jurgensen, A., Hergenroder, R., Poletto, F.and Bernardi, F. (2017). Tuning the Oxygen Vacancy Population of Cerium Oxide (CeO_{2-x}, $0 < x < 0.5$) Nanoparticles. *Applied Surface Science, 422*, 1102-1112.

[116] Tian, W., Yin, J., Wei, L. F., Shen, Q. H., Bibi, R., Liu, M., Yang, B., Li, N. X.and Zhou, J. C. (2017). Hydrothermally Prepared Nanosized and Mesoporous $Ce_{0.4}Zr_{0.6}O_2$ Solid Solutions with Shape Dependence in Photocatalysis for the Degradation of Methylene Blue. *Rsc Advances, 7*, 17020-17029.

[117] Zeng, X. L., Huo, X. Y., Zhu, T. L., Hong, X. W.and Sun, Y. (2016). Catalytic Oxidation of NO over MnO_x-CeO_2 and MnO_x-TiO_2 Catalysts. *Molecules, 21*, 1491.

[118] Dutta, P., Pal, S., Seehra, M. S., Shi, Y., Eyring, E. M.and Ernst, R. D. (2006). Concentration of Ce^{3+} and Oxygen Vacancies in Cerium Oxide Nanoparticles. *Chemistry of Materials, 18*, 5144-5146.

[119] Hartmann, P., Brezesinski, T., Sann, J., Lotnyk, A., Eufinger, J. P., Kienle, L.and Janek, J. (2013). Defect Chemistry of Oxide Nanomaterials with High Surface Area: Ordered Mesoporous Thin Films of the Oxygen Storage Catalyst CeO_2-ZrO_2. *Acs Nano, 7*, 2999-3013.

[120] Babu, S., Thanneeru, R., Inerbaev, T., Day, R., Masunov, A. E., Schulte, A.and Seal, S. (2009). Dopant-mediated Oxygen Vacancy Tuning in Ceria Nanoparticles. *Nanotechnology, 20*, 085713.

[121] Thommes, M., Kaneko, K., Neimark, A. V., Olivier, J. P., Rodriguez-Reinoso, F., Rouquerol, J.and Sing, K. S. W. (2015). Physisorption of Gses, with Special Reference to the Evaluation of Surface Area And Pore Size DIstribution (IUPAC Technical Report). *Pure and Applied Chemistry, 87*, 1051-1069.

[122] Manukyan, K. V., Cross, A., Rouvimov, S., Miller, J., Mukasyan, A. S.and Wolf, E. E. (2014). Low Temperature Decomposition of Hydrous Hydrazine over FeNi/Cu Nanoparticles. *Applied Catalysis a-General, 476*, 47-53.

[123] Bhattacharjee, D.and Dasgupta, S. (2015). Trimetallic NiFePd Nanoalloy Catalysed Hydrogen Generation from Alkaline Hydrous Hydrazine and Sodium Borohydride at Room Temperature. *Journal of Materials Chemistry A, 3*, 24371-24378.

[124] Song-Il, O., Yan, J. M., Wang, H. L., Wang, Z. L.and Jiang, Q. (2014). High Catalytic Kinetic Performance of Amorphous CoPt NPs Induced on CeO_x for H_2 Generation from Hydrous Hydrazine. *International Journal of Hydrogen Energy, 39*, 3755-3761.

[125] Sun, J.-K.and Xu, Q. (2015). Metal Nanoparticles Immobilized on Carbon Nanodots as Highly Active Catalysts for Hydrogen Generation from Hydrazine in Aqueous Solution. *ChemCatChem, 7*, 526-531.

[126] Wu, D. D., Wen, M., Lin, X. J., Wu, Q. S., Gu, C.and Chen, H. X. (2016). A NiCo/NiO-CoO_x Ultrathin Layered Catalyst with Strong Basic Sites for High-performance H_2 Generation from Hydrous Hydrazine. *Journal of Materials Chemistry A, 4*, 6595-6602.

[127] He, L., Huang, Y. Q., Wang, A. Q., Liu, Y., Liu, X. Y., Chen, X. W., Delgado, J. J., Wang, X. D.and Zhang, T. (2013). Surface Modification of Ni/Al_2O_3 with Pt: Highly Efficient Catalysts for H_2 Generation via Selective Decomposition of Hydrous Hydrazine. *Journal of Catalysis, 298*, 1-9.

[128]   Firdous, N., Janjua, N. K., Qazi, I.and Sarwar Wattoo, M. H. (2016). Optimal Co–Ir Bimetallic Catalysts Supported on γ-Al$_2$O$_3$ for Hydrogen Generation From Hydrous Hydrazine. *International Journal of Hydrogen Energy, 41*, 984-995.

[129]   O, S. I., Yan, J. M., Wang, H. L., Wang, Z. L.and Jiang, Q. (2014). Ni/La$_2$O$_3$ Catalyst Containing Low Content Platinum-Rhodium For the Dehydrogenation of N$_2$H$_4$·H$_2$O at Room Temperature. *Journal of Power Sources, 262*, 386-390.

[130]   He, L., Huang, Y., Liu, X. Y., Li, L., Wang, A., Wang, X., Mou, C.-Y.and Zhang, T. (2014). Structural and Catalytic Properties of Supported Ni–Ir Alloy Catalysts for H$_2$ Generation via Hydrous Hydrazine Decomposition. *Applied Catalysis B: Environmental, 147*, 779-788.

[131]   Singh, S. K., Lu, Z. H.and Xu, Q. (2011). Temperature-induced Enhancement of Catalytic Performance in Selective Hydrogen Generation from Hydrous Hydrazine with Ni-based Nanocatalysts for Chemical Hydrogen Storage. *European Journal of Inorganic Chemistry*2232-2237.

[132]   Zhu, Q. L., Zhong, D. C., Demirci, U. B.and Xu, Q. (2014). Controlled Synthesis of Ultrafine Surfactant-Free NiPt Nanocatalysts toward Efficient and Complete Hydrogen Generation from Hydrazine Borane at Room Temperature. *Acs Catalysis, 4*, 4261-4268.

[133]   Chen, J. M., Yao, Q. L., Zhu, J., Chen, X. S.and Lu, Z. H. (2016). Rh-Ni Nanoparticles Immobilized on Ce(OH)CO$_3$ Nanorods as Highly Efficient Catalysts for Hydrogen Generation from Alkaline Solution of Hydrazine. *International Journal of Hydrogen Energy, 41*, 3946-3954.

[134]   Pokol, G., Leskela, T.and Niinisto, L. (1994). Thermal-behavior of Sulfato and Nitrato Complexes of Cerium(Iv). *Journal of thermal analysis, 42*, 343-359.

[135]   Vratny, F., Kern, S.and Gugliotta, F. (1961). The Thermal Decomposition of Cerium (III) Nitrate Hydrate. *Journal of Inorganic and Nuclear Chemistry, 17*, 281-285.

[136]   Shannon, R. (1976). Revised Effective Ionic Radii and Systematic Studies of Interatomic Distances in Halides and Chalcogenides. *Acta Crystallographica Section A, 32*, 751-767.

[137]   Liu, X., Zuo, Y., Li, L., Huang, X.and Li, G. (2014). Heterosturcture NiO/Ce$_{1-x}$Ni$_x$O$_2$: Synthesis and Synergistic Effect of Simultaneous Surface Modification and Internal Doping for Superior Catalytic Performance. *Rsc Advances, 4*, 6397-6406.

[138]   Rao, P. V. R., Kumar, V. P., Rao, G. S.and Chary, K. V. R. (2012). Vapor Phase Selective Hydrogenation of Acetone to Methyl Isobutyl Ketone (MIBK) over Ni/CeO$_2$ catalysts. *Catalysis Science & Technology, 2*, 1665-1673.

[139] Pengpanich, S., Meeyoo, V.and Rirksomboon, T. (2004). Methane Partial Oxidation over Ni/CeO$_2$-ZrO$_2$ Mixed Oxide Solid Solution Catalysts. *Catalysis Today, 93-5*, 95-105.

[140] Shan, W., Luo, M., Ying, P., Shen, W.and Li, C. (2003). Reduction Property and Catalytic Activity of Ce$_{1-x}$Ni$_x$O$_2$ Mixed Oxide Catalysts for CH$_4$ Oxidation. *Applied Catalysis A: General, 246*, 1-9.

[141] Jalowiecki-Duhamel, L., Zarrou, H.and D'Huysser, A. (2008). Hydrogen Production at Low Temperature from Methane on Cerium and Nickel based Mixed Oxides. *International Journal of Hydrogen Energy, 33*, 5527-5534.

[142] Lamonier, C., Ponchel, A., D'Huysser, A.and Jalowiecki-Duhamel, L. (1999). Studies of the Cerium-Metal–Oxygen–Hydrogen system (metal=Cu, Ni). *Catalysis Today, 50*, 247-259.

[143] Biswas, P.and Kunzru, D. (2007). Steam Reforming of Ethanol for Production of Hydrogen over Ni/CeO$_2$-ZrO$_2$ Catalyst: Effect of Support and Metal Loading. *International Journal of Hydrogen Energy, 32*, 969-980.

[144] Ertl, G., Knözinger, H.and Weitkamp, J. (1997). *Handbook of Heterogeneous Catalysis*). Weinheim: VCH.

[145] Davis, M. E.and Davis, R. J. (2003). *Fundamentals of Chemical Reaction Engineering* 1st ed.). Boston: McGraw-Hill.

[146] Zhang, Z. J., Lu, Z. H., Tan, H. L., Chen, X. S.and Yao, Q. L. (2015). CeO$_x$-modified RhNi Nanoparticles Grown on rGO as Highly Efficient Catalysts for Complete Hydrogen Generation from Hydrazine Borane and Hydrazine. *Journal of Materials Chemistry A, 3*, 23520-23529.

[147] He, L., Huang, Y. Q., Wang, A. Q., Wang, X. D.and Zhang, T. (2013). H$_2$ Production by Selective Decomposition of Hydrous Hydrazine over Raney Ni Catalyst under Ambient Conditions. *Aiche Journal, 59*, 4297-4302.

[148] Kang, W.and Varma, A. (2018). Hydrogen Generation from Hydrous Hydrazine over Ni/CeO$_2$ Catalysts Prepared by Solution Combustion Synthesis. *Applied Catalysis B-Environmental, 220*, 409-416.

[149] Wang, J., Li, W., Wen, Y. R., Gu, L.and Zhang, Y. (2015). Rh-Ni-B Nanoparticles as Highly Efficient Catalysts for Hydrogen Generation from Hydrous Hydrazine. *Advanced Energy Materials, 5*, 1401879.

[150] Zhao, P., Cao, N., Su, J., Luo, W.and Cheng, G. (2015). NiIr Nanoparticles Immobilized on the Pores of MIL-101 as Highly Efficient Catalyst toward Hydrogen Generation from Hydrous Hydrazine. *Acs Sustainable Chemistry & Engineering, 3*, 1086-1093.

[151] Wang, H. L., Yan, J. M., Li, S. J., Zhang, X. W.and Jiang, Q. (2015). Noble-Metal-Free NiFeMo Nanocatalyst for Hydrogen Generation from the Decomposition of Hydrous Hydrazine. *Journal of Materials Chemistry A, 3*, 121-124.

[152] Gao, W., Li, C. M., Chen, H., Wu, M., He, S., Wei, M., Evans, D. G.and Duan, X. (2014). Supported Nickel-Iron Nanocomposites as a Bifunctional Catalyst towards Hydrogen Generation from $N_2H_4 \cdot H_2O$. *Green Chemistry, 16*, 1560-1568.

[153] Wu, D. D., Wen, M., Gu, C.and Wu, Q. S. (2017). 2D NiFe/CeO$_2$ Basic-Site-Enhanced Catalyst via in-Situ Topotactic Reduction for Selectively Catalyzing the H_2 Generation from $N_2H_4 \cdot H_2O$. *Acs Applied Materials & Interfaces, 9*, 16103-16108.

[154] Chen, L. C.and Lin, S. D. (2011). The Ethanol Steam Reforming over Cu-Ni/SiO$_2$ Catalysts: Effect of Cu/Ni ratio. *Applied Catalysis B-Environmental, 106*, 639-649.

[155] Saw, E. T., Oemar, U., Tan, X. R., Du, Y., Borgna, A., Hidajat, K.and Kawi, S. (2014). Bimetallic Ni-Cu Catalyst Supported on CeO$_2$ for High-Temperature Water-Gas Shift Reaction: Methane Suppression via Enhanced CO Adsorption. *Journal of Catalysis, 314*, 32-46.

[156] Margossian, T., Larmier, K., Kim, S. M., Krumeich, F., Müller, C.and Copéret, C. (2017). Supported Bimetallic NiFe Nanoparticles through Colloid Synthesis for Improved Dry Reforming Performance. *Acs Catalysis, 7*, 6942-6948.

[157] Djinovic, P., Crnivec, I. G. O., Erjavec, B.and Pintar, A. (2012). Influence of Active Metal Loading and Oxygen Mobility on Coke-free Dry Reforming of Ni-Co Bimetallic Catalysts. *Applied Catalysis B-Environmental, 125*, 259-270.

[158] Yen, H. A., Seo, Y., Kaliaguine, S.and Kleitz, F. (2015). Role of Metal-Support Interactions, Particle Size, and Metal-Metal Synergy in CuNi Nanocatalysts for H_2 Generation. *Acs Catalysis, 5*, 5505-5511.

[159] Aranishi, K., Singh, A. K.and Xu, Q. (2013). Dendrimer-Encapsulated Bimetallic Pt-Ni Nanoparticles as Highly Efficient Catalysts for Hydrogen Generation from Chemical Hydrogen Storage Materials. *ChemCatChem, 5*, 2248-2252.

[160] Tong, D. G., Tang, D. M., Chu, W., Gu, G. F.and Wu, P. (2013). Monodisperse Ni$_3$Fe Single-crystalline Nanospheres as a Highly Efficient Catalyst for the Complete Conversion of Hydrous Hydrazine to Hydrogen at Room Temperature. *Journal of Materials Chemistry A, 1*, 6425-6432.

[161] Singh, S. K.and Xu, Q. A. (2010). Bimetallic Ni-Pt Nanocatalysts for Selective Decomposition of Hydrazine in Aqueous Solution to Hydrogen at Room Temperature for Chemical Hydrogen Storage. *Inorganic Chemistry, 49*, 6148-6152.

[162] Dai, H., Qiu, Y. P., Dai, H. B.and Wang, P. (2017). A study of Degradation Phenomenon of Ni-Pt/CeO$_2$ Catalyst towards Hydrogen Generation from Hydrous Hydrazine. *International Journal of Hydrogen Energy, 42*, 16355-16361.

[163] Studt, F., Abild-Pedersen, F., Wu, Q., Jensen, A. D., Temel, B., Grunwaldt, J.-D.and Nørskov, J. K. (2012). CO Hydrogenation to Methanol on Cu–Ni Catalysts: Theory and Experiment. *Journal of Catalysis, 293*, 51-60.

[164] Shen, Y., Zhou, Y., Wang, D., Wu, X., Li, J.and Xi, J. (2018). Nickel–Copper Alloy Encapsulated in Graphitic Carbon Shells as Electrocatalysts for Hydrogen Evolution Reaction. *Advanced Energy Materials, 8*, 1701759.

[165] Ray, K.and Deo, G. (2017). A Potential Descriptor for the CO$_2$ Hydrogenation to CH$_4$ over Al$_2$O$_3$ Supported Ni and Ni-based Alloy Catalysts. *Applied Catalysis B: Environmental, 218*, 525-537.

[166] Zhang, Q. F., Wu, X. P., Li, Y. K., Chai, R. J., Zhao, G. F., Wang, C. Z., Gong, X. Q., Liu, Y.and Lu, Y. (2016). High-Performance PdNi Nanoalloy Catalyst in Situ Structured on Ni Foam for Catalytic Deoxygenation of Coalbed Methane: Experimental and DFT Studies. *Acs Catalysis, 6*, 6236-6245.

[167] Ahn, S. H., Park, H. Y., Choi, I., Yoo, S. J., Hwang, S. J., Kim, H. J., Cho, E., Yoon, C. W., Park, H., Son, H., Hernandez, J. M., Nam, S. W., Lim, T. H., Kim, S. K.and Jang, J. H. (2013). Electrochemically Fabricated NiCu Alloy Catalysts for Hydrogen Production in Alkaline Water Electrolysis. *International Journal of Hydrogen Energy, 38*, 13493-13501.

[168] Sun, S. M., Zhao, X. L., Lu, H., Zhang, Z. D., Wei, J. J.and Yang, Y. Z. (2013). Unusual Properties of Nanostructured Ce$_{1-x}$Co$_x$O$_{2-y}$, Ce$_{1-x}$Ni$_x$O$_{2-y}$ and Ce$_{1-(x+y)}$Co$_x$Ni$_y$O$_{2-z}$: Structural Studies and Catalytic Activity. *Crystengcomm, 15*, 1370-1376.

[169] Chen, J. F., Zhan, Y. Y., Zhu, J. J., Chen, C. Q., Lin, X. Y.and Zheng, Q. (2010). The Synergetic Mechanism between Copper Species and Ceria in NO Abatement over Cu/CeO$_2$ Catalysts. *Applied Catalysis a-General, 377*, 121-127.

[170] Poole, C. P.and Bar′iakhtar, V. G. e. (2004). *Encyclopedic Dictionary of Condensed Matter Physics* 1st ed.). Amsterdam ; Boston: Elsevier.

[171] Yan, B., Yang, X., Yao, S., Wan, J., Myint, M., Gomez, E., Xie, Z., Kattel, S., Xu, W.and Chen, J. G. (2016). Dry Reforming of Ethane and Butane with CO$_2$ over PtNi/CeO$_2$ Bimetallic Catalysts. *Acs Catalysis, 6*, 7283-7292.

[172] Wang, F., He, S., Chen, H., Wang, B., Zheng, L. R., Wei, M., Evans, D. G.and Duan, X. (2016). Active Site Dependent Reaction Mechanism over Ru/CeO$_2$ Catalyst toward CO$_2$ Methanation. *Journal of the American Chemical Society, 138*, 6298-6305.

[173] Senanayake, S. D., Ramirez, P. J., Waluyo, I., Kundu, S., Mudiyanselage, K., Liu, Z. Y., Liu, Z., Axnanda, S., Stacchiola, D. J., Evans, J.and Rodriguez, J. A. (2016). Hydrogenation of CO_2 to Methanol on CeO_x/Cu(111) and ZnO/Cu(111) Catalysts: Role of the Metal-Oxide Interface and Importance of Ce^{3+} Sites. *Journal of Physical Chemistry C, 120*, 1778-1784.

[174] Chen, G. X., Li, Q. L., Wei, Y. C., Fang, W. P.and Yang, Y. Q. (2013). Low temperature CO oxidation on Ni-promoted CuO-CeO_2 catalysts. *Chinese Journal of Catalysis, 34*, 322-329.

[175] Liu, W.and Flytzanistephanopoulos, M. (1995). Total Oxidation of Carbon Monoxide and Methane over Transition Metal Fluorite Oxide Composite Catalysts: I. Catalyst Composition and Activity. *Journal of Catalysis, 153*, 304-316.

[176] Turco, M., Cammarano, C., Bagnasco, G., Moretti, E., Storaro, L., Talon, A.and Lenarda, M. (2009). Oxidative Methanol Steam Reforming on a Highly Dispersed CuO/CeO_2/Al_2O_3 Catalyst Prepared by a Single-step Method. *Applied Catalysis B: Environmental, 91*, 101-107.

[177] Naghash, A. R., Etsell, T. H.and Xu, S. (2006). XRD and XPS Study of Cu−Ni Interactions on Reduced Copper−Nickel−Aluminum Oxide Solid Solution Catalysts. *Chemistry of Materials, 18*, 2480-2488.

[178] Wei, H., Xie, K., Zhang, J., Zhang, Y., Wang, Y., Qin, Y., Cui, J., Yan, J.and Wu, Y. (2014). In Situ Growth of NixCu1-x Alloy Nanocatalysts on Redox-Reversible Rutile $(Nb,Ti)O_4$ towards High-Temperature Carbon Dioxide Electrolysis. *Scientific Reports, 4*, 5156.

[179] Barbieri, P. F., de Siervo, A., Carazzolle, M. F., Landers, R.and Kleiman, G. G. (2004). XPS and XAES Study of Ag–Pd and Cu–Ni Alloys: Spectra, Shifts and Electronic Structure Information. *Journal of Electron Spectroscopy and Related Phenomena, 135*, 113-118.

[180] Pauly, N., Tougaard, S.and Yubero, F. (2014). Determination of the Cu 2p Primary Excitation Spectra for Cu, Cu_2O and CuO. *Surface Science, 620*, 17-22.

[181] Kim, S. H., Lee, W. D.and Lee, H. I. (2013). Effect of CeO_2 on CO Removal over CeO_2-modfied Ni Catalyst in CO-rich Syngas. *Korean Journal of Chemical Engineering, 30*, 860-863.

[182] Chen, S. Q., Li, L. P., Hu, W. B., Huang, X. S., Li, Q., Xu, Y. S., Zuo, Y.and Li, G. S. (2015). Anchoring High-Concentration Oxygen Vacancies at Interfaces of CeO_{2-x}/Cu toward Enhanced Activity for Preferential CO Oxidation. *Acs Applied Materials & Interfaces, 7*, 22999-23007.

[183] Liang, T., Wang, Y., Chen, M., Yang, Z., Liu, S., Zhou, Z.and Li, X. (2017). Steam Reforming of Phenol-Ethanol to Produce Hydrogen over Bimetallic NiCu Catalysts Supported on Sepiolite. *International Journal of Hydrogen Energy, 42*, 28233-28246.

[184] Ashok, J., Kathiraser, Y., Ang, M. L.and Kawi, S. (2015). Ni and/or Ni–Cu Alloys Supported over SiO_2 Catalysts Synthesized via Phyllosilicate Structures for Steam Reforming of Biomass Tar Reaction. *Catalysis Science & Technology, 5*, 4398-4409.

[185] Murugan, B., Ramaswamy, A. V., Srinivas, D., Gopinath, C. S.and Ramaswamy, V. (2005). Nature of Manganese Species in $Ce_{1-x}Mn_xO_{2-delta}$ Solid Solutions Synthesized by the Solution Combustion Route. *Chemistry of Materials, 17*, 3983-3993.

[186] Hegde, M. S.and Beraba, P. (2015). Noble Metal Ion Substituted CeO_2 Catalysts: Electronic Interaction between Noble Metal Ions and CeO_2 Lattice. *Catalysis Today, 253*, 40-50.

[187] Cheng, Y. X., Wu, X.and Xu, H. (2019). Catalytic Decomposition of Hydrous Hydrazine for Hydrogen Production. *Sustainable Energy & Fuels, 3*, 343-365.

[188] Roiban, L., Koneti, S., Morfin, F., Nguyen, T.-S., Mascunan, P., Aouine, M., Epicier, T.and Piccolo, L. (2017). Uncovering the 3 D Structure of Combustion-Synthesized Noble Metal-Ceria Nanocatalysts. *ChemCatChem, 9*, 4607-4613.

[189] Oliaee, S. N., Zhang, C. L., Hwang, S. Y., Cheung, H. M.and Peng, Z. M. (2016). Hydrogen Production via Hydrazine Decomposition on Model Platinum-Nickel Nanocatalyst with a Single (111) Facet. *Journal of Physical Chemistry C, 120*, 9764-9772.

[190] Kang, W., Guo, H.and Varma, A. (2019). Noble-Metal-Free $NiCu/CeO_2$ Catalysts for H_2 Generation from Hydrous Hydrazine. *Applied Catalysis B: Environmental, 249*, 54-62.

[191] Xiong, L.and Manthiram, A. (2005). Effect of Atomic Ordering on the Catalytic Activity of Carbon Supported PtM (M = Fe, Co, Ni, and Cu) Alloys for Oxygen Reduction in PEMFCs. *Journal of the Electrochemical Society, 152*, A697-A703.

[192] Vayssilov, G. N., Migani, A.and Neyman, K. (2011). Density Functional Modeling of the Interactions of Platinum Clusters with CeO_2 Nanoparticles of Different Size. *Journal of Physical Chemistry C, 115*, 16081-16086.

[193] Lin, L., Yuan, M. W., Sun, Z. M., Li, H. F., Nan, C. Y., Sun, G. B.and Ma, S. L. (2018). The In Situ Growth of Ultrathin Fcc-NiPt Nanocrystals on Graphene for Methanol and Formic Acid Oxidation. *Dalton Transactions, 47*, 15131-15140.

[194] Pal, P., Singha, R. K., Saha, A., Bal, R.and Panda, A. B. (2015). Defect-induced Efficient Partial Oxidation of Methane over Nonstoichiometric Ni/CeO$_2$ Nanocrystals. *Journal of Physical Chemistry C, 119*, 13610-13618.

[195] Piumetti, M., Bensaid, S., Andana, T., Russo, N., Pirone, R.and Fino, D. (2017). Cerium-Copper Oxides Prepared by Solution Combustion Synthesis for Total Oxidation Reactions: From Powder Catalysts to Structured Reactors. *Applied Catalysis B-Environmental, 205*, 455-468.

[196] Li, F. T., Ran, J. R., Jaroniec, M.and Qiao, S. Z. (2015). Solution Combustion Synthesis of Metal Oxide Nanomaterials for Energy Storage and Conversion. *Nanoscale, 7*, 17590-17610.

[197] Bera, P., Priolkar, K. R., Gayen, A., Sarode, P. R., Hegde, M. S., Emura, S., Kumashiro, R., Jayaram, V.and Subbanna, G. N. (2003). Ionic Dispersion of Pt over CeO$_2$ by the Combustion Method: Structural Investigation by XRD, TEM, XPS, and EXAFS. *Chemistry of Materials, 15*, 2049-2060.

[198] Roh, H. S., Jun, K. W., Dong, W. S., Chang, J. S., Park, S. E.and Joe, Y. I. (2002). Highly Active and Stable Ni/Ce-ZrO$_2$ Catalyst for H$_2$ Production from Methane. *Journal of Molecular Catalysis a-Chemical, 181*, 137-142.

[199] Dutta, G., Waghmare, U. V., Baidya, T.and Hegde, M. S. (2007). Hydrogen Spillover on CeO$_2$/Pt: Enhanced Storage of Active Hydrogen. *Chemistry of Materials, 19*, 6430-6436.

[200] Dong, W. S., Roh, H. S., Jun, K. W., Park, S. E.and Oh, Y. S. (2002). Methane Reforming over Ni/Ce-ZrO$_2$ Catalysts: Effect of Nickel Content. *Applied Catalysis a-General, 226*, 63-72.

[201] Du, X., Tan, S., Cai, P., Luo, W.and Cheng, G. (2016). A RhNiP/rGO Hybrid for Efficient Catalytic Hydrogen Generation from an Alkaline Solution of Hydrazine. *Journal of Materials Chemistry A, 4*, 14572-14576.

[202] Kang, W.and Varma, A. (2019). Low Pt Loading NiPt/CeO$_2$ Catalysts for Hydrogen Generation from Hydrous Hydrazine. *Manuscript submitted for publication*.

[203] Miao, X., Chen, M. M., Chu, W., Wu, P.and Tong, D. G. (2016). Mesoporous Face-Centered-Cubic In$_4$Ni Alloy Nanorices: Superior Catalysts for Hydrazine Dehydrogenation in Aqueous Solution. *Acs Applied Materials & Interfaces, 8*, 25268-25278.

[204] Basu, S., Brockman, A., Gagare, P., Zheng, Y., Ramachandran, P. V., Delgass, W. N.and Gore, J. P. (2009). Chemical Kinetics of Ru-catalyzed Ammonia Borane Hydrolysis. *Journal of Power Sources, 188*, 238-243.

[205] Zhang, J. S., Delgass, W. N., Fisher, T. S.and Gore, J. P. (2007). Kinetics of Ru-catalyzed Sodium Borohydride Hydrolysis. *Journal of Power Sources, 164*, 772-781.

[206] Yin, H., Qiu, Y.-P., Dai, H., Gan, L.-Y., Dai, H.-B.and Wang, P. (2018). Understanding of Selective H_2 Generation from Hydrazine Decomposition on Ni(111) Surface. *The Journal of Physical Chemistry C, 122*, 5443-5451.

[207] Satterfield, C. N. (1980). *Heterogeneous Catalysis in Practice*). New York: McGraw-Hill.

[208] Tóth, J. z. (2002). *Adsorption : Theory, Modeling, and Analysis*). New York: Marcel Dekker.

[209] Himmelblau, D. M. (1970). *Process Analysis by Statistical Methods*). New York,: Wiley.

[210] Santacesaria, E., Carrà, S.and Adami, I. (1977). Adsorption of Hexachloroplatinic Acid on γ-Alumina. *Industrial & Engineering Chemistry Product Research and Development, 16*, 41-44.

[211] Piatt, J. J., Backhus, D. A., Capel, P. D.and Eisenreich, S. J. (1996). Temperature-Dependent Sorption of Naphthalene, Phenanthrene, and Pyrene to Low Organic Carbon Aquifer Sediments. *Environmental Science & Technology, 30*, 751-760.

[212] Zhao, J., Li, Y., Zhang, C., Zeng, Q.and Zhou, Q. (2008). Sorption and Degradation of Bisphenol A by Aerobic Activated Sludge. *Journal of Hazardous Materials, 155*, 305-311.

[213] Yang, F., Li, Y. Z., Chu, W., Li, C.and Tong, D. G. (2014). Mesoporous Co–B–N–H Nanowires: Superior Catalysts for Decomposition of Hydrous Hydrazine to Generate Hydrogen. *Catalysis Science & Technology, 4*, 3168-3179.

[214] Levenspiel, O. (1972). Experimental Search for a Simple Rate Equation to Describe Deactivating Porous Catalyst Particles. *Journal of Catalysis, 25*, 265-272.

[215] Meyer, C. I., Marchi, A. J., Monzon, A.and Garetto, T. F. (2009). Deactivation and Regeneration of Cu/SiO_2 Catalyst in the Hydrogenation of Maleic Anhydride. Kinetic Modeling. *Applied Catalysis A: General, 367*, 122-129.

[216] Hattori, H. (1995). Heterogeneous Basic Catalysis. *Chemical Reviews, 95*, 537-558.

[217] Climent, M. J., Corma, A., Iborra, S.and Velty, A. (2002). Synthesis of Methylpseudoionones by Activated Hydrotalcites as Solid Base Catalysts. *Green Chemistry, 4*, 474-480.

[218]   Jang, I. J., Shin, H. S., Shin, N. R., Kim, S. H., Kim, S. K., Yu, M. J.and Cho, S. J. (2012). Macroporous-Mesoporous Alumina Supported Iridium Catalyst for Hydrazine Decomposition. *Catalysis Today, 185*, 198-204.

[219]   Zhao, B. T., Song, J., Ran, R.and Shao, Z. P. (2012). Catalytic Decomposition of Hydrous Hydrazine to Hydrogen overOoxide Catalysts at Ambient Conditions for PEMFCs. *International Journal of Hydrogen Energy, 37*, 1133-1139.

[220]   Adhikari, S.and Fernando, S. (2006). Hydrogen Membrane Separation Techniques. *Industrial & Engineering Chemistry Research, 45*, 875-881.

[221]   Li, Y. S., Liang, F. Y., Bux, H. G., Yang, W. S.and Caro, J. (2010). Zeolitic Imidazolate Framework ZIF-7 based Molecular Sieve Membrane for Hydrogen Separation. *Journal of Membrane Science, 354*, 48-54.

VITA

Wooram Kang was born on December 3, 1986 in Busan, the Republic of Korea. He grew up in Busan and entered Korea University in Seoul on March 2005. He served in the military service in the Republic of Korea Army from January 2007 to December 2008. Then, he received his B.S. degree in Chemical and Biological Engineering from Korea University on February 2011. Subsequently, he pursued his M.S. degree at the same university under Prof. Ki Bong Lee's direction and graduated on February 2013. After this, he worked as a research assistant in the Korea Institute of Science and Technology (KIST) in Seoul until he started his Ph.D. program in the Davidson School of Chemical Engineering at Purdue University, West Lafayette, IN, USA. in the fall of 2014. He joined the research group of Prof. Arvind Varma and has been studying the preparation of various nanomaterials using solution combustion synthesis method, characterization of their physicochemical properties, catalytic performance evaluation of Ni-based catalysts for hydrous hydrazine decomposition and reaction kinetics.

PUBLICATIONS

1. Jang, H.M., **Kang, W.R.** and Lee, K.B. (2013). Sorption-enhanced Water Gas Shift Reaction using Multi-section Column for High-purity Hydrogen Production. *International Journal of Hydrogen Energy*, *38*, 6065-6071.

2. **Kang, W.R.,** and Lee, K.B. (2013). Effect of Operating Parameters on Methanation Reaction for the Production of Synthetic Natural Gas. *Korean Journal of Chemical Engineering*, *30*, 1386-1394.

3. **Kang, W.R.,** and Lee, K.B. (2015). Development of Rare Earth Element-doped Ni-Ba(Ce/Zr)O$_3$ Cermets for Hydrogen-permeable Membranes. *Journal of Industrial and Engineering Chemistry*, *29*, 194-198.

4. **Kang, W.R.**, Lee, A.S., Park, S., Baek, K-Y, Lee, K.B., Lee, J.H., Lee, S.H., Hwang, S.S. and Lee, J.S. (2015). Free-standing, Polysilsesquioxane-based Inorganic/Organic Hybrid Membranes for Gas Separations. *Journal of Membrane Science*, *475*, 384-394.

5. Park. S.[1], **Kang, W.R.[1]**, Kwon, H.T[1]., Kim, S., Seo, M., Bang, J., Lee, S.H., Jeong, H.K. and Lee, J.S. (2015). The Polymeric Upper Bound for N$_2$/NF$_3$ Separation and Beyond; ZIF-8 Containing Mixed Matrix Membranes, *Journal of Membrane Science*, *486*, 29-39.

6. **Kang, W.** and Varma, A. (2018). Hydrogen Generation from Hydrous Hydrazine over Ni/CeO$_2$ Catalysts Prepared by Solution Combustion Synthesis, *Applied Catalysis B: Environmental*, *220*, 409-416.

7. **Kang, W.**, Ozgur, D.O. and Varma, A. (2018). Solution Combustion Synthesis of High Surface Area CeO_2 Nanopowders for Catalytic Applications: Reaction Mechanism and Properties. *ACS Applied Nano Materials*, *1*, 675-685.

8. **Kang, W.**, Guo, H. and Varma, A. (2019). Noble-metal-free $NiCu/CeO_2$ Catalysts for H_2 Generation from Hydrous Hydrazine. *Applied Catalysis B: Environmental*, *249*, 54-62.

9. **Kang, W.**, Walter, E. and Varma, A. Low Pt Loading $NiPt/CeO_2$ Catalysts for Hydrogen Generation from Hydrous Hydrazine. *In the final stage of submission*.

10. **Kang, W.** and Varma, A. Kinetics of Hydrous Hydrazine Decomposition over $NiPt/CeO_2$ Catalysts: Langmuir-Hinshelwood Model and Catalyst Deactivation. *In the final stage of submission*.